KU Leuven
Biomedical Sciences Group
Faculty of Medicine
Department of Microbiology, Immunology
and Transplantation

KU LEUVEN

DOCTORAL SCHOOL
BIOMEDICAL SCIENCES

IP_3R3 VARIANTS AS NOVEL FORM OF HEREDITARY DISORDERS

Julika NEUMANN

Jury:

Supervisor:	Prof. Stéphanie Humblet-Baron
Co-supervisors:	Prof. Adrian Liston
	Prof. Carine Wouters
Chair examining committee:	Prof. Patrick Callaerts
Chair public defence:	Prof. Katrien Lagrou
Jury members:	Prof. Isabelle Cleynen
	Prof. Rik Schrijvers
	Prof. Capucine Picard
	Prof. Martin Bootman

Dissertation presented in partial fulfilment of the requirements for the degree of Doctor in Biomedical Sciences

November 2023

Table of Contents

Table of Contents 4
List of Abbreviations 8
1 Introduction 11
1.1 Variant discovery in monogenic diseases using next-generation sequencing 13
1.1.1 Variant prioritization 14
1.1.2 Functional validation 15
1.1.3 Inborn Errors of Immunity as an example 17
1.2 The Calcium signalling toolkit 19
1.2.1 Calcium homeostasis 19
1.2.2 ER Ca^{2+} depletion and store-operated Calcium entry 21
1.2.3 IP_3R structure and regulation 24
1.2.4 Calcium-dependent downstream signalling 26
1.2.5 Calcium signalling in T-cell development 28
1.3 Defective Calcium signalling in hereditary human disease 30
1.3.1 CRAC-associated disease phenotypes 30
1.3.2 Charcot-Marie-Tooth 31
1.3.3 IP_3R-related diseases 32
2 Research objectives 35
3 *ITPR3* variants causing immunodeficiency 39
3.1 Abstract 41
3.2 Introduction 41
3.3 Materials and Methods 43
3.4 Results 49
3.4.1 Identification of compound heterozygous *ITPR3* variants in two immunodeficient patients 49
3.4.2 Functional impact of the *ITPR3* variants 51
3.4.3 Defective immunological responses in *ITPR3* patients 56
3.5 Discussion 62
3.6 Personal Contribution 66
3.7 Supplementary Material 66
3.7.1 Extended clinical case descriptions 66
3.7.2 Supplementary Figures 70
3.7.3 Supplementary Tables 78

4 *ITPR3* variants causing Charcot-Marie-Tooth disease 83
4.1 Abstract 85
4.2 Introduction 85
4.3 Materials and Methods 86
4.4 Results 88
4.4.1 Autosomal dominant CMT family 88
4.4.2 Single affected individual 91
4.4.3 Genetic findings 92
4.4.4 Protein and mRNA 94
4.4.5 Fibroblast Ca^{2+} flux 94
4.5 Discussion 97
4.6 Personal Contribution 99
4.7 Supplementary Material 99
5 Functional characterization of neuropathy-associated *ITPR3* variants 103
5.1 Abstract 105
5.2 Introduction 105
5.3 Materials and Methods 107
5.4 Results 111
5.4.1 The V615M mutation results in a poorly functional and “leaky” channel 112
5.4.2 The T1424M mutation results in a “leaky” channel that is functional 115
5.4.3 The R2524C mutation forms a functionally dead but leaky channel 119
5.5 Discussion 121
5.6 Personal contribution 125
5.7 Supplementary Material 126
5.7.1 Supplementary Figures 126
5.7.2 Supplementary Videos 135
6 General Discussion 137
6.1 Novel disease entities caused by variants in *ITPR3* 139
6.1.1 Recessive *ITPR3* variants in Inborn Errors of Immunity 140
6.1.2 Dominant *ITPR3* variants in Charcot-Marie-Tooth disease 142
6.1.3 Understanding the different disease phenotypes caused by *ITPR3* variants 144
6.2 Considerations for therapeutic intervention in IP_3R3 deficiency 146
6.3 Conclusion and future perspectives 147
7 References 151
8 Scientific Summary 179

Personal contribution, scientific acknowledgements and conflict of interest 183
Personal contribution 185
Chapter 3 – scientific acknowledgements 185
Author contributions 185
Acknowledgements 185
Conflict of interest 185
Chapter 4 – scientific acknowledgements 186
Author contributions 186
Acknowledgements 186
Conflict of interest 186
Chapter 5 – scientific acknowledgments 187
Author contributions 187
Acknowledgements 187
Conflict of interest 187
Curriculum Vitae 189

List of Abbreviations

(qRT)PCR	(Quantitative real-time) polymerase chain reaction)
(S)CID	(Severe) combined immunodeficiency
BCR	B cell receptor
Ca^{2+}	Calcium
CaM	Calmodulin
CaMK	Calmodulin-dependent protein kinase
CMT	Charcot-Marie-Tooth
CNI	Calcineurin inhibitor
CNS	Central nervous system
CRAC	Calcium-release activated Calcium
CRACR2A	CRAC regulator 2A
CsA	Cyclosporine A
CTD	C-terminal domain
DAG	Diacylglycerol
EDA	Anhidrotic ectodermal dysplasia
ER	Endoplasmic Reticulum
GDAP1	Ganglioside-induced differentiation-associated-protein 1
GDPH	Glycerol phosphate dehydrogenase
GOF	Gain-of-function
GPCR	G-protein coupled receptor
GS	Gillespie syndrome
HSCT	Hematopoietic stem cell transplantation
IEI	Inborn Error of Immunity
IFN	Interferon
IMM	Inner mitochondrial membrane
IP_3	Inositol 1,4,5-trisphosphate
IP_3R1-3	Inositol 1,4,5-trisphosphate receptor subtypes 1-3
IPN	Inherited peripheral neuropathy
IRBIT	IP_3R binding protein released with IP_3
ITPR1-3	Genes encoding Inositol 1,4,5-trisphosphate receptor subtypes 1-3

LBD	Ligand-binding domain
LOE	Loss-of-expression
LOF	Loss-of-function
MAM	Mitochondria-associated membrane
MCU	Mitochondrial Ca^{2+} uniporter
NCX	Na^{+}/Ca^{2+} exchanger
NFAT	Nuclear factor of activated T cells
NGS	Next-generation sequencing
OMM	Outer mitochondrial membrane
PBMC	Peripheral blood mononuclear cell
PCH	Pontine cerebellar hypoplasia
PDH	Pyruvate dehydrogenase
PIP_2	Phosphatidylinositol 4,5-bisphosphate
PKA	Protein kinase A
PLC	Phospholipase C
PMCA	Plasma membrane Ca^{2+} ATPase
ROCC	Receptor-operated Calcium channel
RTK	Receptor tyrosine kinase
RyR	Ryanodine receptor
SCA	Spinocerebellar ataxia
SD	Suppressor domain
SERCA	Sarco-/Endoplasmic Reticulum Ca^{2+} ATPase
SOCE	Store-operated Calcium entry
STAT	Signal transducer and activator of transcription
STIM	Stromal interaction molecule
TCR	T cell receptor
TM	Transmembrane
TREC	T cell receptor excision circles
VDAC	Voltage-dependent anion-selective channel
VOCC	Voltage-operated Calcium channel
WES/WGS	Whole-exome/-genome sequencing

1 Introduction

1.1 Variant discovery in monogenic diseases using next-generation sequencing

Mendelian disorders are disorders caused by the inheritance of a pathogenic variant in a single gene and therefore also called monogenic disorders. According to the well-known principles described by Gregor Mendel in 1865, an allele and hence possible variant would be inherited in a dominant or recessive manner, only one allele – with or without the variant, depending on the genetic status of the individual – would be passed on to the offspring, and different variants would be inherited independently of each other[1]. The Online Mendelian Inheritance in Man (OMIM) database is an impressive testimony to these early findings and contains the description of more than 7,000 phenotypes that are linked to mutations in nearly 5,000 genes (last accessed in August 2023). However, considering that approximately 20,000 protein-coding genes have been identified thus far (The Human Gene Database, last accessed in August 2023), and that each gene can contain different pathogenic variants – occasionally also resulting in different phenotypes – these numbers are expected to keep rising.

Identifying the genetic basis of a disease is usually not only important for the patients themselves, giving them a concrete cause for their condition as well as being important for genetic counselling in case of family planning, but can also guide the management decisions made by the treating physicians. Moreover, monogenic inherited disorders are often referred to as experiments of nature as they can give valuable insight into the physiological functions of a protein by illustrating the consequences of its dysfunction. It is therefore necessary to keep investigating patients with suspected monogenic disorders but an unknown genetic diagnosis to not only improve patient care but also to advance basic scientific knowledge.

Identifying novel variants and genes causing monogenic disorders has greatly been facilitated by the rapid development in next-generation sequencing (NGS) and its analysis. The reduction in cost as well as turn-around time have made it possible to not only consider whole-exome or whole-genome sequencing (WES or WGS) in a research but also clinical diagnostic setting. In some cases, a very distinct clinical presentation of a patient together with the family history can already be suggestive of a small number of possibly involved genes, allowing mutation analysis by Sanger sequencing to obtain a genetic diagnosis[2]. However, such cases are rare and gene panels designed to cover a range of >100 genes linked to the observed phenotype are more frequently performed in a clinical setting as they are more cost- and time-efficient. If this would however not result in the identification of a known or likely pathogenic mutation in the patient, WES would need to be performed in a second step in order to identify previously unidentified genes or variants that could cause the phenotype. For patients presenting with more diffuse phenotypes or unknown features, WES could immediately be prioritized over a possibly negative targeted panel resulting in diagnostic delay and reduced cost efficiency[3]. Additionally, due to the significantly reduced cost of the WES approach and the rather stagnant price of targeted gene panels, it is by now indeed often the preferred option in hospitals with the required infrastructure[4,5]. Similarly,

the higher sequencing costs for WGS compared to WES are partly offset by not needing to perform expensive exon-capture kits and WGS usually provides better coverage even of exons and additionally allows identification of for example intronic variants. Nonetheless, as data storage as well as the bioinformatic infrastructure to process WGS data requires more resources, it is not yet used routinely in a diagnostic setting. In order to facilitate downstream sequencing analysis with a high number of natural variants when compared to the human reference genome, ~20,000 in WES[6], the inclusion of DNA from the parents (trio sequencing) and possible (un-)affected siblings improves strategies for the identification of candidate variants. The informed decision on which variants may be disease-causing and the subsequent validation of the pathogenicity follows a rather defined pipeline and will be described in the following paragraphs.

1.1.1 Variant prioritization

Variant prioritization describes the process of distinguishing likely irrelevant variants from those that are more likely to cause the observed phenotype. To this end, several steps are undertaken to reduce the number of candidate mutations within the pool of variants that differ between the patient and human reference genome[7,8]. Once the sequencing reads for each sequenced family member were compared to the human reference genome and all alternative alleles have been called, they are filtered for variants that are unique to the affected sequenced member(s). Based on the suspected mode of inheritance, lists can be generated containing either heterozygous variants for *de novo* or autosomal dominant variants, (compound) heterozygous variants for autosomal recessive variants, or X-linked variants, which is especially of interest in male patients.

The variants in the list with the suspected mode of inheritance are further prioritized based on their frequency in the general public, using the minor allele frequency reported in genomic databases such as gnomAD[9]. In the case of a suspected dominant inheritance, a cut-off of 1% is often preferred, as variants that are present at a higher rate in the general public are less likely to cause a severe disease phenotype. If a recessive inheritance pattern is suspected, this threshold should however be increased, often to 5% or 10%, as the pathogenic variant may be present and tolerated in a heterozygous state in healthy individuals and therefore be more prevalent in the general public. An additional, usually automated, step is based on the prediction of the functional impact of the respective variant. While synonymous variants are generally considered to have a low impact on protein function, non-synonymous variants can be further prioritized based on their predicted pathogenicity. Tools and scores such as SnpEff[10], PolyPhen[11], or the combined annotation-dependent depletion (CADD) score[12] are used to select those variants that are likely to affect protein function. While complex prediction algorithms are used to calculate these scores, they for example consider whether a variant is located in functionally important protein sites, such as phosphorylation or catalytically active sites, whether they change the charge at a specific domain, or if the position is conserved among species. Candidate variants are those that match the criteria of the suspected inheritance pattern, segregation with the disease phenotype in the family, absence or

low frequency of the variant in public databases, and are predicted to be damaging. While these steps are often automated in bioinformatic pipelines, in addition to monitoring and adapting the aforementioned criteria, trained researchers need to manually screen and prioritize the reminder of variants by considering the likelihood of a specific gene product being involved in the observed clinical phenotype. Thorough literature research is required to for example verify protein expression in relevant cell populations and judge whether decreased – usually in the case of loss-of-expression (LOE) or loss-of-function (LOF) variants – or increased activation – in the case of gain-of-function (GOF) variants – is a plausible pathomechanism explaining the clinical symptoms.

1.1.2 Functional validation

Once a candidate variant has been identified that matches the filtering criteria, functional validation is needed to prove its pathogenicity. In a first step, the presence of mRNA and protein should be analysed in order to identify LOE variants, which could for example be the result of nonsense mediated decay due to homozygous stop-gain variants. If possible, mRNA expression should be investigated in cells directly involved in disease pathology, although fibroblasts or blood are often used as a proxy if this is not feasible. It is important to understand that investigation of mRNA expression by quantitative real-time (qRT) polymerase chain reaction (PCR) is not sufficient to draw conclusions about protein expression levels, as for example ubiquitin-mediated proteasomal degradation of misfolded proteins could result in reduced or absent protein expression, while mRNA expression may be unaffected. Protein expression can be analysed by Western Blot or flow cytometry, the latter allowing to distinguish expression in different cell subsets by including lineage markers in the staining panel.

In the event of a LOE variant, final validation of the pathogenicity of the variant can be established for example by CRISPR-mediated knock-out or siRNA-mediated knock-down of the affected gene in healthy control cells or relevant cell lines and subsequently assessing the effect on downstream signalling pathways that are crucial for cell function. However, if protein expression is not affected by the variant, functional *in vitro* studies are needed to establish the damaging potential of the variant. While these studies can sometimes be performed in primary patient cells if they are readily and sufficiently available, few caveats need to be taken into consideration. While complete LOF variants can often be validated based on the absence of certain signalling intermediates, the extent of residual function of hypomorphic variants can make it difficult to distinguish true pathogenic effects from experimental and inter-individual variation. Similarly, investigation of GOF variants can be challenging due to sometimes marginal increases in activation *in vitro*, that can however be amplified in a self-promoting loop *in vivo* in the patient. In addition, experimental approaches using primary cells are inherently biased by interindividual differences that could unknowingly influence the functional readouts. Ultimate proof of the damaging effect of a variant therefore needs to be given by rescuing a phenotype caused by recessive variants or inducing a phenotype caused by dominant variants. This can be done in either cell lines or primary cells of the patient for a rescue or of a healthy control for a

phenotype induction. The most widely used methods to achieve (over-)expression of a wild-type or mutated protein from a plasmid are chemical transfection or electroporation for generally transient overexpression and lentiviral transduction for stable overexpression. Which method should be chosen is based on the relevant cell-type as well as the nature of the down-stream analysis.

Common read-outs of functional studies vary widely as they are fully dependent on the pathway affected by the variant. Typical approaches investigate *in vitro* activation following cell-specific stimulations by analysing (de-)phosphorylation of pathway components, survival and proliferation, or expression of target genes or cytokines. Often a combination of approaches is needed to verify the pathogenicity of a variant and although some of these basic read-outs may serve to deliver a proof-of-principle, they are often not sufficient to explain the complete pathomechansim and follow-up studies are required to fully explain the variants' impact. An overview of the different steps involved in the bioinformatic and experimental approach for WES/WGS analysis is depicted in **Fig. 1.1**.

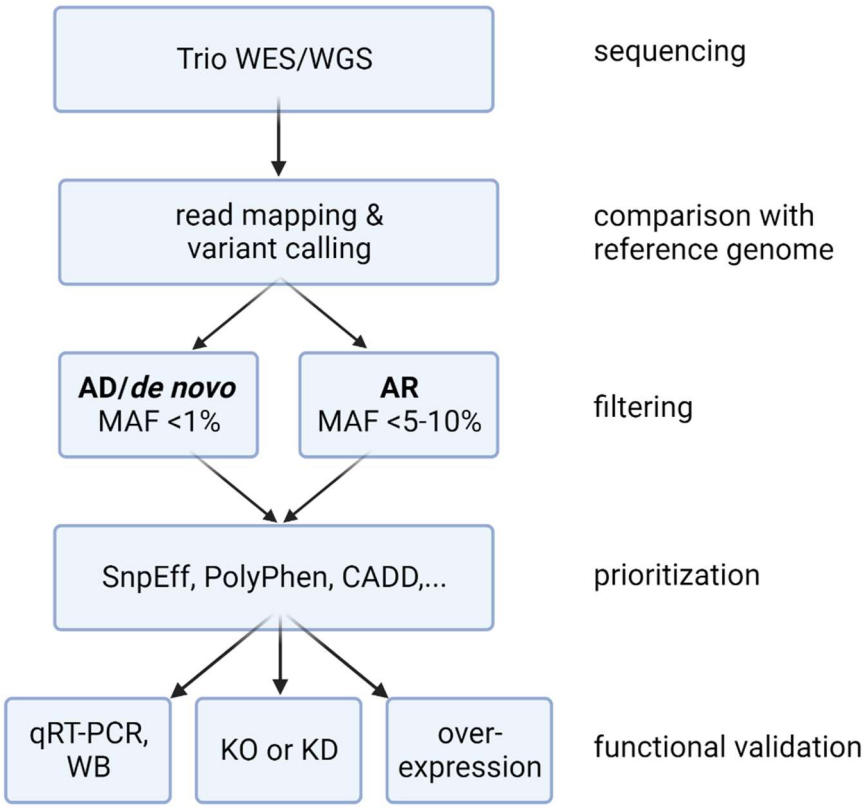

Figure 1.1: WES/WGS analysis workflows for identification of pathogenic variants. Following WES/WGS, reads are mapped to the human reference genome and variants of all individuals are called. Based on the genetic hypothesis, variants are filtered based on the minor allelic frequency (MAF) in public databases for autosomal dominant (AD)/de novo, i.e. homozygous, or autosomal recessive (AR), i.e. (compound) heterozygous, variants. These are then prioritized considering predictions on damage to protein structure or function, conservation, type of amino acid change, etc. Candidate variants are then validated in suitable experimental approaches. For details refer to the main text. qRT-PCR = quantitative real-time PCR; WB = Western Blot; KO = knock-out; KD = knock-down. Figure created with biorender.com.

1.1.3 Inborn Errors of Immunity as an example

One research field that highlights the importance of determining pathology-underlying genetic variants is that of Inborn Errors of Immunity (IEIs). Every day we are exposed to a plethora of foreign organisms that could exert their role as pathogen and make us sick. Most of the time however we are not aware of these encounters as we are protected from these organisms by different mechanisms. While our skin is a first physical barrier to block pathogens from entering our body, the immune system is our internal army fighting off foreign organisms and protecting us from infections. Both the innate immune system, providing a fast but unspecific response to conserved danger- and pathogen-associated molecular patterns, as well as the adaptive immune system, trained throughout our lifetime to recognize foreign antigens and mediate highly specific responses, are cooperating via intricate pathways in the neutralization and elimination of potentially dangerous pathogens. When one or several of these mechanisms are disrupted, this can result in dysregulation of the immune response with different phenotypes based on the affected pathways. For example, impaired activation of the immune system does not allow individuals to fight off infections successfully anymore, which can result in immunodeficiency that is most typically presenting with an increased risk of or especially severe infections. In contrast, genetic defects causing induction of an immune response without an apparent trigger usually show an autoinflammatory phenotype and compromised regulatory pathways or deficits in discriminating self from foreign often manifest in autoimmunity. A combination of these presentations can frequently be observed in patients, owing to the extensive cross-talk between different players of the immune response, such that dysregulations can affect more than one arm of the immune system and highlights the necessity for a tight regulation of the immune system to avoid sometimes devastating effects if dysregulated. If the cause of dysregulation is due to germline variants in one of the components regulating an immune response, this is termed an IEI.

While most individual IEIs only show a low prevalence with sometimes only few patients described in the literature so far, approximately 10 in 10,000 individuals worldwide are estimated to be affected and this is likely still an underestimation of the true number[13]. As discussed above, the advances in NGS techniques as well as our improving understanding of how to interpret variants have led to a rapid increase in genes identified in IEIs. The most recent report of the International Union of Immunological Societies (IUIS) Expert Committee added 55 genetic defects since the last report in 2019, ultimately resulting in a total of 485 gene defects, with this number still exponentially growing[14]. Several variants are described for some genes and their effects have traditionally been categorized as LOE, LOF, or GOF, with the possibility of different variants within one gene resulting in either of these three effects. As an example, only for the transcription factor STAT3 itself, approximately 150 variants have been reported as LOF[15] and more than 70 variants as GOF[16], also resulting in different clinical phenotypes. However, recent years have shown that the spectrum of protein dysfunction is much broader and phenomena such

as hypomorphic functional impairments, haploinsufficiency, and dominant negative effects are increasingly described.

Apart from the obvious benefit of improved patient care following the identification of a disease-causing variant, the in-depth investigation of altered protein functions in these experiments of nature can result in improved basic understanding of immune regulation or even shed light on previously unidentified protein functions. As an example, two independent studies revealed that the previously undefined function of the protein encoded by the *C2orf68* gene is important for mitochondrial function and, if mutated in a homozygous state, can result in autosomal recessive autoinflammation and encephalopathy[17,18].

With the advent of gene therapies in monogenic disorders, for IEIs first performed in adenosine deaminase-deficient (ADA) severe combined immunodeficiency (SCID)[19,20] and resulting in successful correction of disease phenotypes a few years later[21,22], and the steady improvement in its safety and efficacy, identification of genetic determinants will be crucial to make an informed decision about the feasibility and success of such approaches. While as of now gene therapy has only been successfully performed in a handful of IEIs[23–25], gene therapy approaches for a number of additional phenotypes are in pre-clinical development[26]. Although costs remain high and patient numbers are limited, further improvements could make gene therapy a viable alternative to hematopoietic stem cell transplantation (HSCT), which requires the identification of suitable donors and carries a high risk of graft-versus-host disease as well as mortality.

As the rapid identification of the underlying cause of the IEI can be crucial for patient survival and HSCT outcomes are often more favourable when performed early during infancy or childhood, there is a need for screening approaches that could identify candidates with severe disease requiring HSCT. A number of SCID disorders can be detected during newborn screening by assessing the number of T cell receptor excision circles (TRECs) from dried blood spots, as they are a by-product generated during successful V(D)J recombination and therefore a marker for thymic T-cell output[27,28]. While neonates with very low or absent TRECs could profit from pro-active treatment and HSCT, several other severe IEIs will not result in abnormal TREC numbers and will therefore be missed in this approach. Using a sequencing-based screening approach has been proposed to identify patients at risk to improve survival and quality of life and has been shown to be cost-effective due to reduced costs for example associated with intensive care hospitalisation and severe disease complications[29,30]. However, the still substantial costs of sequencing, sometimes insufficient evidence for the benefits of HSCT[31], and a number of additional ethical concerns, such as incidental findings and patient autonomy[32], have so far not resulted in wide-spread implementation of genetic screening approaches in IEI.

1.2 The Calcium signalling toolkit

Calcium (Ca^{2+}) is a universal messenger used by a variety of cell types to regulate crucial cellular functions such as excitation/activation, differentiation, metabolism, survival, and cell death[33–35]. Due to the unique requirements of each cell to sense and respond to different Ca^{2+}-mediated signals, the numerous proteins involved in Ca^{2+} signalling are often expressed and regulated in a cell type- and context-dependent manner. This multitude of proteins has therefore also been termed the "Ca^{2+} signalling toolkit"[34,36], of which each cell expresses those components that are crucial to regulate its functions. The sheer number of identified proteins in this toolkit does not allow the introduction of all of them within the framework of this thesis and I will therefore focus on introducing the most important concepts instead. As the presented work concentrates on two cellular systems that are highly dependent on Ca^{2+} signalling, namely the adaptive immune response and peripheral neuronal signal transduction, the following paragraphs will point out examples involved in their signalling machinery where necessary.

1.2.1 Calcium homeostasis

One of the advantages of Ca^{2+} as an intracellular messenger is its ability to generate signals in fractions of seconds due to the high concentration gradients that are maintained within the cell under resting conditions. While intracellular cytosolic Ca^{2+} concentrations ($[Ca^{2+}]_{cyt}$) range from 50-100 nM, concentrations within the endoplasmic reticulum (ER) as the most important organellar Ca^{2+} store are usually more than 10,000x as high and reach 500-1,000 µM[37]. In addition, the steep concentration gradient with the extracellular space, where $[Ca^{2+}]$ reach 1-2 mM, provides a great driving force in the event of pathway activation. This however also highlights the necessity for ensuring the upkeep of these concentration gradients in resting conditions that is achieved by a number of Ca^{2+} channels and pumps in the plasma membrane as well as the membranes enclosing relevant organelles, such as the ER, lysosomes, and mitochondria.

Membrane-spanning Ca^{2+} channels and transporters

There are several ubiquitously expressed channels and exchangers located in the plasma membrane as well as the ER membrane that make sure that $[Ca^{2+}]_{cyt}$ remains low or reverts back to baseline by actively transporting Ca^{2+} into the extracellular space or ER lumen, respectively. This transport is either coupled to energy consumption via ATP hydrolysis, for example in the case of the plasma membrane Ca^{2+} ATPase (PMCA), or the driving force of the electrochemical Na^+ gradient, in the case of the Na^+/Ca^{2+} exchanger (NCX) combining the import of three Na^+ ions into the cytosol with the export of one Ca^{2+} ion into the extracellular space[38] (**Fig. 1.2**). While the PMCA exclusively operates at the plasma membrane, members of the NCX superfamily have also been found to be localised in the membranes of other cellular organelles such as the nuclear envelope and the inner mitochondrial membrane[39–41]. Although the importance of these homeostatic processes is illustrated by their involvement in human

disease such as hereditary deafness, ataxia, and neurodegenerative diseases[42–44], their more detailed discussion is beyond the scope of this thesis.

Similar to the PMCA, the Sarco-/Endoplasmic Reticulum Ca^{2+}-ATPase (SERCA) located in the ER membrane pumps Ca^{2+} against the concentration gradient into the ER lumen using ATP as an energy source[45,46]. This process serves two purposes, on the one hand it ensures the maintenance of low $[Ca^{2+}]_{cyt}$, on the other hand it is responsible for sustaining the high $[Ca^{2+}]$ in the ER lumen so it is readily available to generate Ca^{2+} signals when specifically induced. Keeping the ER store filled is a crucial task, as there is a passive leak of Ca^{2+} from the ER into the cytosol through various channels, of which over 20 have been identified to date[47]. Some examples of these leak channels are the γ-secretase subunits Presenilin-1 and -2[48], several Transient Receptor Potential (TRP) channels[49], and the Sec61 translocon[50]. Mutations in some of the genes encoding these channels have indeed been linked to altered Ca^{2+} homeostasis due to uncontrolled leak from the ER and are therefore suggested to contribute to disease development[51,52]. Two other channel families that have been described as being responsible for ER Ca^{2+} leak are the inositol 1,4,5-trisphosphate receptor (IP_3R) and Ryanodine receptor (RyR) families[53]. However, as their major role as signal-dependent Ca^{2+} channels is to convert mostly extracellular stimuli to locally or globally increased $[Ca^{2+}]_{cyt}$, their structure and function will be described in the next subchapter of this introduction.

Cytosolic Ca^{2+} buffers

In addition to homeostatic regulation by transporting Ca^{2+} ions between different intracellular compartments or outside of the cell, several proteins in the cytosol but also for example in the ER lumen act as buffering systems[54,55]. This system consists of Ca^{2+}-binding proteins with an EF-hand motif that will bind and sequester Ca^{2+} ions and thereby reduce the availability of free Ca^{2+}. In contrast to Ca^{2+} sensors, that can also bind Ca^{2+} via EF-hands and will be introduced when highlighting downstream signalling events in subchapter 1.2.4, Ca^{2+} buffers usually do not undergo big conformational changes and do not induce Ca^{2+}-dependent pathways. Examples for such buffers are parvalbumin[56,57] and some calbindins[58,59], while the ER lumen contains its own set of Ca^{2+} buffers made up of for example the immunoglobulin binding protein (BiP)[60] and glucose regulated protein of 94-kDA (GRP94)[61]. Interestingly, as both mentioned ER Ca^{2+} buffers do have additional functions as ER stress response proteins and these functions are influenced by Ca^{2+} binding[62–64], they could also be considered downstream-signalling effectors. This relationship also already highlights the complex feedback mechanisms in place to ensure extremely precise signalling events.

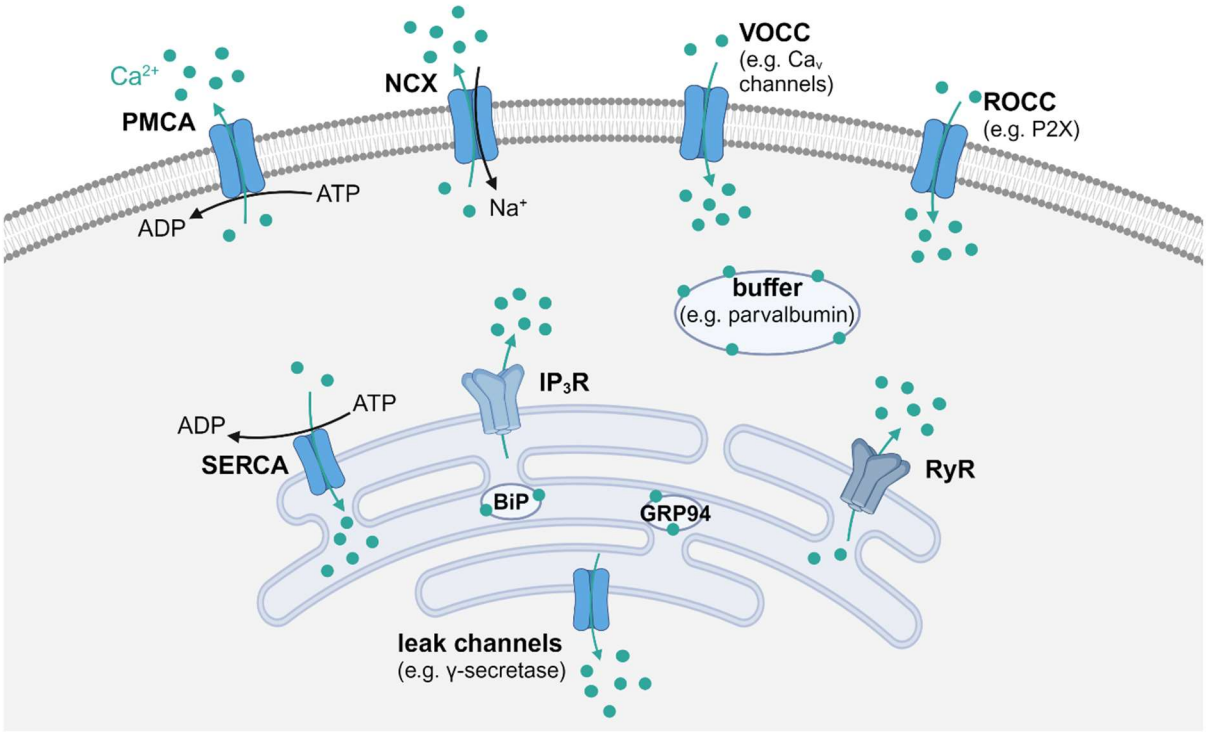

Figure 1.2: Overview of major Ca^{2+} channels and transporters. Simplified depiction of major Ca^{2+} channels and transporters located in the plasma membrane (top) and in the ER membrane (bottom). Direction of Ca^{2+} flux is indicated with arrows. For details refer to the main text. PMCA = plasma membrane Ca^{2+} ATPase; NCX = Na+/Ca^{2+} exchanger; VOCC = voltage-operated Ca^{2+} channel; ROCC = receptor-operated Ca^{2+} channel; SERCA = sarco-/endoplasmic reticulum Ca^{2+} ATPase; RyR = ryanodine receptor; BiP = immunoglobulin binding protein. Figure created with biorender.com.

1.2.2 ER Ca^{2+} depletion and store-operated Calcium entry

Drastic transient or sustained increases in $[Ca^{2+}]_{cyt}$ regulate a multitude of cellular processes that can impact cell fate, and expression of different components of the Ca^{2+} toolkit allows cells to tailor their response machinery to their need, as mentioned before. These increases can either be fuelled by cytosolic influx of extracellular or intraorganellar Ca^{2+}. Increases in $[Ca^{2+}]_{cyt}$ through plasmalemmal Ca^{2+} channels making use of extracellular Ca^{2+} can be achieved through either direct stimulation of the channel or via depolarization of the plasma membrane. Representatives of these receptor-operated Calcium channels (ROCCs) and voltage-operated Calcium channels (VOCCs) are for example the ATP-dependent P2X and L-type Ca_v1 channels, respectively (**Fig. 1.2**). P2X channels in the nervous system are activated by extracellular ATP released from pre-synapses and induce an action potential in the responding cell by allowing influx of Na^+ and Ca^{2+} ions[65]. They are also expressed in lymphocytes, where ATP generated in mitochondria following for example TCR stimulation is released through Pannexin 1 hemichannels in the plasma membrane, binds to P2X receptors in an autocrine manner and allows influx of Ca^{2+}, resulting in enhanced $[Ca^{2+}]_{cyt}$[66,67]. Ca_v1 channels have been shown to be especially important for instance during signal transduction in cardiac myocytes, coupling action potentials that cause a membrane depolarization to the activation and opening of the Ca_v1 channels, resulting ultimately in an

increase in $[Ca^{2+}]_{cyt}$ and activation of troponin C followed by cell contraction[68]. While initially debated, recent studies also supported an important role for Ca_V channels in the activation of specific T lymphocyte subsets[69,70], although at least some of these effects could be mediated independent of increases in $[Ca^{2+}]_{cyt}$[71].

Calcium channels involved in organellar Ca^{2+} release

The second type of $[Ca^{2+}]_{cyt}$ increase is mediated through IP_3R and RyR receptors, which are ligand-gated Ca^{2+} channels primarily located in the ER membrane. Each of these receptor families are made up of 3 isoforms and share substantial intra- as well as interfamilial sequence homology. Based on the structural similarities, they also share the characteristic that four subunits form the final functional channel in the ER membrane and these can be homo- as well as heterotetramers. While IP_3Rs and RyRs are widely expressed throughout the body, their subtypes can have specific tissue tropisms. IP_3R1 is mostly expressed in the central nervous system, IP_3R2 and IP_3R3 are expressed more ubiquitously, for example in the heart and exocrine glands, but usually more than one subtype is expressed[72,73]. RyRs are especially important in muscles and neurons, with RyR1 primarily expressed in skeletal muscle[74], RyR2 in the myocardium[75], and RyR3 more widespread but with high prominence in the brain[76]. Both channel families require the binding of their respective ligand to be activated and opened, also referred to as gating, and several co-factors and post-translational modifications regulate their open probability. As the major topic of this thesis revolves around IP_3Rs, they will also be the focus in this section of the introduction, although it is important to understand that in many cell types the combined activation with RyRs and other Ca^{2+} toolkit components contribute to the generation of physiological Ca^{2+} signals.

IP_3Rs are gated by the binding of the second messenger inositol 1,4,5-trisphosphate (IP_3) which is generated through hydrolysis of the membrane lipid phosphatidylinositol 4,5-bisphosphate (PIP_2) by phospholipase C (PLC) and also results in the generation of diacylgycerol (DAG; **Fig. 1.3**). Phospholipase C in turn is for example activated by G-protein coupled receptors (GPCRs) or receptor tyrosine kinases (RTKs). In T and B cells, PLCγ is primarily activated following the engagement of the T-cell or B-cell receptor (TCR or BCR) through binding of the respective antigen. In neurons and Schwann cells, PLCs are activated downstream of GPCRs such as neurotransmitter receptors like muscarinic acetylcholine receptors (mAChRs) and dopaminergic receptors[77], as well as the RTK ErbB in Schwann cells that is activated by binding to Neuregulin-1 expressed on nerve axons and regulates for example survival and myelination itself[78,79].

Induction of store-operated Ca^{2+} entry

Based on the intensity and duration of stimulation, different patterns of Ca^{2+} flux can be observed in cells ranging from blips – with only single IP_3Rs being activated and allowing very short and small increases in local $[Ca^{2+}]_{cyt}$ – to puffs – the activation of multiple IP_3Rs within a cluster, resulting in higher local Ca^{2+} fluxes in so-called microdomains – to ultimately Ca^{2+} waves, that spread over several

IP_3R clusters and induce a more global increase in $[Ca^{2+}]_{cyt}$[80–82]. Blips are usually not sufficient to induce downstream signalling as their effect is often buffered by the cytosolic Ca^{2+} buffers, hindering the productive activation of neighbouring IP_3Rs. In contrast, the generation of several puffs is usually enough to result in a substantial decrease in $[Ca^{2+}]$ in the lumen of the ER, which is sensed by stromal interaction molecules (STIMs), single-spanning proteins in the ER membrane. While in resting conditions they are associated with Ca^{2+} ions in luminal binding pockets, low Ca^{2+} concentrations will cause them to dissociate and result in a conformational change of STIM[83]. This allows several molecules to multimerize and bind to ORAI channels in the plasma membrane at sites of close proximity[84]. ORAI proteins constitute the pore-forming unit of the Ca^{2+}-release activated channel (CRAC) that is a Ca^{2+}-selective channel mediating influx of extracellular Ca^{2+} upon activation. Once STIM binding allows these channels to open, the high concentration gradient between the extracellular space and cytosol drives a strong influx of Ca^{2+} and elevation of global $[Ca^{2+}]_{cyt}$ to levels up to 1 µM, a process termed store-operated Ca^{2+} entry (SOCE). As opening of ORAI is dependent on the emptying of ER Ca^{2+} stores, the activation of IP_3Rs is crucial to induce sustained global Ca^{2+} signalling and thereby triggering major pathways determining cell fate. Its activation thus needs to be tightly controlled and some of the mechanisms ensuring that this fine-tuning is possible will be discussed next.

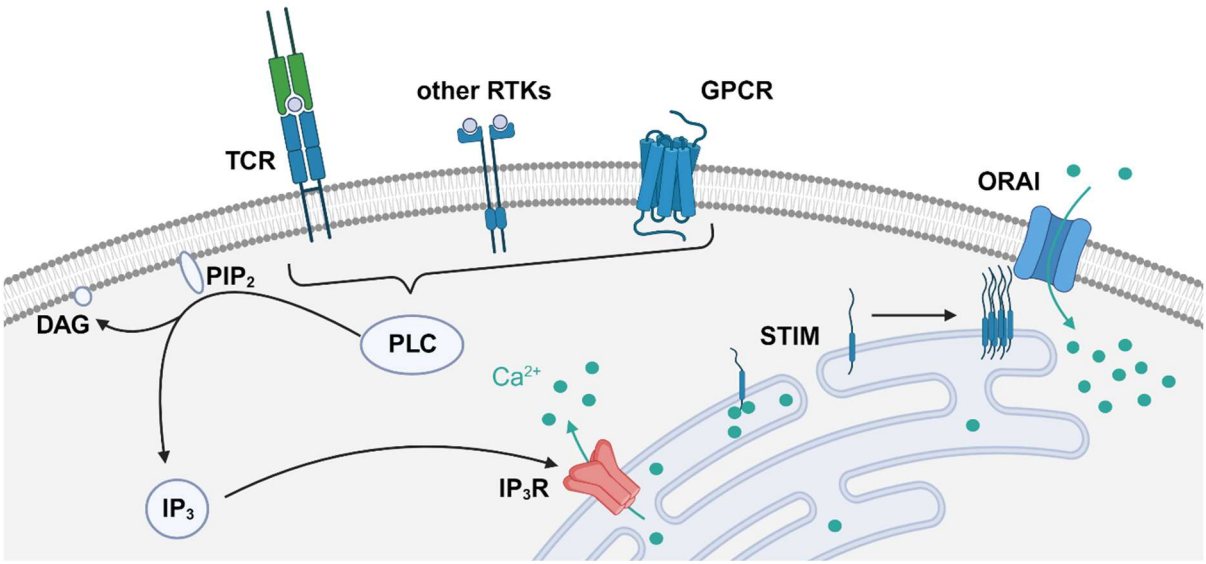

Figure 1.3: Overview of IP_3-mediated store-operated Ca^{2+} entry (SOCE). Engagement of the T cell receptor (TCR), other receptor-tyrosine kinases (RTKs) or G-protein coupled receptors (GPCRs) results in generation of IP_3 and Diacylglycerol (DAG) via Phospholipase C (PLC) activation. Opening of IP_3Rs in the ER membrane decreases $[Ca^{2+}]$ in the ER lumen and dissociation of Ca^{2+} from STIM results in a conformational change. Multimerized STIM molecules then engage with ORAI channels in the plasma membrane and allow SOCE to occur. Figure created with biorender.com.

1.2.3 IP_3R structure and regulation

As previously mentioned, the three different IP_3R subtypes exhibit about 60-70 % sequence homology and therefore also share a common domain structure. The cytoplasmic N-terminal Suppressor Domain (SD) is followed by the Ligand Binding Domain (LBD) that encodes the region responsible for binding IP_3. An extensive regulatory domain located in the cytoplasm exhibits the lowest homology within the protein sequence and already indicates the important function of IP_3Rs as signalling hubs within the cell[85]. Finally, the C-terminal Domain (CTD) contains the highly conserved transmembrane (TM) domain with 6 transmembrane helices that make up the channel domain (~90% sequence homology between subtypes) and are followed by a short terminal cytosolic tail that is also known as gatekeeper domain and appears to be necessary for gating of the channel[86]. Together, largely influenced by the extensive regulatory domain, each receptor subunit has a size of about 300 kDa, resulting in an enormous final multi-subunit channel of more than 1 MDa (**Fig. 1.4A**).

Based on the large distance between the LBD from the TM domain, it is currently hypothesized that binding of IP_3 results in long-range conformational changes throughout the IP_3R subunit that allow rearrangements in the TM domain and permit Ca^{2+} ions to flow through, following the concentration gradient[87,88]. It is important to note that receptors only get fully activated when each subunit undergoes the necessary conformational changes induced by IP_3 binding, a phenomenon also known as cooperative binding[89]. Despite the high sequence homology of the LBD, the affinity of each IP_3R subtype to IP_3 has been shown to vary, with IP_3R2 displaying the highest and IP_3R3 the lowest binding affinity[90,91]. It is therefore hypothesized that the specific stoichiometry within each channel could vary in different cell types and cell states, allowing an additional level of fine-tuning the regulation of Ca^{2+} signalling, but determining the exact stoichiometry has proven to be challenging.

Obligatory binding partners of IP_3Rs

Contrary to what the protein name suggests, IP_3 is not the only molecule determining whether IP_3R channels are in their open or closed state. The second obligatory binding partner necessary for IP_3R activation is actually Ca^{2+} itself with several Ca^{2+}-binding sites identified throughout the LBD and regulatory domain, as well as in luminal portions of the TM[88]. There is however no linear but rather a bell-shaped relationship between Ca^{2+} concentrations and activation of the channel with low and high Ca^{2+} concentrations interfering with Ca^{2+} flux[92,93]. This biphasic regulation forms the basis of Ca^{2+} oscillations and enables signal encoding based on the frequency of Ca^{2+} puffs, while also counteracting excessive signalling after the initial stimulant fades. Modelling based on observations of single-channel response properties in the presence of varying IP_3 and Ca^{2+} concentrations suggested the presence of three different activating or inhibiting Ca^{2+} binding sites[94], however, this hypothesis has not been proven experimentally yet and the exact structural changes induced remain to be elucidated. In recent years, ATP has also been considered an obligatory binding partner for IP_3R activation[95], although previous

reports suggested that its binding would mainly enhance the binding affinity for IP_3 and thereby result in an increased open probability of the channel[96,97].

Post-translational modifications and protein-protein interactions of IP_3Rs

Adding to the complexity of IP_3R regulation, its activity is modulated through post-translational modifications, such as phosphorylation or glycosylation, and (in)direct interaction with activity-modifying enzymes and molecules. As the large regulatory domain already suggests, the number of proteins suggested or experimentally proven to influence IP_3R activity is enormous and underscores the importance of tight regulation through integration of multiple cues in order to avoid misplaced Ca^{2+} signalling. With respect to the limits of this thesis, a few of the more than 100 currently identified regulators of IP_3R activity will be introduced in the following paragraphs to highlight its complexity and intricacy[85]. IP_3R binding protein released with IP_3 (IRBIT) is a crucial molecule raising the IP_3 concentration threshold necessary for channel gating, as it competes for binding the LBD with IP_3 itself by occupying its binding pocket[98,99]. Only when IP_3 concentrations reach a sufficient threshold, IP_3 will displace IRBIT, thereby licensing the IP_3R for gating.

As with many other proteins, phosphorylation is also an important post-translational regulation of IP_3R activity and mediated by a number of different kinases such as the cAMP-dependent protein kinase A (PKA)[100], Calmodulin-dependent protein kinase II (CaMKII)[101–103], and cell-cycle dependent protein kinases[104,105]. PKA phosphorylation of IP_3Rs has been shown to be both sensitizing toward IP_3 binding[106–108] as well as inhibiting[109,110] and the extent of phosphorylation has been shown to differ between the three receptor subtypes[111]. Most likely some of these controversial observations are based on the variability of cell types and physiological contexts used in the respective studies, highlighting the difficulty to draw generalized conclusions about the consequence of interactions. It is often also challenging to dissect the direct effects of phosphorylation from that of other components of the IP_3R signalling machinery influencing each other.

Lastly, the anti-apoptotic Bcl-2 family members Bcl-2 and Bcl-XL have been shown to regulate IP_3R activity[112], possibly in opposing manners with Bcl-2 inhibiting IP_3R activity[112,113]and Bcl-XL enhancing it[114,115]. However, the latter hypothesis has recently been challenged by work from Rosa *et al.*, who propose that binding of Bcl-XL to IP_3R inhibits its activity and thereby limits induction of Ca^{2+}-dependent apoptosis[116].

Together, the examples pointed out here illustrate the complex cell type and context-dependent regulation of IP_3Rs (**Fig. 1.4B**). They highlight the need to better understand the relevant protein interactions in a given situation and to be cautious about transferring findings between different IP_3R subtypes and cell types without experimental evidence. Nonetheless, the sometimes contradictory hypotheses demonstrate that unequivocal characterization can be difficult due to the numerous – and perhaps incompletely identified – interaction partners. Additionally, as will be discussed in the next

chapter, a number of IP_3R regulators are at the same time either downstream effectors of IP_3R-mediated Ca^{2+}-signalling or themselves influenced by Ca^{2+}, thereby adding an additional layer of feedback-regulation.

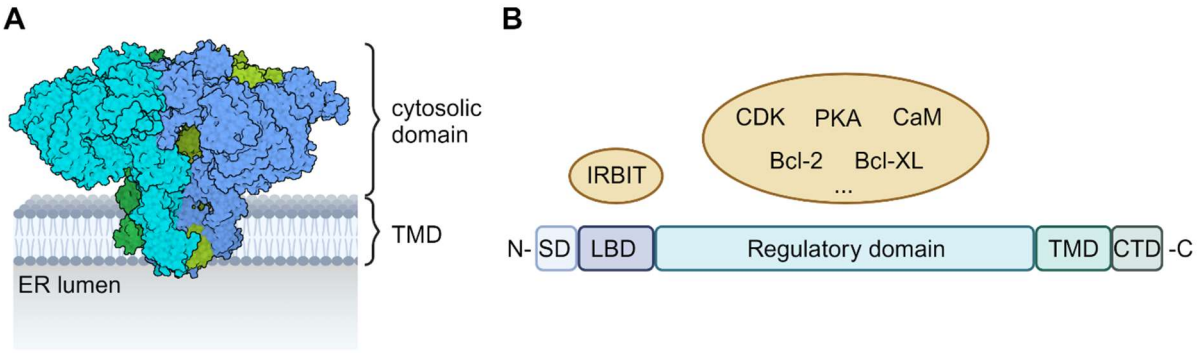

Figure 1.4: Structure and regulation of IP_3Rs. (A) Electron microscopy structure (PDB accession number 6DQJ) of IP_3R3 and its position within the ER membrane. Each subunit of the final tetrameric channel is indicated in a different colour. **(B)** Simplified linear domain structure of IP_3Rs and location of interaction partner binding of the examples introduced. Figure created with biorender.com.

1.2.4 Calcium-dependent downstream signalling

With some of the principles governing IP_3R-mediated Ca^{2+} signalling introduced in the previous sections, the following part of the introduction will focus on the proteins that decode the frequency, duration, and amplitude of the resulting changes in Ca^{2+} concentration and mediate activation or repression of downstream signals. The most extensively studied Ca^{2+} sensor expressed ubiquitously in excitable as well as non-excitable cells is Calmodulin (CaM). CaM contains four EF-hands for Ca^{2+} binding[117,118] and while remaining in a closed state in conditions of low $[Ca^{2+}]_{cyt}$, the binding of Ca^{2+} to the designated pockets induces a conformational change towards an open configuration[119,120]. This change allows Ca^{2+}/CaM to interact with a number of downstream effectors such as different types of Ca^{2+}/CaM-dependent kinases (CaMKs and CaMKKs)[121], the Calcineurin phosphatase[122], and the PMCA[123]. In most cases, the regulated protein itself contains an autoinhibitory domain that interferes with its activity. Once Ca^{2+}/CaM-binds to this domain and induces a conformational change, the inhibitory block is removed, thereby exposing the catalytic subunit and allowing the target protein to exert its function. With regards to the concept of the Ca^{2+} signalling toolkit, while virtually all cells make use of CaM as a mediator of Ca^{2+} signalling, the regulated expression of target proteins allows to control the diverse range of outcomes in each cell individually.

Proteins targeted by CaMKs or Calcineurin are numerous and this paragraph will highlight few examples relevant for the work presented in this thesis. Within the family of CaMKs, CaMKII is ubiquitously expressed and was described to be important in multiple cell types for regulating activation, maturation, and survival of these cells[124]. As an example, phosphorylation of the gap junction protein connexin36 by CaMKII in neurons contributes to the mediation of synapse plasticity and junction coupling[125].

Additionally, the direct phosphorylation of the AMPA and NMDA ion channels by CaMKII forms a positive feedback-loop by reinforcing their open configuration, allowing Na^+ and Ca^{2+} to enter the cell[126,127]. In immune cells, CaMKII has also been described to phosphorylate targets like the signal transducer and activator of transcription 1 (STAT1) following interferon-γ (IFNγ) stimulation, resulting in dimerization and subsequent translocation to the nucleus to regulate expression of target genes[128].

Probably the most prototypical example of Ca^{2+}-mediated signalling in lymphocytes involves the dephosphorylation of nuclear factor of activated T cells (NFAT) by Calcineurin. After Ca^{2+}/CaM binds to Calcineurin and exposes its catalytical subunit, the phosphatase is able to remove the phosphor-group from NFAT transcription factors, allowing them to dimerize and translocate to the nucleus[129]. Here, in combination with other transcription factors, it induces the expression of for example interleukin-2 (IL-2) and genes influencing T cell differentiation[130,131]. The induction of an adaptive immune response through this pathway is regularly exploited in the context of autoimmune disorders or transplantation, where FK506 and cyclosporin A are often used as immunosuppressants in an attempt to dampen damaging overactivation of the adaptive immune system, although they do induce a number of possibly severe side effects[132,133].

Mitochondrial Ca^{2+} and its regulation of cell death and metabolism

An important and universal effect of Ca^{2+} signalling lies in the regulation of cell metabolism and survival/apoptosis. Many involved pathways include the Ca^{2+}-mediated cross-talk between the ER and mitochondria at so called mitochondria-associated ER membranes (MAMs). At these sites, the ER and mitochondria are in close contact due to tethering complexes that are mainly formed by IP_3Rs in the ER membrane, voltage-dependent anion-selective channel 1 (VDAC1) in the outer mitochondrial membrane (OMM) and stabilized by Grp75 linking both of them together[134]. While many other accessory proteins can (de-)stabilize and therefore regulate these complexes, IP_3Rs, VDAC1, and Grp75 seem to be the core components. A fourth member however that is located in very close proximity but has so far not been shown to directly interact with any of the other components is the mitochondrial Ca^{2+} uniporter (MCU) in the inner mitochondrial membrane (IMM), that is ultimately responsible for transport of Ca^{2+} ions from the ER lumen through the intermembrane space to the mitochondrial matrix[135]. The mitochondrial matrix Ca^{2+} concentration ($[Ca^{2+}]_{mit}$), as in the cytosol, regulates the activity of a number of Ca^{2+}-sensitive enzymes. Many of them are part of the ATP-generating machinery, such as glycerol phosphate dehydrogenase (GPDH) and pyruvate dehydrogenase (PDH), forming the link between Ca^{2+} signalling and energy metabolism[136]. As activation of IP_3Rs usually occurs in the context of cell activation, the increased production of ATP ensures sufficient energy resources for necessary protein synthesis and other processes that are required for activation.

Tight regulation of $[Ca^{2+}]_{mit}$ is important for cell survival as both too little and too much Ca^{2+} in the mitochondrial matrix can result in autophagy or apoptosis, respectively[137]. Blocking Ca^{2+} transfer

through IP_3Rs into the mitochondrial matrix has been shown to induce autophagy that could ultimately lead to cell death[138,139], although several other studies seem to indicate that IP_3Rs are necessary to induce autophagy in situations where the cells are chronically starved[140,141]. Once again, this highlights the versatility of Ca^{2+} signalling that occurs in a highly context-dependent manner.

With regards to apoptosis, the previous subchapter already shortly mentioned the inhibitory effect on IP_3R-mediated Ca^{2+} release by anti-apoptotic Bcl-2 and Bcl-XL, with Bcl-XL however most likely acting in a concentration-dependent manner and actually sensitizing IP_3Rs at intermediate concentrations[142]. Excessive $[Ca^{2+}]_{mit}$ results in non-selective permeabilization of the IMM through the opening of mitochondrial permeability transition pores (mPTPs)[143,144], which results amongst others in the release of cytochrome C and activation of caspases[145]. By inhibiting Ca^{2+} transport through the IP_3R/VDAC1/MCU axis, Bcl-2 and Bcl-xL are able to prevent Ca^{2+} overload of mitochondria and thereby apoptosis. While sufficiently high $[Ca^{2+}]_{mit}$ are therefore necessary to ensure adequate energy production for cell survival, prolonged and extremely high $[Ca^{2+}]_{mit}$ or very low $[Ca^{2+}]_{mit}$ can result in cell death.

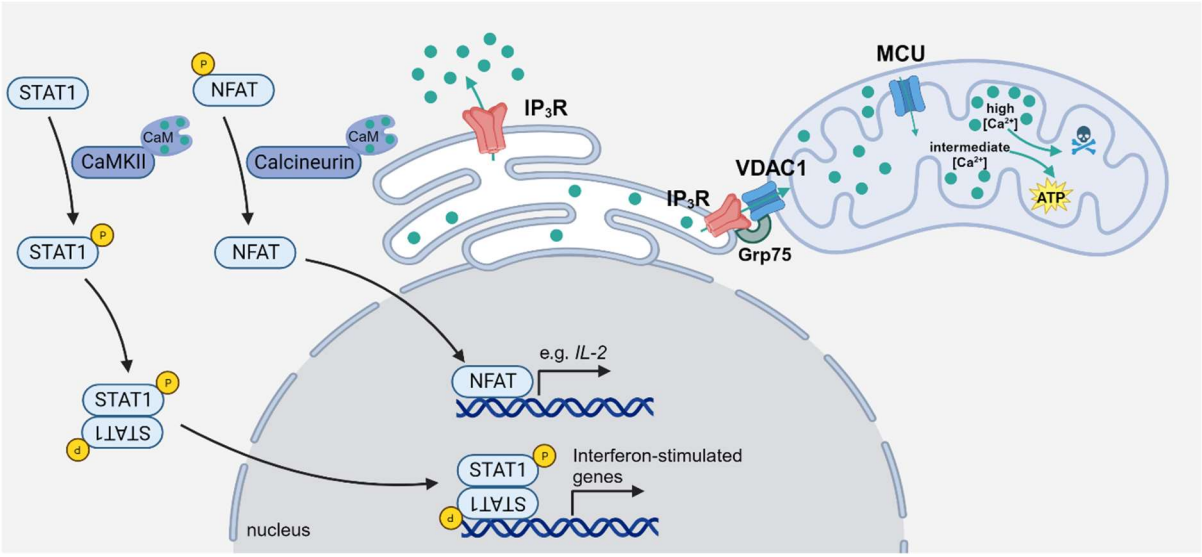

Figure 1.5: Overview of selected downstream pathways of Ca^{2+} signalling. Release of Ca^{2+} from the ER through IP_3Rs into the cytosol, in combination with SOCE, results in activation of Calmodulin (CaM) that in turn can activate CaM-dependent kinase II (CaMKII) or Calcineurin. They for example mediate phosphorylation of STAT1 and dephosphorylation of NFAT, respectively, allowing their translocation into the nucleus where they act as transcription factors inducing gene transcription. Coupling of IP_3R to the mitochondrial voltage-dependent anion-selective channel 1 (VDAC1) via Grp75 allows flux of Ca^{2+} into the intermembrane space and further into the mitochondrial lumen through the mitochondrial Ca^{2+} uniporter (MCU). $[Ca^{2+}]$ in the mitochondrial lumen controls processes such as autophagy, ATP production, and cell death – for details refer to the main text. Figure created with biorender.com.

1.2.5 Calcium signalling in T-cell development

This paragraph aims to exemplify the importance of Ca^{2+} signalling and SOCE as well as their intricate regulation in a well-studied cell type, namely lymphocytes, with a specific focus on thymic T cell development. While Ca^{2+} signalling is also critical for appropriate function of cells of the innate immune

system, the involvement of especially T cells in SOCE-mediated immune disorders discussed below have resulted in thorough investigation of its function during cell development and activation.

T cells are derived from the common lymphocyte progenitor in the bone marrow and develop during lymphopoiesis in the thymus. Thymocytes undergo a number of steps during development that are characterized by the expression of the CD4 and CD8 co-receptors on their surface. When they first enter the thymus, they express neither of the two receptors and are therefore termed double negative (DN) cells. Following successful rearrangement of the β chain of the TCR, – for the purpose of this introduction neglecting the possibility for development of γδ and other DN T cells – they upregulate expression of both CD4 and CD8, entering the double positive (DP) state. While not fully understood, it was suggested that this transition is dependent on IP_3R-mediated Ca^{2+} signalling, as mice lacking all three *Itpr* genes show low numbers of DP thymocytes[146]. If the DP state is reached, rearrangement of the TCRα chain is initiated and once a functional TCR is expressed on the cell surface, several steps of thymic selection have to be passed that are dependent on Ca^{2+}-mediated signalling. First, DP thymocytes need to undergo positive selection to ensure that they are able to recognize peptides presented by self major histocompatibility complex (MHC) class I and II molecules, thereby avoiding death by neglect. This process is also called MHC restriction and induces lineage commitment to CD8 or CD4 single positive (SP) thymocytes based on the recognition of MHCI or MHCII molecules, respectively. Although this selection is Ca^{2+}-dependent[147,148], SOCE does not seem to be critical in this step as mice lacking Stim1/Stim2 or Orai1/Orai2 expression have normal numbers of conventional T cells in peripheral blood[149,150].

SP thymocytes expressing either CD4 or CD8 subsequently migrate to the thymic medulla where they undergo negative selection to prevent self-reactive T cells from entering the periphery. Medullar thymic epithelial cells are able to also express normally repressed tissue-specific proteins and present peptides to the SP thymocytes. If a self-peptide is recognized by the TCR of a thymocyte, downstream signalling will be induced resulting in Ca^{2+}-mediated induction of the pro-apoptotic Bcl-2 family member Bim and ultimately cell death[151]. This process is termed clonal deletion and necessary to avoid an undesired immune response against own tissues. However, high-affinity signalling through the TCR in combination with CD28 co-stimulation as well as IL-2 signalling can also induce the differentiation into regulatory T cells (Tregs) that is SOCE-dependent[152]. Tregs are crucial for tissue homeostasis and preventing autoimmune reactions, as highlighted by the devastating lymphoproliferative phenotype observed in patients lacking Tregs[153]. The dependency on SOCE has also been demonstrated in the differentiation of peripheral Tregs as well as other agonist-selected minor T cell subsets that are not further discussed here. Taken together, although the specific mediators and channels involved in the separate steps of thymocyte development remain to be fully elucidated, it is clear that different Ca^{2+} signal strengths and/or patterns define the fate of thymocytes during T cell development.

1.3 Defective Calcium signalling in hereditary human disease

There are a plethora of disease entities and phenotypes described that are either caused or influenced by defective Ca^{2+} homeostasis and signalling, highlighting its crucial involvement in the regulation of basic cell functions throughout the body. It is therefore not surprising that abnormal Ca^{2+} signalling has been described in the development and progression of cancer and dysfunction of Ca^{2+}-related pathways was reported in pathologies affecting the brain, kidney, liver, and heart, amongst others[154–157]. Due to the large number of associated diseases, the following paragraphs will focus on the current knowledge of primary hereditary Ca^{2+} defects in lymphocytes causing a phenotype of combined immunodeficiency as well as in neurons and Schwann cells resulting in Charcot-Marie-Tooth disease, an inherited peripheral neuropathy, as both disease entities are major subjects of the research articles presented in this thesis. Additionally, the hereditary diseases so far associated with variants in *ITPR* genes and the resulting dysregulation of Ca^{2+} homeostasis on signalling will be introduced.

1.3.1 CRAC-associated disease phenotypes

The involvement of Ca^{2+} signalling in human immune disorders has been appreciated for a long time based on reports of decreased Ca^{2+} signals following lymphocyte stimulation in patients with immunodeficiency[158]. It wasn't before the early 1990's that the term Calcium-release activated Calcium (CRAC) channel was coined for the then still unknown Ca^{2+} channel that was expected to mediate Ca^{2+} influx from the extracellular space into the cytosol after emptying of intracellular stores[159,160]. Only in 2006, Feske *et al.* as well as Vig *et al.* were able to identify the respective proteins and genes of the pore-forming CRAC subunit, namely the ORAI family with 3 members (ORAI1, ORAI2, ORAI3)[161,162], the former through linkage analysis in a family with immunodeficiency, thereby also providing a genetic diagnosis for the described patients. Around the same time, several labs reported the involvement of STIM in regulating the opening of ORAI channels and in 2009 the first immunodeficient patients harbouring a homozygous STIM1 variant were described by Picard *et al.* [163]. With STIM forming the regulatory and ORAI the pore-forming subunit of the CRAC channel, diseases based on variants in either of the genes are termed CRAC channelopathy.

Only recently a third player has been added to the group of proteins causing CRAC channelopathies, with a patient with compound heterozygous variants in *CRACR2A*, a regulatory subunit of the CRAC channel mediating interaction between STIM1 and ORAI1, resulting in a late-onset combined immunodeficiency[164]. While STIM1 and ORAI1 deficient patients present rather early in life due to the severe defect in mounting successful immune responses because of virtually absent SOCE, the CRACR2A-deficient patient presented only later in life with combined immunodeficiency, although the onset of symptoms could be traced back into early adolescence. A typical feature of STIM1 and ORAI1 deficiency is anhidrotic ectodermal dysplasia (EDA), manifesting in impaired dental enamel formation, hypo- or anhidrosis, and abnormalities in hair structure[165,166]. Together with hypotonia from birth, these

two features were however not noted in the CRACR2A-deficient patient, suggesting that the residual CRAC signalling function inducing partial SOCE in this patient is sufficient to prevent full-blown development of the clinical symptoms of STIM1-/ORAI1-deficient patients. Interestingly, in all patients the development of B and T cells that involves signalling through the BCR/TCR was not or only slightly impaired, indicating that SOCE is dispensable for successful positive selection. Additionally, T-cell dependent stimulation of B cells *in vitro* did usually not reveal severe defects which could be due to lower dependence on CRAC-mediated SOCE during B cell activation or to higher redundancy between the different family members.

Although STIM1 and ORAI1 deficiency are often referred to as the prototypical CRAC channelopathies, dominant GOF variants in STIM and ORAI family members have also been described and result in a very different clinical phenotype, namely tubular aggregate myopathy and Stormorken syndrome[167–169]. The inappropriate over-activation of SOCE and therefore excessive influx of Ca^{2+} into the cytosol in these patients results in abnormal platelet function and thrombocytopenia, tubular aggregate myopathy, and in the case of Stormorken syndrome asplenia, growth defects, and cognitive defects. Despite very different phenotypes arising from LOF compared to GOF variants in STIM and ORAI, they impair function in similar cell types and tissues, emphasising the importance of tightly regulated Ca^{2+} homeostasis and the non-redundancy of CRAC-mediated SOCE[166].

1.3.2 Charcot-Marie-Tooth

Charcot-Marie-Tooth (CMT) is a type of Inherited peripheral neuropathy (IPN) that has first been described in 1886 and presents with progressive weakness especially in distal limbs that slowly progresses and goes along with muscle atrophy in the feet and legs. Patients additionally show deformities of the feet, such as pes cavus (high-arched foot) and hammertoe, and may show absence of tendon reflexes[170,171]. With an estimated prevalence of 1 in 2,500[172], CMT is the most common IPN but is characterised by a very heterogeneous presentation. The major separation of disease subtypes is based on the median motor nerve conduction velocity that is lowest in demyelinating CMT1 (<38 m/s) and highest in axonal CMT2 (>45 m/s), with intermediate CMT showing velocities between 30 and 45 m/s[173]. As in many other fields of clinical research, NGS techniques allowed the identification of a growing number of disease-associated genes with variants in more than 80 genes currently suggested to be involved in the development of CMT[174,175], although not all have been functionally validated. While genes associated with CMT1 usually exert an important function in Schwann cells, genes associated with CMT2 are predominantly important for signal transduction in the neurons themselves[176], although a number of genes ubiquitously expressed and still resulting in a specific CMT phenotype have been described[177,178].

Dysregulated Ca^{2+} homeostasis and signalling is known to be a potential cause and/or driver of IPNs[179]. Many different variants have been identified in ganglioside-induced differentiation-associated-protein 1

(GDAP1), a protein located in the OMM, that alter ER-mitochondria interaction and result in decreased SOCE[180,181]. As both, axons and Schwann cells express GDAP1 and are highly dependent on Ca^{2+} for signal transduction and mitochondrial energy production, both demyelination and axonal CMT can be caused by GDAP1 variants[182]. Similarly, two different heterozygous variants in *C1orf194*, suspected to be a regulator of ER calcium homeostasis, were identified in two families with the intermediate or demyelinating form of CMT and knock-in in a mouse model revealed increased $[Ca^{2+}]_{cyt}$ and decreased $[Ca^{2+}]_{mit}$, together with an altered expression profile of proteins involved in Ca^{2+} signalling[183]. However, no direct Ca^{2+} measurements were performed in this study and the function of the protein itself is not well characterized yet, rendering additional studies necessary.

1.3.3 IP_3R-related diseases

As introduced in chapter 1.2.3, there are three different subtypes of IP_3Rs and all of them have already been linked to human disease, but only few mutations have experimentally been characterised regarding their effect on protein function. Both IP_3R1 and IP_3R2 have experimentally been linked to hereditary diseases, while IP_3R3 had only been reported as potential diseases-causing candidate in association studies prior to the publications presented in this thesis. Despite the substantial sequence homology between the subtypes, the clinical phenotypes caused by mutations in either family member are usually quite distinct and preferentially affect specific cell types or organs. While this observation can partly be attributed to the differential expression of one subtype in a certain cell type, such as that of IP_3R1 in neurons of the central nervous system, it may also be an effect of pathway-specific disruptions that could be important, or non-redundant, only in some cells.

Mutations in IP_3R1 are most frequently studied as they result in a very distinct phenotype affecting the central nervous system (CNS) due to the predominant expression of this subtype. Especially in Purkinje cells in the cerebellum, IP_3R1 is almost exclusively expressed[184]. Therefore, patients with LOF mutations in this subtype typically present with impaired motor coordination, resulting in clinical phenotypes such as spinocerebellar ataxia (SCA), Gillespie syndrome (GS), and pontine cerebellar hypoplasia (PCH). The severity of disease is highly dependent on the location of the mutation and more than 40 different mutations in IP_3R1 have been described so far. However, most of the mutations have not been characterized functionally and the observed incomplete penetrance and pleiotropy, i.e. a different clinical presentation arising from the same mutation, complicate predictions of the impact of new mutations. It is also interesting to note that not only autosomal dominant LOF mutations can cause SCA, but also a GOF mutation in the suppressor domain enhancing IP_3-binding affinity has been described, resulting in the same phenotype[185].

Inherited mutations in IP_3R2 have for now only been shown experimentally to cause anhidrosis in 5 individuals of a consanguineous family, in which heterozygous individuals were asymptomatic[186]. The affected individuals presented with an inability to sweat and intolerance to heat. Although mice with a

specific loss of IP_3R2 did not show a clear phenotype in previous studies[187], when specifically investigated for sweat secretion this was actually shown to be decreased, resembling the impairment seen in humans.

In 2014, Schabhüttl *et al.* identified a heterozygous private variant, i.e. non-reported in a public database, in *ITPR3* through WES and linkage analysis as a potential cause for CMT[188]. After addition of *ITPR3* to a targeted gene panel used in a study to evaluate its performance for genetic diagnosis in a cohort of selected CMT patients, Laššuthová *et al.* identified another variant in *ITPR3* suspected of causing the phenotype[189]. However, it wasn't the aim of either study to provide functional evidence of pathogenicity and the consideration as a disease-causing variant solely relies on the segregation within the family as well as the plausible involvement of IP_3R signalling in disease pathogenesis.

Similar exploratory WES studies have also led to the identification of disease-associated variants in *ITPR2*. In a two-generation family with familial isolated primary hyperparathyroidism, an autosomal dominant disorder characterized by excessive activity of one or more parathyroid glands potentially resulting in osteoporosis[190], a missense variant in *ITPR2* was identified in two affected family members, but not in three unaffected ones[191]. Similar to the studies associating *ITPR3* variants with CMT, functional validation however has not been performed and further research is needed to causally link the genotype with the phenotype.

Somatic mutations in IP_3R-coding genes were described in other diseases such as Sézary syndrome, a cutaneous T cell lymphoma, (IP_3R1 and IP_3R2)[192] or head and neck squamous cell carcinoma (IP_3R3)[193], and especially changes in IP_3R3 expression are found in various types of cancer[194,195]. These findings again highlight the importance of IP_3R-mediated Ca^{2+} signalling in cell survival and proliferation – pathways that are of great importance during cancer growth – although no hereditary susceptibility has been reported to date.

Intriguingly, previous to the work presented in this thesis, no direct link had been made between variants in any of the IP_3R subtypes and immunodeficiency. This is despite the importance of Ca^{2+} signalling for mounting immune responses, as illustrated in patients with STIM1 and ORAI1 deficiency. While triple knockout mice lacking all IP_3Rs were shown to exhibit disturbed thymocyte development by interfering with their transition from the DN to the DP stage, this impairment was not seen in single knockout mice, arguing in favour of subtype redundancy[196]. The role of single IP_3Rs in signal transduction of T and B cells has been debated, with early studies suggesting that siRNA-mediated knockdown of IP_3R1 is sufficient to fully abrogate SOCE in T cells[197], which could not be observed in studies of T cells from *Itpr1*$^{-/-}$ mice[198]. Similarly, in chicken DT40 B cells, only absence of all three IP_3R subtypes but not that of only one subtype led to impaired BCR-mediated SOCE[199]. It is thus clear that IP_3Rs also play an important role in lymphocyte activation and that variants altering their function could cause immunological diseases.

2 Research objectives

The work presented in this thesis aimed to identify and functionally validate and characterise inherited disease-causing variants in genetically undiagnosed patients. Following careful patient selection and variant filtering of WES data, we identified variants predicted to be damaging in *ITPR3* in a total of 4 independent kindreds with varying clinical presentation ranging from immune dysregulation to peripheral neuropathy, or a combination thereof. Therefore, we subsequently sought to provide functional evidence that the resulting functional impairments could result in the clinical phenotype observed. While this would not only allow to better delineate the physiological importance of IP_3R3 in different cellular contexts, it would also allow the patients to receive a genetic diagnosis that could support management of the disease as well as provide valuable knowledge for future family planning.

Chapter 3 describes the investigation of a total of 3 different variants in *ITPR3* identified in two compound heterozygous patients presenting with combined immunodeficiency at varying severity. We aimed to establish the impact of the variants on both protein expression as well as function by also investigating the homozygous parents where possible.

In Chapter 4 we focused on a three-generation kindred presenting with isolated inherited peripheral neuropathy and an additional isolated case from an Ashkenazi Jewish family. For the variant of the family we again investigated its effect on protein expression and function.

Finally, the research described in Chapter 5 aimed to further characterize the impact of the variants on a molecular level, not only investigating gating of the channels following stimulation but also establishing whether and how homeostatic signalling is altered.

Altogether, the combined work presented in this thesis aimed to clarify the previously undescribed causal role of IP_3R3 in human hereditary disorders following its identification through NGS analysis. Through functional characterization of the mutational impact, the work aimed to shed light on the involvement of IP_3R3 in physiological signalling. This could pave the way for improved diagnosis of future patients and hopefully lead to the identification and/or development of targeted treatment approaches.

3 *ITPR3* variants causing immunodeficiency

Adapted from:

Neumann J*, Van Nieuwenhove E*, Terry LE*, Staels F, Knebel TR, Welkenhuyzen K, Ahmadzadeh K, Baker MR, Gerbaux M, Willemsen M, Barber JS, Serysheva II, De Waele L, Vermeulen F, Schlenner S, Meyts I, Yule DI, Bultynck G, Schrijvers R, Humblet-Baron S, Liston A. Disrupted Ca^{2+} homeostasis and immunodeficiency in patients with functional IP_3 receptor subtype 3 defects. *Cell Mol Immunol* 2023 Jan;20(1):11-25. doi: 10.1038/s41423-022-00928-4.

* Shared first authorship

3.1 Abstract

Calcium signalling is essential for lymphocyte activation, with genetic disruptions of store-operated calcium (Ca^{2+}) entry resulting in severe immunodeficiency. The inositol 1,4,5-trisphosphate receptor (IP_3R), a homo- or heterotetramer of the IP_3R1-3 isoforms, amplifies lymphocyte signalling by releasing Ca^{2+} from endoplasmic reticulum stores following antigen stimulation. Although knockout of all IP_3R isoforms in mice causes immunodeficiency, the seeming redundancy of the isoforms is thought to explain the absence of variants in human immunodeficiency. In this study, we identified compound heterozygous variants of *ITPR3* (gene encoding IP_3R subtype 3) in two unrelated Caucasian patients presenting with immunodeficiency. To determine whether *ITPR3* variants act in a nonredundant manner and disrupt human immune responses, we characterized the Ca^{2+} signalling capacity, the lymphocyte response, and the clinical phenotype of these patients. We observed disrupted Ca^{2+} signalling in patient-derived fibroblasts and immune cells, with abnormal proliferation and activation responses following T-cell receptor stimulation. Reconstitution of IP_3R3 in IP_3R knockout cell lines led to the characterization of the variants as functional hypomorphs that showed reduced ability to discriminate between homeostatic and induced states, validating a genotype–phenotype link. These results demonstrate a functional link between defective endoplasmic reticulum Ca^{2+} channels and immunodeficiency and identify IP_3Rs as diagnostic targets for patients with specific inborn errors of immunity. These results also extend the known cause of Ca^{2+}-associated immunodeficiency from store-operated entry to impaired Ca^{2+} mobilization from the endoplasmic reticulum, revealing a broad sensitivity of lymphocytes to genetic defects in Ca^{2+} signalling.

3.2 Introduction

Genetic studies of patients with severe immunodeficiency have led to the identification of defects in Ca^{2+} signalling as key causes of T-cell and B-cell functional deficiency[158,200]. Ca^{2+} signalling is not a single event but the result of orchestrated spatiotemporal changes in Ca^{2+} flux from different cellular and extracellular compartments[37] acting in concert with other signalling pathways[201]. In lymphocytes, the key event following the engagement of a T-cell receptor (TCR) or B-cell receptor (BCR) is the elevation of the cytosolic Ca^{2+} concentration ($[Ca^{2+}]_{cyt}$)[202,203]. Identifying the genes involved in T-cell and B-cell immunodeficiency sheds light on the rate-limiting biochemical steps critical for this activation process.

The Ca^{2+} flux triggered by TCR and BCR engagement is realized via both Ca^{2+} release from intracellular Ca^{2+} stores and influx from the extracellular compartment in multiple phases. The first step is mediated by the second messenger inositol 1,4,5-trisphosphate (IP_3), which is generated upon activation of phospholipase $C\gamma$[204]. IP_3 binds to and opens tetrameric IP_3 receptors (IP_3Rs), thereby releasing Ca^{2+} from endoplasmic reticulum (ER) stores into the cytosol[197,205]. Although this event only transiently increases $[Ca^{2+}]_{cyt}$, in the second stage, the ER transmembrane (TM) protein stromal interaction molecule 1

(STIM1) senses lower ER [Ca^{2+}], and via a conformational change directly triggers the opening of plasmalemmal ORAI1 channels[206–208]. ORAI1 is a calcium-release activated Ca^{2+} (CRAC) channel that mediates the influx of extracellular Ca^{2+}, a process known as store-operated Ca^{2+} entry. This sustained increase in [Ca^{2+}]cyt triggers downstream signalling, notably the NF-κB and calcineurin/nuclear factor of activated T cells (NFAT) pathways[209,210], thereby activating antigen-stimulated lymphocytes. In principle, defects in any step in the distal pathway between TCR stimulation and NFAT nuclear translocation can result in a dysfunctional immune response. Most commonly, however, genetic drivers of immunodeficiency originate from points of the pathway with rate-limiting and nonredundant single-protein bottlenecks. Furthermore, with Ca^{2+} signalling being a critical pathway in a multitude of physiological processes, from neuron excitation to cellular apoptosis[37], only variants that confer immunodeficiency without preventing foetal development are observed.

Due to the centrality of Ca^{2+} regulation, a large diversity of genetic disorders are associated with disrupted Ca^{2+} pathways[211–213]. Genetic defects in extracellular Ca^{2+} influx have been formally associated with primary immunodeficiency, with defects in the store-operated Ca^{2+} entry stage of Ca^{2+} signalling through the demise or loss-of-function of ORAI1 or STIM1 causing severe immunodeficiency[162,163,214] and defective nuclear translocation of NFAT blocking the production of cytokines, resulting in immunodeficiency[215]. Patients with immunodeficiency cannot mount effective immune responses, but many of these patients also present symptoms associated with autoimmune conditions such as autoimmune cytopenia or inflammatory bowel disease[216,217]. These outcomes may indicate the crucial role played by intact TCR signalling not only in immunogenic processes but also in tolerogenic processes such as central and peripheral tolerance[218,219]. In contrast, primary ER Ca^{2+} release through IP_3R channels, although associated with several nonimmunological disorders[220,221], has yet to be linked to primary immunodeficiencies. *ITPR1*, *ITPR2* and *ITPR3* variants have been suggested to cause (spino-)cerebellar ataxia[222,223], anhidrosis[186], and Charcot–Marie–Tooth disease[224], respectively. In mice, lymphocyte defects were not observed when individual genes were knocked out; in contrast, they were observed only in triple-knockout mice[196,199,225]. Based on the 60–80% sequence homology among the isoforms[226] and the formation of either homo- or heterotetramers, subunits may show redundancy in lymphocytes. However, whether lymphocytes are susceptible to genetic variants that can impair primary Ca^{2+} efflux from the ER in humans remains unknown.

In this study, we identified two unrelated patients with immunodeficiency and immune dysregulation who harboured compound heterozygous *ITPR3* variants. We found that the three identified variants differentially impact channel function and intracellular calcium homeostasis, with proliferation and activation defects observed in stimulated lymphocytes. Together, these results demonstrate that human lymphocytes are susceptible to genetic defects in the primary ER Ca^{2+} release system, with niche-filling *ITPR3* variants altering IP_3R sensitivity. This study thus establishes genetic defects in IP_3Rs as a new class of inborn errors of immunity.

3.3 Materials and Methods

Written informed consent was obtained from all participants, and the Ethics Committee of UZ/KU Leuven approved the study (S52653, S58466).

Whole-exome sequencing and analysis

For the kindred of P1, whole-exome sequencing was performed using genomic DNA isolated from whole blood using the QIAmp DNA Blood Midi kit (Qiagen, Hilden, Germany) according to the manufacturer's instructions. The sequencing library was prepared using ligation-mediated PCR and hybridized to the SureSelect Biotinylated RNA library (Agilent Technologies, Santa Clara, CA) for enrichment by BGI (Shenzhen, China) before paired-end sequencing on a HiSeq2000 (Illumina, San Diego, CA) platform. The generated FastQ files were mapped to the human genome version 19 (hg19) using the Burrows-Wheeler Aligner (BWA, v0.7.5a). Duplicates were removed using Picard MarkDuplicates, and realignment was performed according to the Genome Analysis Toolkit 3.1 best practices guidelines. Variants were called using HaplotypeCaller and coding nonsynonymous variants with a high CADD score and a mean allelic frequency of <0.005 in the gnomAD database were retained.

For the kindred of P2, whole-exome sequencing was performed by Macrogen (Seoul, Korea). Exome capture using SureSelect Human All Exon V7 (Agilent) preceded paired-end sequencing on a NovaSeq6000 (Illumina) platform. A computational pipeline was developed using bcbio-nextgen as a backend (https://github.com/bcbio/bcbio-nextgen, v1.1.5-b) to process the read data and perform tasks such as quality control, variant discovery, annotation, and filtering. Briefly, the sequencing reads in FASTQ format were aligned to the human reference genome (GRCh37) using BWA (v0.7.17). The resulting BAM files were further processed to remove duplicate reads using biobambam (v2.0.87). The resulting variants were annotated using snpEff (v4.3.1t) for functional prediction and vcfanno (v0.3.1) to add information from public databases such as dbSNP (v151), dbNSFP (v3.5a), ExAC, gnomAD (v r2.1), 1000 genomes (v3), and ClinVar (v2019-05-13). Likely disease-causing variants were selected and prioritized based on quality score, allele frequency, functional impact, and probable inheritance model.

Sanger confirmation for individuals from both kindreds was performed by amplification of variant-specific gene products by PCR using KOD polymerase (Sigma–Aldrich, St. Louis, MO, US), and the primers are listed in **Supplementary Table 3.5**. After gel purification with the NucleoSpin Gel and PCR Clean-up (Macherey-Nagel, Düren, Germany), according to the manufacturer's instructions, sequencing was performed by Eurofins (Ebersberg, Germany).

Variant effect prediction on protein structure

The cryo-EM structure of IP_3R3 with the PDB accession number 6DQJ was used to analyse the identified variants. Computational mutagenesis was performed in COOT[227], and subsequent molecular refinements

to R2524C were performed in PHENIX[228]. Calculations of electrostatic potential and all molecular visualizations were generated using UCSF Chimera[229].

RNA isolation and quantification

Total RNA was isolated from PBMCs and primary fibroblast cell lines generated from skin biopsy samples using TRIzol reagent (Ambion, Thermo Fisher, Waltham, MA) according to the manufacturer's protocol. Complementary DNA was synthesized using the GoScript™ Reverse Transcription System (Promega, Madison, WI). Quantitative PCR was performed on a StepOnePlus real-time PCR system (ABI, Thermo Fisher) with Fast SYBR Green Master Mix (Applied Biosystems, Foster City, CA) supplemented with gene-specific primers (see **Supplementary Table 3.6**). Experiments were performed in duplicate and repeated three times. Gene expression was calculated using the $2^{-\Delta\Delta Ct}$ method and normalized to the mean of two housekeeping genes before normalizing to the mean expression of all healthy controls across experiments.

Western blotting

Primary fibroblasts and PBMCs were solubilized in lysis buffer containing 20 mM Tris-HCl, pH 7.5; 150 mM NaCl; 1% Triton-X; 1.5 mM $MgCl_2$; 0.5 mM DTT; and protease inhibitor. Protein concentrations were determined by BCA, and 20 µg of protein per sample was separated on a 3–8% Tris-acetate gel. Proteins were blotted on a PVDF membrane and incubated with protein-specific primary antibodies after blocking. The primary antibodies, used at a 1/1000 dilution, included an in-house made rabbit anti-IP_3R1 Rbt03antibody[230]. In addition, rabbit anti-IP_3R2 (Abicode C2) and mouse anti-IP_3R3 (IP_3R3, BD Biosciences) antibodies were obtained. A rabbit pan-IP_3R Rbt475 antibody raised against a peptide corresponding to amino acids 127–141 of human IP_3R1 was produced in-house[231,232]. Vinculin (Sigma) was used as a loading control at a 1/2000 dilution. Secondary goat anti-mouse/rabbit IgG (Thermo Scientific, 1/10,000 dilution) were coupled to HRP. Membranes were developed using the Pierce™ ECL kit (Thermo Fisher) with a ChemiDoc MP Imaging system (Bio-Rad, Hercules, CA). Quantification of the protein expression was performed with ImageJ software[233,234]. The fold change in protein expression was normalized using Excel to the mean of all healthy controls within each independent experiment.

HEK-3KO cells, HEK293 cells expressing only endogenous IP_3R3, and HEK-3KO cells stably expressing IP_3R constructs were solubilized in RIPA lysis buffer supplemented with Halt™ protease inhibitor cocktail (Thermo Fisher). Protein concentrations were determined using the Dc protein assay kit (Bio-Rad), and 7.5 µg of protein per sample was prepared in SDS loading buffer and separated by 7.5% SDS–PAGE. Subsequently, proteins were transferred overnight to a nitrocellulose membrane (Pall Corporation, New York, NY), which was probed using the indicated primary antibodies (a mouse monoclonal antibody recognizing residues 22-230 of human IP_3R3 (BD Transduction Laboratories, San Jose, CA, 1/1000 dilution) and rabbit monoclonal antibody recognizing Calnexin (Cell Signaling Technology, Danvers, MA, 1/2000 dilution)) and corresponding secondary antibodies (goat anti-

mouse/rabbit, Invitrogen, 1/10,000 dilution). Membranes were imaged with an Odyssey infrared imaging system (LICOR Biosciences, Lincoln, NE). The resulting scans were exported to LICOR Image Studio, where the band intensity was calculated. In Excel, the hR3 band intensity values were normalized to the value of the calnexin loading control. Subsequently, these values were further normalized to the value of the corresponding endogenous hIP_3R3. Averages and statistical analysis were performed in GraphPad Prism.

Plasmid cloning

All plasmids used in this study were based on the primary sequence of human IP_3R3 in a pcDNA3.1 plasmid backbone. Mutagenesis to introduce base changes identified in the reported patients was performed with the primers listed in **Supplementary Table 3.7**, which had been synthesized by Integrated DNA Technologies. Suitable sequences were amplified by PCR and subcloned into a pJet1.2/blunt plasmid using the CloneJET PCR Cloning kit (Thermo Fisher) according to the manufacturer's instructions. Mutagenesis PCR was performed with outward-facing complementary primers introducing the desired base change and amplifying the full plasmid. DpnI digestion in Tango Buffer (both from Thermo Scientific) was performed overnight, and the resulting circularized plasmids were used to transform chemically competent DH5α bacteria. Following ampicillin selection, the plasmids were purified from liquid cultures of single colonies using the NucleoSpin Plasmid EasyPure kit (Macherey-Nagel), and base exchange was verified by Sanger sequencing (Eurofins). Restriction enzyme-based cloning was then performed to introduce the mutated sequences into the original pcDNA3.1 construct, and the sequences were reverified.

Generation of HEK-3KO cell lines stably expressing IP_3R3 mutants

HEK-3KO cells are HEK293 cells engineered with CRISPR/Cas9 editing to delete three endogenous IP_3R isoforms[89], and cells expressing endogenous IP_3R3 are HEK293 cells modified with CRISPR/Cas9 editing to express only endogenous IP_3R3. HEK-3KO cells, cells expressing endogenous IP_3R3, and HEK-3KO cells stably expressing exogenous IP3R constructs were grown at 37 °C with 5% CO_2 in DMEM supplemented with 10% foetal bovine serum, 100 U/mL penicillin, and 100 µg/mL streptomycin. The cell lines were maintained by subculturing as necessary, and any selection required was carried out using G418 (VWR, Radnor, PA). HEK-3KO transfection was performed similar to the previously described methods[89,221]. In brief, 1×10^6 cells were pelleted, washed once with PBS, and resuspended in an in-house transfection reagent containing ATP-disodium salt, $MgCl_2$, KH_2PO_4, $NaHCO_3$, and glucose at pH 7.4. DNA (2–5 µg) was mixed with the resuspended cells and electroporated using Amaxa cell nucleofector program Q-001. Cells recovered in fresh DMEM supplemented as described above for 48 h prior to culturing in new 10-cm dishes containing DMEM supplemented with 1.5–2 mg/mL G418. Approximately 7 days after the start of the selection, individual colonies were selected by hand and transferred to 24-well plates containing fresh DMEM with G418. Ten to fourteen

days after transfection, wells that exhibited growth were expanded and screened by western blotting to verify the stable expression of the desired protein.

Immunocytochemistry and confocal microscopy

HEK-3KO cells stably expressing exogenous IP_3R constructs were plated on poly-D-lysine-coated coverslips. When approximately 50% confluent, the cells were fixed using 4% PFA at RT for 15 min. Subsequently, the coverslips were washed with PBS, and the cells were blocked in 10% bovine serum albumin (BSA) in PBS-T (PBS with 0.2% Tween 20) for 1.5 h. Following blocking, the cells were incubated with an anti-IP_3R3 primary antibody in BSA overnight at 4 °C. The following day, the primary antibody was removed, and the coverslips were washed three times with PBS-T for 10 min with gentle rocking. Subsequently, a secondary antibody conjugated to Alexa Fluor 488 was incubated for 1 h in BSA at RT with gentle rocking. After incubation, the coverslips were washed with PBS-T and mounted on slides. After the slides were allowed to dry, the coverslips were sealed onto slides and imaged by confocal microscopy.

Fluorescence measurement of calcium flux

Fibroblasts were seeded in 96-well plates (Greiner, Kremsmünster, Austria) and assessed for $[Ca^{2+}]_{cyt}$ using Fura-2/AM (Eurogentec, Seraing, Belgium). Briefly, cells were loaded with the ratiometric fluorescent Ca^{2+} indicator Fura2/AM (1 µM) at RT for 30 min in a modified Krebs solution (containing 150 mM NaCl, 5.9 mM KCl, 1.2 mM $MgCl_2$, 11.6 mM HEPES (pH 7.3), and 1.5 mM $CaCl_2$). Cells were allowed to rest for 30 min at RT in the absence of Fura2/AM to allow complete dye de-esterification before analysis was performed on a FlexStation 3 microplate reader (Molecular Devices, Sunnyvale, CA, USA). The indicator was alternately excited at 340 and 380 nm, and fluorescence emission at 510 nm was recorded. EGTA was added after 30 s in all conditions to a final concentration of 3 mM to chelate Ca^{2+} ions in the buffer, and the fluorescence was recorded for 60 s prior to stimulation. The responses to stimuli prepared in Ca^{2+}-free modified Krebs solution containing 3 mM EGTA were acquired for 6 min. Ionomycin and the irreversible sarco-/endoplasmic reticulum Ca^{2+}-ATPase (SERCA) inhibitor thapsigargin were added to final concentrations of 10 µM, and bradykinin was added to a final concentration of 50 nM. All traces are shown as the ratio of both emission wavelengths F_{340}/F_{380}.

PBMCs from different donors were first stained with different anti-CD4 antibodies for multiplexing (all RPA-T4, eBioscience, BD Biosciences, Invitrogen). After mixing together, the PBMCs were loaded with the ratiometric fluorescent Ca^{2+} indicator dye FuraRed AM (Thermo Fisher) as described above. For TCR stimulation experiments, the cells were incubated on ice with 10 µg/mL anti-CD3 (OKT3) and anti-CD28 antibodies (CD28.2, both eBioscience) for 30 min. Ionomycin and the irreversible SERCA inhibitor thapsigargin were each added to a final concentration of 10 µM, and a cross-linking goat anti-mouse IgG antibody (Abcam, Cambridge, UK) was added for TCR stimulation to a final concentration of 10 µg/mL. Differences in baseline Ca^{2+} between ionomycin/thapsigargin and TCR stimulation

experiments are due to separate acquisition in different experimental sets and therefore changes in PMT voltages of the machine.

The cells were analysed on a BD FACSCanto flow cytometer (BD Biosciences, Franklin Lakes, NJ, US). The data on the ratio of emission at 450/50 nm after excitation at 405 nm and emission at 670 nm after excitation at 488 nm were exported using the Kinetics platform of FlowJo™ software (v10.7.1, Ashland, OR). A gating strategy was used to select living single lymphocytes before distinguishing cells from different individuals based on the fluorochromes of the anti-CD4 antibodies, for details please refer to **Supplementary Fig. 3.1A**. Raw data from both approaches were smoothened using a second-order running average of 5 in GraphPad Prism (v9.0.0, San Diego, CA). A baseline value was calculated for each measurement as the mean fluorescence during the 60 s before the addition of the stimulus. This baseline was used for calculating the area under the curve (AUC) and the peak amplitude using GraphPad Prism; the minimum peak height was 10% of the distance from the minimum to the maximum Y.

HEK-3KO cells and HEK-3KO cells stably expressing exogenous IP_3R constructs were analysed with a FlexStation 3 microplate reader (Molecular Devices) after loading with 4 µM Fura2/AM (TEFLabs, Austin, TX) in complete DMEM. After 1 h, the cells were harvested, washed, and resuspended in Ca^{2+} imaging buffer (10 mM HEPES; 1.26 mM Ca^{2+}; 137 mM NaCl; 4.7 mM KCl; 5.5 mM glucose; 1 mM Na_2HPO_4; and 0.56 mM $MgCl_2$, pH 7.4) before being dispensed into a black-walled flat-bottom 96-well plate (Greiner). The plate was centrifuged (200 ×g for 2 min) and incubated at 37 °C for 30 min prior to commencing the assay. Excitation was applied as described above, and Ca^{2+} imaging buffer or varying concentrations of CCh were added to induce IP_3R-mediated Ca^{2+} release. Readings were taken every 4 s for a total of 200 s, and the data were exported from SoftMax® Pro Microplate Data Acquisition and Analysis software to Excel, where the F_{340}/F_{380} ratio was calculated. The ratios were normalized to the average of the first five ratio values, and the AUC and peak amplitude were calculated in GraphPad Prism as described above. The data averages were derived on the basis of at least three individual plates, and the fit of each logistic curve was calculated with GraphPad Prism.

NFAT translocation assay

Frozen PBMCs were thawed in RPMI 1640 (GibcoTM, Thermo Fisher) supplemented with 10% FBS (Tico Europe, Amstelveen, Netherlands) and 100 U/mL penicillin/streptomycin (GibcoTM, Thermo Fisher) and allowed to rest at 37 °C prior to incubation with 10 µg/mL anti-CD3 (OKT3) and 10 µg/mL anti-CD28 antibodies (CD28.2, both eBioscience) on ice for 30 min. Cross-linking goat anti-mouse IgG (Abcam) was added to a final concentration of 20 µg/mL for 30 min at 37 °C. As positive controls, 1 µM ionomycin and 50 ng/mL phorbol 12-myristate 13-acetate (PMA) were added and incubated for 30 min at 37 °C. Cells were fixed in 2% paraformaldehyde and permeabilized with 100% methanol prior to staining for CD4 (RPA-T4, eBioscience), CD8 (OKT8, Invitrogen), and NFAT1 (D43B1, Cell Signaling

Technology) followed by AF488-conjugated secondary anti-rabbit IgG (Invitrogen, Thermo Fisher) and DAPI staining. Cells were acquired on an ImageStreamX MkII (Amnis Corporation) at 40x magnification. The data were analysed using IDEAS software (Amnis Corporation), which enabled the identification of focused cells before gating on single $DAPI^{+}NFAT^{+}CD4^{+}$ cells (see **Supplementary Fig. 3.2**). The percentage of cells with nuclear NFAT and the extent of NFAT translocation were analysed with the Nuclear Localization Wizard, and the latter is presented as Similarity Score.

Phosphorylation assay

Frozen PBMCs were thawed, plated, and rested in complete RPMI at 37 °C prior to stimulation with 5 µg/mL anti-CD3 (UCHT1) and 5 µg/mL anti-CD28 (CD28.2) antibodies (both from eBioscience) or anti-human IgA/IgG/IgM (Jackson ImmunoResearch, West Grove, PA) for the indicated durations. Cells were fixed in 2% paraformaldehyde and permeabilized with 100% methanol prior to staining for CD14 (M5E5, BioLegend), CD4 (RPA-T4, eBioscience), CD8 (SK1, eBioscience), CD19 (HIB19, eBioscience), and phospho-Erk (Thr202/Tyr204, MILAN8R, eBioscience). Cells were acquired on a BD FACSCanto flow cytometer (BD Biosciences). After exclusion of doublets and monocytes via CD14, T cells were gated as $CD19^{-}$, and B cells were gated as $CD4^{-}CD8^{-}CD19^{+}$ cells (**Supplementary Fig. 3.1B**). The fold change in the median fluorescence intensity was calculated based on the whole unstimulated population of the respective sample.

Proliferation assay

Frozen PBMCs were thawed in RPMI 1640 (GibcoTM, Thermo Fisher) supplemented with 10% FBS (Tico Europe) and 100 U/mL penicillin/streptomycin (GibcoTM, Thermo Fisher) prior to labelling with 1 µM CFSE (InvitrogenTM, Carlsbad, CA) at 37 °C with regular shaking. The reaction was quenched with ice-cold FBS, and the cells were plated after washing in complete medium containing 10% FBS, 100 U/mL penicillin/streptomycin, 25 mM HEPES, and nonessential amino acids. T-cell stimulation was either performed in wells coated with 10 µg/mL anti-human CD3 (UCHT1) monoclonal antibody and 5 µg/mL anti-human CD28 (CD28.2) monoclonal antibody (both from eBioscience, San Diego, CA) supplemented in the medium or with both monoclonal antibodies, each at 5 µg/mL, supplemented in the medium. B-cell stimulation was performed with 10 µg/mL AffiniPure goat anti-IgA/IgG/IgM (Jackson ImmunoResearch) and 1 µg/mL CD40L with or without 20 ng/mL IL-21 (both from BioLegend). Cells were stained for CD4 (RPA-T4, Invitrogen), CD8 (OKT8, Invitrogen), and CD19 (HIB19, eBioscience) and analysed by flow cytometry on a BD FACSCanto (BD Biosciences, Franklin Lakes, NJ, US) on days 3 and 4 after stimulation. For the gating strategy, refer to **Supplementary Fig. 3.1C**.

Statistical analysis

All statistical analyses were done by performing ordinary one-way ANOVA with Dunnett's multiple comparison test by comparing each individual to the healthy donors using GraphPad Prism 9.0.0 (San Diego, CA).

3.4 Results

3.4.1 Identification of compound heterozygous *ITPR3* variants in two immunodeficient patients

To identify the cause of immunodeficiency in two patients without a genetic diagnosis, comprehensive clinical, immunological, and genetic analyses were performed. Both patients were born to nonconsanguineous parents of European descent (**Fig. 3.1A**). P1 was a 12-year-old male patient who presented with combined immunodeficiency with profoundly low numbers of B and T cells and required hematopoietic stem cell transplantation (HSCT) at the age of 6 years. He developed an EBV-induced leiomyoma after transplantation and showed abnormal tooth eruption and mineralization as well as thin hair since birth. At the age of 11, P1 presented with peripheral neuropathy and was diagnosed with Charcot–Marie–Tooth. P2 was a 36-year-old male who presented with recurring immune thrombocytopenia, requiring splenectomy at the age of 19 years. He subsequently suffered from autoimmune haemolytic anaemia, susceptibility to infections, and enteropathy. Hypogammaglobulinemia and low numbers of switched memory B cells led to a diagnosis of CVID and monthly treatment with intravenous immunoglobulins. The patient did not show signs of neuromuscular disorder. Additional clinical details are available in the Supplemental Data (**extended clinical case descriptions**, **Supplementary Tables 3.1–3**). None of the parents showed a clinically apparent immunological phenotype, and all self-reported to be healthy.

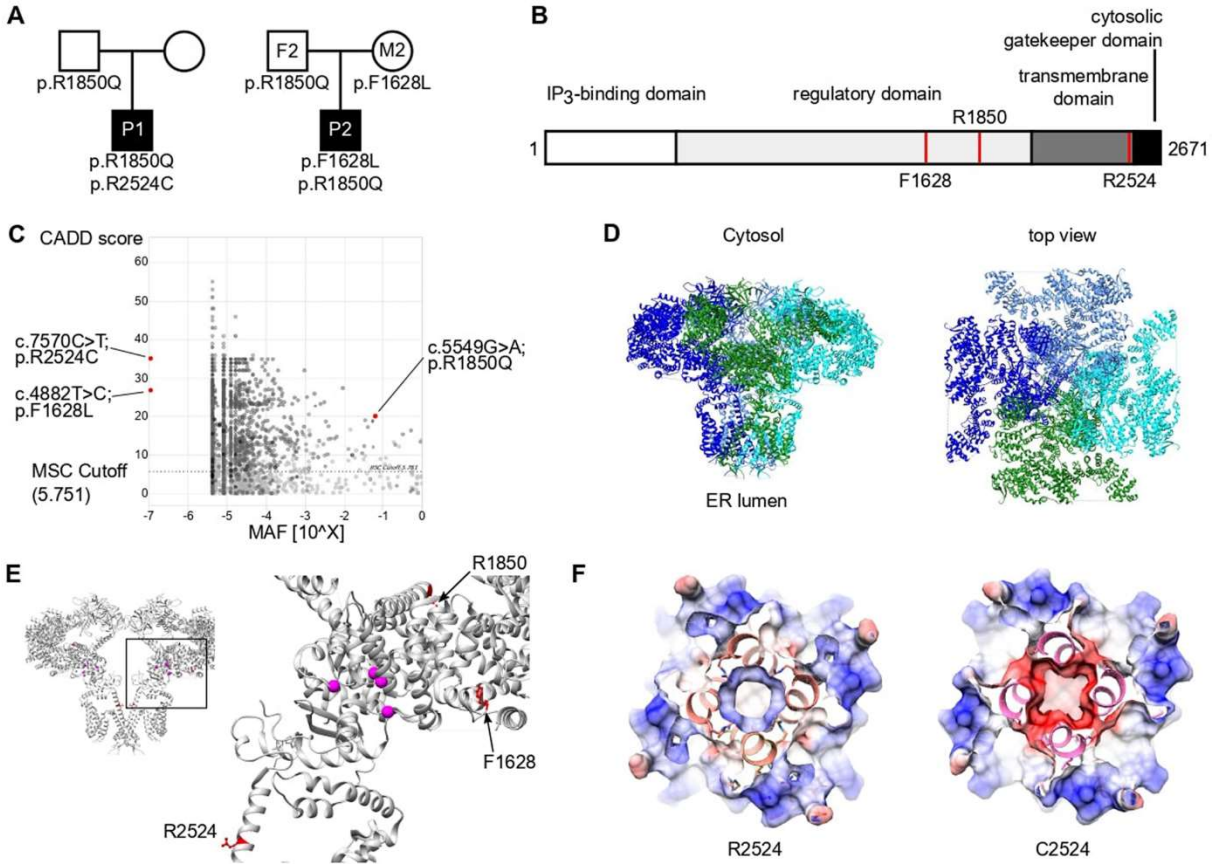

Figure 3.1: Identification of compound heterozygous variants in *ITPR3* in two patients with immunodeficiency or immune dysregulation. (A) Pedigrees of two unrelated families illustrating the genotype of the tested individuals. **(B)** Schematic domain structure of IP_3R3 with positions of the variants indicated by red lines. **(C)** PopViz plot showing the minor allele frequency (MAF) and the Combined Annotation Dependent Depletion (CADD) score with the identified variants in red. The dashed line indicates the gene-specific mutation significance cutoff (MSC). **(D)** Cryo-EM structure of homotetrameric IP_3R3 (6DQJ) depicted in a ribbon diagram with different subunits in different colours. Two orthogonal views are shown: a side view along the membrane plane (left) and a view from the cytosol (right). **(E)** Illustration of the identified variants mapped onto the 3D structure of IP_3R3 (6DQJ). Two opposing subunits are shown in side view. Unresolved sequences are indicated by dashed lines. The red dashed line spans a known phosphorylation region including the R1850 residue. Putative residues involving Ca^{2+} binding to the receptor are rendered as pink spheres. **(F)** Slices through the space-filled model of the IP_3R3 TM region perpendicular to the 4-fold axis as seen from the cytosol. Surfaces are color-coded according to electrostatic charges calculated for the model (red: negative; blue: positive).

Whole-exome sequencing was performed for both patients, filtering for rare damaging variants after excluding the presence of known variants of inborn errors of immunity. We identified compound heterozygous candidate variants in *ITPR3* encoding inositol 1,4,5-trisphosphate receptor subtype 3 (IP_3R3; NM_002224.4). Three distinct variants were identified in the two compound heterozygous patients. P1 harboured a *de novo* variant not reported in any public database but recently suggested to be a cause of Charcot–Marie–Tooth syndrome[224] (c.7570C>T:p.Arg2524Cys, referred to as R2524C). In addition, P1 inherited a c.5549G>A:p.Arg1850Gln (referred to as R1850Q) substitution from his father that was also found in P2 and his father F2; this mutation is reported with an allelic frequency of 6%. P2 inherited a second private variant from his mother M2, resulting in a c.4882T>C:p.Phe1628Leu

(referred to as F1628L) substitution. All variants were validated by Sanger sequencing (**Supplementary Fig. 3.3A**), and their position within the protein is depicted in **Fig. 3.1B**. All protein-coding variants were predicted to be damaging by Sorting Intolerant from Tolerant[235] and Deleterious Annotation of Genetic Variants Using Neural Networks[236] algorithms (**Supplementary Table 3.4**). In addition, all variants had a CADD score above the mutation significance cutoff (MSC 5.7) and were therefore predicted to exert a high impact on protein structure and function[237] (**Fig. 3.1C**). Importantly, there were no additional variants identified in the genes causing CRAC channelopathies, such as ORAI1 or STIM1. These results demonstrate the identification of two reportedly unrelated patients with immunodeficiency and compound heterozygosity of predicted damaging *ITPR3* variants.

To further investigate the potential impact of the identified variants, we mapped them onto the IP_3R3 structure resolved via cryo-EM[238,239]. All the altered residues are highly conserved across species. Moreover, residues F1628 and R2524 are conserved among all three IP_3R isoforms: IP_3R1, IP_3R2, and IP_3R3 (**Supplementary Fig. 3.3B, C**). *In vivo*, these isoforms assemble as homo- or heterotetramers to form functional IP_3-regulated Ca^{2+} channels in the ER membrane. Each IP_3R monomer consists of a cytosolic N-terminal IP_3-binding domain followed by a large coupling/regulatory multidomain region, a pore-forming region comprising six TM helices, and a C-terminal cytosolic tail[226,238] (**Fig. 3.1B, D**). The F1628L and R1850Q variants are located in one of the regulatory alpha-helical domains. The R1850Q variant is close to the functionally important S1832 phosphorylation site[240], while F1628L is in close proximity to several predicted phosphorylation and ubiquitination sites[241] (**Fig. 3.1E**). The *de novo* R2524C variant is located in the sixth TM domain helix (S6). The S6 helices from each subunit shape the channel's ion conduction pathway and form the constriction gate that controls ion translocation across the ER membrane. R2524 is located in the cytosolic extension of the S6 helix just beyond the gate[239], and its positive charge is likely neutralized through coordination with neighbouring aspartate residues[242]. According to computational modelling, replacement of the positively charged arginine residue with an uncharged cysteine residue abolishes the charge coordination in the TM helix S6, thereby changing the pore charge in this region (**Fig. 3.1F** and **Supplementary Fig. 3.3D**). Due to the strong conservation of all the identified variants and their location in or close to predicted functionally relevant sites, we hypothesized that these variants alter channel function, leading to defective calcium mobilization and subsequent impaired lymphocyte activation.

3.4.2 Functional impact of the *ITPR3* variants

To assess the functional impact of *ITRP3* variants, we investigated expression levels and Calcium flux in patient fibroblasts and PBMCs. While PBMCs are more relevant to the observed phenotype in the probands, PBMCs were not available due to HSCT in P1. We therefore included fibroblasts to enable us to study primary cells from this patient, with the added advantage that measurements of intracellular Ca^{2+} fluxes are very sensitive and standardized by using automated pipetting devices with adherent cells such as fibroblasts. We first analysed the influence of the variants on mRNA and protein expression

levels of all IP_3R subtypes in both cell types using isoform-specific primer pairs and antibodies selectively recognizing one of the isoforms or all of them simultaneously (pan-IP_3R). mRNA expression was normal in fibroblasts (**Fig. 3.2A**); however, *ITPR3* levels were reduced in PBMCs from both patients and the parents of P2 (**Fig. 3.2B**). Immunoblot analysis yielded clear immunoreactive bands for IP_3R1 and IP_3R3 (**Fig. 3.2C, D**), while the signals for IP_3R2 and an antibody recognizing all IP_3R subtypes were weaker (**Supplementary Fig. 3.4**). Despite weak bands in some individual samples, expression levels were effectively quantified, as they were consistent across different experiments. In contrast to the mRNA levels, we detected reduced levels of IP_3R3 in P1 fibroblasts (PBMCs were not available due to HSCT) (**Fig. 3.2C**). Protein expression levels in PBMCs were also variable among healthy donors, with a tendency toward reduced IP_3R1 and IP_3R3 in M2 and P2, consistent with the mRNA levels (**Fig. 3.2D**). While the expression of the IP_3R subtypes and the impact of variants varied across investigated cell types, these results suggest a reduction of *ITPR3* in both patients at the mRNA and protein levels and in PBMCs of P2. The reduction of IP_3R1 and IP_3R3 levels in M2 and P2 may result from the F1628L variant alone and be a result of a baseline feedback mechanism acting at the transcriptional level, as mRNA levels were also reduced in both of these individuals.

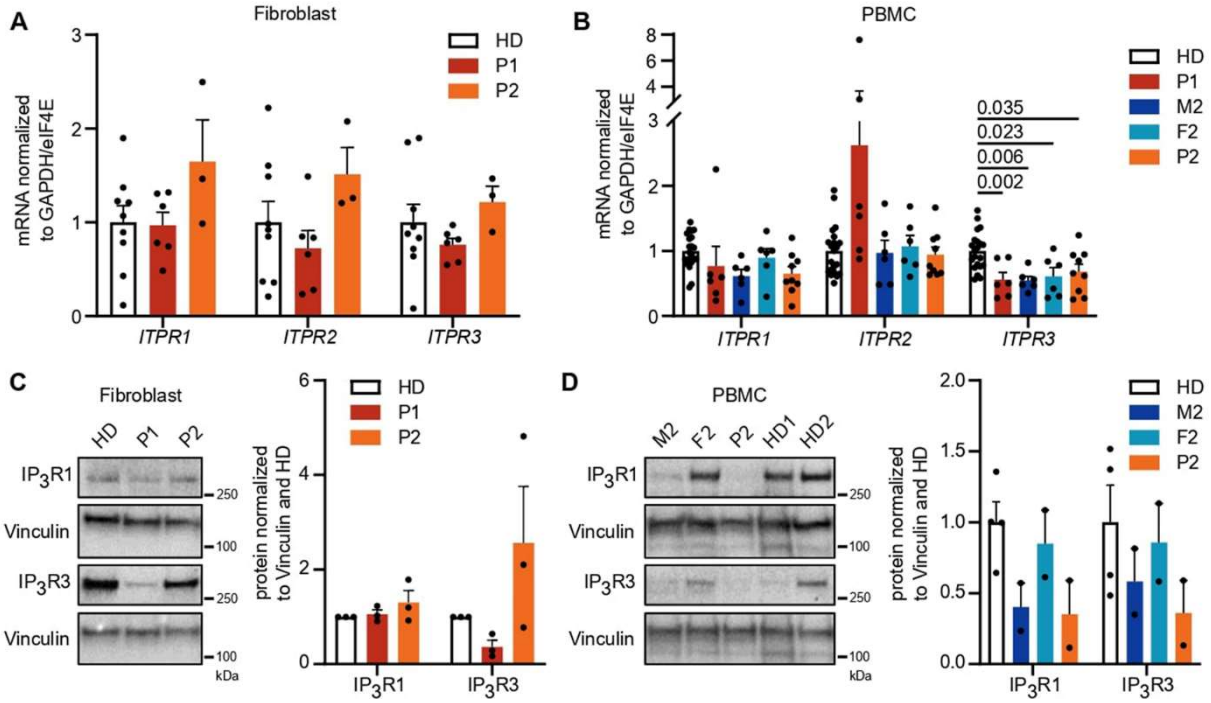

Figure 3.2: IP_3R3 expression is reduced by variants in a cell type-dependent and variant-specific manner. **(A, B)** mRNA expression of all three receptor subtypes was measured in primary fibroblasts and PBMCs with isoform-specific primers. Dots represent the mean of duplicates for independent runs normalized to the mean values of the housekeeping genes GAPDH and eIF4E. Expression in **(A)** fibroblasts and **(B)** PBMCs. **(C, D)** Western blot analysis of IP_3R1 (314 kDa) and IP_3R3 (304 kDa) isoform protein expression was performed using subtype-specific antibodies. Representative blots with the molecular weight marker indicated (left) and the quantification of protein expression normalized to the housekeeping gene vinculin (124 kDa, right) are shown. Quantification was performed in **(C)** fibroblasts and **(D)** PBMCs. Number of independent experiments: **(A)** n=3 with 2 different HDs. **(B)** n=3 with 5 different HDs. **(C)** n=3 with 2 different HDs. **(D)** n=2 with 3 different HDs. Individuals were sampled at multiple time points. The values are presented as the mean + SEM. One-way ANOVA was performed with a multiple comparison test.

As IP_3Rs are crucial for Calcium dynamics and mediating IP_3-induced Ca^{2+} flux, we sought to investigate Ca^{2+} responses in primary patient cells to test IP_3R functionality. To this end, we first studied Ca^{2+} flux in patient fibroblasts cultured from skin biopsies and monitored the change in $[Ca^{2+}]_{cyt}$ in response to various stimuli using a ratiometric Ca^{2+} indicator (Fura-2/AM). Stimulation with the Ca^{2+} ionophore ionomycin and the sarco-/endoplasmic reticulum Ca^{2+}-ATPase (SERCA) inhibitor thapsigargin in the presence of extracellular EGTA, a Ca^{2+}-chelating agent, revealed dysregulated intracellular Ca^{2+} homeostasis in fibroblasts of P1 (**Supplementary Fig. 3.5A, B**). When directly monitoring IP_3R-mediated Ca^{2+} release in fibroblasts in response to the physiological G-protein coupled receptor (GPCR) agonist bradykinin, we also observed a decreased response in P1, as assessed by the integrated response (area under the curve, AUC) as well as the peak amplitude normalized to the respective sample background (**Fig. 3.3A**). P2 displayed a comparable response to the HDs.

We then studied PBMCs to confirm impaired Ca^{2+} signalling by analysing $CD4^+$ T cells from P2 and his parents (P1 PBMCs were not available due to successful HSCT). By labelling $CD4^+$ T cells from different donors with different fluorochromes before combining the samples, we minimized sample-to-sample variation. The cells were loaded with the ratiometric Ca^{2+} indicator FuraRed and stimulated with ionomycin or thapsigargin to investigate calcium homeostasis or anti-CD3 and anti-CD28 to assess physiological IP_3R-mediated calcium responses. While Ca^{2+} homeostasis was disrupted in P2 and his parents (**Supplementary Fig. 3.5C, D**), physiological Ca^{2+} responses after TCR engagement were impaired only in P2, with F2 showing an intermediate phenotype (**Fig. 3.3B, C**). This finding illustrates insufficient subtype redundancy in lymphocytes to rescue the phenotype in P2, in contrast to the sufficient redundancy that was observed in fibroblasts. Together, these results suggest disrupted Ca^{2+} homeostasis and defects in IP_3R-mediated Ca^{2+} release in both patients, with P1 potentially the more severe (also being detected in fibroblasts), although the direct comparison between patient PBMCs was not possible due to HSCT. Ca^{2+} homeostasis but not signalling defects were also observed in the heterozygous parents of P2.

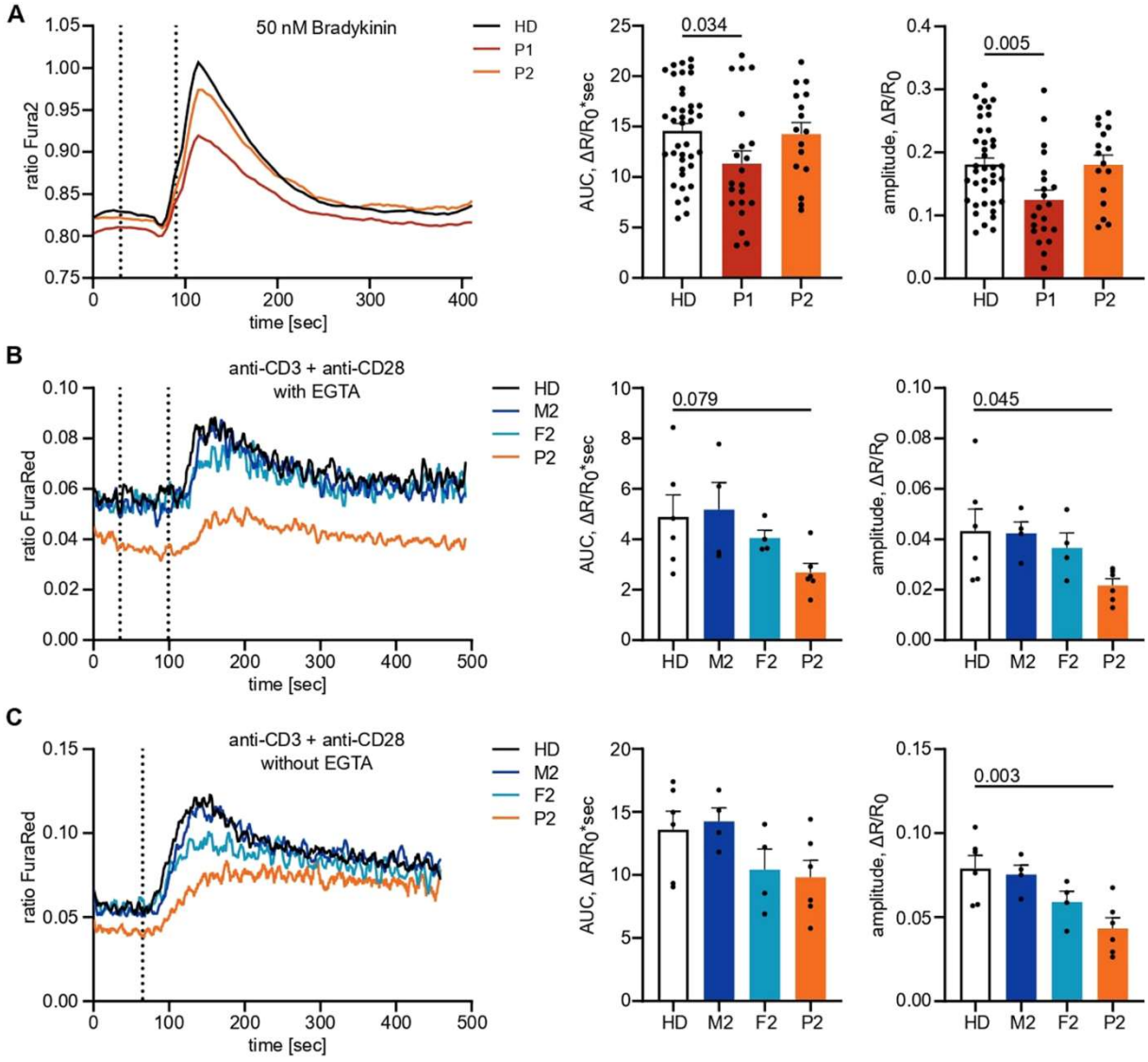

Figure 3.3: Variants in *ITPR3* impede IP_3-mediated calcium signalling. (A) Adherent fibroblasts were loaded with the ratiometric Ca^{2+} indicator Fura-2/AM, and calcium flux was monitored over time. The first dashed line indicates the addition of EGTA for the acquisition of the background, and the second dashed line indicates the addition of 10 µM bradykinin. The area under the curve (AUC) and maximal amplitude of the response were calculated with respect to individual background values. **(B)** PBMCs were stained for CD4, loaded with the ratiometric Ca^{2+} indicator FuraRed and pre-incubated with anti-CD3 and anti-CD28 on ice before monitoring changes in cytosolic Ca^{2+} concentrations at room temperature by flow cytometry. The first dashed line indicates the addition of EGTA, and the second dashed line indicates the addition of 10 µg/mL cross-linking antibody to induce TCR ligation in the absence of extracellular Ca^{2+}. **(C)** The experiment was performed as in **(B)** with the first dashed line indicating the addition of 10 µg/mL cross-linking antibody to induce TCR ligation in the presence of extracellular Ca^{2+}. Number of independent experiments: **(A)** n=9 with 2 different HDs. **(B, C)** n=3 with 3 different HDs. Individuals in **(B, C)** were sampled at multiple time points. Traces represent the mean values of all experiments, and response quantification is shown as the mean + SEM. One-way ANOVA was performed with a multiple comparison test.

To formally evaluate the impact of the *ITPR3* variants on calcium signalling in a model allowing direct comparison in the absence of compensatory mechanisms, we used HEK cells that had been engineered to eliminate endogenous expression of all three IP_3R subtypes[89] (HEK-3KO) and reintroduced mutant IP_3R3. Double-knockout of IP_3R1 and IP_3R2, resulting in a cell line expressing only endogenous IP_3R3

(WT), was used as a control with physiological expression levels. WT IP_3R3 in HEK-3KO cells was overexpressed (WT OE) to measure the maximum Ca^{2+} signalling capacity. We generated multiple monoclonal cell lines with transgenic expression of each mutant allele, confirmed the localization of each encoded protein to the ER via immunohistochemistry, and used western blotting to benchmark protein expression levels against endogenous WT expression (**Supplementary Fig. 3.6A, B**). Using these knockout cell lines reconstituted with mutant alleles, we investigated the calcium flux induced by different concentrations of the muscarinic GPCR agonist carbachol (CCH) and analysed the magnitude of the responses (**Supplementary Fig. 3.6C–E**). The private F1628L variant of P2 inherited from his mother resulted in highly reduced responses even when protein expression was increased 40- to 60-fold compared to that of the endogenous WT (**Fig. 3.4A** and **Supplementary Fig. 3.6F**). Although the R1850Q variant shared by P1 and P2 as well as their fathers resulted in absent responses with protein levels similar to those of the WT, overexpression of more than 60-fold restored full channel function (**Fig. 3.4B** and **Supplementary Fig. 3.6G**). This outcome suggests that neither variant showed complete loss-of-function but instead displays reduced signalling capacity. In contrast, the *de novo* R2524C variant identified in P1 showed more severe defects with absent Ca^{2+} mobilization across all the clones, suggesting complete loss-of-function (**Fig. 3.4C** and **Supplementary Fig. 3.6H**). Together, these results clearly demonstrate IP_3R-mediated Ca^{2+} release defects in the F1628L, R1850Q, and R2524C mutants in an overexpression model, with the most striking defect found in the variant borne by P1, who presented with the more severe clinical manifestations of immunodeficiency.

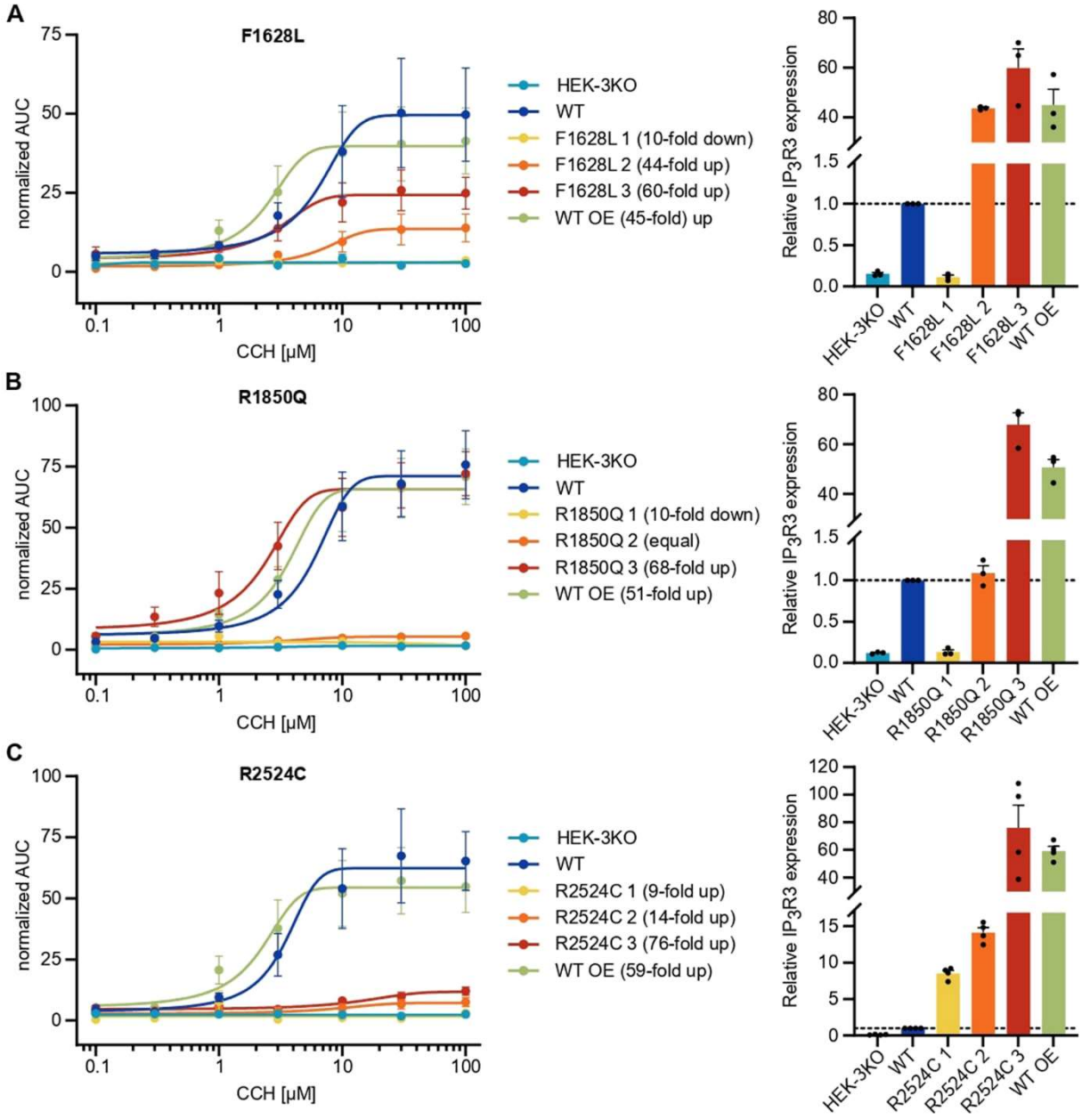

Figure 3.4: IP_3-induced Ca^{2+} flux is reduced through F1628L-, R1850Q-, and R2524C-mutant IP_3R3. HEK-3KO cells, not expressing any IP_3R subtype, were stably transduced with the wild-type (WT OE – overexpressing) or mutated versions of the IP_3R3 receptor, subcloned, and stimulated with different concentrations of the GPCR agonist carbachol (CCH) in Ca^{2+} imaging buffer. Cells expressing only endogenous IP_3R3 (WT) and HEK-3KO cells were used as positive and negative controls, respectively. Dose–response curves of the AUC of representative cell lines stably expressing IP_3R3 with the **(A)** F1628L (n=3), **(B)** R1850Q (n=3), or **(C)** R2524C (n=3) variant are shown on the left. Fold changes in IP_3R3 protein expression in transduced cells normalized to endogenous IP_3R3 protein expression were determined after WB (for representative blots, see **Supplementary Fig. 3.6B**) and are indicated in brackets and plotted on the right. Dotted lines indicate the reference protein expression of the WT. Values are presented as the mean + SEM.

3.4.3 Defective immunological responses in *ITPR3* patients

Following our observations that Ca^{2+} signalling was disrupted in immune cells of our patients, we investigated the downstream effects on immune cell function. P1 was, of necessity, excluded due to

successful transplantation of the hematopoietic compartment. First, we investigated the impact of variants in *ITPR3* on early downstream Ca^{2+}-dependent translocation of NFAT from the cytoplasm to the nucleus, where it acts as a transcription factor to induce the expression of, among other genes, IL-2, which is crucial for a productive immune response[243,244]. TCR engagement by cross-linking anti-CD3 and anti-CD28 antibodies resulted in translocation of NFAT1 to the nucleus (**Fig. 3.5A**). Quantification of the translocation response was performed by calculating the Similarity Score, which is a measure of correlated pixels between stained NFAT1 and the DAPI-stained nucleus. P2 showed impaired nuclear NFAT1 translocation compared to the healthy controls, but translocation after stimulation with PMA and ionomycin was normal (**Fig. 3.5B–D**). Although the mother responded normally, translocation in F2 was impaired, which was in line with the aforementioned intermediate phenotype in the Ca^{2+} response.

Next, we investigated activation by phosphorylation of another important protein mediating immune cell activation, namely, Erk. Following TCR stimulation, the percentage of $pErk^{+}$ positive cells was reduced in P2 at different time points, while the heterozygous parents presented an intermediate phenotype (**Fig. 3.6A, B**). Cells that responded showed comparable phosphorylation of Erk (**Fig. 3.6C**), indicating that the defect was in triggering pathway activation. Stimulation of the BCR resulted in relatively normal pErk positivity in B cells (**Fig. 3.6D–F**). These results suggest a functional defect of IP_3R3 in P2 resulting in impaired TCR signalling.

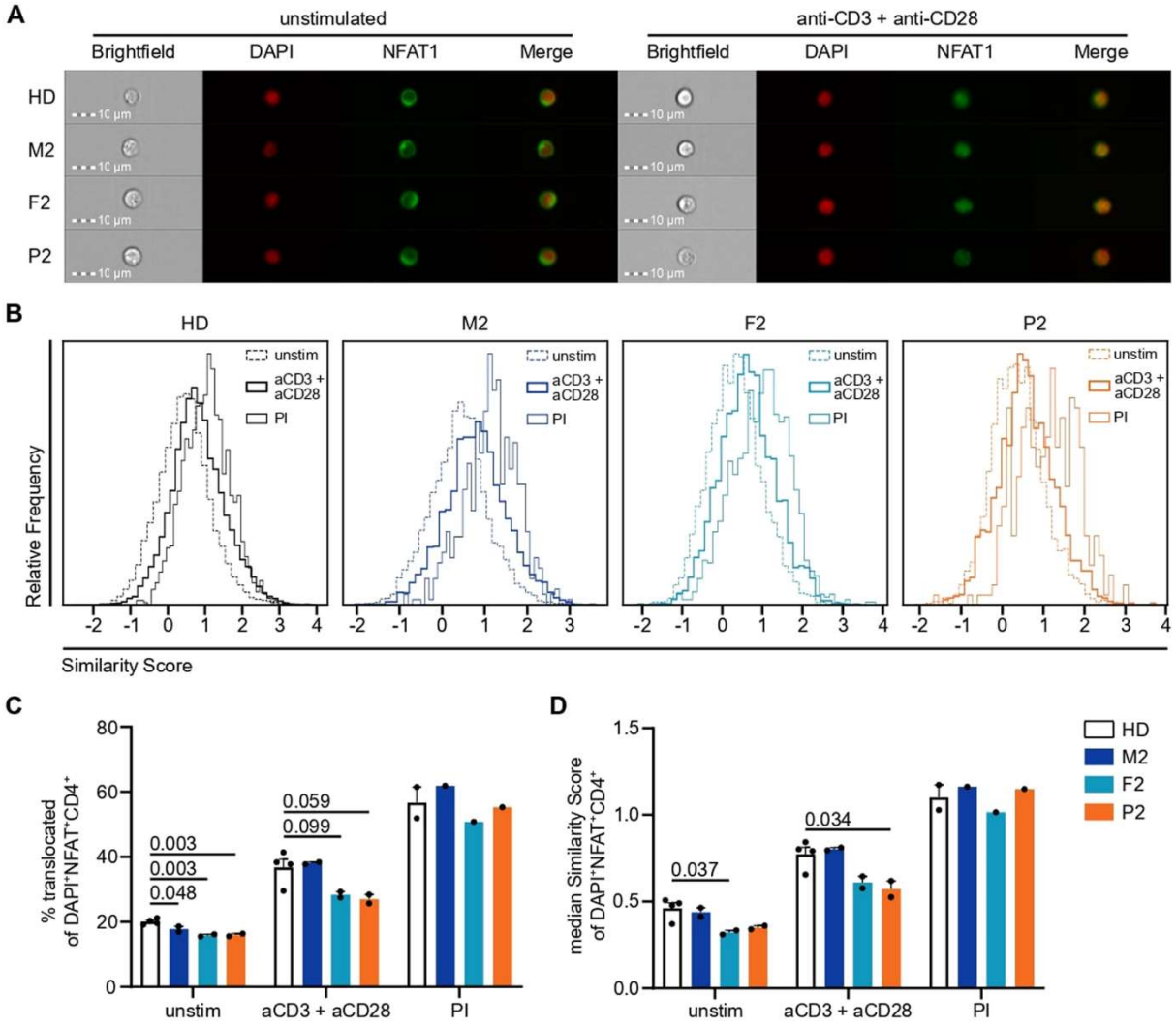

Figure 3.5: Nuclear translocation of NFAT1 is impaired by variants in IP_3R3 following TCR but not PMA + ionomycin stimulation. PBMCs were incubated with anti-CD3 and anti-CD28 (both 10 µg/mL) antibodies on ice before cross-linking was induced for 30 min at 37 °C by adding 20 µg/mL of a cross-linking antibody for TCR stimulation (aCD3 + aCD28). PMA + ionomycin (PI) stimulation was performed simultaneously as a positive control. Nuclear translocation was assessed by ImageStream analysis in $CD4^+$ T cells. **(A)** Representative images of unstimulated and TCR-stimulated cells from all the individuals. **(B)** Histograms of the Similarity Score as a measure of nuclear NFAT1 localization for unstimulated, TCR-stimulated, and PI-stimulated $CD4^+$ T cells. **(C)** Percentage of unstimulated, TCR-stimulated, and PI-stimulated $CD4^+$ T cells with nuclear NFAT1. **(D)** Median Similarity Score of unstimulated, TCR-stimulated, and PI-stimulated $CD4^+$ T cells. Number of independent experiments: n=2 with 4 different HDs for unstimulated and TCR-stimulated cells, n=1 with 2 different HDs for PI-stimulated cells. Individuals were sampled at different time points. The values are presented as the mean + SEM. One-way ANOVA was performed with a multiple comparison test.

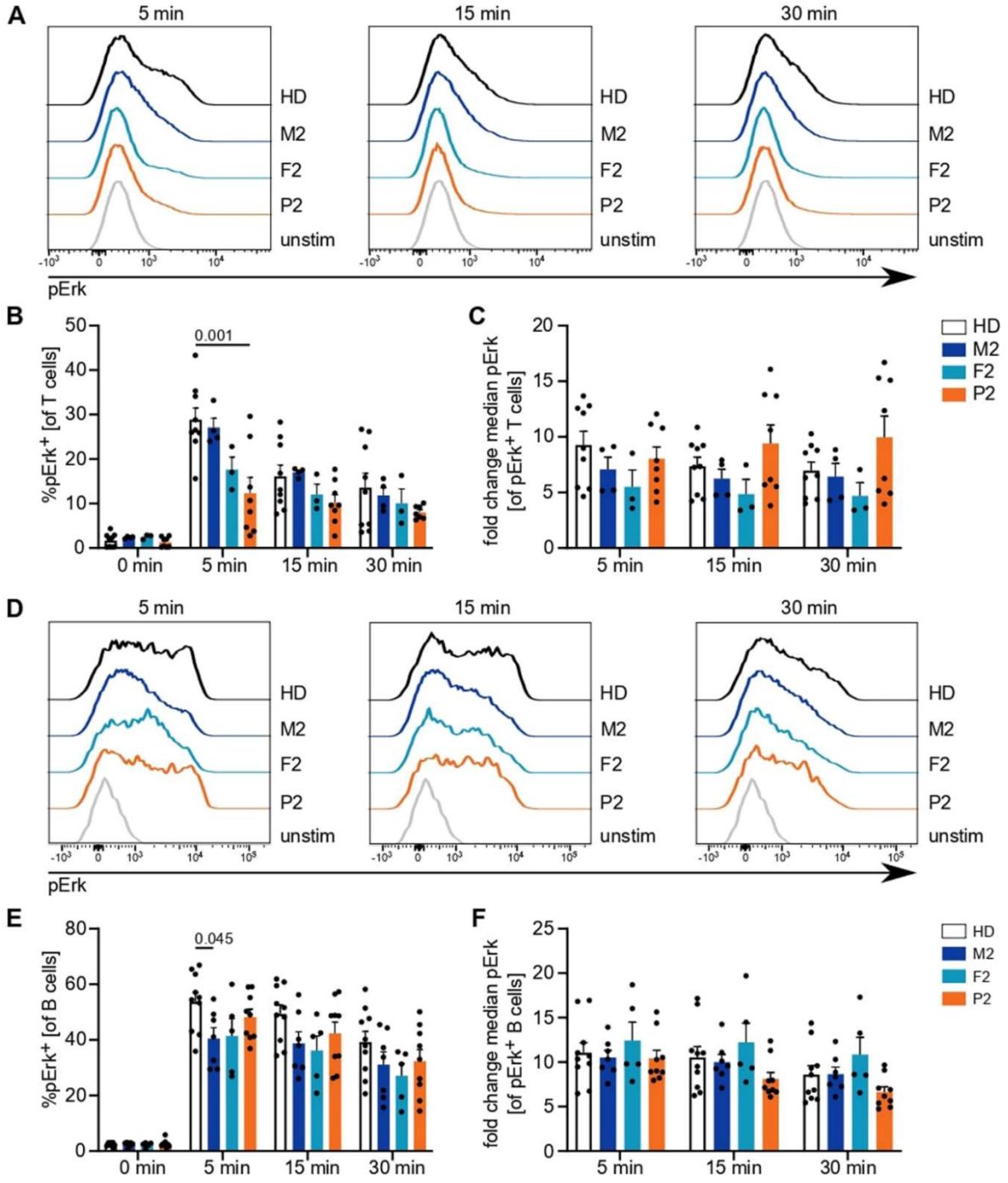

Figure 3.6: Antigen receptor downstream phosphorylation events are reduced in P2. PBMCs were stimulated with anti-CD3 and anti-CD28 antibodies or immunoglobulins for 5, 15, or 30 min. **(A)** Representative histograms illustrating Erk phosphorylation following TCR stimulation after different stimulation intervals. **(B)** Percentage of T cells with phosphorylated Erk among total T cells. **(C)** Fold change of median fluorescence intensity in $pErk^+$ cells compared to that in the total unstimulated cell population. **(D)** Representative histograms illustrating Erk phosphorylation following BCR stimulation after different stimulation intervals. **(E)** Percentage of B cells with phosphorylated Erk in total B cells. **(F)** Fold change of median fluorescence intensity in $pErk^+$ cells compared to that in the total unstimulated cell population. Number of independent experiments: **(A–C)** n=4 with 4 different HDs. **(D–F)** n=6 with 5 different HDs. Individuals were sampled at multiple time points. The values are presented as the mean + SEM. One-way ANOVA was performed with a multiple comparison test.

Finally, we assessed the downstream results of lymphocyte activation by analysing the proliferative potential of $CD4^+$ and $CD8^+$ T cells in response to TCR engagement and $CD19^+$ B cells in response to BCR engagement. The total cell numbers after TCR stimulation were reduced in all individuals in the kindred of P2 compared to healthy donors (**Supplementary Fig. 3.7A, B**). TCR-induced cell division was substantially reduced in $CD4^+$ and $CD8^+$ T cells of P2, with intermediate phenotypes acquired by the heterozygous parents (**Fig. 3.7A, B** and **Supplementary Fig. 3.7C, D**). The reduced proliferative capacity of P2 T cells was even more pronounced when PBMCs were stimulated with soluble anti-CD3 and soluble anti-CD28 antibodies, mimicking suboptimal stimulation conditions (**Fig. 3.7D, E** and **Supplementary Fig. 3.7F, G**). Interestingly, bystander activation of $CD19^+$ B cells[245] was also profoundly impeded in P2 cells (**Fig. 3.7C, F** and **Supplementary Fig. 3.7E, H**), which might result from reduced cytokine production by fewer and less activated T cells. Direct stimulation of B cells with anti-Ig and CD40L with or without IL-21 only showed a trend toward impairment in B-cell proliferation (**Supplementary Fig. 3.7I, J**). Taken together, our results demonstrate impaired immunological responses, especially to TCR stimulation, in P2, with weak effects observed in the heterozygous parents, consistent with the defects in Calcium flux and phosphorylation of Erk.

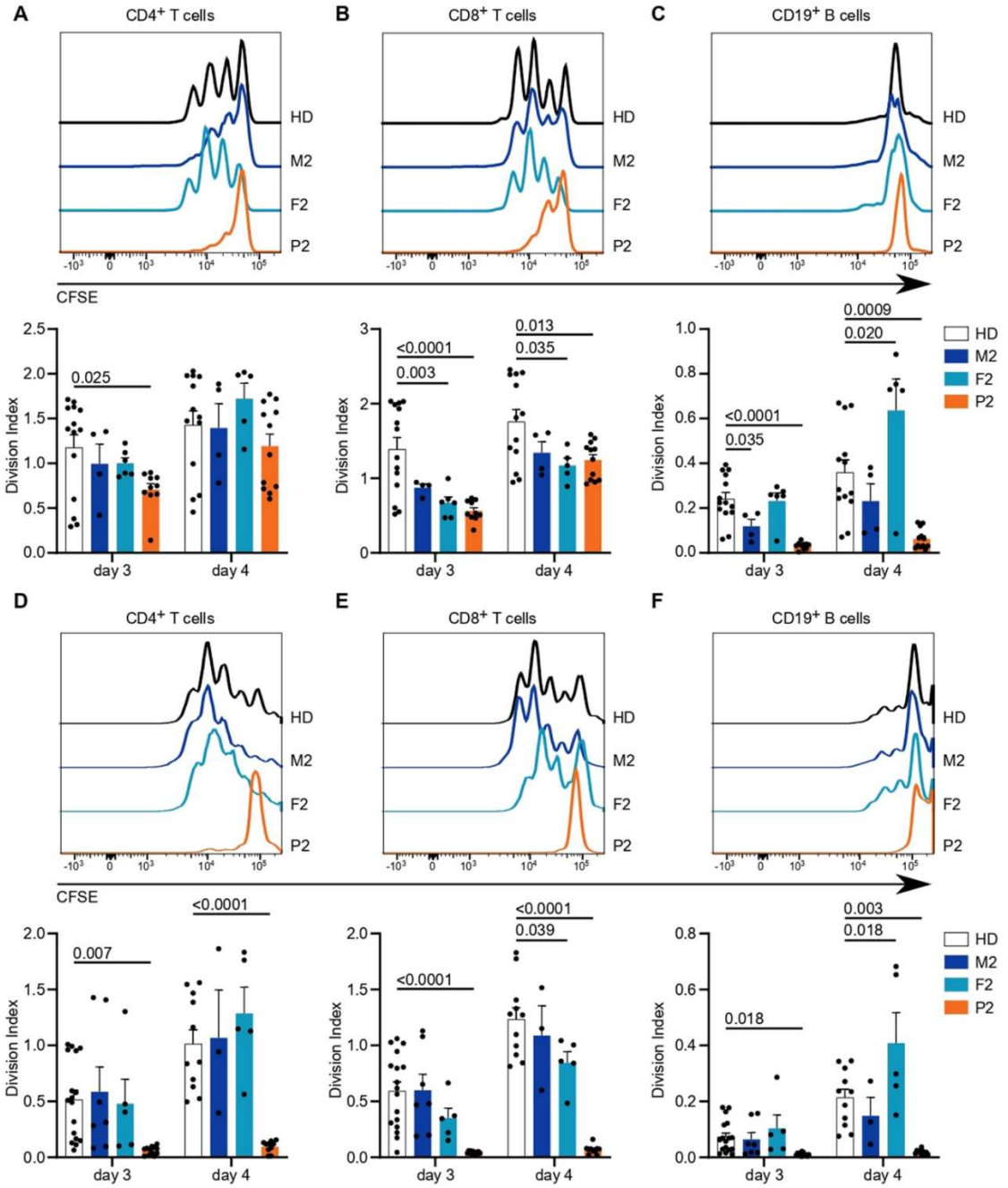

Figure 3.7: Altered cellular responses with *ITPR3* variants. PBMCs were labelled with the CFSE cell proliferation dye and stimulated with anti-CD3 and anti-CD28 antibodies for up to 4 days. The mean number of proliferations in the whole cell population, including undivided cells, was calculated for $CD4^+$, $CD8^+$, and $CD19^+$ cell subsets (Division Index). Stimulation was performed in plates coated with 10 µg/mL anti-CD3 antibody and 5 µg/mL soluble anti-CD28 antibodies. Exemplary histograms are shown on top, and the Division Indexes are shown on the bottom for **(A)** $CD4^+$ T cells, **(B)** $CD8^+$ T cells, and **(C)** B cells, with the latter reading indicating bystander activation and not direct stimulation. **(D)** Stimulation was performed with 5 µg/mL soluble anti-CD3 and 5 µg/mL soluble anti-CD28 antibodies. Exemplary histograms (top) and Division Indexes (bottom) are shown for $CD4^+$ T cells, **(E)** $CD8^+$ T cells and **(F)** B cells. Number of independent experiments: **(A–C)** n=4 with 3 different HDs. **(D–F)** n=5 with 5 different HDs. Individuals were sampled at multiple time points. The values are presented as the mean + SEM. One-way ANOVA was performed with a multiple comparison test.

3.5 Discussion

Store-operated Ca^{2+} entry has been established to be a critical event in immune cell activation, with disruption resulting in human diseases described as CRAC channelopathies[246]. In this work, we identify variants in IP_3R3, a channel mediating Ca^{2+} release from the ER into the cytosol prior to and necessary for store-operated Ca^{2+} entry initiation, resulting in similar clinical phenotypes that are characterized by combined immunodeficiency. Three different variants in two unrelated compound heterozygous patients demonstrated impaired IP_3-mediated Ca^{2+} responses *in vitro*, translating into deficient T-cell activation and proliferation (**Fig. 3.8**). Our results suggest a more severe impact on channel function induced by the R2524C variant, which was consistent with the clinically more severe combined immunodeficiency observed in P1. For P2, who harboured the F1628L and R1850Q variants, we found defects in all *in vitro* assays, with partially reduced sensitivity of channel activation correlating with a weaker clinical phenotype. Although decreased protein expression of IP_3R1 and IP_3R3 in P2 was also observed in his mother and may therefore be an effect specifically attributed to the F1628L variant, this reduction was not sufficient to induce proliferation defects in M2. Similarly, although Ca^{2+} homeostasis was impaired in the clinically healthy heterozygous parents of P2 in a dominant way, IP_3-mediated Ca^{2+} signalling and the integration of stimulating signals were intact in the parents. Together, these results suggest a spectrum of escalating clinical severity with progressive decline in channel function.

ITPR3 belongs to an intriguing class of immunodeficiency genes involved in common cellular pathways. While defects in lymphocyte-specific processes, such as VDJ recombination, show a clear route to immunodeficiency, multiple immunodeficiencies have also been described based on genes in pathways such as DNA replication and cellular metabolism pathways, or shared signalling pathways such as Ca^{2+} signalling pathways[218]. Complete defects in these processes often manifest in embryonic lethality; therefore, the clinically relevant variants observed in these pathways must exist within a narrow band of mutational space that permits normal development but causes defects in cell types not necessary for development. The breadth of this mutational space varies by gene and influences the frequency at which clinically relevant variants arise. In the case of *ITPR3*, these constraints would require that variants exert a sufficient impact on a clinically relevant cell type, such as T cells and B cells, while maintaining sufficient functionality in developmental cell types, such as fibroblasts and neurons. This mutational balance could potentially be achieved via several different molecular mechanisms. The observation that the effect of a variant on mRNA expression differs between fibroblasts and T cells is consistent with early reports suggesting distinct subtype-specific expression profiles in various cell lines[73,247]. Alternatively, the IP_3R subtypes have been reported to exhibit differential regulatory and functional properties[220,226,248–250], which may account for the lack of a Ca^{2+} signalling phenotype in the fibroblasts of P2. The F1628L and R1850Q variants of P2 are located in the regulatory domain known for functioning as a signalling hub and interacting with a plethora of proteins[85,251]. Considering that this domain is less conserved among subtypes, compared to, for example, the IP_3-binding or TM domain[252],

enhanced diversity of interaction partners may drive the acquisition of different phenotypes of mutated proteins, with a subset of these interactions disrupted. In this scenario, even variants in a single IP_3R3 subunit in a heterotetramer may impair channel function in a specific cell type due to a reduced ability to bind a cooperative partner necessary for channel activation in that cell type[89,253]. Further studies on the interaction partners required in different cell types may be aided by the identification of variants such as those presented herein, which display cell type-specific defects in signalling function.

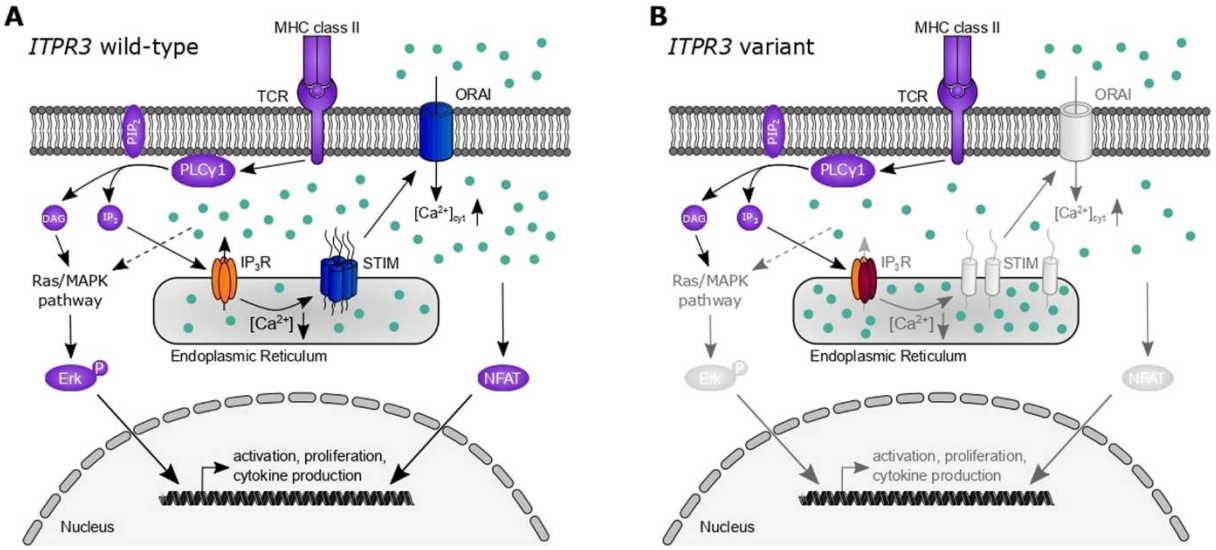

Figure 3.8: Dysfunctional IP_3R3 subunits impair channel function and T-cell activation. Simplified schematic representation of T-cell activation pathways relevant to the presented results. **(A)** T-cell receptor (TCR) stimulation results in the activation of phospholipase C (PLC) γ and the subsequent generation of diacylglycerol (DAG) and inositol 1,4,5-trisphosphate (IP_3) from phosphatidylinositol 4,5-bisphosphate (PIP_2). While DAG activates the Ras/mitogen-activated protein kinase (MAPK) pathway and ultimately phosphorylation of Erk, allowing its nuclear translocation, IP_3 binds to the tetrameric IP_3 receptor (IP_3R). Its activation results in Ca^{2+} (light blue dots) efflux from the endoplasmic reticulum, which in turn activates STIM and the opening of the plasmalemmal ORAI channels that mediate store-operated Ca^{2+} influx. Variants in both of these proteins (dark blue) have been previously described in the human immunodeficiency context. The influx from extracellular Ca^{2+} through ORAI results in an increase in cytosolic Ca^{2+} ($[Ca^{2+}]_{cyt}$) that results in nuclear translocation of nuclear factor of activated T cells (NFAT) and other effects. These processes result in the transcription of essential genes for cell activation, proliferation, and cytokine production. **(B)** Damaging variants of IP_3R3 (dark red subunits) result in impaired function of homo- or heterotetrameric receptor complexes with reduced Ca^{2+} efflux into the cytosol. Reduced signalling via STIM/ORAI and impaired activation of Erk and NFAT pathways are insufficient for adequate lymphocyte activation and manifest in clinical immunodeficiency. Figure created in PowerPoint.

We propose a partially recessive mode of inheritance for the F1628L (M2 and P2) and R1850Q (P1, F2, and P2) variants. This recessive inheritance may be explained via the location of the variants in the regulatory domain of IP_3R3. Point mutations in this domain may be expected to impair only a specific aspect of regulation, which can be partially, but not entirely, compensated for, leading to impaired Ca^{2+} homeostasis *in vitro* even in heterozygous individuals under steady-state conditions. Despite the relatively high allelic frequency of the R1850Q variant, we present evidence that this mutant impairs

channel function in a homotetramer without causing a clinical phenotype in heterozygous individuals due to partial compensation. While clinically silent, we postulate that the partial loss-of-function of one allele through R1850Q allows phenotypes to emerge when pathogenic variants constitute the alternative allele. This mode of inheritance is similar to that recently described for an adult patient with compound heterozygous variants of CRACR2A, a regulator of store-operated Ca^{2+} entry, who presented with T-cell dysfunction and hypogammaglobulinemia with normal *in vitro* B-cell function[164]. In this case, each of the variants was inherited from one clinically healthy parent, suggesting compensation of a heterozygous defect. In this model, the compound heterozygous loss of two regulatory mechanisms in IP_3R3 was sufficient to induce combined immunodeficiency in P2. A similar inheritance pattern may account for the effect of the R2524C variant in P1; however, the *de novo* nature of the second variant precluded clear characterization of the R2524C variant as recessive. The R2524C allele has, however, been implicated with dominant inheritance for Charcot–Marie–Tooth, as reported in Rönkkö *et al.*[224]. The absence of a reported immunological phenotype in this patient, who inherited only a R2524C variant, suggests that a second hit with the potentiating R1850Q variant is necessary for immunodeficiency.

In addition to insights into the differential sensitivity of cell types to IP_3R3 deficiency and the identification of the R1850Q, F1628L, and R2524C variants as pathogenic, this study provides potential insight into the molecular regulation of IP_3R3. Despite advances in the accuracy of electron microscopy techniques that can reveal conformational changes and interactions in specific activation states of IP_3Rs[238,239,242], receptor regulation remains incompletely understood, with the effects of posttranslational modifications and interactions with accessory proteins being continuously discovered[85]. Genetic variants leading to human disease provide a unique way for better understanding protein regulation and function. Our results demonstrate that the F1628L (P2) and R1850Q (P1 and P2) variants each result in reduced sensitivity to channel activation while still maintaining channel gating ability. Interestingly, PBMCs of P2 consistently showed reduced basal $[Ca^{2+}]$ in our experiment warranting more in-depth investigation to understand the impact of the two variants alone and in combination on the leak properties of the channel. In contrast to the hypomorphic F1628L and R1850Q variants, we see that the *de novo* R2524C variant in P1 appears to have a biochemically distinct effect, completely abolishing the gating of a homotetrameric receptor. This may therefore exert a dominant negative effect on channel function in heterotetramers. The conserved residue analogous to R2524C in the related Ryanodine receptor family has been shown to stabilize both the closed and open state of the channel by alternating its interaction with two other highly conserved residues[254] and has recently been identified as a crucial residue for IP_3R3 channel activation in humans[255]. In line with the prediction of a drastic change in the pore charge introduced by this variant, its counterpart in the rat IP_3R1 protein has been suggested to exhibit a crucial function in signal transmission, as mutation into different amino acids markedly reduced channel function[242,256]. Further identification of pathogenic *ITPR3* variants and systematic investigation of these

mutated receptors may reveal protein interactions and/or conformational changes that are hampered in different cell types, providing better insight into channel regulation.

With this study, we add variants in *ITPR3* as underlying causes for disrupted Ca^{2+} signalling that results in immunodeficiency. Some clinical characteristics of the patients we describe overlap with those of patients suffering from ORAI1 and STIM1 deficiency, who present with severely reduced or absent store-operated Ca^{2+} entry *in vitro* and normal lymphocyte counts but impaired T-cell proliferation following *in vitro* stimulation[163,200]. Comparable to the patients we describe, ORAI1- and STIM1-deficient patients suffer from recurrent severe infections and can exhibit signs of lymphoproliferation and autoimmune disease, although the disease course is often more severe, with patients requiring HSCT very early in life to prevent a lethal disease course[257,258]. Clinical presentation does, however, vary greatly in STIM1 deficiency, with several STIM1-deficient patients described with late-onset or absent clinical immunodeficiency[259,260]. In P1, we observed nonimmunological disease manifestations, including dental mineralization defects, abnormalities of the hair and Charcot–Marie–Tooth disease. These nonimmunological effects, also observed in an unrelated R2524C patient, partially overlap with the dental enamel formation defects and myopathy in ORAI1 and STIM1 patients[163,259,261,262], although the latter phenotypes are congenital and nonprogressive.

Here, we provide evidence showing that inherited variants in *ITPR3* alter physiologically relevant Ca^{2+} signalling responses, driving defects in immune responses, and are associated with clinical immunodeficiency. Limitations of our work include the limited number of cases, only two patients, and the lack of primary immune cells from P1 due to successful HSCT. Because of the inheritance pattern, we also lacked primary immune cells harbouring only the R2524C variant, that would have allowed us to clarify the recessive or dominant nature of this mutation in lymphocytes. The identification of new patients in subsequent studies will be highly informative for identifying the mutational space in *ITPR3* associated with immunodeficiency. Additional studies investigating the effect of *ITPR3* variants on cellular processes such as apoptosis and autophagy, which are known to be regulated by IP_3Rs coupling Ca^{2+} signalling between the ER and mitochondria, will also be interesting[263,264]. Any defects in these pathways may alter immune cell activation and potentially contribute to the clinical presentations observed. While additional studies are needed, we propose that *ITPR3* should be considered as a candidate gene in patients with B- and T-cell defects in association with impaired Ca^{2+} signalling function, adding variants in *ITPR3* as causes of inborn errors of immunity.

3.6 Personal Contribution

The study presented in this chapter was driven by me and I designed, performed, and analysed all experiments with the exception of performing the Western Blots of primary cell material (performed by Kirsten Welkenhuyzen, Fig. 3.2C, D and Supplementary Fig. 3.4) and the experiments in the triple knockout HEK cell model (performed and analysed by Lara E. Terry and Taylor Knebel, Fig. 3.4 and Supplementary Fig. 3.6). I wrote the full first draft of the manuscript with the exception of the extended clinical case descriptions and Supplementary Tables 3.1-3 containing clinical information (written by Erika van Nieuwenhove and Frederik Staels).

3.7 Supplementary Material

3.7.1 Extended clinical case descriptions

Patient 1 is a 12-year-old male, born to non-consanguineous parents of Caucasian ethnicity. A summary of demographic, clinical, laboratory, technical and treatment data is shown in **Supplementary Table 3.1**. He was born at term and first admitted to hospital at 3 months of age due to bronchitis with bacterial superinfection. Low absolute numbers of T and B lymphocytes were first detected at 5 months during a hospitalization for recurrent viral respiratory tract infections with failure to thrive (**Supplementary Table 3.2**). He was started on inhalation therapy with salbutamol and budesonide and continued respiratory tract infections prompted the initiation of prophylactic antibiotics. Chest x-ray and CT scan showed a thymic shadow but thickened bronchial walls, segmentary consolidation zones in multiple lobes with subatelectatic strands. Exploratory analyses at 7 months revealed a $B^{-}T^{-}NK^{+}$ lymphopenia with hypergammaglobulinemia. Hypomorphic forms of SCID were unlikely due to normal relative numbers of naïve T cells, normal cytometric analysis of the Vbeta repertoire and lymphocyte proliferative responses (to Candida, PWM, PHA, and ConA) by thymidine incorporation assay within normal limits (**Supplementary Table 3.2**). At age 10 months, his language and gross motor skills were delayed by 4 months but he achieved walking independently at 16 months. Bronchoscopy examination revealed purulent secretions in trachea and both main bronchi. Since negative BAL bacterial and mycobacterial cultures could not guide treatment, a course of Tazocin was given empirically. While there was no history of ear, skin or gastro-intestinal infections, he suffered from oral candidiasis and diaper dermatitis. Further clinical examination revealed thin and brittle hair, mollusca contagiosum, severe postnatal growth delay (-4SD), delayed deciduous eruption of conical teeth (22 months), low muscle mass, frontal bossing and hepatosplenomegaly. He suffered from flares of watery diarrhoea with adenovirus positive in stool. Additional investigations were normal including a sweat test, transfontanellar ultrasound, OPG, gastroscopy with biopsies, x-ray of the upper gastro-intestinal tract and impedance-pH monitoring. While his first bone marrow analysis was unremarkable, at age 2 years bone marrow examination demonstrated a normochrome normocytic anaemia and leukopenia with

absolute lymphopenia. Common gamma chain expression (CD132), VDJ recombination, DHR oxidation, and CD40 ligand expression were within normal limits. Pneumococcal polysaccharide antibody response was abnormal and repeat TLR testing was suboptimal. Combined immune deficiency was diagnosed and he was started on subcutaneous immunoglobulin replacement therapy at age 2.5 years. Serial bronchoscopy revealed frail mucosae and secretions. BAL bacterial, mycobacterial and fungal cultures were unrevealing on multiple occasions. The patient was treated with empiric antibiotics, respiratory physiotherapy and started on azithromycin at an anti-inflammatory dosage. At age 4 years a mycobacterial infection was suspected due to worsening CT thorax with consolidation, unilateral hilar lymph nodes and compression on the left main bronchus, with a caseous lesion viewed with bronchoscopy. Despite negative quantiferon test and negative gastric lavage cultures, a 6-month course of antimycobacterial therapy was administered with good effect. IGF-1 was on the lower limit of normal with a delay in bone age of 4 years at age 7 years. However, glucagon response testing and IGF-1 generation tests were normal, with insufficient response to exogenous growth hormone. Hypercaloric nutrition was started. Sequential sanger sequencing had ruled out RMRP, NEMO, RAG1/2, ADA, SBDS and JAK3 mutations. Karyotyping and FISH for 22q11 were normal.

The patient received an allogenic hematopoietic stem cell transplant from a matched unrelated donor at the age of 6 years (**Supplementary Table 3.2**) after conditioning with treosulfan 42g/m², fludarabine 150mg/m², Campath 5x0.2mg/kg. Full donor chimerism was observed on day 30 with no signs of GvHD. Pre-transplant screening showed a positive EBV PCR (2.92 log EBV IU/mL). Aspergillus antigen proved positive on blood with negative fungal cultures and negative aspergillus antigen on BAL 3 months post-transplant. Chest CT didn't show any typical characteristics of angio-invasive aspergillosis. Amphotericine B was initiated. 5 months post-transplant P1 developed diarrhoea and red blood loss, treated with anti-TNF after ruling out GvHD (EBV PCR positive on biopsy). Immune haemolysis with negative antinuclear antibodies 6 months post-transplant was treated with high dose CS and responded to rituximab treatment. P1 developed multiple endobronchial EBV-induced leiomyomas approximately one year after transplantation necessitating multiple debulking surgeries. Both mollusca and leiomyomas resolved with immune reconstitution. Recognition of the patient's areflexia and progressive distal muscular weakness were delayed by the onset of bilateral avascular necrosis of the hip at the age of 10 years requiring therapeutic use of a wheelchair. Upon presentation with peripheral neuropathy at the age of 11 years, EMG revealed reduced ulnar and medial sensory and motor nerve conduction velocities as well as typical EMG patterns for an axonal form of Charcot-Marie-Tooth. He is now 6 years post-HSCT with full donor chimerism and good immune reconstitution but with severely impaired lung function. Whole exome sequencing on genomic DNA extracted from pre-transplantation blood cells of the patient and both parents was performed and led to the identification of two candidate variants in *ITPR3*, inherited in a compound heterozygous way (c.5549G>A:p.Arg1850Gln inherited from father and c.7570C>T:p.Arg2524Cys *de novo*).

Patient 2 is a 36-year-old male, born to non-consanguineous parents of Caucasian ethnicity. A summary of demographic, clinical, laboratory, technical, and treatment data is shown in **Supplementary Table 3.1**. He presented at the age of 18 years with diffuse petechiae and severely decreased thrombocytes in peripheral blood ($9x10^9$/L, reference 150-$450x10^9$/L, **Supplementary Table 3.3**). A diagnosis of idiopathic immune thrombocytopenia (ITP) was made and he was treated with a high dose corticosteroid tapering regimen. After treatment cessation he quickly relapsed, and subsequently underwent splenectomy at the age of 19 years. At the age of 24 he was admitted because of severe fatigue, anorexia and weight loss. On clinical examination jaundice was noticed. Laboratory examination (**Supplementary Table 3.3**) showed profound macrocytic anaemia (nadir haemoglobin 2.6 g/dL, reference 14-18 g/dL), with high reticulocytes ($107x10^9$/L, reference 20-100), elevated total bilirubin (2.14mg/dL, reference <1 mg/dL) and low haptoglobin (<0.20 g/L, reference 0.3-2 g/L). Direct coombs test was positive, confirming the suspicion of auto-immune haemolytic anaemia (AIHA). As underlying aetiology, a precedent infection in the past month before onset of AIHA (either gastrointestinal caused by *Blastocystis hominis* or respiratory caused by *Mycoplasma pneumoniae*) was suspected. Bone marrow examination did not suggest the presence of a myeloproliferative disorder or lymphoma and additional clinical and laboratory tests were negative for autoimmune diseases (ANF, ANCA negative), paroxysmal nocturnal haemoglobinuria (normal expression of CD55/CD59 on erythrocytes and granulocytes) and viral infections (Parvovirus B19, HIV, EBV, and HCV were negative). He was treated with red blood cell transfusions, erythropoietin (Aranesp 150 µg/week), anti-CD20 (Rituximab 700 mg IV once weekly for a total of 4 doses), corticosteroids (125 mg, tapered over time) and cyclosporin (Neoral, initiated after induction at a dose of 150 mg twice daily). Haemoglobin levels recovered to a normal level after 9 months and cyclosporin was tapered to a dose of 50 mg twice daily. During follow up he reported recurrent upper respiratory tract infections (sinusitis), treated with multiple courses of antibiotics. Immunoglobulin G levels, two years after the last rituximab administration, were still decreased to a level of 6.83 g/dL (**Supplementary Table 3.3**). On immunophenotyping he had normal B-cell numbers (352/µL, reference 82-$476x10^9$/L) but severely decreased switched memory B cells (1.1% $CD27^+IgM^-IgD^-$ of total B cells). At that time, he was given intravenous immunoglobulins monthly to prevent infections. Despite treatment he continued to suffer from respiratory tract infection and pulmonary CT scan showed multiple nodular infiltrates. Subsequent bronchoscopy with bronchoalveolar lavage (BAL) revealed a positive galactomannan test with negative microbial cultures and viral PCR. Galactomannan testing on peripheral blood was also positive. A lung biopsy was performed and demonstrated a predominantly lymphoplasmocytary infiltrate. Based on the revised EORTC criteria, probable invasive pulmonary aspergillosis was diagnosed. Despite multiple antifungal treatments given for a total period of two years (variconazole, posaconazole), he continued to have migrating pulmonary infiltrates. A new bronchoscopy was done and BAL did not reveal signs of aspergillosis nor other relevant pathogens by PCR or culture. In this period he also reported progressive gastro-intestinal symptoms of secretory diarrhoea, nausea and anorexia with a weight loss of 8 kg.

Ileocolonoscopy with biopsies was normal and gastroscopy showed signs of chronic gastritis and mildly increased intraepithelial lymphocytosis in the duodenal biopsy. No enteropathogens were identified on faecal culture. Tissue transglutaminase was normal (<1.9, reference ≤20 CU). Subsequently he was referred to the immunology clinic for a suspicion of common variable immunodeficiency (CVID) with infectious susceptibility and associated autoimmunity (AIHA, ITP), granulomatous and lymphocytic interstitial lung disease (GLILD), and enteropathy. Clinical immunophenotyping at that time (**Supplementary Table 3.3**) was consistent with CVID (low IgG before start of IvIG and IgM, normal B-cell count but undetectable switched memory B cells, with the absence of profound T-cell deficiency and exclusion of other defined secondary causes of hypogammaglobulinemia). Treatment with IvIG was continued and vaccination status was optimized. Throughout follow up the patient reported recurrent respiratory tract infections and was hospitalized twice (**Supplementary Table 3.3**) for a bronchopneumonia (*H. influenzae*) and a primary cytomegalovirus infection presenting with fever, liver function test disorders and hepatomegaly necessitating hospitalization and ganciclovir treatment. Further diagnostic exploration by targeted sequencing using a primary immunodeficiency (PID) panel (PID target capture v1, Nimblegen) was negative. Whole exome sequencing on genomic DNA extracted from blood cells of the patient and both parents was performed and led to the identification of two candidate variants in *ITPR3*, inherited in a compound heterozygous way (c.4482T>C:p.Phe1628Leu inherited from mother and c.5549G>A:p.Arg1850Gln inherited from father).

3.7.2 Supplementary Figures

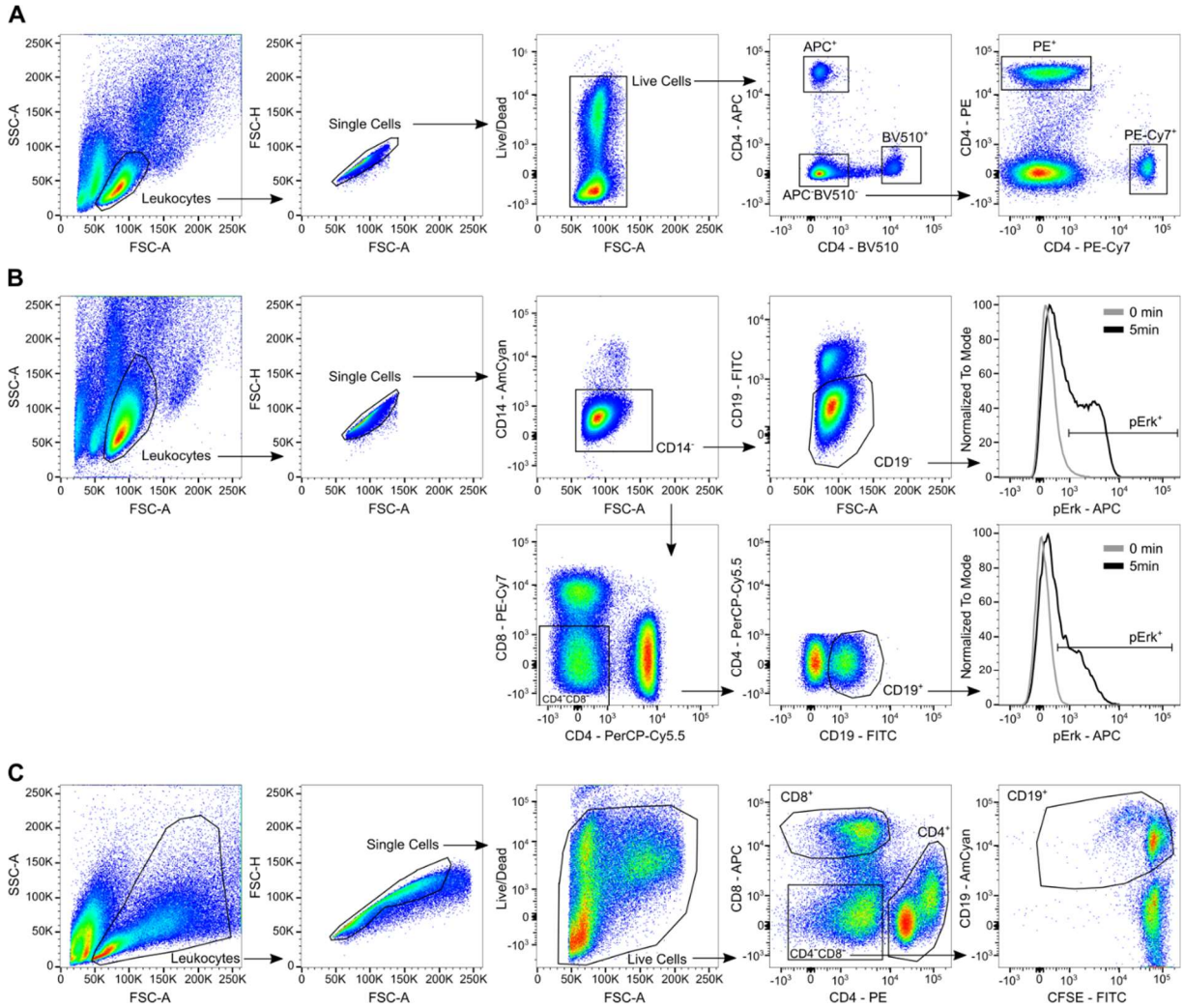

Supplementary Figure 3.1: Gating strategies for flow cytometry experiments. **(A)** For Ca^{2+} flux measurements in primary $CD4^+$ T cells, gating was first performed to exclude debris, doublets, and dead cells. Gating on four different fluorochromes used to label $CD4^+$ T cells of single individuals was performed, with the fluorochromes for a single individual exchanged in repeats of the same experiment to exclude impact of the compensation on Ca^{2+} flux measurements. **(B)** Analysis of phosphorylated Erk was performed by gating on leukocytes before excluding doublets and monocytes. T cells were gated as being $CD19^-$ while B cells were gated as being $CD4^-CD8^-$ and $CD19^+$. The percentage of $pErk^+$ cells as well as the MFI of pErk in $pErk^+$ cells was used as readout. **(C)** Proliferation of B and T cells was analysed by gating on leukocytes, single, and live cells before distinguishing $CD4^+$ and $CD8^+$ T cells and $CD4^-CD8^-$ and $CD19^+$ B cells.

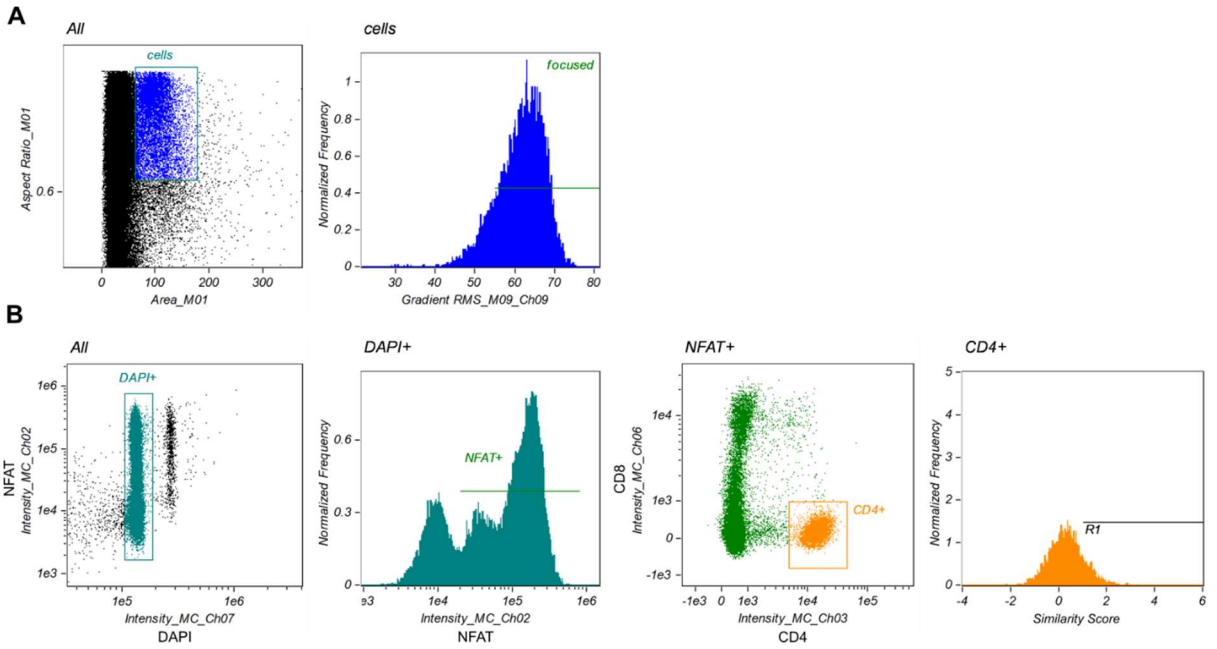

Supplementary Figure 3.2: Gating strategy for ImageStream experiment. (A) Raw .rif files were gated on cells to exclude beads and subsequently on focused cells. This cell population was exported as a new .rif file and used for further downstream gating. **(B)** Single cells were selected based on DAPI staining before gating on NFAT1^{+} and CD4^{+}CD8^{-} T cells. R1 gating identifies the percentage of cells with nuclear NFAT1.

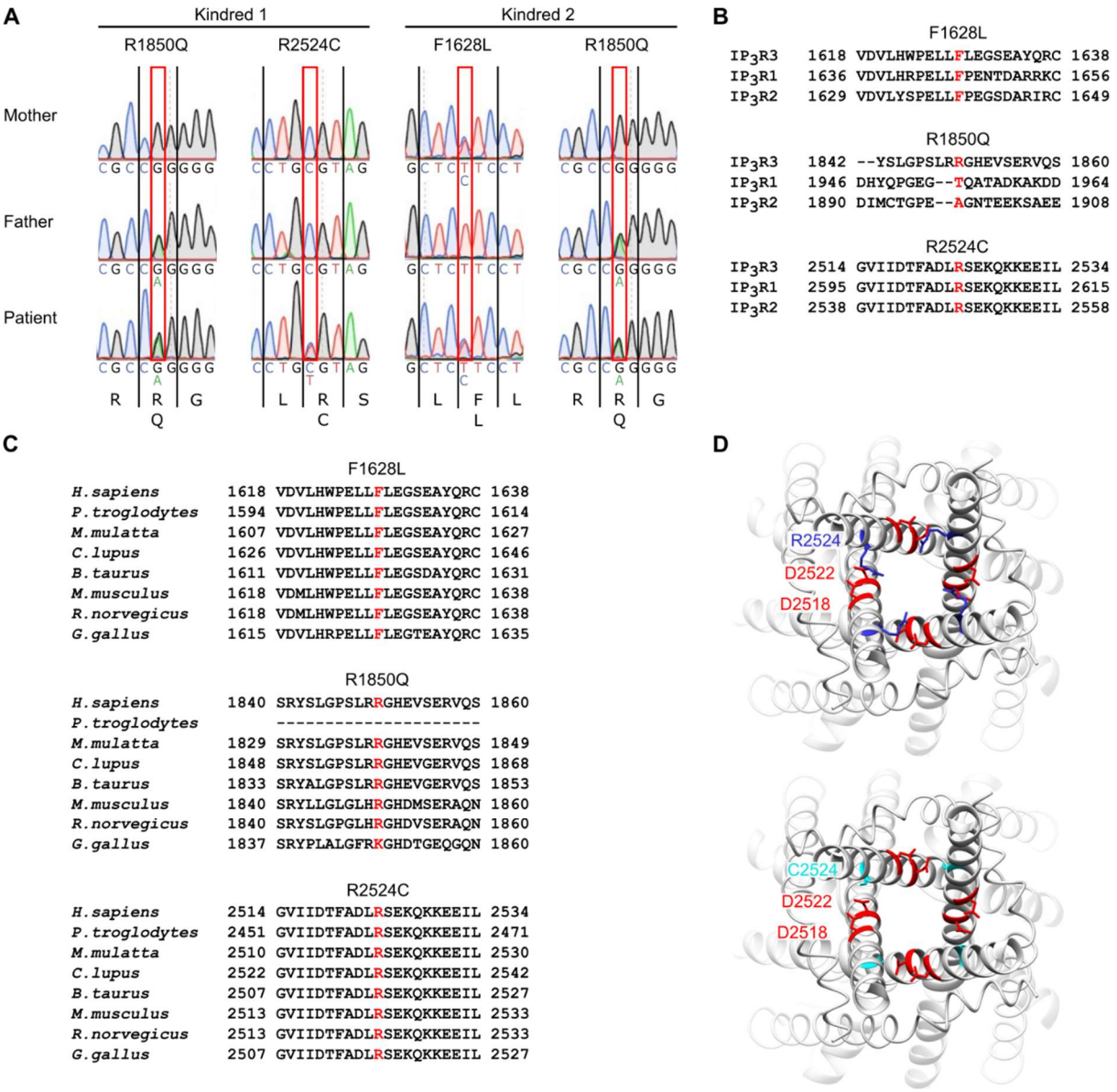

Supplementary Figure 3.3: Identified variants in *ITPR3* are highly conserved. (A) Sequencing results for the variants identified in the two kindreds. The relevant base is marked in red and alternative bases and amino acids indicated below the reference. **(B)** Conservation of the relevant residues in *ITPR3* across species. **(C)** Conservation of the relevant residues within the IP_3R family in humans. **(D)** View of the IP_3R3 channel pore structure in the plane of the R2524 amino acid. Illustration of the positively charged amino acid side chain of R2524 on the left (blue, positive charge) and how it shields the negative charge of amino acid side chains of D2522 and D2518 (red, negative charge). Location of the side chains in the case of the C2524 variant with its neutral side chain (cyan, neutral charge).

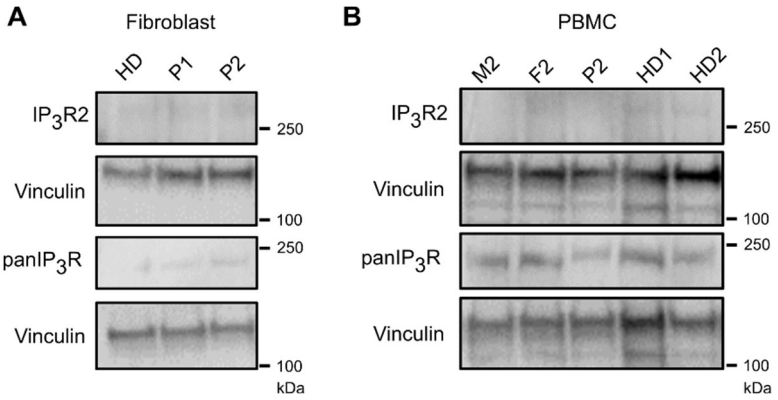

Supplementary Figure 3.4: Western blot analysis of IP_3R2 and total IP_3R expression is not reliably quantifiable. (A) Western blot analysis of IP_3R2 (308 kDa) protein expression was performed using a subtype-specific antibody as well as a non-specific antibody (pan-IP_3R, 314/304/308 kDa for subtypes 1/2/3, respectively) with Vinculin (124 kDa) as housekeeping gene. Representative blots are shown for fibroblasts and **(B)** PBMCs with indications of the molecular weight marker.

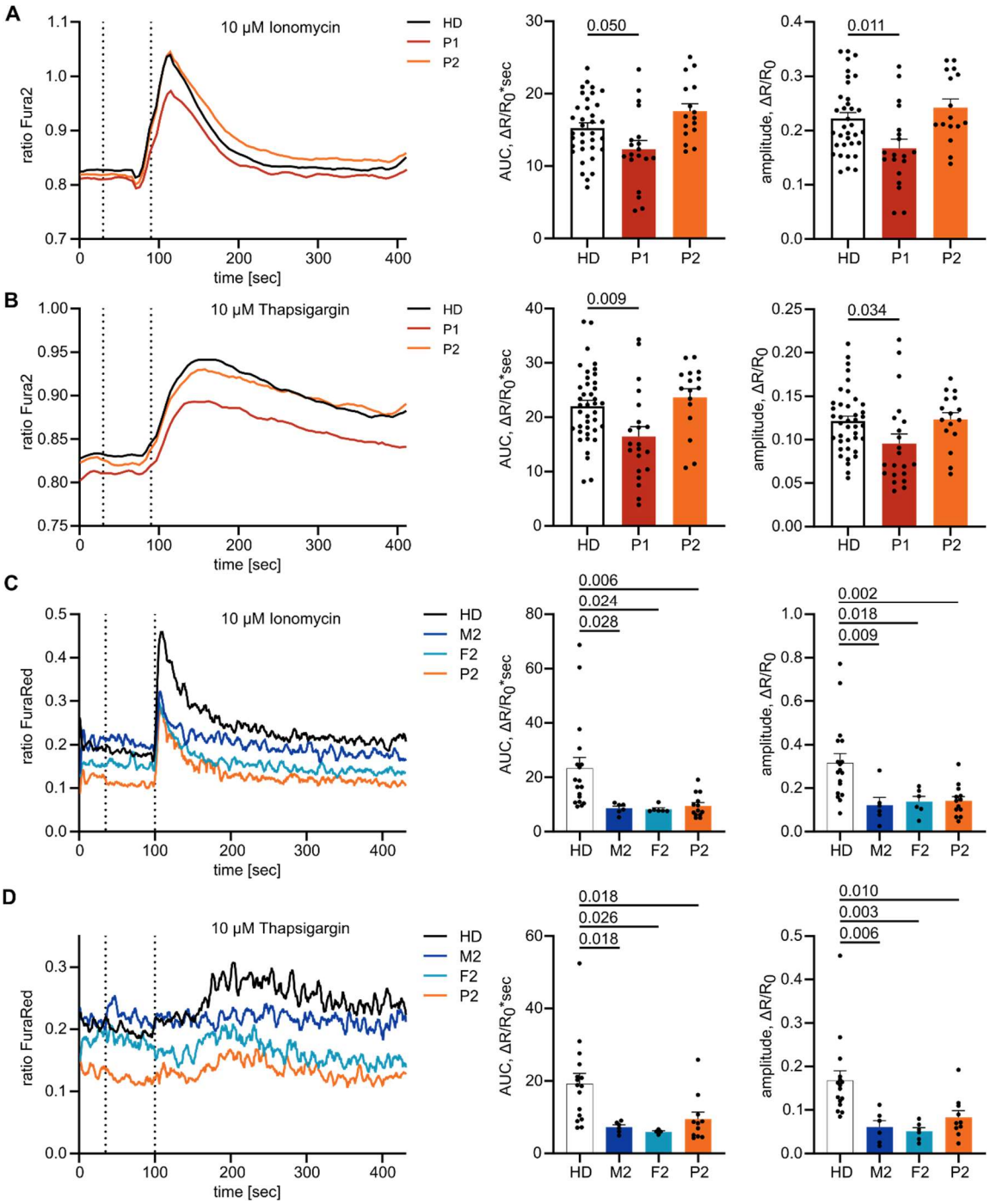

Supplementary Figure 3.5: Variants in *ITPR3* impede Calcium homeostasis. Adherent fibroblasts were loaded with the ratiometric Ca^{2+} indicator Fura-2/AM, and Calcium flux was monitored over time. The first dashed line indicates addition of EGTA for acquisition of background, the second dashed line indicates addition of **(A)** 10 µM Ionomycin or **(B)** 10 µM Thapsigargin. Area under the curve (AUC) and maximal amplitude of the response were calculated respective to background values. **(C)** PBMCs were stained for CD4, loaded with the ratiometric Ca^{2+} indicator FuraRed and monitored for changes in cytosolic Ca^{2+} concentrations by flow cytometry. First dashed lines indicate addition of EGTA and second dashed lines indicate addition of **(C)** 10 µM Ionomycin or **(D)** 10 µM Thapsigargin. Number of independent experiments: (A,B) n=9 with 2 different HD. (C,D) n=6 with 4 different HD. Individuals in (C,D) were sampled at multiple time points. Traces represent mean values of all experiments and response quantification is shown as mean + SEM. One-way ANOVA with multiple comparisons.

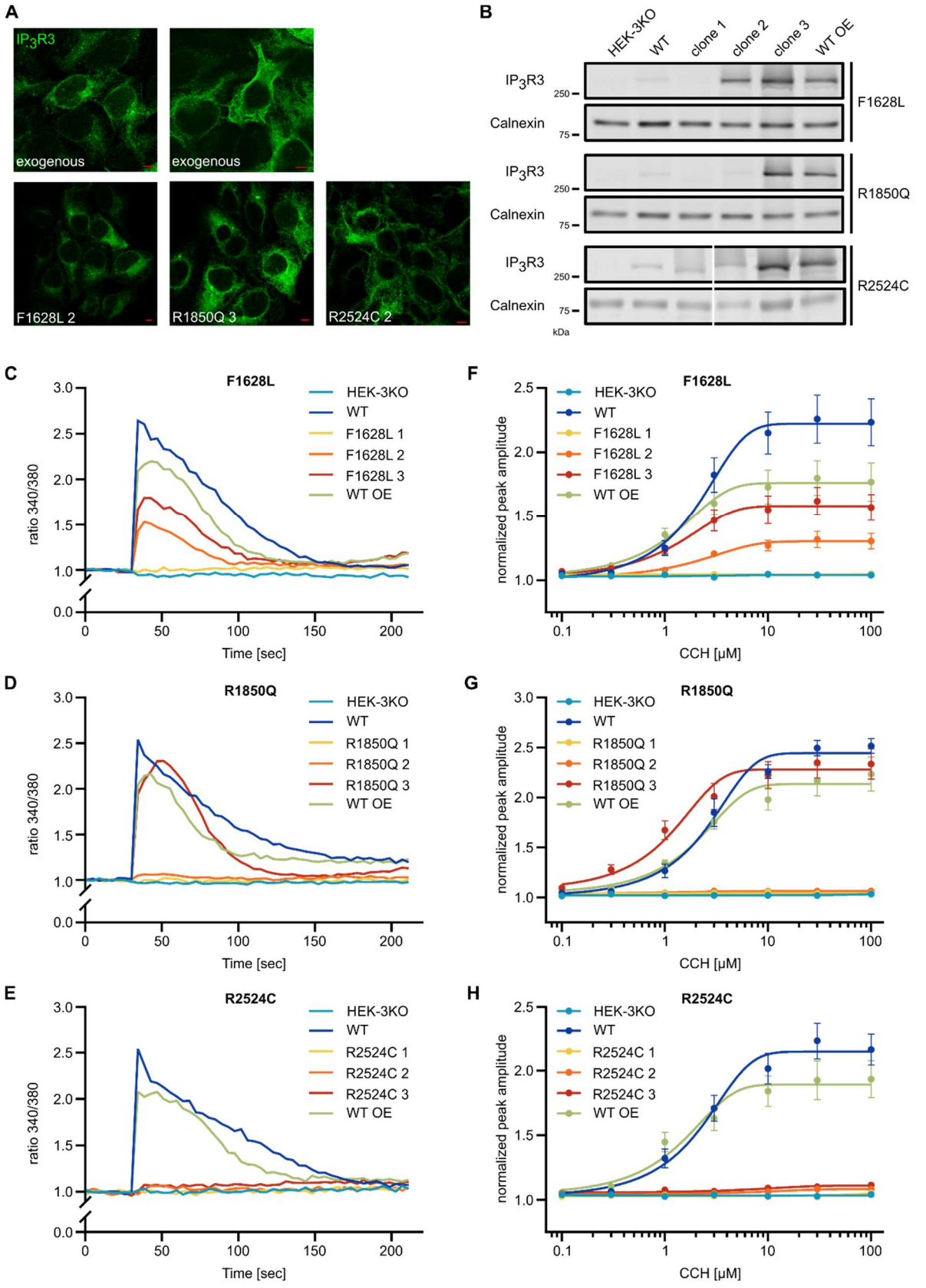

Supplementary Figure 3.6: Reconstitution of HEK-3KO cells with mutated IP$_3$R3 results in stable protein expression and reveals impaired channel function. (A) Immunocytochemistry for IP$_3$R3 (green) was performed to validate physiological localization in HEK-3KO cell lines expressing either exogenous wild-type IP$_3$R3 (top) or mutant IP$_3$R3 (bottom). Representative images are shown. Red scale bars, 5 µm. **(B)** Exogenous overexpressed wild-type IP$_3$R3 (WT OE) and mutant IP$_3$R3 (both 308 kDa) stable cell lines were western blotted alongside HEK293-

3KO and HEK293 cell lines modified to express only endogenous wild-type IP_3R3 (WT). Representative blots are shown also for Calnexin (90 kDa) as housekeeping gene and molecular weight markers are indicated. One lane with a clone not represented in the results was removed. **(C)** HEK-3KO cell lines stably transduced with the wild-type (WT OE - overexpressed) or mutated versions of the IP_3R3 receptor were stimulated with different concentrations of the GPCR agonist Carbachol in Ca^{2+} imaging buffer. Cells only expressing endogenous IP_3R3 (WT) and HEK-3KO cells were used as controls. Representative traces of one well stimulated with 100 µM CCH are shown for F1628L, **(D)** R1850Q or **(E)** R2524C as 340/380 ratio normalized to the first 5 values of the measurement. **(F)** Dose-response curves of the peak amplitude of representative cell lines stably expressing IP_3R3 with the F1628L (n=3), **(G)** R1850Q (n=3) or **(H)** R2524C (n=3) variant at different concentrations of Carbachol (CCH) are shown as mean ± SEM.

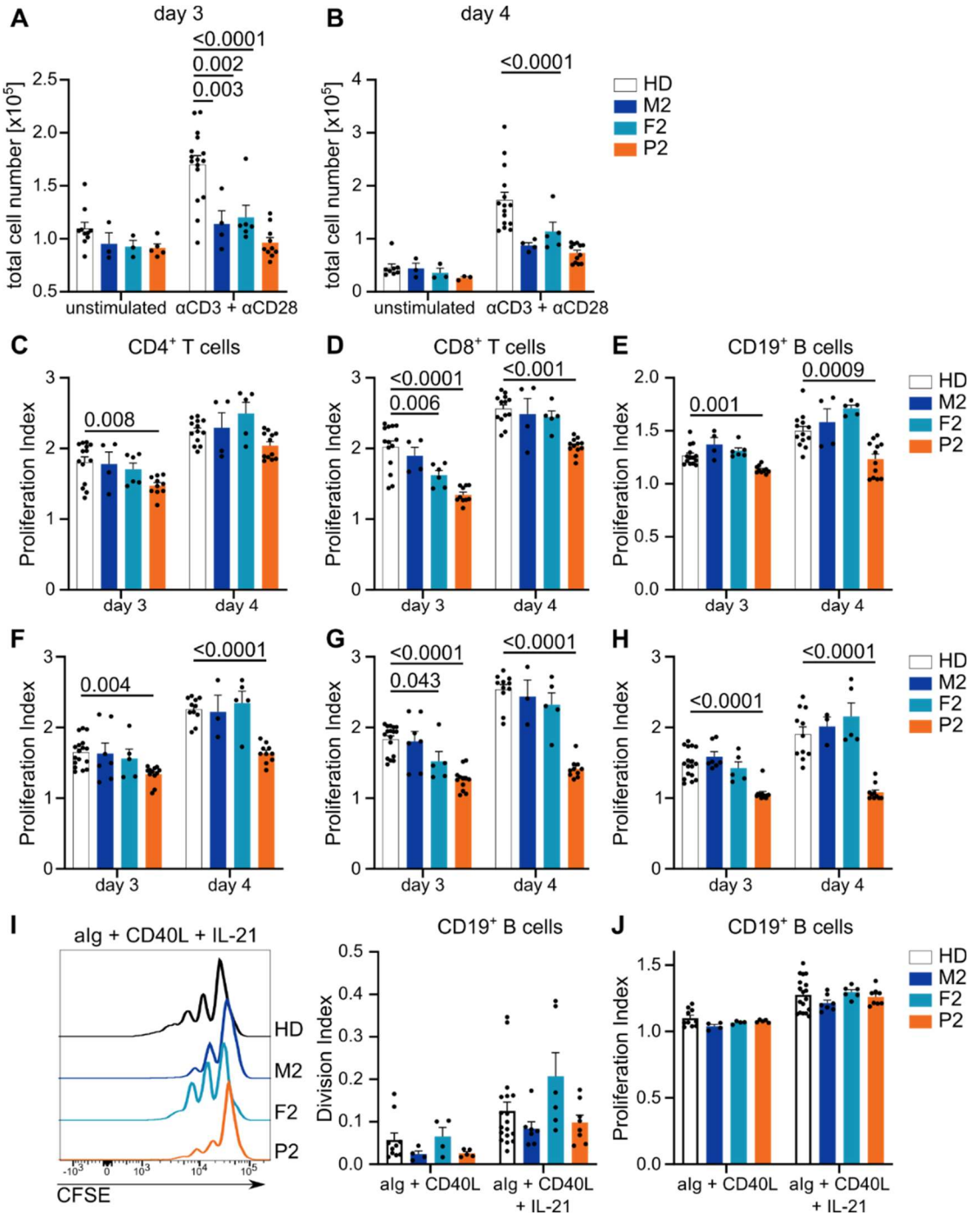

Supplementary Figure 3.7: Defective TCR-induced T cell proliferation in individuals from kindred 2. PBMCs were labelled with the CFSE cell proliferation dye and stimulated with 10 µg/mL plate-bound anti-CD3 and 5 µg/mL soluble anti-CD28 for 3 and 4 days. **(A)** Total cell numbers in unstimulated or stimulated wells after 3 and **(B)** 4 days. The mean number of proliferations of cells that divided at least once (Proliferation Index) was calculated for **(C)** $CD4^+$, **(D)** $CD8^+$ and **(E)** $CD19^+$ subsets. **(F)** Stimulation was performed with 5 µg/mL soluble anti-CD3 and 5 µg/mL soluble anti-CD28. The Proliferation Index is shown for $CD4^+$ T cells, **(G)** $CD8^+$ T cells and **(H)** B cells. **(I)** CFSE labelled PBMCs were stimulated with 10 µg/mL anti-Ig and 1 µg/mL CD40L with or without 20 ng/mL IL-21 for 3 days. The Division Index and **(J)** Proliferation Index for $CD19^+$ gated B cells are shown together with representative histograms. Number of independent experiments: (A-E) n=4 with 3 different HD. (F-H) n=5 with 5 different HD. **(I,J)** n=4 with 6 different HD. Values are represented as mean + SEM. One-way ANOVA with multiple comparisons.

3.7.3 Supplementary Tables

Supplementary Table 3.1. Demographic, clinical, laboratory, technical and treatment data for investigated patients. TLC = total lung capacity, DLCO = diffusion capacity for carbon monoxide.

	PRE-HSCT PATIENT 1	PATIENT 2
DEMOGRAPHIC/GENETIC		
AGE OF ONSET	3 months	18 years
ITPR3 *VARIANT*	c.5549G>A; p.Arg1850Gln c.7570C>T; p.Arg2524Cys	c.4882T>C; p.Phe1628Leu c.5549G>A; p.Arg1850Gln
CLINICAL SPECTRUM AND LABORATORY FINDINGS		
HEMATOPOIETIC	$T^-B^-NK^+$ CID 6 years post HSCT	ITP AIHA
LYMPHOPROLIFERATION		GLILD
GASTROINTESTINAL	Enteropathy	Enteropathy Chronic gastritis
INFECTIONS	Bronchopneumonia (chronic colonization with *H. influenzae*, *P. aeruginosa*, *S. aureus*) Suspected mycobacterial disease (granulomatous airway infection) Multiple viral infections (RSV, Molluscum contagiosum, Parainfluenza virus,…)	Bronchopneumonia (*H. influenzae, M. pneumoniae)* Recurrent URTI Invasive pulmonary aspergillosis Gastrointestinal (*Blastocystis hominis*) Primo CMV infection
OTHER	Brittle hair Delayed dentition, conical teeth Peripheral neuropathy	
LABORATORY EXAMINATIONS	Elevated IgG Absent pneumococcal vaccine response	Low IgG Low switched memory B cells Absent pneumococcal vaccine response
TECHNICAL EXAMINATIONS		
CT SCAN	Consolidation zones Bronchiectasis	GLILD, aspergillus related lesions
PULMONARY FUNCTION TEST	Obstructive	Mild restrictive (TLC 83% predicted value) and decreased diffusion capacity (DLCO 73% predicted value)
ABDOMINAL ULTRASOUND	Cholecystolithiasis	Normal (post splenectomy)
TRANSTHORACAL ECHOCARDIOGRAPHY	Normal	NA
BIOPSY		Lung: lymphoplasmocytic infiltrate Stomach: chronic gastritis. Helicobacter pylori negative.
IMMUNOMODULATORY TREATMENT (INDICATION)		
CORTICOSTEROIDS		Prednisone (ITP, AIHA)
ANTI-CD20		Rituximab (AIHA)
IVIG/SCIG	SCIG	IVIG
OTHER		Cyclosporin (AIHA) Cyclophosphamide (AIHA)

Supplementary Table 3.2. Laboratory values of P1 at different relevant time points. Values out of range are italicized and underlined. ND = not-detectable. *corticosteroid treatment.

	REFERENCE	LAST FOLLOW UP 6 YEARS POST-HSCT	REFERENCE	CONTROL BEFORE HSCT	2 YEARS OF AGE	1 YEAR OF AGE	10 MONTHS OF AGE	RESPIRATORY EXACERBATION	ONSET OF LYMPHOPENIA AT 6 MONTHS, RSV INFECTION
COMPLETE									
HEMOGLOBIN	13.0-16.0 g/dL	13.3	11.0-13.5 g/dL 11.5-13.5 g/dL	*10.3*	11.6	ND	*10.3*	*10.8*	*9.9*
THROMBOCYTES	150-450x10⁹/L	193	150-450x10⁹/L	243	198	ND	262	393	233
TOTAL LEUKOCYTES	4.5-13 x10⁹/L	*3.98*	5.5-15.5x10⁹/L 6-17.5x10⁹/L	*3.64*	7.31	2.86	*5.56*	*5.46*	*4.51*
LYMPHOCYTES	2.0-8.0x10⁹/L	*1.7*	4.0-13.5x10⁹/L 2.0-8.0x10⁹/L	*1.3*	*0.7*	*0.6*	*2.5*	*1.9*	*0.4*
IMMUNOGLOBULINS									
IGG	5.76-12.65 g/L	*13.80*	3.54-9.34 g/L 5.58-12.54 g/L	*19.4*		ND	*16.00*	ND	*13.7*
IGA	0.81-2.32 g/L	*<0.07*	0.14-0.86 g/L			ND	*1.88*	ND	*2.95*
IGM	0.30-1.59 g/L	0.33	0.29-1.39 g/L			ND	0.60	ND	0.41
LYMPHOCYTE COUNTS									
B CELLS (CD19⁺)	200-600/mm3	248	600-2700/mm³ 200-2100/mm³	*92*	*153*	*123*	*244*	ND	*301*
SWITCHED B MEMORY (CD27⁺IGM⁺IGD⁻)	% of CD19⁺ B cells	2.8	% of CD19⁺ B cells			15.8	ND	ND	ND
T CELLS (CD3⁺)	800-3500/mm³	1408	1600-6700/mm³ 900-4500/mm³	995	*344*	*278*	*1068*	ND	*182*
CD4⁺ T CELLS	400-2100/mm³	849	1000-4600/mm³ 500-2400/mm³	*217*	*159*	*105*	*545*	ND	ND
CD8⁺ T CELLS	200-1200/mm³	466	400-2100/mm³ 300-1600/mm³	*774*	*156*	*152*	*382*	ND	ND
NAÏVE T CELLS (CD27⁺CD45RA⁺)			% of CD3		47				
NK CELLS	70-1200/mm³	72	200-1200/mm³ 100-1000/mm³		139	238	992	ND	ND
LYMPHOCYTE STIMULATION									
PHA	≥5 x10³ cpm	30.48	≥5 x10³ cpm				ND	280.71	ND
CANDIDA	≥5 x10³ cpm		≥5 x10³ cpm				ND	8.73	ND
TETANUS TOXOID	≥5 x10³ cpm		≥5 x10³ cpm				ND	*0.96*	ND
VACCINATION RESPONSE									
HEPATITIS B SURFACE AS			>=10 IU/L				ND	ND	*0*
POLIOMYELITISVIRUS TYPE 1 AS			>= 1/8				ND	ND	1/4
TYPE 2 AS									*1/32*
TYPE 3 AS									*1/128*

Supplementary Table 3.3. Laboratory values of P2 at different relevant time points referred to in the manuscript. Values out of range are italicized and underlined. NA = non-applicable, ND = not-detectable. *corticosteroid treatment.

	REFERENCE	LAST FOLLOW UP	HOSPITALIZATION BRONCHO-PNEUMONIA	HOSPITALIZATION PRIMO CMV INFECTION	DIAGNOSIS CVID	START IVIG	RE-ADMISSION AIHA*	INITIAL PRESENTATION ITP
COMPLETE								
HEMOGLOBIN	12-18 g/dL	16.9	17.1	14.6	16.8	14	*2.6*	15.9
THROMBOCYTES	150-450x10⁹/L	305	450	262	352	425	198	*9*
LEUKOCYTES	4-10x10⁹/L	*14.69*	*19.6*	*17.64*	*10.32*	*13.4*	*84.8*	6.7
IMMUNOGLOBULINS								
IGG	7.51-15.6 g/L	13.4	*18.7*	8.92	14	*6.83*	*22.2*	9.42
IGA	0.82-4.53 g/L	*4.89*	3.9	3.10	3.41	NA	1.61	1.73
IGM	0.46-3.04 g/L	1.64	0.92	*0.43*	*0.44*	NA	0.5	*0.25*
LYMPHOCYTE COUNTS								
B CELLS (CD19⁺)	82-476/µL	NA	429	NA	250	352	NA	NA
SWITCHED B MEMORY (CD27⁺IGM⁻IGD⁻)	% of CD19⁺ B cells	NA	NA	NA	ND	1.1	NA	NA
T CELLS (CD3⁺)	798-2823/µL	NA	2056	NA	*602*	1385	*3512*	NA
CD4⁺ T CELLS	455-1885/µL	NA	517	NA	*418*	920	*2149*	NA
CD8⁺ T CELLS	219-1124/µL	NA	*1461*	NA	*157*	NA	*1219*	NA
LYMPHOCYTE STIMULATION								
PHA	≥5 [x10³] cpm	NA	NA	NA	1640.91	NA	NA	NA
CANDIDA	≥5 [x10³] cpm	NA	NA	NA	191.14	NA	NA	NA

Supplementary Table 3.4. Protein-coding variants in *ITPR3* are predicted to be damaging. Gene-specific Mutation Significance cut-off (MSC) for the CADD score is 5.7. CADD: Combined Annotation Dependent Depletion (https://cadd.gs.washington.edu/snv). SIFT: Sorting Intolerant From Tolerant.

variant	CADD	SIFT	DANN
p.Phe1628Leu	25.8	damaging	damaging
p.Arg1850Gln	19.9	tolerated	damaging
p.Arg2524Cys	32.0	damaging	damaging

Supplementary Table 3.5. Primers for Sanger sequencing of identified variants.

variant	FW primer (5' → 3')	RV primer (5' → 3')
p.Phe1628Leu	CAGACATCACGCTGTGTTCAGGG	CTCCGACTCCATGAGGTCTTG
p.Arg1850Gln	CAACATGAATGACCTGGGCAGCC	CTGGGAAGCACGATCTTGTGTG
p.Arg2524Cys	CTGGGTCCTCAATATCACAGCCC	GGCTCATGTCCTCACCTAGAAACC

Supplementary Table 3.6. Primers used for subunit-specific qPCR analysis.

	FW primer (5' → 3')	RV primer (5' → 3')
ITPR1	CTCAACAAACTGCACCACGC	AGGAGCTGGATCACATTGCC
ITPR2	TTCATCATGACCCATGCCGT	TCAGGATTAAGCTCTGCAGCTA
ITPR3	GCACCTTCATCCGGGGCTATAAG	CGGTAGATGAGGTCAAAGAGCAGG

Supplementary Table 3.7. Primers used for cloning. Base changes to introduce the desired mutation are underlined.

	FW primer (5' → 3')	RV primer (5' → 3')
subcloning F1628L	CAGACGATTGTGGTGCAGCTG	CTTTGGTGGTGGGGTCGACT
subcloning R1850Q	AGTCGACCCCACCACCAAAG	CACCTCCGAGTTCTCACGCTCTTC
subcloning R2524C	GGTGCCCTCAATCTGACCAACAAG	GCAACTAGAAGGCACAGTCGAGG
mutagenesis F1628L	CTGGCCTGAGCTGCTCCTCCTGG AGGGCAGTG	CACTGCCCTCCAGGAGGAGCAGCTCAG GCCAG
mutagenesis R1850Q	CAGCCTGCGCCAGGGGCACGAGG TGAG	CTCACCTCGTGCCCCTGGCGCAGGCTG
mutagenesis R2524C	CATCTTTGGGGTAATCATCGACAC CTTCGCTGACCTGTGTAGTGAGAA GCAG	CTGCTTCTCACTACACAGGTCAGCGAA GGTGTCGATGATTACCCCAAAGATG

4 *ITPR3* variants causing Charcot-Marie-Tooth disease

Adapted from:

Rönkkö J, Molchanova S, Revah-Politi A, Pereira EM, Auranen M, Toppila J, Kvist J, Ludwig A, **Neumann J**, Bultynck G, Humblet-Baron S, Liston A, Paetau A, Rivera C, Harms MB, Tyynismaa H, Ylikallio E. Dominant mutations in *ITPR3* cause Charcot-Marie-Tooth disease. *Ann Clin Transl Neurol* 2020 Oct;7(10):1962-1972. doi: 10.1002/acn3.51190.

4.1 Abstract

Objective: *ITPR3*, encoding inositol 1,4,5-trisphosphate receptor type 3, was previously reported as a potential candidate disease gene for Charcot-Marie-Tooth (CMT) neuropathy. Here, we present genetic and functional evidence that *ITPR3* is a CMT disease gene.

Methods: Whole-exome sequencing of four affected individuals in an autosomal dominant family and one individual who was the only affected individual in his family was used to identify disease-causing variants. Skin fibroblasts from two individuals of the autosomal dominant family were analysed functionally by western blotting, quantitative reverse transcription PCR, and Ca^{2+} imaging.

Results: Affected individuals in the autosomal dominant family had onset of symmetrical neuropathy with demyelinating and secondary axonal features at around age 30, showing signs of gradual progression with severe distal leg weakness and hand involvement in the proband at age 64. Exome sequencing identified a heterozygous *ITPR3* p.Val615Met variant segregating with the disease. The individual who was the only one affected in his family had disease onset at age 4 with demyelinating neuropathy. His condition was progressive, leading to severe muscle atrophy below the knees and atrophy of proximal leg and hand muscles by age 16. Trio exome sequencing identified a de novo *ITPR3* variant p.Arg2524Cys. Altered Ca^{2+}-transients in p.Val615Met patient fibroblasts suggested that the variant has a dominant-negative effect on inositol 1,4,5-trisphosphate receptor type 3 function.

Interpretation: Together with two previously identified variants, our report adds further evidence that *ITPR3* is a disease-causing gene for CMT and indicates altered Ca^{2+} homeostasis in disease pathogenesis.

4.2 Introduction

Charcot-Marie-Tooth disease (CMT) is a group of hereditary neuropathies characterized by progressive distal sensory and motor impairment which affects 1:2,500 individuals[265]. The disease is categorized into demyelinating CMT1, where the median motor nerve conduction velocity (NCV) is <38 m/s and axonal CMT2 where the median motor NCV is >38 m/s but compound muscle action potentials (CMAP) are decreased. Cases with features of both demyelination and axonopathy and NCV in the 30-45 m/s range are sometimes referred to as intermediate CMT[173]. A large number of CMT disease gene discoveries have led to insights into disease mechanisms and potential therapies[266]. Dominant variants in *ITPR3*, encoding the inositol 1,4,5-trisphosphate (IP_3) receptor (IP_3R) type 3, were recently suggested as potential causes of CMT[188,189]. Linkage analysis combined with exome sequencing revealed a p.Thr1424Met variant that segregated with a CMT phenotype in three patients from a single family[188]. Furthermore, gene panel screening found a p.Met1064Val variant in a single index case for which no additional clinical details were provided[189]. The pathogenicity of these variants was not confirmed by functional studies or by segregation of the variants in additional families.

Humans have three IP_3R isoforms: IP_3R1, IP_3R2, and IP_3R3. They are largely homologous in sequence but differ in physiological functions and tissue expression[267,268]. IP_3 is for example produced after activation of G protein coupled receptors (GPCRs), and binds the tetrameric IP_3Rs, which release Ca^{2+} from the ER into the cytoplasm[37]. The resulting elevation of intracellular Ca^{2+} concentration has several downstream effects on the cell[211]. The importance of IP_3R signalling in neurons is underscored by the defects in IP_3R1 leading to ataxia or Gillespie syndrome[269–272]. Furthermore, the ER associated degradation pathway of activated IP_3Rs is disrupted by inactivating variants in the genes ERLIN1, ERLIN2, and RNF170, causing hereditary spastic paraplegia and other neurodegenerative diseases[273,274]. IP_3R3 itself has been implicated in apoptosis control, while alterations in its activity and/or expression levels drive oncogenesis and impact the survival of malignant cells[275,276].

In this study, we provide confirmatory evidence for the association of *ITPR3* with CMT. We introduce a CMT family with an autosomal dominant mutation and one case with a *de novo* mutation in *ITPR3*. In addition, we provide functional evidence of altered Ca^{2+} dynamics in patient fibroblasts.

4.3 Materials and Methods

Patients and sequencing

Individuals P1, P2, P3, and P4 gave written informed consent and the ethics review board of HUS Helsinki University Hospital approved the study. Control fibroblast cells were from anonymous donors, who consented to the use of the cells in scientific research. The fibroblast cells were collected from skin biopsies and cultured in Dulbecco's Modified Eagle Medium (DMEM), supplemented with 10% FBS (Life Technologies), 1% penicillin/streptomycin (Life Technologies), 1% L-glutamine (Life Technologies), and 0.2% uridine (Sigma). Cells were incubated at 37 °C in 5% CO_2.

Exome sequencing for the Finnish family was performed as described previously[277]. Sanger sequencing primers are shown in **Supplementary Table 4.1**. Research trio whole-exome sequencing (WES) was done on individual P5 and parents after written informed consent was obtained through an institutional review board-approved research study at the Institute for Genomic Medicine at Columbia University (protocol AAAO8410). DNA was extracted from maternal, paternal, and proband samples, exome sequenced on a HiSeq 2500 or NovaSeq 6000 with the Kapa Biosystem's Library Preparation Kit, and whole-exome captured with NimbleGen SeqCap EZ v.3.0 rapid or v.4.

Western blot

Fibroblasts were lysed in RIPA buffer (Cell Signaling #9806) and an aliquot containing 10 µg of total protein was boiled, separated in 4-20% Criterion™TGX™ gels, and transferred to 0.2 µm nitrocellulose using Trans-Blot Turbo (all Bio-Rad). Blocking was done with 10% milk in 0.1% TBS-T. Antibodies were: $IP_3R1^{(CT-1)}$, $IP_3R2^{(NT-2)}$ (gift from Dr. David Yule, University of Rochester, NY), IP_3R3 (BD-Transduction #610312), and β-tubulin (Cell Signaling #2146S). Anti-rabbit and anti-mouse (Jackson

Immunoresearch #111-035-144 and #115-035-146) secondary antibodies coupled to HRP were used. Detection was done by WesternBright™ ECL-spray (Thermo Scientific) and imaging with Molecular Imager ChemiDoc XRS+ with ImageLab (Bio-Rad).

Quantitative PCR and siRNA

RNA was extracted using the NucleoSpin® RNA extraction kit (Macherey-Nagel #740955) and reverse transcribed using the Maxima first strand cDNA synthesis kit (Thermo Fischer). RT-qPCR was performed using DyNAmo Flash SYBR Green qPCR Kit (Thermo Scientific) with specific primers for *ITPR1*, *ITPR2*, *ITPR3*, and *GAPDH* (**Supplementary Table 4.2**) using Bio-Rad CFX Maestro 1.1 software (Bio-Rad). *ITPR3* siRNA knockdown experiments were conducted as previously described[194] using *ITPR3* ON-TARGETplus SMARTpool siRNA (Dharmacon #L-006209-00-0005) and ON-TARGETplus Non-targeting siRNA (Dharmacon #D-001810-01-05).

Fibroblast Ca^{2+} imaging

We performed fibroblast Ca^{2+} imaging using two different methods in two different laboratories: a non-ratiometric manual Ca^{2+} assay using ATP stimulation (performed in University of Helsinki), and a ratiometric automated Ca^{2+} assay using ionomycin, thapsigargin, and bradykinin stimulation (performed in KU Leuven).

Non-ratiometric manual Ca^{2+} assay: Cells were washed two times with Hank's Balanced Salt Solution (HBSS) (in mM: 130 NaCl, 2.5 KCl, 1.8 CaCl2, 1.2 MgCl2, 10 HEPES, pH 7.4) and incubated for 50 min in the dark at RT with 5 µg/mL Fluo-4 AM Ca^{2+} indicator. After incubation, cells were washed three times with HBSS. For imaging, coverslips were placed on MatTek glass bottom dish (MatTek #P35G-1.5-14-C) and imaged with a Zeiss Axio Observer Z1 inverted phase contrast fluorescence microscope. During the experiment, cells were perfused with the Peristaltic Multichannel perfusion system PPS2. Before every experiment, cells were allowed to rest for 5 min under HBSS perfusion. The excitation light was filtered through a 494 nm band pass filter and the emission light collected through a 506 nm band pass filter. Emission was captured using a Photometrics Prime BSI sCMOS Camera with the ZEISS ZEN 3.1 (blue edition) imaging software. Acquisition protocol lasted a total of 12 minutes under constant perfusion at a rate of 2 mL/min. The cells were first perfused with HBSS containing 1.8 mM Ca^{2+} for 3 min and then with HBSS solution containing no Ca^{2+} (0-Ca^{2+} HBSS) for another 3 min. Then Ca^{2+} release from the ER was evoked by perfusion with 0-Ca^{2+} HBSS containing 80 µmol/L adenosine 5'-triphosphate (ATP) magnesium salt (Sigma-Aldrich #A9187) for 2 min. After ATP-evoked Ca^{2+} response, the perfusion solution was changed back to 0-Ca^{2+} HBSS for 2 min and finally back to 1.8 mmol/L Ca^{2+} containing HBSS solution for another 2 min to induce store-operated Ca^{2+} entry (SOCE) as a positive control.

The results were analysed using MatLab (MATLAB R2019b) and RStudio (version 1.2.5033). Regions of interest (cells) were masked from each experiment and the mean pixel intensity was measured at each

time point (frame) using a modified version of the previously described MatLab script[278,279]. The baseline (F_0) was selected from the first 0-Ca^{2+} period, from frames with stable intensity values. Relative intensities were calculated by first subtracting the baseline value from each frame and then dividing it by the baseline value [$\Delta F_t/F_0=(F_t-F_0)/F_0$]. To analyse the kinetics of the Ca^{2+} response peaks, we created an R-script, which allows automatic analysis of the peaks. The area under the curve (AUC), peak amplitude and time to peak were measured from each cell, and the averages per coverslip were calculated. The scripts used are available online (https://github.com/JuliusRonkko/Ca2-analysis).

Ratiometric automated Ca^{2+} assay: Cytosolic Ca^{2+} levels of fibroblasts seeded in 96-well plates (Greiner) were monitored using the ratiometric fluorescent Ca^{2+} indicator dye Fura-2 AM (Eurogentec, Belgium). Cells were loaded with Fura2-AM (1 µmol/L) at RT for 30 min in a modified Krebs solution (in mM: 150 NaCl, 5.9 KCl, 1.2 $MgCl_2$, 11.6 HEPES (pH 7.3), and 1.5 $CaCl_2$). After loading, cells were rested for 30 min at RT in the absence of Fura-2 AM to allow complete dye de-esterification before proceeding to analysis on a FlexStation 3 microplate reader (Molecular Devices, Sunnyvale, CA, USA). The Ca^{2+} indicator was alternately excited at 340 and 380 nm and emission of fluorescence at 510 nm recorded. EGTA was added after 30 seconds in all conditions at a final concentration of 3 mmol/L. After another 60 seconds, cells were exposed to stimuli prepared in Ca^{2+}-free modified Krebs solution containing 3 mmol/L EGTA and Ca^{2+} transients were monitored for 6 min. Ionomycin and the irreversible SERCA-inhibitor thapsigargin were both added at a final concentration of 10 µmol/L and bradykinin at a final concentration of 50 nmol/L. All traces are shown as the ratio of both emission wavelengths F_{340}/F_{380} and were smoothened using a running average of 5. For quantification purposes, a baseline value was determined for each measurement as mean fluorescence between 30 sec and 90 sec. Fluorescence ratio F_{340}/F_{380} was then normalized to the baseline values, and AUC of the peak, the peak amplitude (both analysed between 90 and 450 sec) and the time to the peak were measured.

4.4 Results

4.4.1 Autosomal dominant CMT family

The proband of the Finnish family (P1) first came to neurologic investigations at age 38. His first symptoms had started slightly before age 30 with weakened foot dorsiflexion and a tendency to foot drop. Around age 33 he also started to experience increased clumsiness in his hands. He was last evaluated at age 64. His symptoms have been slowly progressive with increasing difficulty in walking in rough terrain. He uses supportive insoles but has remained ambulant without external aids. He has severe muscle atrophy in his lower legs, hammer toes, pes cavus, and thenar muscle atrophy (**Fig. 4.1A**). Sensation to light pressure was decreased distally from wrists and in foot soles. Vibration sense was decreased at ankles but present at wrists. Foot dorsiflexion or plantarflexion did not overcome gravity.

Deep tendon reflexes were absent. He was additionally diagnosed with hypothyroidism, hypercholesterolemia, and severe obstructive sleep apnoea.

The proband had two brothers (**Fig. 4.1B**), one of whom had no neuropathic symptoms, while the other (P3) had pes cavus and progressive distal muscle weakness and wasting. His diseased father (P4) had been diagnosed with hereditary neuropathy of unknown cause but was otherwise relatively healthy and lived to an age of 93 years. He had remained ambulant until that age. The daughter of the proband (P2) first came to neurologic examination at age 35. She had had hammertoes and other deformities of the small bones of the feet since childhood, which had been operated on first at age 27. Despite this, she was ambulant without aids and able to play sports. She was able to walk on toes and heels. Marked pes cavus and hammertoes were noted (**Fig. 4.1C**), in addition to mild impairment of vibration sense at the right ankle.

Nerve conduction studies (NCS) of P1, P2, and P3 were consistent with demyelinating neuropathy, which were graded at least mild. The reduction in NCV was clearly less than is typical for CMT1A (**Table 4.1**). In addition, there were variable degrees of axonal neuropathy, which tended to worsen with age. Biopsies from P1 had been obtained at age 38. In sural nerve biopsy, a clear hypertrophic neuropathy with prominent onion bulbs was seen (**Fig. 4.1D**). Muscle biopsy from the tibialis anterior muscle showed prominent small group atrophy, fibre type grouping, and secondary myopathic change (**Fig. 4.1E**).

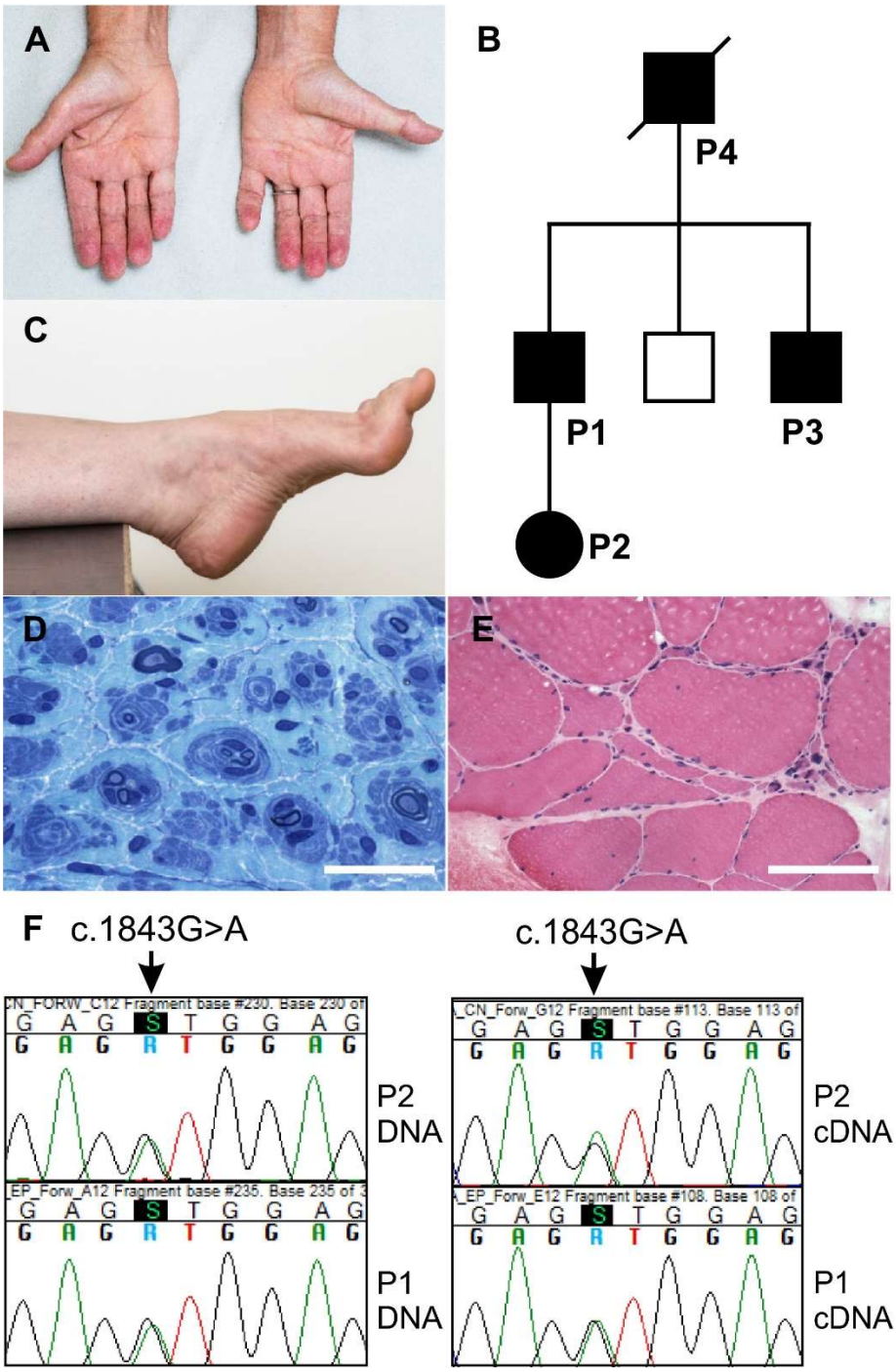

Figure 4.1: Clinical features and sequencing. (A) Photographed at age 64, the index patient P1 had distal muscle atrophy. **(B)** In the family, his father (P4) and one of his two brothers (P3) had been similarly affected. **(C)** His daughter (P2) had had foot deformities since an early age and was noted to have pes cavus when examined at age 35. **(D)** In sural nerve biopsy of P1, a clear hypertrophic neuropathy with prominent onion bulbs was seen (plastic section toluidine blue staining, scale bar 25 µm). **(E)** Muscle biopsy from the tibialis anterior muscle of P1 showed prominent small group atrophy, fibre type grouping and secondary myopathic change (frozen section HE-staining, scale bar 125 µm). **(F)** Sanger sequencing confirmed the presence of *ITPR3* c.1843G>A (p.Val615Met) in all affected individuals, shown are P1 and P2 chromatograms, and it was absent in the unaffected brother.

Table 4.1: Clinical and neurophysiological findings. CMAP: compound muscle action potential, SNAP: sensory nerve action potential, n.r. no response, n.a. not available.

CASE	P2	P1	P3	P4	P5
ETHNICITY	Finnish	Finnish	Finnish	Finnish	Ashkenazi Jewish
SEX	F	M	M	M	M
AGE AT ONSET	20s	27	n.a.	n.a.	4
AGE AT EXAMINATION	35	63	31	Died age 93	16
DISTAL WEAKNESS	-	+	+	+	+
DISTAL SENSORY IMPAIRMENT	+	+	+	+	+
FOOT SKELETAL DEFORMITY	+	+	+	n.a.	+
MEDIANUS MOTOR CONDUCTION VELOCITY M/S	39	33	45	n.a.	32
MEDIANUS MOTOR DISTAL LATENCY MS	4.92	7.48	4.1	n.a.	7.34
MEDIANUS CMAP AMPLITUDE MV DIST/PROX	6.6/5.8	3.8/2.7	n.a.	n.a.	4.0/2.9
RADIALIS SENSORY CONDUCTION VELOCITY M/S	52	48	n.a.	n.a.	n.a
RADIALIS SNAP AMPLITUDE µV	15	7.0	n.a	n.a.	n.a
MEDIAN AND ULNAR SNAP AMPLITUDE µV	n.a	n.a	n.a	n.a	6.7/5.1
PERONEUS MOTOR CONDUCTION VELOCITY M/S	30	n.r.	43	n.a.	n.r
PERONEUS MOTOR DISTAL LATENCY MS	5.79	n.r.	6.4	n.a.	n.r
PERONEUS CMAP AMPLITUDE DIST/PROX MV	4.9/3.8	n.r.	n.a.	n.a.	n.r
TIBIALIS CMAP AMPLITUDE DIST MV	1.1	n.r.	n.a.	n.a.	n.r
TIBIALIS MOTOR DISTAL LATENCY MS	4.76	n.r.	n.a	n.a.	n.r
SURALIS SENSORY CONDUCTION VELOCITY M/S	42	n.r.	35	n.a.	n.r
SURALIS SNAP AMPLITUDE µV	1.8	n.r.	4.3	n.a.	n.r

4.4.2 Single affected individual

The proband of the Ashkenazi Jewish family (P5) was developing normally until 4 years of age when he began falling. An evaluation at that time was concerning for pes cavus with hammertoes, and a motor only NCS showed a small tibial CMAP (0.5 mV) with a demyelinating range conduction velocity (20 m/sec). The median CMAP was normal (4.0 mV) but the NCV was 35 m/sec. No temporal dispersion or conduction block was present in either nerve. He was diagnosed with a demyelinating CMT and over the intervening decade he experienced progressive loss of leg strength and sensation in a symmetric distal to proximal gradient. After this evaluation he was not evaluated by a neurologist until 16 years of age when he established care at Columbia University Irving Medical Center (CUIMC).

On neurological examination at age 16, he had pes planus with complete loss of muscle below the knees, and atrophy of proximal leg and hand intrinsic muscles. There was no movement at the ankles, anti-gravity strength at the knees, and mild weakness of hip flexion and the hand intrinsics. Temperature, pin prick, and vibration sensations were severely reduced at the toes and ankles, but remarkably, joint position sense was preserved. All reflexes were absent. Otherwise, general examination, cognitive evaluation, and neurological examination were normal.

The proband was the product of a consanguineous union (parents are second cousins). His father is known to have flat feet and mildly reduced distal sensation in his early 40's but no demonstrable weakness. His mother's examination was normal. Of the proband's 11 full siblings, none are suspected by the family to have similar symptoms but have not been formally tested.

Repeat EMG/NCS showed absent motor and sensory responses in the legs (**Table 4.1**). The median and ulnar nerves showed normal CMAP amplitudes and slowed conduction velocities (32 m/sec), with mildly reduced SNAP amplitudes and conduction velocities of 38 m/sec.

4.4.3 Genetic findings

In P1, we first excluded PMP22 duplication, MFN2 and GJB1 mutations. After this we performed exome sequencing on P1 and P3. We filtered the exome data for (1) shared nonsynonymous changes (excluding in frame insertions/deletions), (2) absence in SNP database (dbSNP), (3) prevalence $\leq 10^{-5}$ in the Finnish subpopulation of gnomAD (v2.1.1), and (4) CADD score[12] of 15 or more. The analysis left nine variants (**Supplementary Table 4.3**) of which c.1843G>A (p.Val615Met) in exon 16 of *ITPR3* (NM_002224.4) was of interest. We confirmed the segregation of the variant with disease in the family by Sanger sequencing (**Fig. 4.1F**). The other identified variants had no previous studied function in Schwann cells or suggested association with CMT.

In P5, a chromosomal analysis and SNP microarray were within normal limits though the SNP microarray showed long contiguous runs of homozygosity consistent with the history of consanguinity. A CMT gene panel that included sequencing and deletion/duplication analysis of 42 genes identified single missense variants of uncertain significance in each of two autosomal recessive CMT genes (IGHMBP2 and NDRG1) without other coding or copy number variants in those genes. A clinical exome was reported as negative. Trio sequence data were subsequently analysed with an updated version of the Institute for Genomic Medicine's established trio sequencing framework[280] which identifies "qualifying" genotypes not observed in the parents, 12,044 control individuals from the Institute for Genomic Medicine, or two external databases of 6,503 and 60,706 control individuals provided by the National Heart, Lung, and Blood Institute (NHLBI) Exome Sequencing Project (ESP6500SI [March 2013 release]) and the Exome Aggregation Consortium (ExAC Browser v.0.3 [January 2015 release]), respectively. The analysis identified a *de novo* missense variant in exon 55 of the *ITPR3* gene (NM_002224.4, c.7570C>T, p.Arg2524Cys). The variant is absent from the gnomAD V2.1.1 database and has a CADD score of 32.

Both *ITPR3* variants are predicted to be deleterious and damaging to protein structure and/or function based on *in silico* analyses (damaging by SIFT, probably damaging by PolyPhen2). The affected amino acids are highly conserved (**Fig. 4.2A**). We assessed the affected residues using published IP_3R structures[238,239,281]. p.Val615 is located in the armadillo repeat domain (ARM1), just after the IP_3-binding

domain (running from aa 1 to ~aa 600). p.Arg2524 is located in the transmembrane domain (TMD) and lies in the channel pore (**Fig. 4.2B, C**).

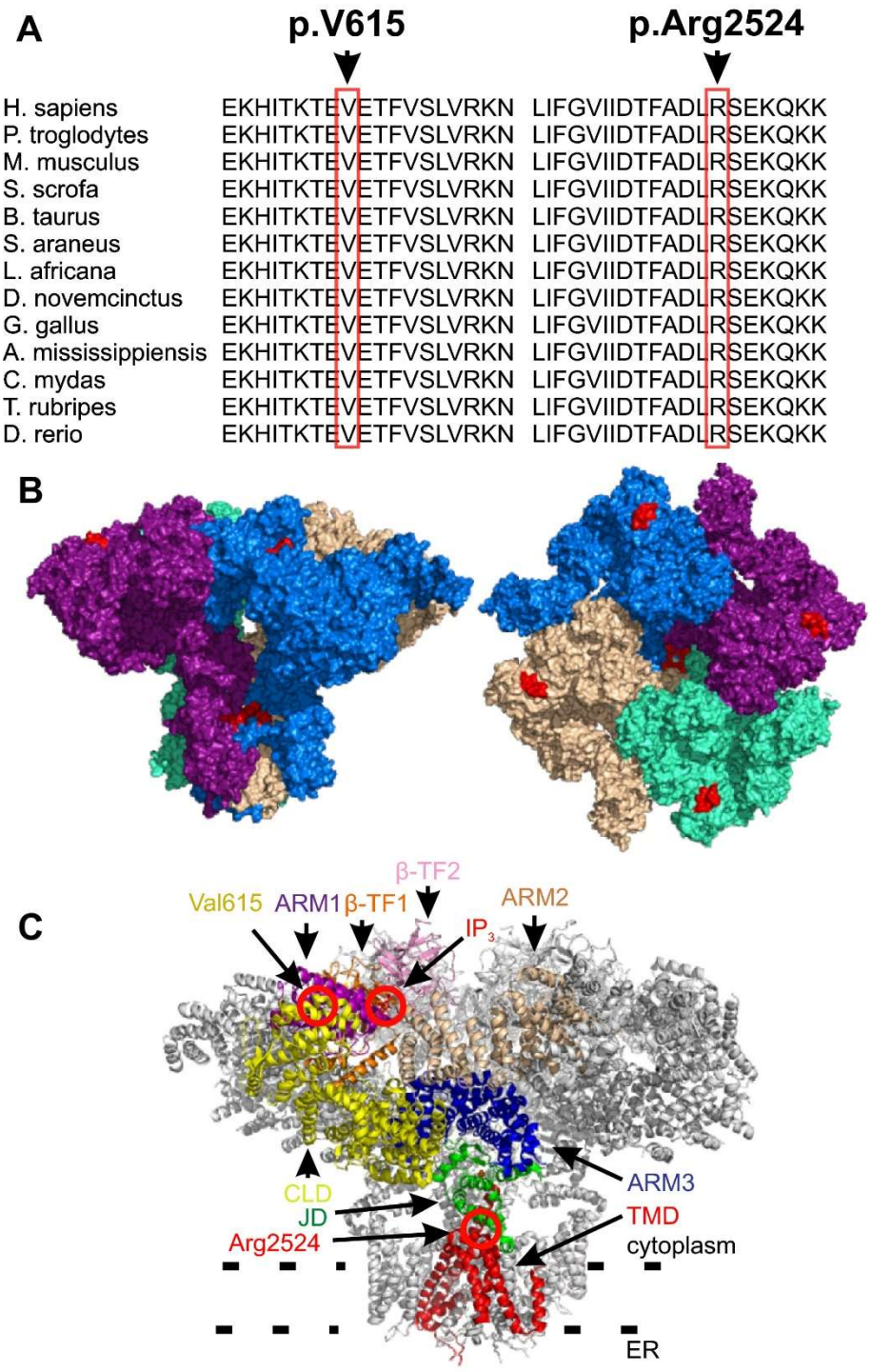

Figure 4.2: Conservation and position of IP_3R3 mutations. (A) The p.Val615Met and the p.Arg2524Cys mutations affect a conserved stretch of amino acids. **(B,C)** The p.Val615Met mutation lies adjacent to the cytoplasmic surface of IP_3R3 and in proximity to the IP_3 binding site, while the p.Arg2524Cys mutation lies in the channel pore, as predicted based on the previously published model of the tetramer[280]. **(B)** The amino acids 610-620 and 2520-2530 are highlighted in red. Different subunits are indicated by different colours. **(C)** Key domains of the IP_3R3 channel and IP_3-molecule at its binding site are highlighted in the figure. ARM1-3 = armadillo repeat domains 1-3, BTF1-2 = β-trefoil domains 1-2, CLD = centre linker domain, JD = juxtamembrane domain, TMD = transmembrane domain.

4.4.4 Protein and mRNA

Skin fibroblasts of P1 and P2 were available for study. We assessed the levels of IP_3R proteins and corresponding mRNAs. IP_3R3 protein level was decreased in the skin fibroblasts of P2 but not in P1, as compared with controls (**Fig. 4.3A, B**). However, P1 fibroblasts had significantly elevated *ITPR3* mRNA levels as compared with controls (**Fig. 4.3C**), which suggests a compensatory mRNA upregulation to preserve the normal IP_3R3 protein level. IP_3R2 protein level was also decreased in P2, while those of IP_3R1 were unaffected. Also, *ITPR1* and *ITPR2* mRNA levels were unchanged in both patient lines.

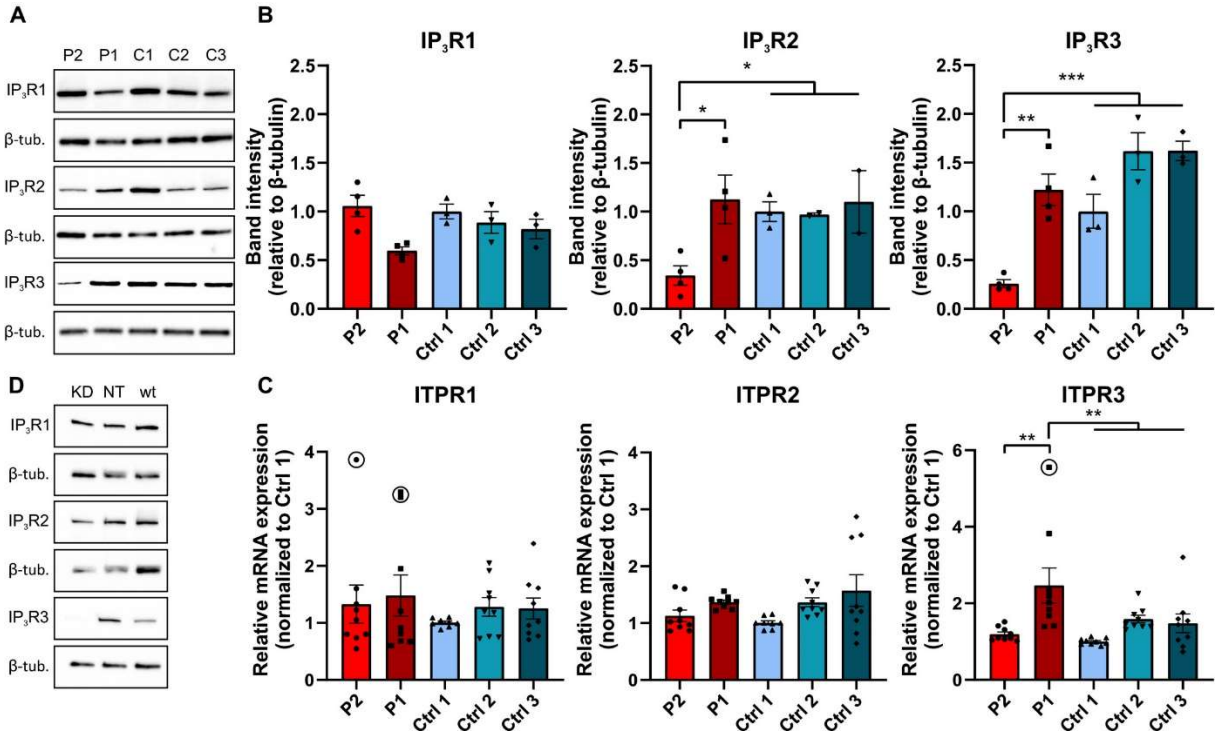

Figure 4.3: Fibroblast protein levels in Finnish family patients. (A, B) Western blots of fibroblast lysates show the levels of IP_3R1, IP_3R2, and IP_3R3 in the patients and controls. **(C)** qPCR showing mRNA levels of *ITPR1*, *ITPR2*, and *ITPR3* in patient and control fibroblasts. **(D)** IP_3R1, IP_3R2, and IP_3R3 protein levels following siRNA knockdown of *ITPR3* in control fibroblasts by western blot. KD = *ITPR3* siRNA knockdown, NT = non-targeting siRNA, wt = non-treated. Data points marked in the figures were excluded from the data-analysis (* p<0.05, ** p<0.01, *** p<0.001).

4.4.5 Fibroblast Ca^{2+} flux

Next, we performed siRNA knockdown of *ITPR3* in control fibroblasts. The knockdown was confirmed by Western blot (**Fig. 4.3D**) and led to altered Ca^{2+} flux dynamics in response to the GPCR agonist ATP, with delayed peak of response but no change in amplitude or area under the curve (AUC) (**Fig. 4.4A**). This experiment confirmed that loss of IP_3R3 produces a detectable phenotype in fibroblasts.

After this, we analysed Ca^{2+} homeostasis in primary fibroblasts from P1 and P2 and healthy controls. The response to the GPCR agonist ATP, which results in IP_3-mediated signalling and thus opening of IP_3Rs, was analysed by manual non-ratiometric assay in the absence of extracellular Ca^{2+}. The ATP-evoked Ca^{2+} release was altered in both patient fibroblasts. P1 fibroblasts had a statistically significant

decrease in the AUC of the response, while P2 fibroblasts had an increased time to peak (**Fig. 4.4B**). We performed additional Ca^{2+}-signalling analyses in cell populations using ratiometric automated technique. In these experiments, cells were first exposed to EGTA, an extracellular Ca^{2+} chelator. The response to the Ca^{2+} ionophore ionomycin, which provides an estimate of the total intracellular Ca^{2+} content, was decreased in P1 fibroblasts (**Fig. 4.4C**). The SERCA inhibitor thapsigargin, which gives an estimate of ER Ca^{2+} store content, did not cause statistically significant changes in the patient fibroblasts (**Fig. 4.4D**). Finally, the alternative GPCR agonist bradykinin evoked smaller cytosolic Ca^{2+} transients in P1 and P2 fibroblasts, the latter having a significantly lower peak amplitude (**Fig. 4.4E**). Overall, the results suggest that the p.Val615Met mutation in *ITPR3* affects Ca^{2+} homeostasis and IP_3-mediated Ca^{2+} release.

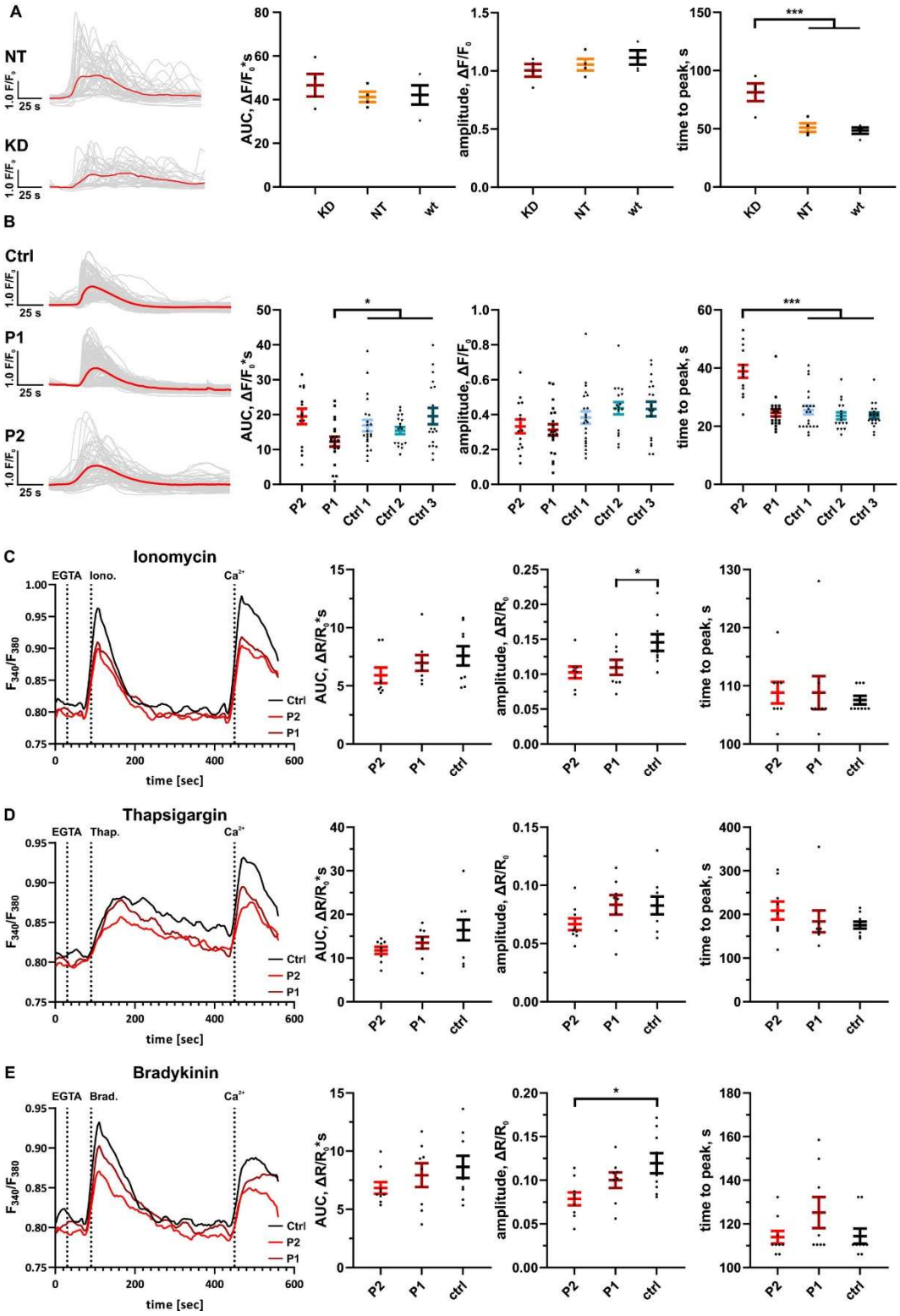

Figure 4.4: Ca^{2+} flux analysis in patient fibroblasts is altered compared to controls. The Ca^{2+} flux measurements were performed with two different methods, using cell-permeant Fluo-4 AM and Fura-2 AM fluorescent Ca^{2+} indicators. **(A, B)** Fluorescence microscopy was used to monitor Ca^{2+} in single cells, and 80 µmol/L ATP as GPCR agonist was added to evoke Ca^{2+} release. In each case, representative Ca^{2+} response curves after addition of ATP are shown. Grey thin lines are recordings from single cells whereas the thick line represents the averaged trace for all the cells in the given experiment. **(A)** Quantification of responses in fibroblasts treated with *ITPR3*-specific siRNA (KD), non-targeting siRNA (NT) or left untreated (wt) (n=4 individual experiments). **(B)** Quantification of responses to ATP in patient and control fibroblasts (P1 n=20, P2 n=14 and three controls n=17-22 individual experiments). **(C–E)** In the second method we measured Ca^{2+} in single wells of a 96-well plate, using **(C)**

10 µmol/L ionomycin, **(D)** 10 µmol/L thapsigargin or **(E)** 50 nmol/L bradykinin to evoke responses, and compared patient cells to one control line performing five independent experiments in each setting. All stimuli (added after 90 sec, 2nd dotted line) were added in the presence of EGTA (added after 30 sec, 1st dotted line). All results are presented as mean ± SEM of independent experiments and statistical comparisons performed with one-way ANOVA. (* $p<0.05$, ** $p<0.01$, *** $p<0.001$).

4.5 Discussion

This study provides genetic and functional evidence for *ITPR3* as a dominant CMT disease gene. We describe two new mutations: p.Val615Met in adult-onset and p.Arg2524Cys in childhood-onset CMT. The reduction in median motor NCV in these patients was consistent with demyelinating neuropathy, which was also confirmed by nerve biopsy in one patient. However, the magnitude of reduction was less severe than is usually observed in CMT1A (OMIM #118220), which is the most common form of CMT[173]. Our patients' NCV was in the 30-45 m/s range suggesting it should be considered in those with "intermediate CMT"[173]. However, in CMT, conduction velocities vary by nerve, disease duration and patient, thus additional patients will be required to more conclusively define whether this is a demyelinating or intermediate CMT. Axonal involvement in our patients tended to become worse with age, which suggests that the axonal degeneration was secondary to demyelination.

Both of the identified mutations affect highly conserved residues. Being located in the central modulatory region of IP_3R3, shortly after the ligand-binding domain[238], the p.Val615Met variant might influence IP_3R3 activity, for example, through interfering with allosteric regulators[211]. The p.Arg2524Cys variant, which localizes to the channel pore, may affect the channel properties and/or the ion flux directly, thus accounting for the earlier onset, faster progression, and more severe phenotype in this patient. The previously reported variant of unknown significance, p.Thr1424Met[188], was in a patient who - similarly to our patients - had a moderately decreased median motor NCV of 34.7 m/s. Onset was at age 40, and two additional individuals in the same family were similarly affected[188]. The p.Thr1424Met variant localizes to the armadillo repeat domain 2 near the subunit contact site. It may therefore affect oligomerization of the channel. Finally, the variant p.Met1064Val, previously found in one index case of hereditary neuropathy[189], affects a conserved residue on the channel surface at the centre linker domain. Similarly, as the p.Val615Met and p.Arg2524Cys variants, both variants reported earlier are predicted to be deleterious and damaging to protein structure and/or function (damaging by SIFT, probably damaging by PolyPhen2). Thus, the dominant missense variants may have different molecular effects on IP_3R3 function, which may also influence disease severity and penetrance.

Our measurements of Ca^{2+} flux demonstrate altered Ca^{2+} homeostasis in p.Val615Met patient cells. The primary fibroblasts express *ITPR3* and thus are a useful tool to study the effects of the mutation under physiological conditions. The weakness of this model is that it does not account for possible neuron- or Schwann cell-specific effects of the mutation and additional (epi-)genetic factors that differ between

individuals apart from the *ITPR3* mutation. Treatment with *ITPR3* siRNA was used to confirm that IP_3R3 is active in fibroblasts under normal conditions and to model the effect of loss-of-expression of the channel. We found altered GPCR agonist responses in both patient lines. The slowed response in P2 fibroblasts was similar but less pronounced than in siRNA-treated cells. In addition, the P1 cells showed a decreased amplitude of the Ca^{2+} response to ATP. The differences in the Ca^{2+} responses between the two patient cell lines may be related to reduction in the amounts of IP_3R2 and IP_3R3 in P2 cells, which were compensated by *ITPR3* mRNA upregulation in P1 cells. In addition, the difference in sex or other possible genetic differences may in part account for the differences between P1 and P2 fibroblasts. Based on these results, the p.Val615Met variant may exert a dominant negative effect on channel function. The effect appears to be subtle in physiologic conditions with homozygous IP_3R1 and IP_3R2 as well as heterozygous IP_3R3 wild-type alleles, which is consistent with the late onset and slowly progressive nature of our patients' phenotype. As ionomycin and thapsigargin-induced Ca^{2+} release tended to be lower in patient fibroblasts, it cannot be excluded that IP_3R3 p.Val615Met is leaky, that is, has an increased likelihood of being open compared with the wild type situation, thereby lowering steady state ER Ca^{2+} levels and thus dampening Ca^{2+} release into the cytosol upon agonist exposure. More targeted experiments, optimally in a model expressing only the IP_3R3 mutant channel with knockout of other endogenous isoforms, will be needed to further verify and refine these hypotheses on the functional impact of the mutation.

Our results suggest an important role of IP_3R3 in peripheral nerve maintenance. This is supported by its localization in paranodal regions of rat Schwann cells, where its proximity to another CMT gene product, gap junction protein beta-1 (GJB1), may allow swift propagation of Ca^{2+} signals from cell to cell[282]. Abnormal Ca^{2+} flux could contribute to altered axonal Ca^{2+} microdomains that disturb mitochondrial transport, as has been suggested for dominant mutations in the plasma membrane cation channel transient receptor potential cation channel, subfamily V, member 4 (TRPV4)[283–286] which cause CMT2C[287–289]. Furthermore, mutations in other components of the IP_3 signalling pathway, for example FIG4 and SBF2, cause demyelinating CMT[290,291], which highlights the importance of this pathway for peripheral myelin maintenance. Studies focusing on investigating wild-type and mutated IP_3R3 in neuronal or Schwann cells, for example differentiated from induced pluripotent stem cells, could shed further light on their role in health and pathology. Finally, IP_3R3 has important implications for regulation of mitochondrial function and cell death and survival by participating in Ca^{2+} transfer between the ER and mitochondria[275,292], a process which is also dependent on another important CMT gene, mitofusin 2 (MFN2)[293]. IP_3R3 defects may decrease mitochondrial Ca^{2+} and predispose to defective bioenergetic or ER membrane function, which have been found in other forms of CMT[294,295].

In conclusion, our results provide further evidence that *ITPR3* is a disease gene for CMT. Additional studies, ideally in neuronal or animal models, will be needed to elucidate the effects of the disease

variants on IP_3R3 function and evaluate the potential of targeting Ca^{2+} flux as a therapeutic target in CMT.

4.6 Personal Contribution

For this chapter I designed and performed the experiment as well as the analysis of the data presented in Fig. 4.4C-E and provided guidance for the design and analysis of the remaining Ca^{2+} flux experiments presented in this figure. I wrote the results and methods sections associated with the experiments I performed and reviewed and edited the final manuscript.

4.7 Supplementary Material

Supplementary Table 4.1. Sequencing primers.

MATERIAL	DIRECTION	TARGET	SEQUENCE
GENOMIC DNA	Forward	*ITPR3*-ex16	TTTCCTGGACCTC TGCCTTT
GENOMIC DNA	Reverse	*ITPR3*-ex16	GTTCACACAACCAGCAGAGT
CDNA	Forward	*ITPR3*-cDNA ex16	GCAAGAACCAGGAGCACATT
CDNA	Reverse	*ITPR3*-cDNA ex16	CACACACAGGTCAGAGAGGT

Supplementary Table 4.2. Quantitative PCR primers.

GENE	DIRECTION	SEQUENCE
ITPR1	Forward	CTCAACAAACTGCACCACGC
ITPR1	Reverse	AGGAGCTGGATCACATTGCC
ITPR2	Forward	TTCATCATGACCCATGCCGT
ITPR2	Reverse	TCAGGATTAAGCTCTGCAGCTA
ITPR3	Forward	CTTCATCAGCACTTTGGGGC
ITPR3	Reverse	ACCTTGAAGAGGCAGTCACG
GAPDH	Forward	CGCTCTCTGCTCCTCCTGTT
GAPDH	Reverse	CCATGGTGTCTGAGCGATGT

Supplementary Table 4.3. Exome sequencing findings (see next page). Chr = chromosome, pos = position, ref = reference allele, alt = alternative allele, HGVS = human genome variant society, OMIM = online mendelian inheritance in man, AR = autosomal recessive, CADD = combined annotation dependent depletion, gnomAD = genome aggregation database, nt = not tested. Chromosome positions are from hg19.

CHR	POS	REF	ALT	GENE	CANONICAL TRANSCRIPT CONSEQUENCE	HGVS PROTEIN LEVEL	HGVS DNA LEVEL	OMIM	CADD SOCRE	GNOMAD	SEGRE-GATION
1	19422101	G	A	*UBR4*	missense	ENSP00000364403.3: p.Arg4522Trp	ENST00000375254.3: c.13564C>T		35.00		**NT**
1	19430739	G	A	*UBR4*	missense	ENSP00000364403.3: p.Ser4247Phe	ENST00000375254.3: c.12740C>T		25.30		**YES**
1	32827403	G	T	*TSSK3*	intron		ENST00000574315.1: c.-80-1793G>T		23.20		**NT**
1	32827403	G	T	*FAM229A*	missense	ENSP00000454338.1: p.Ser8Tyr	ENST00000428500.1: c.23C>A		23.20		**NT**
1	75098984	A	G	*CRYZ*	5'-UTR		ENST00000417775.1: c.-397T>C		33.00	8.24E-06	**NT**
1	75098984	A	G	*TYW3*	missense	ENSP00000359904.3: p.Asp19Gly	ENST00000370867.3: c.56A>G		33.00	8.24E-06	**NT**
6	33635698	G	A	*ITPR3*	missense	ENSP00000363435.4: p.Val615Met	ENST00000374316.5: c.1843G>A	Susceptibility to Diabetes, type 1, 222100 (2), AR	28.60		**YES**
14	61190125	C	T	*SIX4*	missense	ENSP00000216513.4: p.Gly223Asp	ENST00000216513.4: c.668G>A		27.10		**YES**
19	8660650	T	C	*ADAMTS10*	missense	ENSP00000270328.4: p.Tyr492Cys	ENST00000270328.4: c.1475A>G	Weill-Marchesani syndrome 1, 277600 (3), AR	24.20		**NO**
19	15563475	C	A	*RASAL3*	missense	ENSP00000341905.5: p.Arg941Leu	ENST00000343625.7: c.2822G>T		17.58	0.0001	**NT**
20	1317279	G	A	*AL136531.1*	stop gain	ENSP00000440123.1: p.Arg18Ter	ENST00000537552.1: c.52C>T		23.30	0.002085	**NT**
20	1317279	G	A	*SDCBP2-AS1*	intron		ENST00000609470.1: n.120+11106G>A		23.30	0.002085	**NT**

5 Functional characterization of neuropathy-associated *ITPR3* variants

Adapted from:

Terry LE, Arige V, **Neumann J**, Wahl AM, Knebel TR, Chaffer JW, Malik S, Liston A, Humblet-Baron S, Bultynck G, Yule DI. Missense mutations in inositol 1,4,5-trisphosphate receptor type 3 result in leaky Ca^{2+} channels and activation of store-operated Ca^{2+} entry. *iScience* 2022 Nov 7;25(12):105523. doi: 10.1016/j.isci.2022.105523.

5.1 Abstract

Mutations in all subtypes of the inositol 1,4,5-trisphosphate receptor Ca^{2+} release channel are associated with human diseases. In this report, we investigated the functionality of three neuropathy-associated missense mutations in IP_3R3 (V615M, T1424M, and R2524C). The mutants only exhibited function when highly over-expressed compared to endogenous hIP_3R3. All variants resulted in elevated basal cytosolic Ca^{2+} levels, decreased endoplasmic reticulum Ca^{2+} store content, and constitutive store-operated Ca^{2+} entry in the absence of any stimuli, consistent with a leaky IP_3R channel pore. These variants differed in channel function; when stably over-expressed the R2524C mutant was essentially dead, V615M was poorly functional, and T1424M exhibited activity greater than that of the corresponding wild type following threshold stimulation. These results demonstrate that a common feature of these mutations is decreased IP_3R3 function. In addition, these mutations exhibit a novel phenotype manifested as a constitutively open channel, which inappropriately gates SOCE in the absence of stimulation.

5.2 Introduction

Mutations in the inositol 1,4,5-trisphosphate (IP_3) receptors (IP_3Rs) are increasingly associated with human disease[220,221]. IP_3Rs are calcium (Ca^{2+}) channels predominantly located in the endoplasmic reticulum (ER) membrane that mediate Ca^{2+} release from the ER Ca^{2+} store upon binding of IP_3[296,297]. IP_3 is produced as the result of a signal transduction cascade initiated by agonist binding to G protein-coupled receptors or receptor tyrosine kinases at the plasma membrane (PM)[298]. Both receptor classes result in the activation of phospholipase C isozymes, which cleave phosphatidylinositol 4,5-bisphosphate into membrane-bound diacylglycerol and freely diffusible IP_3. The spatial and temporal aspects of the resulting Ca^{2+} release into the cytosol allow for the interaction of Ca^{2+} with various effectors leading to a diverse set of cell functions including apoptosis, gene transcription, fertilization, proliferation, growth and development, metabolism, fluid secretion, and exocytosis[33,34,304,35,264,298–303]. A secondary effect of the Ca^{2+} release is the depletion of the ER Ca^{2+} store, which when sensed by the Stromal Interaction Molecule (STIM) activates Ca^{2+} entry into the cytoplasm through the ORAI channels resident in the PM—a process known as store-operated calcium entry (SOCE). In order to maintain homeostasis, excess Ca^{2+} is removed from the cytosol through extrusion from the cell via the plasma membrane Ca^{2+} ATPase (PMCA), through reuptake into the ER via the sarcoplasmic ER Ca^{2+} ATPase (SERCA) or sequestration by mitochondria through the mitochondrial Ca^{2+} uniporter (MCU)[34].

Three IP_3R genes in the human genome (*ITPR1*, *ITPR2*, *ITPR3*) produce monomeric (~300 kDa) isoforms of the receptor (IP_3R1, IP_3R2, and IP_3R3), which share ~60-70% sequence homology[226,298,305–308]. A single subunit consists of a highly conserved N-terminal suppressor domain (SD; 1-226 (Sequence used here is human IP_3R3 (NP_002215.2) and domains are based on previously identified domains and structures in rat IP_3R1 (NP_001007236))[309] and ligand-binding domain (LBD; 227-578)[310] and a highly

conserved C-terminal channel pore and cytosolic tail (2201-2671)[311–313]. These termini are separated by a large, non-conserved regulatory and coupling domain (579-2200)[314] where regulation by Ca^{2+}, ATP, PKA phosphorylation, and other small molecules and binding partners occurs[238,242,255,281,315,316]. As a result, IP_3 binding to the N-terminal LBD, which is about 70 Å from the channel pore induces long-range conformational changes in the cytosolic domain enabling pore opening[242,281].

The three isoforms of the receptor are obligate tetramers and can assemble as both homo- or hetero-tetrameric complexes[317,318]. While IP_3Rs are ubiquitously expressed, one isoform or a combination of isoforms are preferentially expressed in various tissues and cell types[72,73,184,252,268,319]. Thus, the stoichiometry of the IP_3R tetramers is likely dependent upon the distribution and endogenous expression level of each isoform[184]. Previous studies have established that IP_3R1 is highly expressed in the nervous system and is essential for the normal development of the nervous system. Mice engineered to lack native IP_3R1 often die prior to birth, or if born, suffer from severe ataxia and seizures prior to early postnatal death[272,320,321]. In contrast, IP_3R2 and IP_3R3 are commonly co-expressed in the periphery such as in secretory cells of the digestive system and exocrine system, though they can also be expressed in isolation, for example, IP_3R2 in the sweat glands. As a result, IP_3R2 or IP_3R3 single knock-out mice develop subtle phenotypes[186,249]. However, IP_3R2 and IP_3R3 compound knockout mice exhibit severe salivary and pancreatic insufficiencies resulting in death shortly after weaning due to the inability to assimilate macronutrients from dry food[249].

Mutations in all three IP_3R isoforms, located in all the major functional domains, are associated with several human diseases[220,221]. The majority of the mutations described thus far, are found in the IP_3R1 isoform and mainly impact nervous system function consistent with the IP_3R1 null mouse models[185,192,326–335,222,336–344,269–271,322–325]. In contrast, fewer mutations have been identified in the IP_3R2 and IP_3R3 isoforms and are associated with diseases including Sézary Syndrome, familial isolated primary hyperparathyroidism (FIHP)[191], anhidrosis[186], head and neck squamous cell carcinoma[193], neuropathy[188,189,224,345], and immunopathy[345]. Since most reports present case studies, the functional consequences of particular mutations on the overall structure and function of the receptors remain poorly understood. Of those published, most previous studies indicate mutations in IP_3Rs are associated with either diminished or complete loss of channel activity[221,345,346], while a few mutations are associated with increased channel activity[347,348].

Recently, there has been an increase in the number of IP_3R3 missense mutations reported (**Fig. 5.1**). Most of these mutations are in the regulatory and coupling domain and associated with peripheral neuropathies[188,189,224,345]. Two studies investigated the functional consequences of these mutations on Ca^{2+} signalling in patient-derived cells; however, the consequences of these mutations on IP_3R3 function were difficult to discern likely due to a contribution and compensation from endogenous wild-type IP_3R1 and IP_3R2 isoforms present in these cells[224,345]. To unambiguously probe any alteration in human IP_3R3

function, in this study we generated individual stable cell lines expressing human IP_3R3 (hIP_3R3) V615M, T1424M, R2524C mutations associated with neuropathy in a HEK-3KO background. This cell line was previously generated in the Yule laboratory by CRISPR-Cas technology to lack all the three native IP_3Rs[89]. Interestingly, the hR V615M, T1424M, and R2524C stable cell lines all exhibited elevated basal intracellular Ca^{2+} concentration ($[Ca^{2+}]_{cyt}$), reduced ER Ca^{2+} content and constitutive SOCE activation under basal conditions. These data are consistent with a "leaky" channel phenotype. However, all three mutations exhibited drastically different Ca^{2+} release profiles in response to agonist stimulation. The V615M was poorly functional, R2524C was non-functional, and T1424M exhibited increased function at low agonist concentrations. Overall, we report the functional consequences of three neuropathy-associated IP_3R3 mutations including the first reports of IP_3R disease-associated mutations that result in leaky channels.

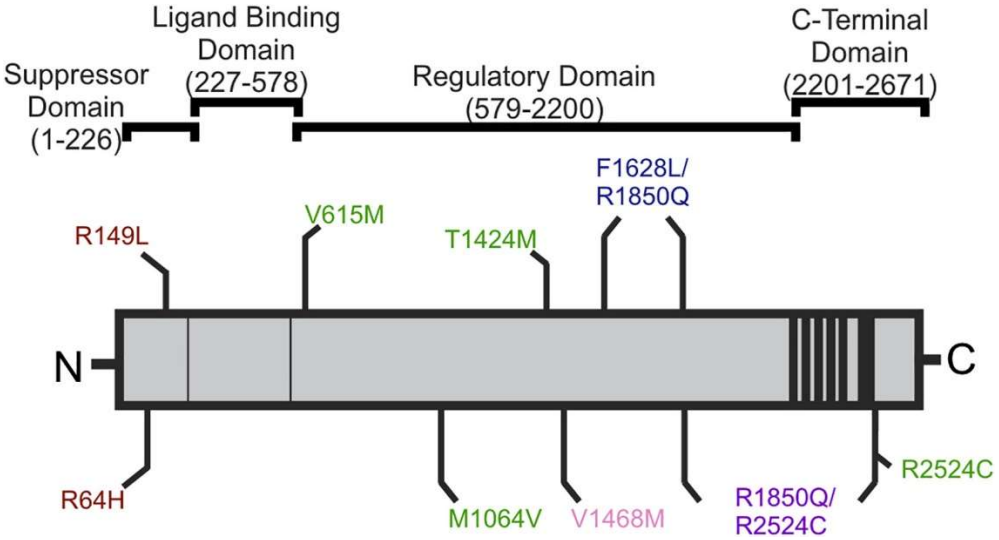

Figure 5.1: Linear-schematic of disease-associated mutations in the four main functional domains of the IP_3R3. Disease-associated mutations in IP_3R3 have been identified in the suppressor domain, regulatory and coupling domain, and C-terminal channel domain. These diseases include head and neck squamous cell carcinoma (red), neuropathy (green), immunopathy (blue), and immunopathy and neuropathy (purple). One family with mutations in IP_3R3 exhibited multiple diseases including chronic fatigue syndrome, small fibre neuropathy, and IgG3 deficiency (pink).

5.3 Materials and Methods

Cell culture

All cell lines used were derived from female, human embryonic kidney epithelial cells (HEK293) originally obtained from ATCC and their identity was authenticated by genomic sequencing prior to gene editing. HEK-3KO cells, HEK293 cells engineered through CRISPR/Cas9 gene editing for the deletion of the three endogenous IP_3R isoforms[345,349] and HEK293 cells modified by CRISPR/Cas9 to only express endogenous hIP_3R3 (Endo. hR3) were used in this study. Gene editing was confirmed by genomic sequencing[89]. The cells were grown at 37 °C with 5% CO_2 in Dulbecco's Modified Eagle

Medium (DMEM) supplemented with 10% foetal bovine serum, 100 U/mL penicillin, 100 µg/mL streptomycin (Gibco/Life Technologies). HEK-3KO cells stably expressing mutant IP_3R3 (hR3 V615M, hR3 T1424M, and hR3 R2524C) were grown at 37 °C with 5% CO_2 in DMEM supplemented with 10% foetal bovine serum, 100 U/mL penicillin, 100 µg/mL streptomycin, and 1.5–2 mg/mL Geneticin sulphate (G418; Gibco/Life Technologies).

Generation of IP_3R mutants

A two-step QuikChange mutagenesis protocol was used to introduce amino acid substitutions into cDNA encoding the human IP_3R3 (hIP_3R3; NM_002224.4) in pcDNA3.1. Mutagenesis and all DNA modifications were carried out using Pfu Ultra II Hotstart 2X Master Mix (Agilent). Mutagenesis primers for hIP_3R3 T1424M forward (CTGCTACGTAGACATGGAGGTGGAGATG), hIP_3R3 T1424M reverse (CATCTCCACCTCCATGTCTACGTAGCAG) were synthesized by Integrated DNA Technologies (IDT). In addition to encoding the specified mutations, primers also silently introduced a restriction site for verification purposes. The coding regions for all constructs were confirmed by sequencing. hIP_3R3 V615M and hIP_3R3 R2524C mutant cDNAs were obtained from Julika Neumann (KU Leuven).

Generation of stable HEK cell lines

Transfection of HEK-3KO cells to exogenously express desired hIP_3R3 WT or mutant constructs stably was performed as previously described[345,349]. In brief, 5 million cells were pelleted, washed once with Phosphate Buffered Saline (PBS), and resuspended in a transfection reagent (362.88 mM ATP-disodium salt, 590.26 mM $MgCl_2*6H_2O$, 146.97 mM KH_2PO_4, 23.81 mM $NaHCO_3$, and 3.7 mM glucose at pH 7.4). 4-6 µg of DNA was mixed with the resuspended cells and electroporated using the Amaxa cell nucleofector (Lonza Laboratories) program Q-001. Cells were allowed to recover for 48 h before passage into new 10 cm plates containing DMEM media supplemented with 1.5–2 mg/mL G418. Following 7 days of selection, cell colonies were picked and transferred to 24-well plates containing DMEM media supplemented with 1.5–2 mg/mL G418. Wells that exhibited growth were expanded and those expressing the desired constructs were confirmed by western blotting.

Cell lysis and SDS-PAGE analyses

HEK-3KO cells, Endo. hR3 cells, and HEK-3KO cells stably expressing IP_3R constructs were harvested by centrifugation (200 ×g for 5 min), washed once with PBS, and solubilized in membrane-bound extraction lysis buffer containing 10 mM Tris-HCl, 10 mM NaCl, 1 mM EGTA, 1 mM EDTA, 1 mM NaF, 20 mM $Na_4P_2O_7$, 2 mM Na_3 VO4, 1% Triton X-100 (v/v), 0.5% sodium deoxycholate (w/v), and 10% glycerol supplemented with a cocktail of protease inhibitors (Pierce). Lysates were incubated for a minimum of 30 min on ice and cleared by centrifugation (16,000 ×g for 10 min) at 4 °C. Protein concentrations in cleared lysates were determined using Dc protein assay kit (Bio-Rad) and 4x SDS gel loading buffer was subsequently added to 5 µg of lysate. Proteins were resolved using 8% SDS-PAGE

and transferred to a nitrocellulose membrane (Pall Corporation). Membranes were probed with a mouse monoclonal antibody against IP_3R3 (R3; #610313, BD Transduction) at a 1:1000 dilution and GAPDH (AM4300, Invitrogen) at a 1:75,000 dilution, followed by the goat anti-mouse Dylight™ 800CW secondary antibodies at a 1:10,000 dilution (SA535521; Invitrogen). Membranes were imaged with an Odyssey infrared imaging system (LICOR Biosciences).

Immunocytochemistry and confocal microscopy

HEK-3KO cells stably expressing WT and mutant IP_3R3 constructs were plated on poly-D-lysine coated coverslips. At roughly 50% confluency cells were fixed using 4% PFA at room temperature for 10 min. Subsequently, coverslips were washed with PBS, and cells were blocked in 10% Bovine Serum Albumin (BSA) for 1 h. Following blocking, cells were incubated in primary antibody against IP_3R3 (BD Transduction) overnight at 4 °C. The following day, the primary antibody was removed, and coverslips were washed 3 times with PBS for 10 min with gentle rocking. Subsequently, the anti-mouse secondary antibody conjugated to Alexa Fluor 488 (Invitrogen) was incubated for 1 h at room temperature with gentle rocking. After incubation, coverslips were washed with PBS and mounted on slides. After allowing slides to dry, coverslips were sealed onto slides and imaged using confocal microscopy using an Olympus Fluoview 1000 microscope.

Single-cell Ca^{2+} imaging

Single-cell Ca^{2+} imaging was performed in intact cells as described previously[345,349]. Glass coverslips were plated with HEK-3KO, Endo. hR3, Exo. hR3, or HEK-3KO cells stably expressing IP_3R mutant constructs at least 18 h prior to imaging experiments. Subsequently, the glass coverslips were mounted onto a Warner chamber and the cells were loaded with 2 μM Fura-2/AM (Invitrogen) in Ca^{2+}-containing imaging buffer (Ca^{2+} IB: 10 mM HEPES, 1.26 mM Ca^{2+}, 137 mM NaCl, 4.7 mM KCl, 5.5 mM glucose, 1 mM Na_2HPO_4, 0.56 mM $MgCl_2$, at pH 7.4) at room temperature for 25 min. Following loading, cells were perfused with Ca^{2+} IB which provided a basal 340/380 ratio of the [Ca^{2+}]. To obtain measurements of agonist-induced Ca^{2+} release into the cytoplasm cells were stimulated with 0.3–100 μM Carbachol (CCh). To interrogate the leakiness of the expressed IP_3R, perfusion was switched from Ca^{2+} IB to Ca^{2+}-free imaging buffer (Ca^{2+}-free IB; 10 mM HEPES, 137 mM NaCl, 4.7 mM KCl, 5.5 mM glucose, 1 mM Na_2HPO_4, 0.56 mM $MgCl_2$, 1 mM EGTA at pH 7.4) and in the absence of extracellular Ca^{2+}, cells were treated with 30 μM cyclopiazonic acid (CPA; TOCRIS) to measure ER Ca^{2+} content. Finally, 10 μM GSK-7975a (Sigma Aldrich) was used to probe the contribution of ORAI to cytosolic [Ca^{2+}].

Ca^{2+} imaging was performed using an inverted epifluorescence Nikon microscope with a 40x oil immersion objective. Cells were alternately excited at 340 and 380 nm, and emission was monitored at 505 nm. Images were captured every second with an exposure of 15 ms and 4 × 4 binning using a digital camera driven by TILL Photonics software. Image acquisition was performed using TILLvisION software and data was exported to Microsoft Excel where means were calculated.

Population-based Ca^{2+} imaging

Population-based fluorescence imaging was carried out using a FlexStation3 (Molecular Devices), a high-throughput benchtop optical system utilizing micro-fluidics. HEK-3KO cells or HEK-3KO cells stably expressing IP_3R constructs were loaded with 4 μM Fura-2/AM in complete DMEM media. After 1 h, cells were harvested and subsequently washed, resuspended in Ca^{2+} IB, counted, and dispensed into a black-walled flat-bottom 96-well plate (~300,000 cells/well). The plate was centrifuged (200 ×g for 2 min) and placed at 37 °C for 30 min prior to commencing the assay. Ca^{2+} IB and varying concentrations of CCh (0.1–100 μM CCh) were added to induce Ca^{2+} release through the IP_3R. Excitation of cells loaded with Fura-2/AM alternated between 340 and 380 nm and emission was measured at 510 nm. The total experiment time was set for 200 s, with readings taken every 4 s (~51 readings/run). Data from SoftMax© Pro Microplate Data Acquisition and Analysis software was exported to Microsoft Excel where appropriate ratios, normalizations, and means were calculated.

Detection of Ca^{2+} puffs using TIRF microscopy

HEK-3KO cells exogenously expressing WT or mutant hIP_3R3 were cultured on 15-mm glass coverslips coated with poly-D-lysine (100 μg/mL) in a 35-mm dish for 36 h. Prior to imaging, the cells were washed three times with imaging buffer. The cells were subsequently incubated with Cal520-AM (5 μM; AAT Bioquest #21130) and ci-IP_3/PM (0.1 or 1 μM, Tocris #6210) in imaging buffer with 0.01% BSA in the dark at RT. After 1 h incubation, the cells were washed three times with imaging buffer and incubated in imaging buffer containing EGTA-AM (5 μM, Invitrogen #E1219). After 45 min incubation, the media was replaced with fresh imaging buffer and incubated for additional 30 min at room temperature to allow for de-esterification of loaded reagents. Following loading, the coverslip was mounted in a chamber and imaged using an Olympus IX81 inverted Total Internal Reflection Fluorescence Microscope (TIRFM) equipped with oil-immersion PLAPO TIRFM 60x objective lens/1.45 numerical aperture. Olympus CellSens Dimensions 2.3 (Build 189,987) software was used for imaging. The cells were illuminated using a 488 nm laser to excite Cal-520 and the emitted fluorescence was collected through a band-pass filter by a Hamamatsu ORCA-Fusion CMOS camera. The angle of the excitation beam was adjusted to achieve TIRF with a penetration depth of ~140 nm. Images were captured from equal areas using a 4 X 4 or 2 X 2 pixel binning (433.333 or 216 nm/pixel) at a rate of ~166 or ~50 frames/second by directly streaming into RAM. To photo-release IP_3, UV light from a laser was introduced to uniformly illuminate the field of view. Both the intensity of the UV flash and the duration (1 s) for uncaging IP_3 were optimized to prevent spontaneous puffs in the absence of loaded ci-IP3. Images were exported as vsi files.

Quantification of SDS-PAGE

Membranes were quantified using Image Studio Lite (LICOR Biosciences), while the mean of at least 3 experiments (n=3) and SEM were calculated using GraphPad Prism (GraphPad).

Analysis of single-cell Ca^{2+} imaging

In Microsoft Excel mean basal [Ca^{2+}], change in 340/380 amplitude, and percentage of responding cells for each experiment (multiple cells) was calculated. Area under the curve (AUC) was calculated using GraphPad Prism as increases above baseline that are greater than 10% of the distance from the minimum to the maximum Y using the 20 data points prior to agonist addition as the baseline. The mean and SEM of at least n=3 experiments for each cell line was calculated in GraphPad Prism and statistical analysis was performed using one-way ANOVA with Tukey's test.

Analysis of population-based Ca^{2+} imaging

In Microsoft Excel, peak amplitude of CCh-induced Ca^{2+} release was calculated by normalizing the 340/380 ratio to the average of the first 5 340/380 ratio data points. Area under the curve (AUC) was calculated using GraphPad Prism as increases above baseline that are greater than 10% of the distance from the minimum to the maximum Y using the five data points prior to agonist addition as the baseline. Means and SEM from at least 3 individual plates and nonlinear curve fits were calculated in GraphPad Prism. Statistical analysis was performed in GraphPad Prism using one-way ANOVA with Tukey's test.

Analysis of Ca^{2+} puffs using TIRF microscopy

Images, 5 s prior and 30–60 s after flash photolysis of ci-IP_3, were captured, as described previously[350,351]. The vsi files were converted to tiff files using Fiji[233] and further processed using FLIKA, a Python programming-based tool for image processing[352]. From each recording, ~100 frames (~2 s) before photolysis of ci-IP_3 were averaged to obtain a ratio image stack (F/F_0) and standard deviation for each pixel for recording up to 30 s following photolysis. The image stack was Gaussian-filtered, and pixels that exceeded a critical value (1.0 for our analysis) were located. The 'Detect-puffs' plug-in was utilized to detect the number of clusters (puff sites), number of events (number of puffs), amplitudes and durations of localized Ca^{2+} signals from individual cells. All the puffs identified automatically by the algorithm were manually confirmed before analysis. The results from FLIKA were saved to Microsoft Excel and graphs were plotted using GraphPad Prism 8 where the mean and SEM were calculated for at least 3 individual experiments. Statistical analysis was performed in GraphPad Prism using a two tailed t-test.

5.4 Results

While the functional effects of disease-associated mutations in IP_3R1 and IP_3R2 have been previously investigated[185,186,345,346], little work has been done to characterize mutations in the IP_3R3 isoform. Several novel mutations in IP_3R3 (**Fig. 5.1**) have been identified in the past decade with most associated with hereditary motor and sensory neuropathies (HMSN) such as Charcot-Marie-Tooth (CMT), which is characterized by progressive distal motor and sensory impairments (**Supplementary Table**

5.1)[188,189,224,345,353]. In this study, we characterized the functional consequences of three mutations in hIP$_3$R3 located at different locations within the regulatory and coupling domain or channel domain, in order to gain mechanistic insight into how these mutations alter channel function and ultimately contribute to the disease phenotype.

5.4.1 The V615M mutation results in a poorly functional and "leaky" channel

Valine 615 is located in the regulatory and coupling domain of the IP$_3$R3 armadillo repeat domain (ARM) 1 (**Fig. 5.2A**), distal to the LBD[310,354]. The hydrophobic/non-polar Val615 residue is replaced by a larger, hydrophobic/non-polar, sulphur-containing Met (V615M). Individuals from three generations of a Finnish family express this variant on a single IP$_3$R3 allele (**Supplementary Table 5.1**). The patients were diagnosed with demyelinating neuropathy (CMT) inherited in an autosomal dominant manner, and presented with progressive muscle weakness, wasting in the legs and sometimes hands, as well as intermediately reduced nerve conduction values (NCV)[224]. The Val615 residue is not conserved among hIP$_3$R isoforms, but is evolutionarily well conserved between IP$_3$R3 in different species (**Supplementary Fig. 5.1A**). We mutated the codon encoding the Val615 residue in hIP$_3$R3 cDNA to Met and expressed the variant in isolation in HEK-3KO cells (hR3 V615M) (**Fig. 5.2B**)[89]. The hIP$_3$R3 V615M mutation localized properly to the ER membrane (**Supplementary Fig. 5.1B**). Our approach was to generate several stable cell lines expressing hR3 V615M homo-tetramers at varying levels (**Fig. 5.2C**) allowing for comparison of channel function with wild-type (WT) cell lines of a similar expression level. For example, HEK293 IP$_3$R1/2 double knockout cells expressing endogenous levels of IP$_3$R3 were previously generated through CRISPR/Cas9 gene editing to only express endogenous hIP$_3$R3 (Endo. hR3)[355], while high IP$_3$R3 expressing HEK-3KO cells were generated by stably over-expressing hIP$_3$R3 cDNA (Exo. hR3). In Fura2/AM loaded hR3 V615M cells, agonist-induced Ca^{2+} release was utilized as a measurement of channel function. Prior to any agonist addition, all three V615M mutant cell lines exhibited significantly increased basal 340/380 ratios when compared to WT hR3 expressing cells and HEK-3KOs, indicative of elevated basal $[Ca^{2+}]_{cyt}$ (**Fig. 5.2D, E**). The mean basal $[Ca^{2+}]_{cyt}$ corelated with V615M hIP$_3$R3 protein level, such that the lowest expressing hR3 V615M cell line (hR3 V615M #503), with the expression between that of the Endo. hR3 and Exo. hR3, exhibited only a small increase compared to the null and WT cell lines. In contrast, the hR3 V615M #524 cell line, with expression slightly greater than that of the Exo. hR3, and the V615M #506 cell line, with expression several-fold greater than the Exo. hR3 cell line exhibited a much larger increase in basal $[Ca^{2+}]_{cyt}$. In response to stimulation with increasing concentrations of carbachol (CCh), a muscarinic receptor agonist, which results in an increase in intracellular IP$_3$, all three hR3 V615M cell lines exhibited a significant attenuation of the initial Ca^{2+} release (**Fig. 5.2F**) and percentage of responding cells (**Supplementary Fig. 5.1C**) compared to the Endo. hR3 and Exo. hR3 cell lines. Of note, those hR3 V615M cells with larger basal $[Ca^{2+}]_{cyt}$ were those that exhibited decreased function, while the small percentage of

individual hR3 V615M cells with larger changes in Ca^{2+} release were those with lower basal $[Ca^{2+}]_{cyt}$ (**Supplementary Fig. 5.1D**).

In population-based Ca^{2+} imaging assays performed on a FlexStation3 with micro-fluidics, all three hR3 V615M cells lines similarly showed significantly diminished Ca^{2+} release (**Fig. 5.2G**) together with the area under the curve (AUC) (**Supplementary Fig. 5.1E**) in response to increasing [CCh]. Likewise, in Total Internal Reflection Microscopy (TIRFM) experiments, measuring the Ca^{2+} release from small clusters of IP_3R3, the highest expressing hR3 V615M cell line exhibited significantly decreased numbers of Ca^{2+} puff sites (**Fig. 5.2H, I**) and Ca^{2+} puffs per cell (**Fig. 5.2H, J**) as compared to the Exo. hR3 cell line (**Supplementary Video 5.1, 5.2**). These results further support the single-cell Ca^{2+} imaging data showing that the hR3 V615M Ca^{2+} channel is poorly functional.

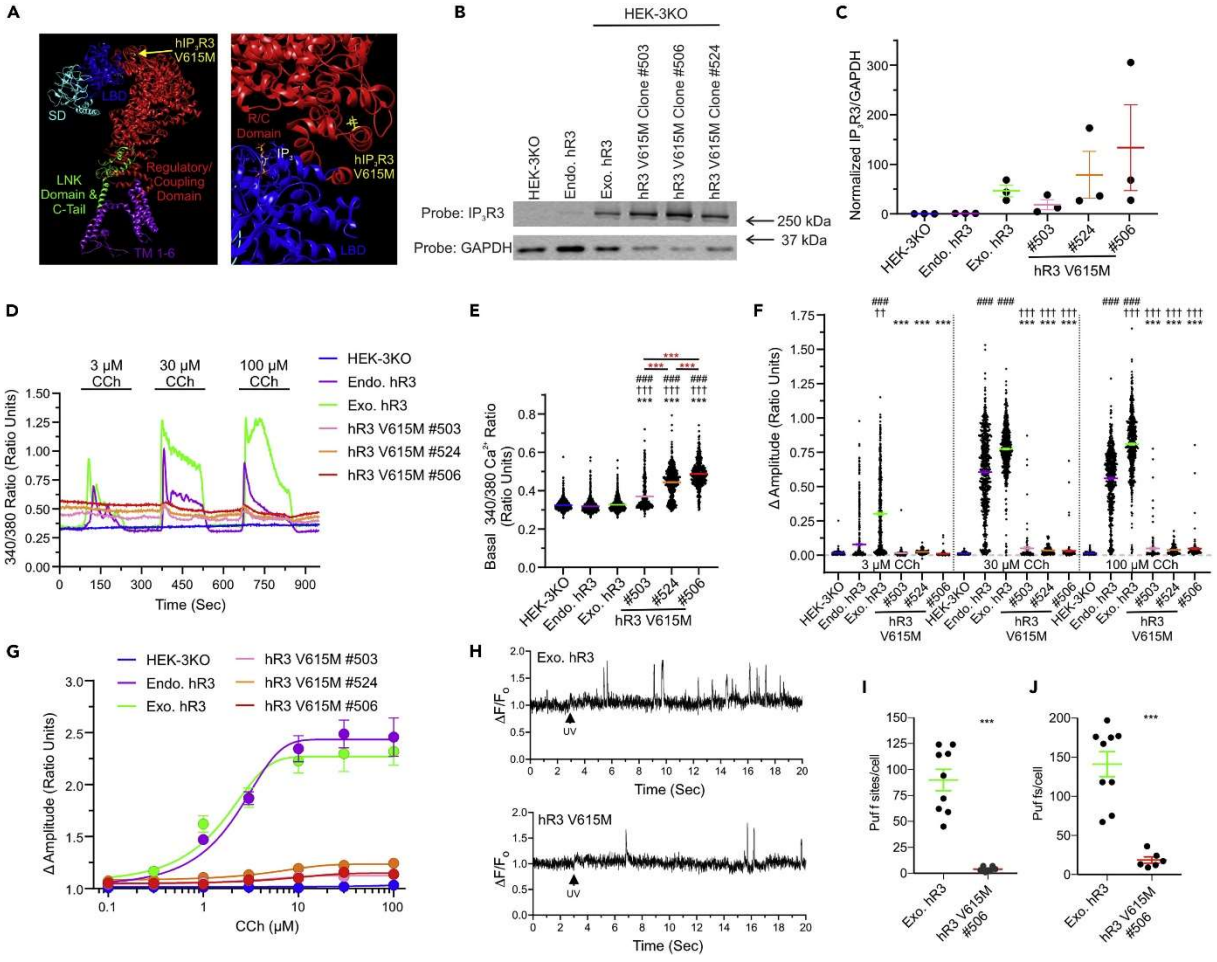

Figure 5.2: hR3 V615M is a poorly functional Ca^{2+} channel with elevated basal cytosolic $[Ca^{2+}]$. (A) Chimera (PDB: 6DR0) was used to visualize Val615 (yellow) in ARM1 of the regulatory and coupling domain (red) of IP_3R3. **(B)** Cell lines with varying expression of human IP_3R3 harbouring the V615M mutation (hR3 V615M) were generated in IP_3R-null HEK-3KO cells and western blotted alongside WT cell lines, either endogenously expressing hIP_3R3 (Endo. hR3) or exogenously expressing hIP_3R3 (Exo. hR3). **(C)** Quantification of expression of hIP_3R3 with respect to GAPDH in HEK-3KO (blue), Endo. hR3 (purple), Exo. hR3 (green), and hR3 V615M (pink, orange, red) cell lines. Coloured lines represent the mean of at least n=3 experiments, and error bars represent SEM. Averages were normalized to that of the Endo. hR3 cell line. **(D)** Representative traces of Ca^{2+} signals in Fura-2/AM loaded cells in response to the addition of indicated concentrations of CCh. **(E)** Scatterplot summarizing the basal Ca^{2+} (average of the initial 20, 340/380 ratio points in Ca^{2+}-containing media) from experiments similar to those in (D). **(F)**

Scatterplot summarizing change in amplitude (Peak 340/380 ratio – Basal 340/380 ratio (E)) of cell lines in response to CCh in single-cell imaging experiments similar to those in (D). **(G)** Dose-response curve showing the change in amplitude of Ca^{2+} signals of Fura-2/AM loaded cell lines when treated with increasing [CCh] using a FlexStation3 96-well plate reader. **(H)** Representative traces of Ca^{2+} puffs recorded by TIRFM in Exo. hR3 or hR3 V615M. Uncaging of ci-IP_3 at the arrowhead. **(I)** Number of Ca^{2+} puff sites per cell in Exo. hR3 (green) and hR3 V615M (red) cell lines loaded with Cal-520 in TIRFM experiments and treated with1 μM ci-IP_3. **(J)** Number of Ca^{2+} puff per cell in Exo. hR3 (green) and hR3 V615M (red) cell lines loaded with Cal-520 in TIRFM microscopy experiments and treated with 1 μM ci-IP_3. All data are mean ± SEM of at least three (n=3) independent experiments. ### p<0.001 when compared to HEK-3KO; ttt p<0.001, tt p<0.01 when compared to Endo. hR3; ∗∗∗ p<0.001 when compared to Exo. hR3; and ∗∗∗(red) p<0.001 when compared to other stably expressed hR3 V615M cell lines; one-way ANOVA with Tukey's test performed in E, F and two-tailed t-test performed in (I and J).

Next, we performed experiments to investigate the mechanism underlying the raised basal $[Ca^{2+}]_{cyt}$ in the V615M hIP_3R3 cells. In contrast to WT hR3 expressing cells or HEK-3KOs, removal of extracellular Ca^{2+} resulted in a significant decrease in basal cytosolic $[Ca^{2+}]_{cyt}$ in the hR3 V615M cell lines (**Fig. 5.3A, B**) to levels similar to the IP_3R null and WT cell lines. A direct correlation was observed between the basal $[Ca^{2+}]_{cyt}$ and the magnitude of change in amplitude seen following the removal of extracellular Ca^{2+} (**Supplementary Fig. 5.2A**). These data indicate that Ca^{2+} influx across the PM contributed to the elevated basal $[Ca^{2+}]_{cyt}$ in hR3 V615M expressing cells. Thus, we hypothesized that the elevated cytosolic Ca^{2+} was derived, at least in part, from Ca^{2+} leaking from the ER store through the mutant channel and subsequently gating SOCE. First, to evaluate the ER Ca^{2+} store content, the SERCA pump was inhibited by exposure to 30 μM cyclopiazonic acid (CPA), in the absence of extracellular Ca^{2+} (**Fig. 5.3A**). Consistent with decreased ER store content, the CPA-induced Ca^{2+} leak in the hR3 V615M cell lines was less (amplitude in **Fig. 5.3A** and **Supplementary Fig. 5.2B** and AUC in **Supplementary Fig. 5.2C**) when compared to the WT hR3 cell lines with similar IP_3R3 expression. Additionally, these changes in amplitude (**Fig. 5.3C**) and AUC (**Supplementary Fig. 5.2D**) were clearly correlated with the basal $[Ca^{2+}]_{cyt}$, as individual cells with elevated basal 340/380 ratios exhibited smaller changes in amplitude and AUC. Overall, these data suggest that the elevated basal $[Ca^{2+}]_{cyt}$ in hR3 V615M expressing cells results from ER Ca^{2+} leak and subsequent Ca^{2+} influx across the PM.

Depletion of the ER Ca^{2+} store triggers SOCE through the interaction of STIM and ORAI proteins[356]. To investigate the contribution of Ca^{2+} influx via ORAI-based channels to the elevated $[Ca^{2+}]_{cyt}$ in the hR3 V615M mutants, we utilized the ORAI inhibitor GSK-7975a[357]. In HEK293 cells, GSK-7975a inhibited 67.4% of CCh-induced Ca^{2+} influx (**Supplementary Fig. 5.3A, B**) and 50.8% of CPA-induced Ca^{2+} influx (**Supplementary Fig. 5.3C, D**). The addition of GSK-7975a resulted in a significant decrease in the basal $[Ca^{2+}]_{cyt}$ in the hR3 V615M cell lines, which was not observed in the WT hR3 and HEK-3KO cell lines (**Fig. 5.3D, E** and **Supplementary Fig. 5.3E**). The more elevated basal $[Ca^{2+}]_{cyt}$ levels correlated with a greater effect of GSK-7975a to reduce the elevated basal $[Ca^{2+}]_{cyt}$ levels (**Fig. 5.3F**). In total, these results suggest that the mutation of V615M in hIP_3R3 results in a poorly functional, "leaky" channel. Ca^{2+} leak through the mutant channel leads to the partial depletion of ER Ca^{2+} stores thereby activating SOCE via ORAI-based channels.

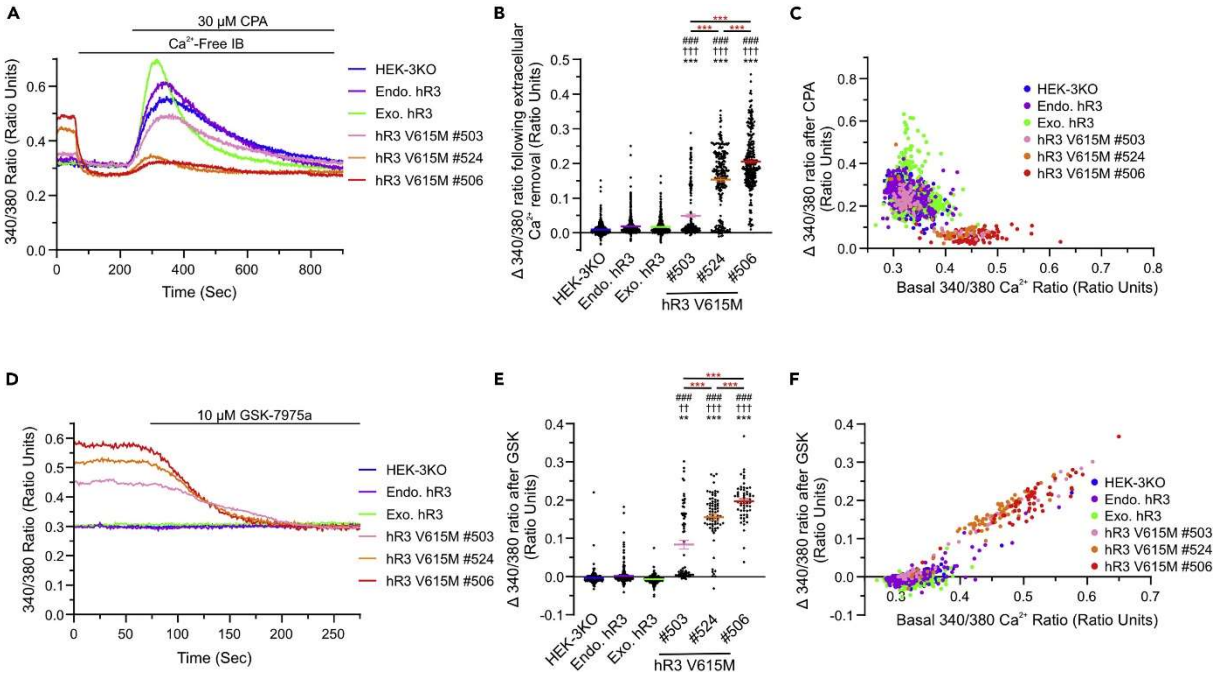

Figure 5.3: hR$_3$ V615M cell lines exhibited depleted ER [Ca^{2+}] and SOCE in the absence of agonist stimulation. (A) Representative traces of changes in cytosolic [Ca^{2+}] following removal of extracellular Ca^{2+} in HEK-3KO (blue), Endo. hR3 (purple), Exo. hR3 (green), and hR3 V615M (pink, orange, red) cell lines loaded with Fura-2/AM. Cells were subsequently treated with 30 μM CPA allowing the measurement of the ER Ca^{2+} store content. **(B)** Scatterplot summarizing the change in the basal 340/380 ratio following removal of extracellular Ca^{2+} in experiments similar to those in (A). Coloured lines represent the mean of at least n=3 experiments, and error bars represent SEM. **(C)** Scatterplot summarizing the correlation between an elevated basal 340/380 Ca^{2+} ratio (Fig. 5.2E) and the change in 340/380 ratio following treatment with 30 μM CPA (maximum CPA-induced amplitude – basal 340/380 ratio following removal of extracellular Ca^{2+}) in experiments similar to those in (A). **(D)** Representative traces of Ca^{2+} signals in Fura-2/AM loaded cells in response to the addition of 10 μM GSK-7975a. **(E)** Scatterplot summarizing the change in 340/380 ratio following the addition of GSK-7975a (average of 20, 340/380 ratio points prior to GSK-7975a addition – average of 20, 340/380 ratio points following 200 s of GSK-7975a addition) from experiments similar to those in (D). **(F)** Scatterplot summarizing the correlation between an elevated basal 340/380 Ca^{2+} ratio (Fig. 5.2E) and the change in 340/380 ratio following treatment with 10 μM GSK-7975a (E) in experiments similar to those in (D). All data are mean ± SEM of at least three (n=3) independent experiments. ### p<0.001 when compared to HEK-3KO; ttt p<0.001, tt p<0.01 when compared to Endo. hR3; ∗∗∗ p<0.001, ∗∗ p<0.01 when compared to Exo. hR3; and ∗∗∗(red) p<0.001 when compared to other stably expressed hR3 V615M cell lines; one-way ANOVA with Tukey's test performed in (B and E).

5.4.2 The T1424M mutation results in a "leaky" channel that is functional

The T1424M variant was identified as one of the two potential candidate gene mutations in a mother and her two daughters diagnosed with late-onset lower limb muscle weakness and sensory loss (**Supplementary Table 5.1**, Phenotypes of relevant IP$_3$R3 mutations associated with neuropathy, related to Fig. 5.1)[188]. In these subjects, the hydrophilic/polar Thr1424 harbouring a hydroxyl group is exchanged for a larger, hydrophobic/non-polar Met (T1424M) containing a sulphur group. Again, this mutation is present only on one *ITPR3* allele and thus the effect of the mutation appears to be dominantly inherited. The T1424M mutant is located within the regulatory and coupling domain of IP$_3$R3 in the

ARM2 domain (**Fig. 5.4A**). The T1424 residue is conserved both among all human IP_3R isoforms, as well as across multiple species in hIP_3R3 (**Supplementary Fig. 5.4A**). Multiple cell lines stably expressing hR3 T1424M in HEK-3KO were generated, with the hR3 T1424M #203 cell line expressing a low level of the IP_3R3 similar to that of the Endo. hR3, while the hR3 T1424M #209 and #204 cell lines expressed intermediate amounts of IP_3R3 between that of the Endo. hR3 and Exo. hR3 (**Fig. 5.4B, C**). Homo-tetramers of hR3 T1424M were properly localized to the ER membrane (**Supplementary Fig. 5.4B**).

While the low IP_3R3 expressing hR3 T1424M line (#203) did not exhibit an increased basal $[Ca^{2+}]_{cyt}$ (**Fig. 5.4D, E**), the intermediate level expressing hR3 T1424M (#209) and hR3 T1424M (#204) cell lines both exhibited significantly increased basal $[Ca^{2+}]_{cyt}$ (**Fig. 5.4D, E**). Ca^{2+} release in the low expressing hR3 T1424M cell line was refractory in response to any tested [CCh]. In contrast, the Endo. hR3 cell line, with the most similar expressions exhibited robust responses to [CCh] greater than 3 μM (**Fig. 5.4F** and **Supplementary Fig. 5.4C**). Notably, the higher expressing hR3 T1424M cell lines, both exhibited significantly higher Ca^{2+} release and number of responding cells following stimulation with lower [CCh] (**Fig. 5.4F** and **Supplementary Fig. 5.4C**). Once again, individual hR3 T1424M cells with elevated basal $[Ca^{2+}]_{cyt}$ exhibited smaller changes in CCh-induced Ca^{2+} release than cells with more normal basal $[Ca^{2+}]_{cyt}$ (**Supplementary Fig. 5.4D**). Remarkably, despite only intermediate levels of IP_3R3 expression in the hR3 T1424M #209 and #204 cell lines the amplitude of Ca^{2+} release was greater in these lines than the WT hR3 cell lines at lower [CCh] indicating that the mutant channel is perhaps in a pre-activated confirmation (**Fig. 5.4F**). Nevertheless, at higher [CCh] greater Ca^{2+} release was observed in the WT hR3 lines reinforcing the importance of this conserved residue for proper gating of the channel. In population-based FlexStation3 assays, the functionality of the higher expressing hR3 T1424M cell lines was confirmed and exhibited a shift in sensitivity at lower [CCh] (**Fig. 5.4G** and **Supplementary Fig. 5.4E**).

Notably, in TIRFM imaging experiments, spontaneous Ca^{2+} puffs were readily evident in the hR3 T1424M #204 cell line but were uncommon in Exo. hR3 expressing cells (**Fig. 5.4H**) indicating that the mutant channel is active, even under basal conditions in absence of agonist stimulation (**Fig. 5.4I, Supplementary Videos 5.3, 5.4**). Additionally, upon stimulation through the uncaging of ci-IP_3, the number of Ca^{2+} puffs and Ca^{2+} puff sites per cell (**Fig. 5.4J**) were significantly higher in the hR3 T1424M #204 cell line as compared to the Exo. hR3 cell line and signals tended to globalize in the hR3 T1424M expressing cells (**Supplementary Videos 5.5, 5.6**).

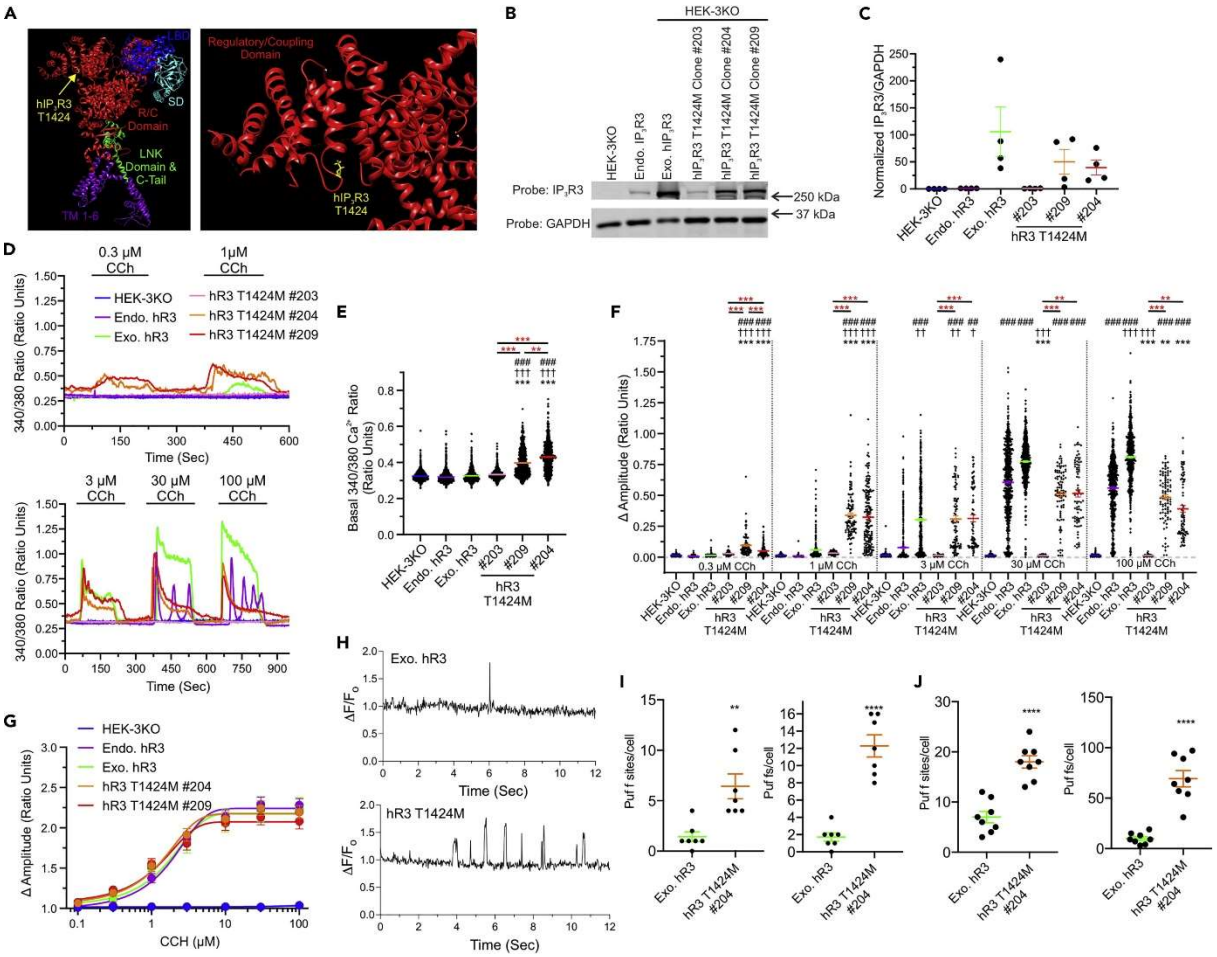

Figure 5.4: hR3 T1424M increased Ca^{2+} channel function with elevated basal cytosolic [Ca^{2+}]. (A) Chimera (PDB: 6DR0) was used to visualize Thr1424 (yellow) in the regulatory and coupling domain (red) of IP_3R3. **(B)** Cell lines containing varying expression of human IP_3R3 harbouring the T1424M mutation (hR3 T1424M) were generated in IP_3R-null HEK-3KO cells and western blotted alongside WT cell lines Endo. hR3 and Exo. hR3. **(C)** Quantification of hIP_3R expression with respect to GAPDH of HEK-3KO (blue), Endo. hR3 (purple), Exo. hR3 (green), and hR3 T1424M (pink, orange, red) cell lines. Coloured lines represent the mean of at least n=3 experiments, and error bars represent SEM. Averages were normalized to that of the Endo. hR3 cell line. **(D)** Representative traces of Ca^{2+} signals in cells expressing the indicated variant in response to the addition of increasing [CCh]. **(E)** Scatterplot summarizing the basal Ca^{2+} (average of the initial 20, 340/380 ratio points in Ca^{2+}-containing media) from experiments similar to those in (D). **(F)** Scatterplot summarizing change in amplitude (Peak 340/380 ratio – Basal 340/380 ratio (E)) of cell lines in response to increasing [CCh] in single-cell imaging experiments similar to those in (D). **(G)** Dose-response curve showing the change in amplitude of Ca^{2+} signals when treated with increasing [CCh] using a FlexStation3 96-well plate reader. **(H)** Representative traces of Ca^{2+} puffs in the absence of stimulation in Exo. hR3 and hR3 T1424M expressing cells. **(I)** Number of Ca^{2+} puff sites and Ca^{2+} puffs per cell in Exo. hR3 (green) and hR3 T1424M #204 (red) cell lines loaded with Cal-520 in TIRFM microscopy experiments without photo release of ci-IP_3. **(J)** Number of Ca^{2+} puff sites and Ca^{2+} puffs per cell in Exo. hR3 (green) and hR3 T1424M (red) cell lines loaded with Cal-520 in TIRFM microscopy experiments following photo-release of 0.1 µM ci-IP_3. All data are mean ± SEM of at least three (n=3) independent experiments. Control HEK-3KO (blue), Endo. hR3 (purple), and Exo. hR3 (green) data in E, F repeated from Figure 5.2 above. ### p<0.001, ## p<0.01 when compared to HEK-3KO; ttt p<0.001, tt p<0.01, t p<0.05 when compared to Endo. hR3; ∗∗∗ p<0.001 when compared to Exo. hR3; and ∗∗∗(red) p<0.001, ∗∗(red) p<0.01 when compared to other stably expressed hR3 T1424M cell lines; one-way ANOVA with Tukey's test performed in (E and F) and two-tailed t-test performed in (I and J).

Despite differences in functionality, the elevated basal $[Ca^{2+}]_{cyt}$ of the higher expressing hR3 T1424M cell lines again suggests that the T1424M mutation results in a leaky IP_3R3 similar to the V615M mutation. In the higher expressing hR3 T1424M cells, removal of extracellular Ca^{2+} resulted in a significantly larger reduction in $[Ca^{2+}]_{cyt}$ than in the HEK-3KO and WT hR3 cell lines (**Fig. 5.5A, B**). Similarly, the magnitude of the elevated basal $[Ca^{2+}]_{cyt}$ of individual hR3 T1424M mutant cells correlated with larger changes in the $[Ca^{2+}]_{cyt}$ following the removal of extracellular Ca^{2+} (**Supplementary Fig. 5.5A**). SERCA pump inhibition resulted in a significantly smaller Ca^{2+} leak from the ER Ca^{2+} store in the hR3 T1424M mutant cell lines with elevated basal $[Ca^{2+}]_{cyt}$ levels (**Fig. 5.5A** and **Supplementary Fig. 5.5B, C**) and the degree of inhibition was again correlated with the magnitude of the elevated basal $[Ca^{2+}]$ in individual cells (**Fig. 5.5C** and **Supplementary Fig. 5.5D**). Similar to V615M expressing cell lines, the ORAI inhibitor GSK-7975a effectively decreased the elevated basal $[Ca^{2+}]_{cyt}$ (**Fig. 5.5D-F** and **Supplementary Fig. 5.5E**) of the higher expressing hR3 T1424M mutant cell lines. Overall, these data demonstrate that expression of hR3 T1424M at levels greater than that of Endo. hR3 led to a leaky channel that results in the inappropriate activation of SOCE in the absence of stimulation similar to the hR3 V615M mutation. However, unlike the V615M mutation, which resulted in poorly functional IP_3R3 channels, the T1424M mutation, when over-expressed, leads to a variant with increased channel function at threshold levels of stimulation when compared to WT hIP_3R3 lines with comparable expression.

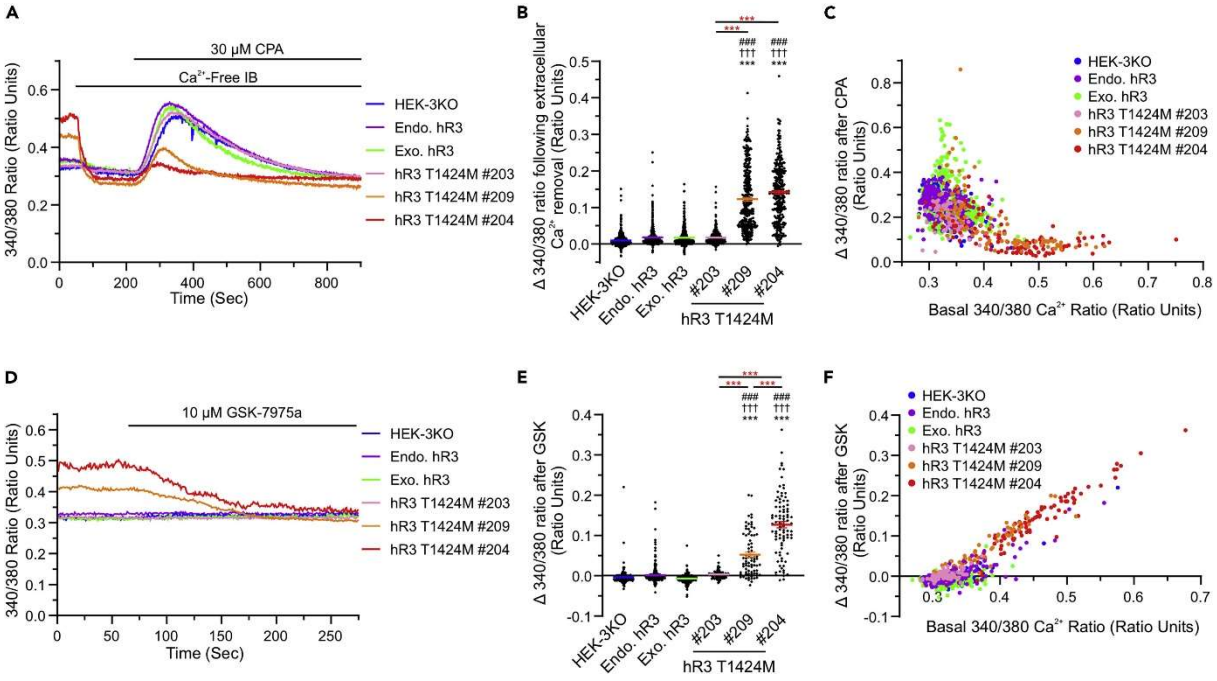

Figure 5.5: hR3 T1424M cell lines exhibited depleted ER $[Ca^{2+}]$ and SOCE in the absence of agonist stimulation. (A) Representative traces of changes in cytosolic $[Ca^{2+}]$ following removal of extracellular Ca^{2+} in HEK-3KO (blue), Endo. hR3 (purple), Exo. hR3 (green), and hR3 T1424M (pink, orange, red) cell lines. Cells were subsequently treated with 30 μM CPA allowing the measurement of the ER Ca^{2+} store content. **(B)** Scatterplot summarizing the change in the basal 340/380 ratio following removal of extracellular Ca^{2+} in experiments similar to those in (A). Coloured lines represent the mean of at least n=3 experiments, and error bars represent SEM. **(C)** Scatterplot summarizing the correlation between an elevated basal 340/380 Ca^{2+} ratio (Figure 5.4E) and the change

in 340/380 ratio following treatment with 30 μM CPA (maximum CPA-induced amplitude – basal 340/380 ratio following removal of extracellular Ca^{2+}) in experiments similar to those in (A). **(D)** Representative traces of Ca^{2+} signals in response to the addition of 10 μM GSK-7975a when loaded with Fura-2/AM. **(E)** Scatterplot summarizing the change in 340/380 ratio following the addition of GSK-7975a (average of 20, 340/380 ratio points prior to GSK-7975a addition – average of 20, 340/380 ratio points following 200 s of GSK-7975a addition) from experiments similar to those in (D). **(F)** Scatterplot summarizing the correlation between an elevated basal 340/380 Ca^{2+} ratio (Fig. 5.4E) and the change in 340/380 ratio following treatment with 10 μM GSK-7975a (E) in experiments similar to those in (D). All data are mean ± SEM of at least three (n=3) independent experiments. Control HEK-3KO (blue), Endo. hR3 (purple), and Exo. hR3 (green) data in (B, C, E, and F) repeated from Fig. 5.3 above. ### p<0.001 when compared to HEK-3KO; ttt p<0.001 when compared to Endo. hR3; ∗∗∗ p<0.001 when compared to Exo. hR3; and ∗∗∗(red) p<0.001 when compared to other stably expressed hR3 T1424M cell lines; one-way ANOVA with Tukey's test performed in (B and E).

5.4.3 The R2524C mutation forms a functionally dead but leaky channel

The R2524 residue is located in the channel domain at the junction of the 6th transmembrane (TM) and the linker (LNK) domain (**Fig. 5.6A**) and is highly conserved in hIP_3R subtypes and across different species (**Supplementary Fig. 5.6A**). The R2524C mutation was reported as a *de novo* mutation in two unrelated individuals (**Supplementary Table 5.1**, Phenotypes of relevant IP_3R3 mutations associated with neuropathy, related to Fig. 5.1). One individual, harbouring solely the R2524C mutant on one *ITPR3* allele, exhibited a phenotype associated with neuropathy[224]. The second individual, who also expressed an additional mutation (R1850Q) on their second *ITPR3* allele, also presented with immunopathy symptoms resulting in a diagnosis of severe combined immunodeficiency disease (**Supplementary Table 5.1**)[345]. In these individuals, the positively charged Arg2524 residue is mutated to an uncharged, smaller Cys with a reactive thiol (-SH) group. The R1850Q mutation is present in 5% of the population as a polymorphism and when present alone in a parent of this individual did not result in an obvious phenotype and was previously characterized as poorly functional when expressed at endogenous levels[345]. We therefore mutated the Arg2524 residue to Cys in WT hIP_3R3 (hR3 R2524C) and stably expressed the mutant in IP_3R-null HEK-3KO cells. As before, we generated several stable cell lines of hR3 R2524C homo-tetramers with varying expression levels (**Fig. 5.6B**). The hR3 R2524C mutant was expressed at similar levels to Endo. hR3 in the hR3 R2524C #607 line (**Fig. 5.6B, C**). hR3 R2524C #612 and #616 exhibited expression levels similar to and greater than Exo. hR3, respectively. The hR3 R2524C mutant appeared properly localized to ER membranes (**Supplementary Fig. 5.6B**). The basal $[Ca^{2+}]_{cyt}$ levels of the hR3 R2524C mutant cell lines were significantly increased in the absence of stimulation and the extent of the increase correlated with the relative expression level of the mutant (**Fig. 5.6D, E**). However, in contrast to the V615M and T1424M mutants, channel function in the hR3 R2524C mutant in response to stimulation was completely absent (**Fig. 5.6F** and **Supplementary Fig. 5.6C**), irrespective of the basal $[Ca^{2+}]_{cyt}$ (**Supplementary Fig. 5.6D**) when measured using single cell or population-based[345] paradigms.

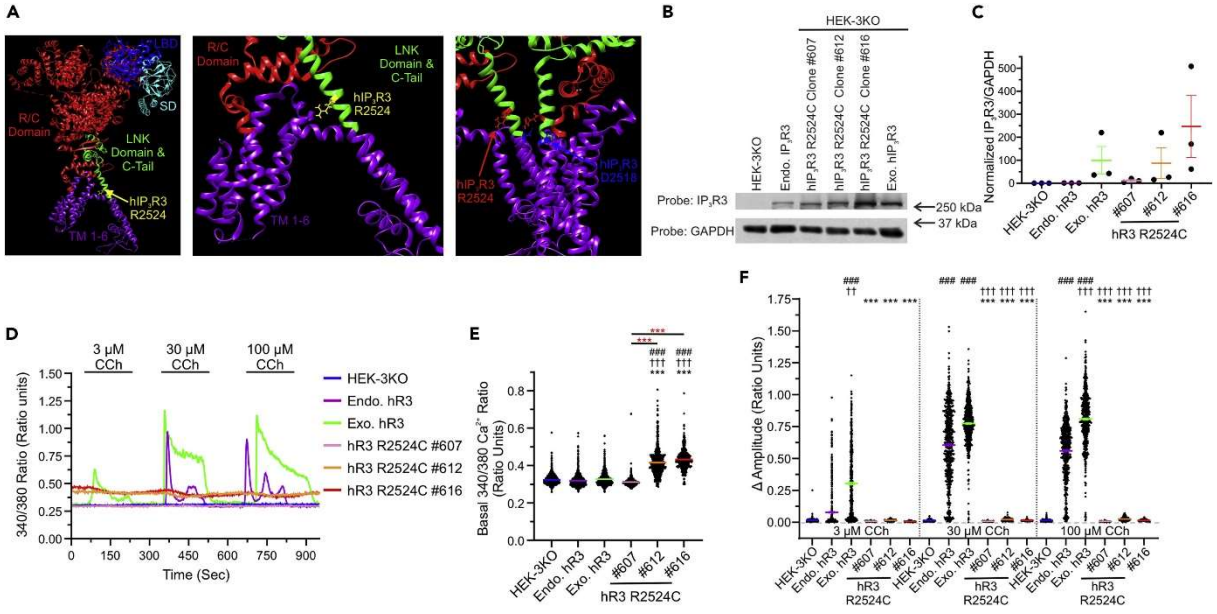

Figure 5.6: hR3 R2524C exhibited absent Ca^{2+} channel function and an elevated basal cytosolic $[Ca^{2+}]$. (A) Chimera (PDB: 6DR0) was used to visualize Arg2524 (yellow) at the junction of the 6th TM (purple) and LNK domain (green) in the channel pore near the negatively charged Asp2518 of neighbouring IP_3R3 monomers (blue). **(B)** Cell lines with varying expression of human IP_3R3 harbouring the R2524C mutation (hR3 R2524C) were generated in IP_3R-null HEK-3KO cells and western blotted alongside WT cell lines – Endo. hR3 and Exo. hR3. **(C)** Quantification of expression of hIP_3R3 with respect to GAPDH, in HEK-3KO (blue), Endo. hR3 (purple), Exo. hR3 (green), and hR3 R2524C (pink, orange, red) cell lines. Coloured lines represent the mean of at least n=3 experiments, and error bars represent SEM. Averages were normalized to that of the Endo. hR3 cell line. **(D)** Representative traces of Ca^{2+} signals from the indicated cell lines in response to the addition of increasing [CCh]. **(E)** Scatterplot summarizing the basal Ca^{2+} (average of the initial 20, 340/380 ratio points in Ca^{2+}-containing media) from experiments similar to those in (D). **(F)** Scatterplot summarizing the change in amplitude (Peak 340/380 ratio – Basal 340/380 ratio (E)) of cell lines in response to increasing [CCh] in single-cell imaging experiments similar to those in (D). All data are mean ± SEM of at least three (n=3) independent experiments. Control HEK-3KO (blue), Endo. hR3 (purple), and Exo. hR3 (green) data in (E and F) repeated from Fig. 5.2 and 5.4 above. ### p<0.001 when compared to HEK-3KO; ttt p<0.001, tt p<0.01 when compared to Endo. hR3; ∗∗∗ p<0.001 when compared to Exo. hR3; and ∗∗∗(red) p<0.001 when compared to other stably expressed hR3 R2524C cell lines; one-way ANOVA with Tukey's test performed in (E and F).

The removal of extracellular Ca^{2+} again resulted in a decrease in basal $[Ca^{2+}]_{cyt}$ in the high R2524C expressing cells (**Fig. 5.7A, B** and **Supplementary Fig. 5.7A**). Similarly, the CPA-induced Ca^{2+} leak from the ER was also decreased in the higher expressing hR3 R2524C cell lines indicating reduced ER Ca^{2+} store content in these cell lines (**Fig. 7.5A, C** and **Supplementary Fig. 5.7B-D**). Addition of GSK-7975a resulted in a significant decrease in the elevated basal $[Ca^{2+}]_{cyt}$ of the higher expressing hR3 R2524C cell lines in the absence of stimulation (**Fig. 5.7D-F and Supplementary Fig. 5.7E**), again suggesting the inappropriate activation of SOCE. Overall, these results indicate that the R2524C mutant is a completely non-functional Ca^{2+} channel, which again exhibits a leaky phenotype similar to the V615M and T1424M mutants.

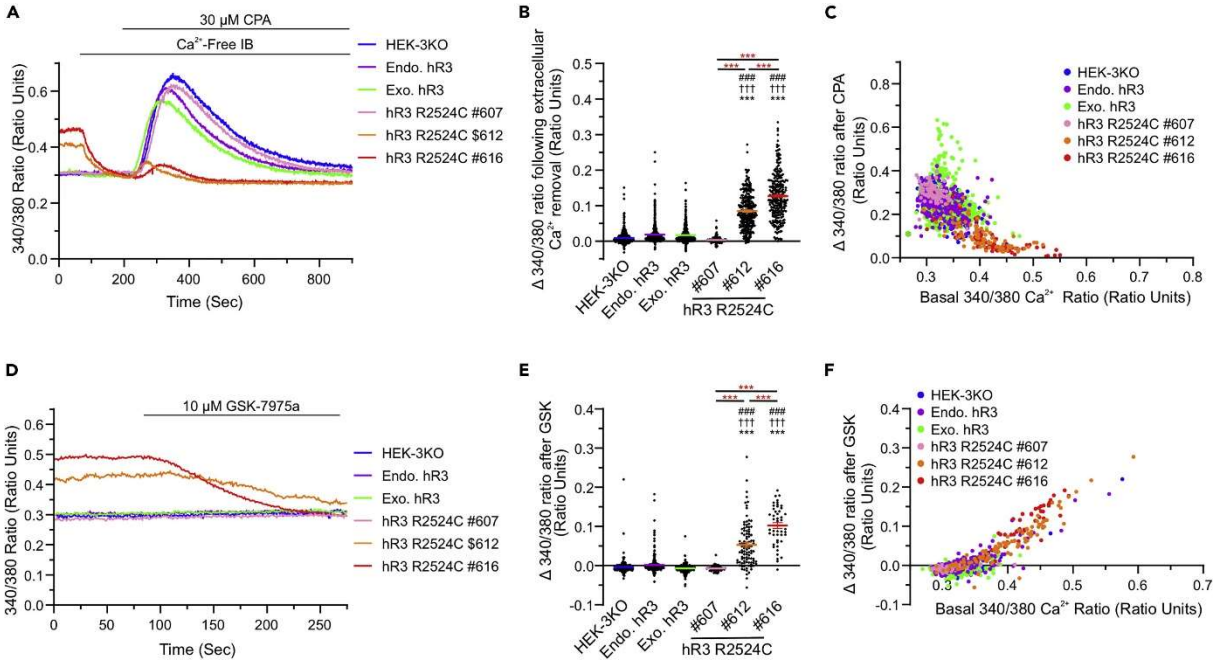

Figure 5.7: hR3 R2524C cell lines exhibited depleted ER [Ca^{2+}] and SOCE in the absence of agonist stimulation. (A) Representative traces of changes in cytosolic [Ca^{2+}] following removal of extracellular Ca^{2+} in HEK-3KO (blue), Endo. hR3 (purple), Exo. hR3 (green), and hR3 R2524C (pink, orange, red) cell lines. Cells were subsequently treated with 30 μM CPA allowing the measurement of the ER Ca^{2+} store content. **(B)** Scatterplot summarizing the change in the basal 340/380 ratio following removal of extracellular Ca^{2+} in experiments similar to those in (A). Coloured lines represent the mean of at least n=3 experiments, and error bars represent SEM. **(C)** Scatterplot summarizing the correlation between an elevated basal 340/380 Ca^{2+} ratio (Fig. 5.6E) and the change in 340/380 ratio following treatment with 30 μM CPA (maximum CPA-induced amplitude – basal 340/380 ratio following removal of extracellular Ca^{2+}) in experiments similar to those in (A). **(D)** Representative traces of Ca^{2+} signals in the indicated cell lines in response to the addition of 10 μM GSK-7975a. **(E)** Scatterplot summarizing the change in 340/380 ratio following the addition of GSK-7975a (average of 20, 340/380 ratio points prior to GSK-7975a addition – average of 20, 340/380 ratio points following 200 s of GSK-7975a addition) from experiments similar to those in (D). **(F)** Scatterplot summarizing the correlation between an elevated basal 340/380 Ca^{2+} ratio (Fig. 5.6E) and the change in 340/380 ratio following treatment with 10 μM GSK-7975a in experiments similar to those in (D). All data are mean ± SEM of at least three (n=3) independent experiments. Control HEK-3KO (blue), Endo. hR3 (purple), and Exo. hR3 (green) data in (B, C, E, and F) repeated from Fig. 5.3 and 5.5 above. ### p<0.001 when compared to HEK-3KO; ttt p<0.001 when compared to Endo. hR3; ∗∗∗ p<0.001 when compared to Exo. hR3; and ∗∗∗(red) p<0.001 when compared to other stably expressed hR3 R2524CM cell lines; one-way ANOVA with Tukey's test performed in (B and E).

5.5 Discussion

While disease-associated mutations have been identified in all three human isoforms of the IP_3R, the functional consequences of mutations in IP_3R3 are yet to be determined. Previous reports using patient-derived fibroblasts with neuropathy-associated IP_3R3 mutations exhibited drastically disparate mRNA levels and protein expression of all three IP_3R isoforms[224,345]. While the patient's fibroblasts exhibited a trend toward decreased Ca^{2+} signalling, the presence and potential compensation by endogenous IP_3R1 and IP_3R2 isoforms may have confounded elucidating the full, functional effect of these mutant IP_3R3. As a result, no consensus could be reached regarding any change in channel function observed in fibroblasts harbouring the V615M or compound heterozygous R1850Q/R2524C mutation[224,345]. Our

functional studies were designed to study the mutations as homotetramers on an unambiguous null background. We demonstrate that all mutations tested exhibited markedly reduced or absent function when expressed at levels close to endogenous hR3 levels in IP_3R-null HEK-3KO cells. Notably, our studies have identified a novel molecular and cellular phenotype associated with a subset of the variants tested. Over-expression of hR3 V615M, T1424M, and R2524C led to an elevated basal $[Ca^{2+}]_{cyt}$, decreased ER store Ca^{2+} content, and subsequent inappropriate activation of SOCE through ORAI channels. This phenotype is consistent with these mutations resulting in a constitutively leaky IP_3R3 channel pore, revealed as over-expression results in Ca^{2+} leak through the receptor, effective coupling to the SOCE machinery, and subsequent Ca^{2+} influx across the PM that is not matched by Ca^{2+} clearance mechanisms resulting in an elevated basal $[Ca^{2+}]_{cyt}$. In combination with reduced IP_3-stimulated activity, it is possible that even when expressed at endogenous levels, the leaky phenotype of these variants contributes to the aetiology of the disease in affected individuals through local, inappropriate activation of effectors. In this scenario, a subtype-specific blocker of the IP_3R3 pore may ameliorate disease, if other IP_3R subtypes present can compensate for the decreased mutant IP_3R3 channel activity. However, it needs to be taken into account that heterotetramers are present under physiological conditions and further studies are needed to determine the effect of the variants in such settings, as discussed in more detail below. For example, no significant changes in ER Ca^{2+} store content were observed in fibroblasts of the Finnish V615M CMT patients[224]. This could be due to the insufficient effect of possibly only one "leaky" subunit in a tetramer according to the co-operational activity of the channel, while the negative impact on IP_3-induced gating would be dominant. Over-expression also revealed that hR3 V615M and T1424M retained, to some limited extent, their ability to be gated by elevated IP_3, while hR3 R2524C was refractory to stimulation and thus appears to form a dead channel. Only following expression at levels similar to, or greater than that of Exo. hR3 was channel function measurable. We have previously shown that increased expression of IP_3R mutants in HEK-3KO cells compared to IP_3R-null HEK-3KO cells facilitated measurable changes in the channel function when not previously evident[345]. These observations indicate that over-expression of channels allows for the visualization of changes in channel gating resulting in measurable cytosolic Ca^{2+} signals. This may result from increased clustering of IP_3R channels on the ER membrane possibly allowing for increased amplification of signals through Ca^{2+}-induced Ca^{2+} release and interactions with licensing proteins such as KRAP[358]. Among the partially functional channels, different degrees of functionality were evident. Detectable Ca^{2+} release was only evident in a small percentage of hR3 V615M cells at expression levels above or equal to Exo. hR3 and at high [CCh]. Remarkably, when over-expressed, the T1424M hR3 mutation exhibited increased function when compared to WT hIP_3R3 at similar expression levels such that at lower concentrations of agonist, larger evoked responses were observed. The efficacy of Ca^{2+} release through this mutant was however somewhat reduced because the magnitude of Ca^{2+} release achieved at high [CCh] was diminished. A remaining question is why this mutant uniquely exhibits increased activity compared to WT only when over-expressed? As stated, over-expression might reasonably lead to receptor clusters of

increased size with enhanced function. In turn, these channels appear to be inherently poorly functioning although gating competent channels with a leaky pore, and a possibility is that this Ca^{2+} leak sensitizes these channels to low levels of IP_3, ultimately resulting in augmented Ca^{2+} signals at low [CCh]. The observation that significant Ca^{2+} puff activity was observed in cells expressing this variant even without an elevation in IP_3 is consistent with this idea.

Structural changes underlying alterations in channel function of IP_3R1 and IP_3R2 have been proposed for mutations in the SD, LBD, and channel pore[185,221,333,359]. However, the mechanisms underlying the changes in channel function in the regulatory and coupling domain, where two of the neuropathy-associated IP_3R3 mutations are located, are harder to identify. As the human V615M and T1424M variants are all properly localized to the ER membrane and would not be predicted to interfere with ligand binding or directly alter the channel pore structure, the functional effects of these mutations are likely mediated by the disruption of channel modulation by regulatory input or by channel gating mechanisms. Notably, in all mutations the amino acid substitution results in substitution to either a methionine residue or cysteine residue, both containing sulphur moieties. Methionine residues have a unique combination of size, flexibility, and chemistry to act as an effective latch for sulphur-aromatic interactions. Sulphur-aromatic interactions occur in the majority of native protein structures, yet little is known about their roles in ion channels and how this substitution in variants might alter function. Of note, both methionine and cysteine residues are subject to modification by reactive oxygen species (ROS) which have been shown to alter IP_3R activity[360,361]. Future work may involve investigating whether these mutant residues are modified by ROS[362].

In contrast to the uncertain mechanisms underlying changes in channel function in the neuropathy-associated IP_3R3 mutations in the regulatory and coupling domain, the R2524C mutation in IP_3R3 at the junction of the 6th TM and the LNK domain likely directly alters the channel pore, similar to the G2498S mutation in IP_3R2[345]. Based on recently published structures of the IP_3R1[242,281] and IP_3R3 pores[255], the positively charged Arg2524 is proposed to interact with Asp2518 of the neighbouring subunit. As a result, mutation of the positively charged Arg2524 to an uncharged Cys would likely alter the structure of the channel pore by hindering its interaction with Asp2518. This may result in a re-arrangement of Arg2524 and Asp2518 that in the absence of ligand binding weakens the hydrophobic interactions that hold the TM region together and thus results in a non-functional, open IP_3R3 channel, depletion of the ER, and activation of SOCE culminating in an increased basal $[Ca^{2+}]_{cyt}$.

Given that the location of individual mutations is widely spread through different domains of the protein, together with the dissimilar effects on IP_3-gated activity, it is not clear whether a common mechanism is responsible for the leaky channel phenotypes and decreased activity observed. It seems likely that the structural disruption imparted by the amino acid substitution alters both long-distance IP_3-induced conformational changes from the LBD to the channel domain to different degrees, but also results in

structural changes to the channel domain which dilate the pore without IP_3 binding. In the case of V615M and T1424M, in contrast to R2425C, it appears that the pore can be further expanded by the ligation of the LBD. Further high-resolution structural studies will be necessary to define how each mutation alters channel structure.

Since all the mutations are present on a single *ITPR3* allele, a question is whether the disease phenotype results from the variants acting in a dominant negative fashion when incorporated into IP_3R heterotetramers. Our previous study investigating mutants associated with ataxia in IP_3R1 or anhidrosis in IP_3R2[345] suggests that this is dependent on the region of the IP_3R harbouring the mutant, but nevertheless is not necessarily intuitively predictable. For example, incorporation of a mutation in critical residues important for IP_3 binding within the LBD in a single monomer results in an inactive tetramer, consistent with the requirement for all LBDs to be occupied with IP_3 before channel opening[89]. Since IP_3R subtypes readily form heterotetrameric assemblies, this dominant negative scenario likely leads to disabling a large proportion of the complement of IP_3R expressed in a particular cell. Clearly, the extent of the disruption of activity by mutations in other regions such as the channel domain depends on how radical the changes in properties of the substituted amino acid are and how inter-subunit interactions are disrupted. For example, somewhat unexpectedly, while a mutation in the selectivity filter of the pore-forming region of the IP_3R2 resulted in a dead channel when expressed as a homotetramer, IP_3R2 retained significant activity when only two of the monomers harboured the variant. This concatenated receptor approach is powerful because the subunit components of the tetramer can be precisely defined as the cell machinery faithfully only assembles tetrameric IP_3R structures without re-arrangement of the linked subunits or forming higher order structures[89,363–365] that occurs in other systems[366]. We envision a similar concatenated IP_3R3 approach, with defined numbers of mutant monomers within the tetramer will be required to define whether these variants act as dominant-negative subunits to disable function.

Disruption of signalling in Purkinje cells of the cerebellum, which abundantly and almost exclusively express IP_3R1 is central to understanding the disturbances in gait characteristic of SCA, pontocerebellar ataxia, and Gillespie Syndrome-associated mutations in IP_3R1[221,320,367]. We have identified here two distinct molecular effects of neuropathy-associated mutations on IP_3R3 function, however, the impacted cell type, which underpins the pathological phenotype, remains to be established. The pathophysiology of peripheral neuropathies is generally associated with abnormalities in genes that regulate myelin assembly and axonal transport resulting in demyelination and axonopathy. Mutations resulting in the dysregulation of myelin assembly, cytoskeletal structure, endosomal sorting and cell signalling, proteasome and protein aggregation, and the mitochondria may result in CMT[368–370]. In addition to roles in several of the processes that may result in CMT, IP_3Rs have also been identified in Schwann cells, with the dominant isoform IP_3R3 expressed in distinct regions from the other isoforms in dense patches in the perinodal region in close proximity to connexin 32[282,371]. It is therefore possible that the unique

location or predominant expression of IP_3R3 in Schwann cells underlies the aetiology of disease. The presence of IP_3R3 in this region and its role in the other processes that result in CMT suggest that further work looking at the downstream effects of these IP_3R3 mutations on mitochondrial function, cell structure, and propagation of Ca^{2+} signalling in Schwann cells may be necessary to identify the specific pathophysiological mechanism.

Limitations of this study: The activity of IP_3R3 variants in this study was monitored by assessing changes in $[Ca^{2+}]_{cyt}$ which is an indirect, global readout of the cellular Ca^{2+} signalling machinery. Further experiments with more direct measurements of IP_3R activity, for example using "on nucleus" patch clamp will be necessary to define the biophysical mechanism whereby these disease-associated mutants alter function. Similarly, electrophysiological measurements of SOCE in cells expressing these mutants will define how efficiently the mutants activate Ca^{2+} influx.

5.6 Personal contribution

The work presented in this chapter was based on a collaboration initiated based on my work from chapter 3 and performed using plasmids I generated for this study. I was involved in the experimental design and contributed to put the study into clinical context. I reviewed and edited the final manuscript.

5.7 Supplementary Material

5.7.1 Supplementary Figures

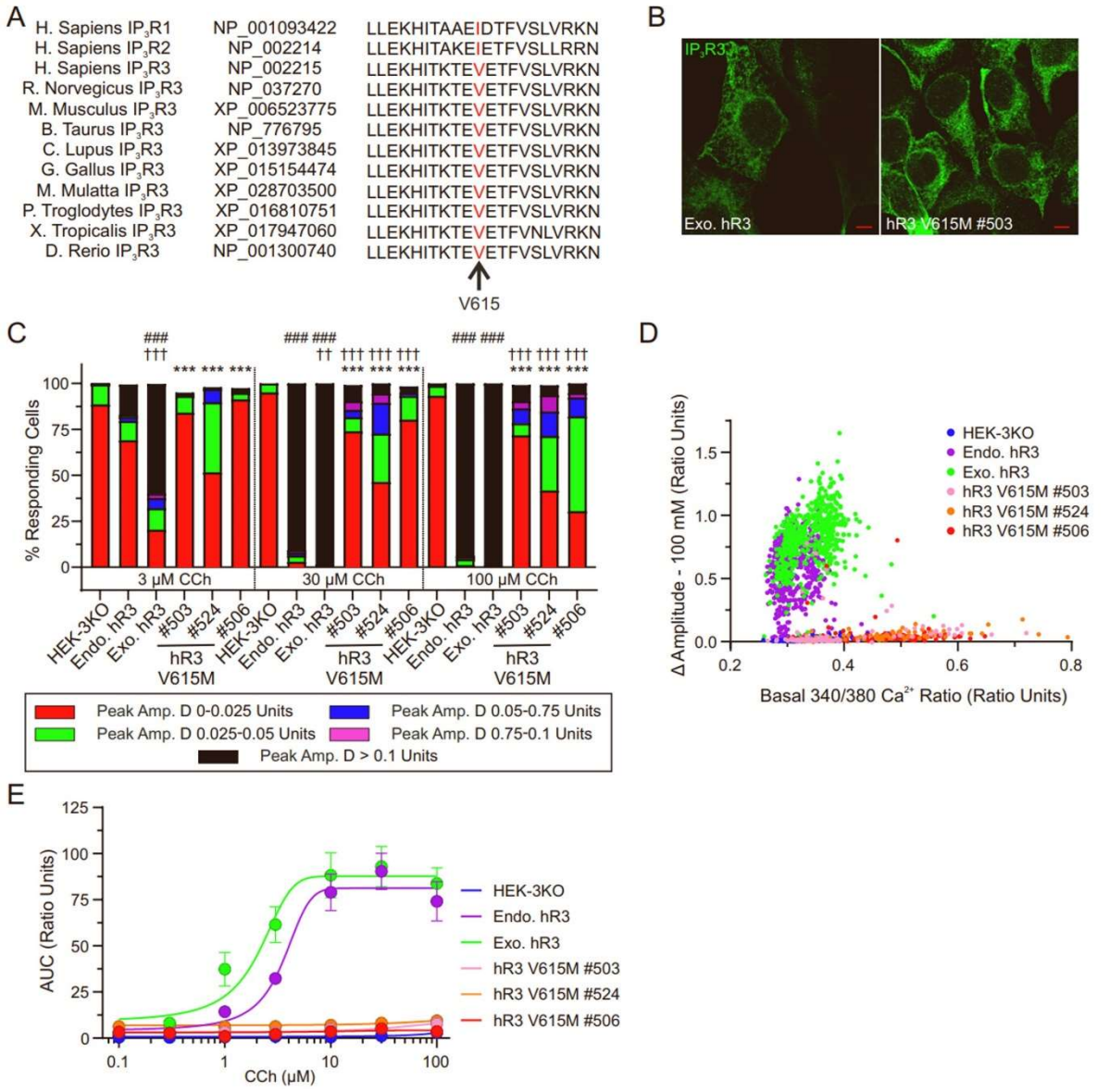

Supplementary Figure 5.1: hR3 V615M is a semi-conserved, properly localized, poorly functional Ca^{2+} channel. Related to Fig. 5.2. **(A)** Multiple sequence alignment of Val615 (red) in human IP_3R1, human IP_3R2, human IP_3R3, and multiple species of the IP_3R3 isoform. **(B)** Localization of IP_3R3 in Exo. hR3 and hR3 V615M #503 using immunocytochemistry. **(C)** Stacked bar graph summarizing the changes in 340/380 ratio from Fig. 5.2F with the percentage of those that are considered to be responding to the CCh stimulus shown in black. **(D)** Scatter plot summarizing the correlation between an elevated basal 340/380 Ca^{2+} ratio (Fig. 5.2E) and the change in 340/380 ratio following treatment with 30 µM CPA (Fig. 5.2F: maximum 100 µM CCh-induced amplitude – average of 20 340/380 ratio points prior to CCh addition) in HEK-3KO (blue), Endo. hR3 (purple), Exo. hR3 (green), and hR3 V615M (pink, orange, red) cell lines in experiments similar to those in Fig. 5.2D. **€** Dose-response curve showing the AUC of Ca^{2+} signals of Fura-2/AM loaded cell lines when treated with increasing concentrations (100 nM, 300 nM, 1 µM, 3 µM, 10 µM, 30 µM, and 100 µM) of CCh using a FlexStation3 96-well plate reader. All data are mean ± SEM of at least three (n=3) independent experiments. ### p<0.001 when compared to HEK-3KO; ttt p<0.001, tt p<0.01 when compared to Endo. hR3; and *** p<0.001, when compared to Exo. hR3; one-way ANOVA with Tukey's test performed in (C).

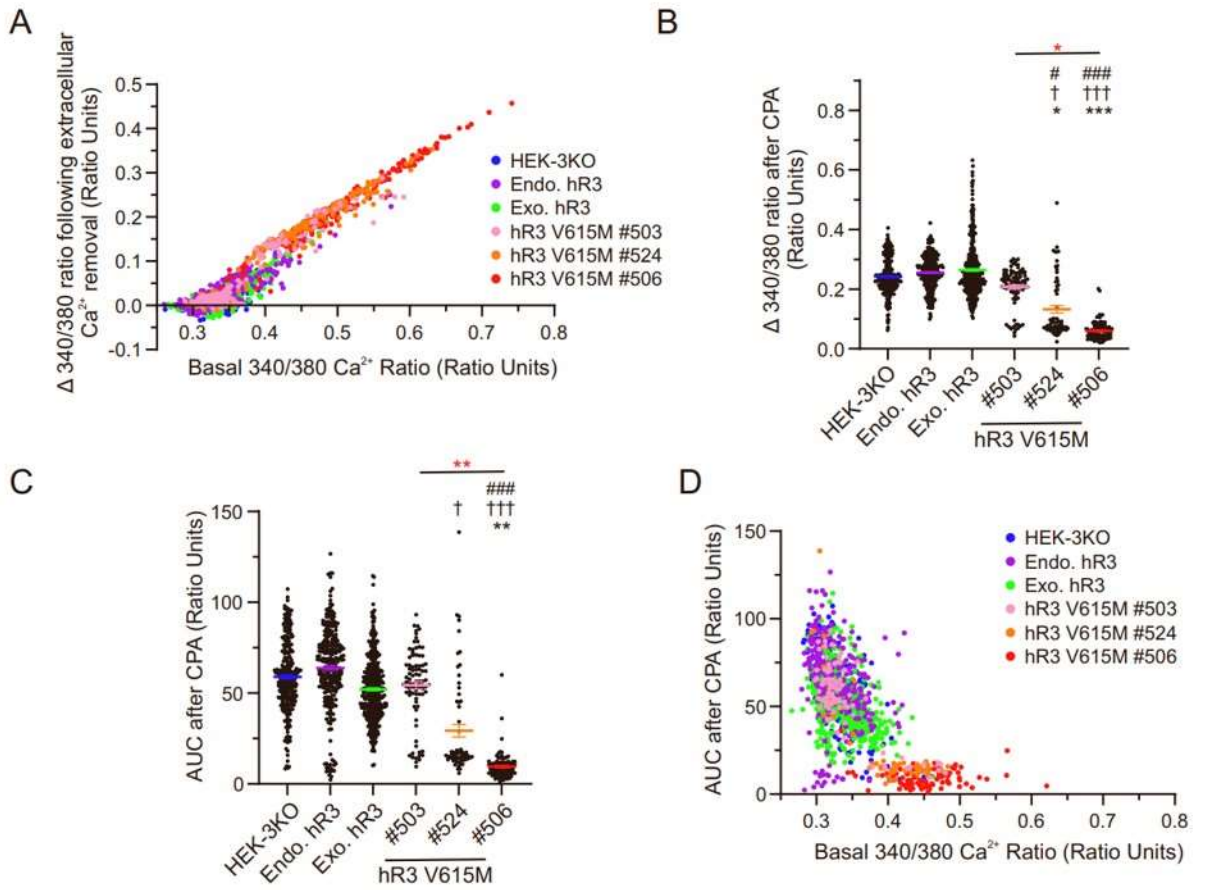

Supplementary Figure 5.2: hR3 V615M cell lines exhibit depleted ER [Ca^{2+}]. Related to Fig. 5.3. **(A)** Scatter plot summarizing the correlation between an elevated basal 340/380 Ca^{2+} ratio (Fig. 5.2E) and the change in 340/380 ratio following removal of extracellular Ca^{2+} (Fig. 5.3B) in HEK-3KO (blue), Endo. hR3 (purple), Exo. hR3 (green), and hR3 V615M (pink, orange, red) cell lines in experiments similar to those in Fig. 5.3A. **(B)** Scatter plot summarizing the change in the change in 340/380 ratio following treatment with 30 μM CPA (maximum CPA-induced amplitude – basal 340/380 ratio following removal of extracellular Ca^{2+}) in experiments similar to those in Fig. 5.3A. **(C)** Scatter plot summarizing the AUC following treatment with 30 μM CPA in experiments similar to those in Fig. 5.3A. **(D)** Scatter plot summarizing the correlation between an elevated basal 340/380 Ca^{2+} ratio (Fig. 5.2E) and AUC following treatment with 30 μM CPA in experiments similar to those in Fig. 5.3A. All data are mean ± SEM of at least three (n=3) independent experiments. ### p<0.001, # p<0.05 when compared to HEK-3KO; ttt p<0.001, t p<0.05 when compared to Endo. hR3; *** p<0.001, ** p<0.01, * p<0.05 when compared to Exo. hR3; **(red) p<0.01, *(red) p<0.05 when compared to other stably expressed hR3 V615M cell lines; one-way ANOVA with Tukey's test performed in (B, C).

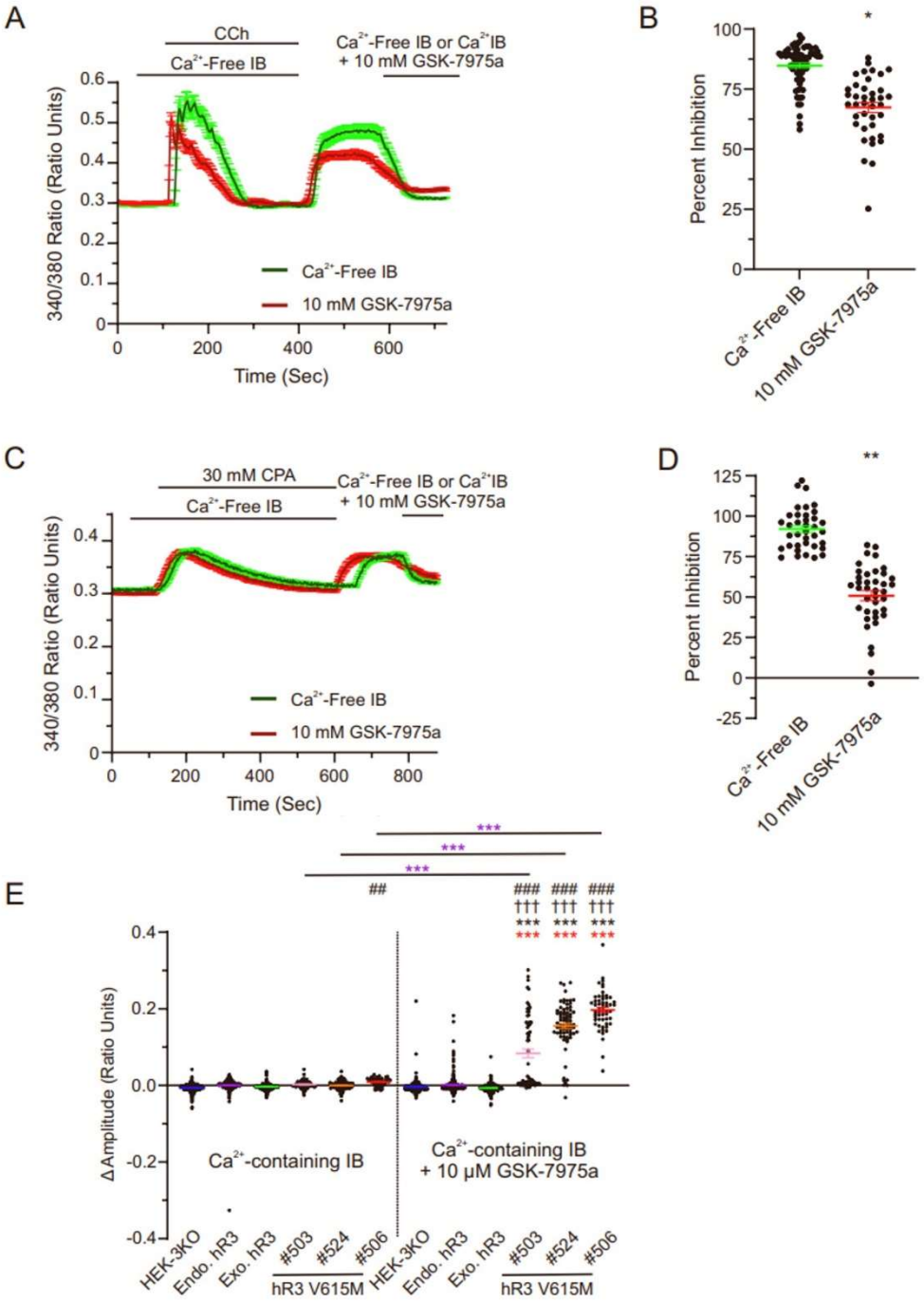

Supplementary Figure 5.3: Effect of ORAI-inhibitor GSK-7975a on inhibition of SOCE in WT and hR3 V615M cell lines. Related to Fig. 5.3. **(A)** Average trace (black) ± SEM (red or green) for Fura-2/AM loaded cells treated with CCh in Ca^{2+}-free imaging buffer to empty the ER Ca^{2+} store. Cells were re-loaded with Ca^{2+} and Ca^{2+} influx was inhibited either by removal of extracellular Ca^{2+} (green) or addition of 10 µM GSK-7975a (red) in the presence of extracellular Ca^{2+}. **(B)** Quantification of the percent of SOCE inhibited in (A) when extracellular Ca^{2+} was removed (green) or GSK-7975a was added in the presence of extracellular Ca^{2+} (red); * $p<0.05$. **(C)** Average trace (black) ± SEM (red or green) for Fura-2/AM loaded cells treated with CPA in Ca^{2+}-free imaging buffer to empty the ER Ca^{2+} store. Cells were re-loaded with Ca^{2+} and Ca^{2+} influx was inhibited either by removal of extracellular Ca^{2+} (green) or addition of 10 µM GSK-7975a (red) in the presence of extracellular Ca^{2+}. **(D)** Quantification of the percent of SOCE inhibited in (C) when extracellular Ca^{2+} was removed (green) or GSK-7975a was added in the presence of extracellular Ca^{2+} (red); ** $p<0.01$. **€** Scatter plot summarizing the changes in 340/380 ratio in the absence of any external addition and following the addition of GSK- 7975a as shown in Fig. 5.3C, D. The change in 340/380 ratio

was calculated by subtracting the average of 20 340/380 ratio points following 200 sec of Ca^{2+} IB in the absence of external stimulation or GSK- 7975a addition from the average of the same 20 340/380 ratio points (prior to GSK-7975a addition). All data are mean ± SEM of at least three (n=3) independent experiments. ### p<0.001, ## p<0.01 when compared to HEK-3KO; ttt p<0.001 when compared to Endo. hR3; *** p<0.001 when compared to Exo. hR3; ***(red) p<0.001 when compared to other stably expressed hR3 V615M cell lines; ***(purple) p<0.001 when compared to the same hR3 V615M cell line under different conditions; one-way ANOVA with Tukey's test performed in €.

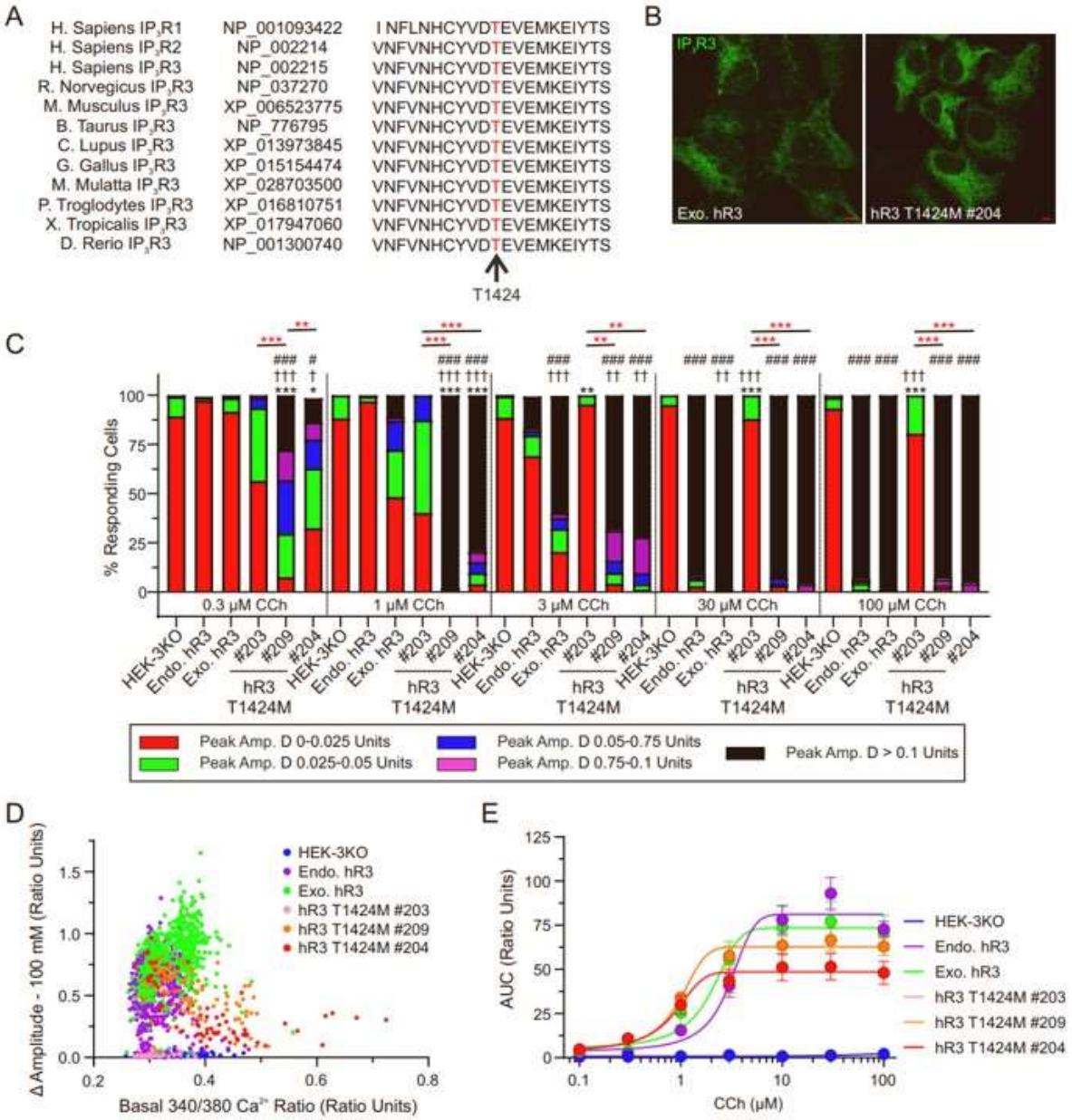

Supplementary Figure 5.4: hR3 T1424M is a conserved, properly localized mutant that increases Ca^{2+} channel function. Related to Fig. 5.4. **(A)** Multiple sequence alignment of Thr1424 (red) in human IP_3R1, human IP_3R2, human IP_3R3, and multiple species of the IP_3R3 isoform. **(B)** Localization of IP_3R3 in Exo. hR3 and hR3 T1424M #204 using immunocytochemistry. **(C)** Stacked bar graph summarizing the changes in 340/380 ratio from Fig. 5.4F with the percentage of those that are considered to be responding to the CCh stimulus shown in black. **(D)** Scatter plot summarizing the correlation between an elevated basal 340/380 Ca^{2+} ratio (Fig. 5.4E) and the change in 340/380 ratio following treatment with 30 µM CPA (Fig. 5.4F: maximum 100 µM CCh-induced amplitude – average of 20 340/380 ratio points prior to CCh addition) in HEK-3KO (blue), Endo. hR3 (purple), Exo. hR3 (green), and hR3 T1424M (pink, orange, red) cell lines in experiments similar to those in Fig. 5.4D. **€** Dose-response curve showing the AUC of Ca^{2+} signals of Fura-2/AM loaded cell lines when treated with increasing concentrations (100 nM, 300 nM, 1 µM, 3 µM, 10 µM, 30 µM, and 100 µM) of CCh using a FlexStation3 96-well plate reader. All data are mean ± SEM of at least three (n=3) independent experiments. Control HEK-3KO (blue), Endo. hR3 (purple), and Exo. hR3 (green) data in C, D repeated from Supplementary Fig. 5.1 above. ### p<0.001, # p<0.05 when compared to HEK-3KO; ttt p<0.001, tt p<0.01, t p<0.05 when compared to Endo. hR3; *** p<0.001, ** p<0.01, * p<0.05 when compared to Exo. hR3; ***(red) p<0.001, **(red) p<0.01 when compared to other stably expressed hR3 V615M cell lines; one-way ANOVA with Tukey's test performed in (C).

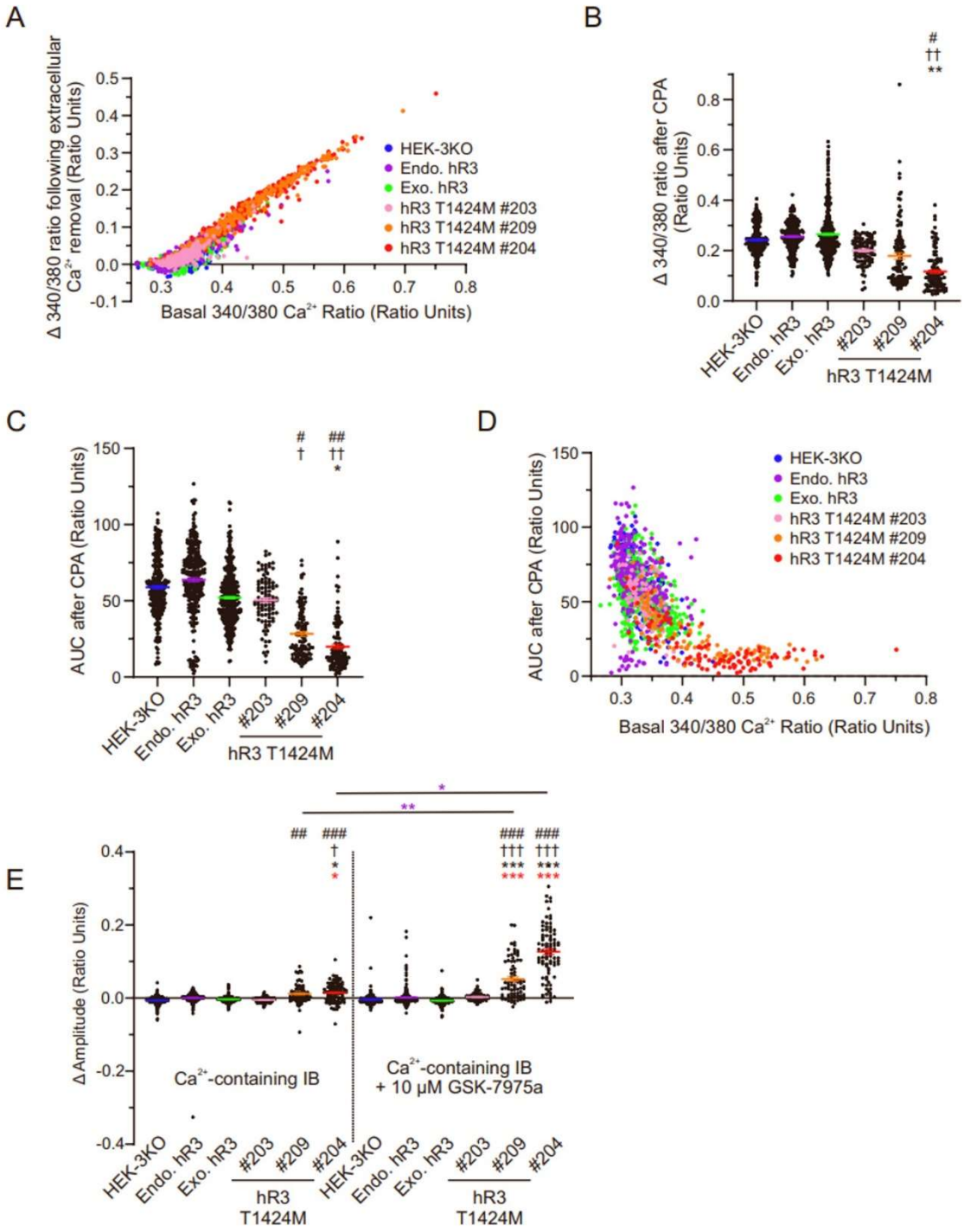

Supplementary Figure 5.5: hR3 T1424M cell lines exhibit depleted ER [Ca^{2+}] and SOCE in the absence of agonist stimulation. Related to Fig. 5.5. **(A)** Scatter plot summarizing the correlation between elevated basal 340/380 Ca^{2+} ratios (Fig. 5.4E) and the change in 340/380 ratio following removal of extracellular Ca^{2+} (Fig. 5.5B) in HEK-3KO (blue), Endo. hR3 (purple), Exo. hR3 (green), and hR3 T1424M (pink, orange, red) cell lines in experiments similar to those in Fig. 5.5A. **(B)** Scatter plot summarizing the change in the change in 340/380 ratio following treatment with 30 μM CPA (maximum CPA-induced amplitude – basal 340/380 ratio following removal of extracellular Ca^{2+}) in experiments similar to those in Fig. 5.5A. **(C)** Scatter plot summarizing the AUC following treatment with 30 μM CPA in experiments similar to those in Fig. 5.5A. **(D)** Scatter plot summarizing the correlation between an elevated basal 340/380 Ca^{2+} ratio (Fig. 5.4E) and AUC following treatment with 30 μM CPA in experiments similar to those in Fig. 5.5A. **€** Scatter plot summarizing the changes in 340/380 ratio in the absence of any external addition similar and following the addition of GSK-7975a as shown in Fig. 5.5C, D. The change in 340/380 ratio was calculated by subtracting the average of 20 340/380 ratio points following 200 sec of Ca^{2+} IB in

the absence of external stimulation or GSK-7975a addition from the average of the same 20 340/380 ratio points (prior to GSK-7975a addition). All data are mean ± SEM of at least three (n=3) independent experiments. Control HEK-3KO (blue), Endo. hR3 (purple), and Exo. hR3 (green) data in A, B, C, and D repeated from Supplementary Fig. 5.2, 3 above. ### p<0.001, ## p<0.01, # p<0.05 when compared to HEK-3KO; ttt p<0.001, tt p<0.01, t p<0.05 when compared to Endo. hR3; *** p<0.001, ** p<0.01, * p<0.05 when compared to Exo. hR3; ***(red) p<0.001, *(red) p<0.05 when compared to other stably expressed hR3 T1424M cell lines; **(purple) p<0.01, *(purple) p<0.05 when compared to the same hR3 T1424M cell line under different conditions; one-way ANOVA with Tukey's test performed in (B, C).

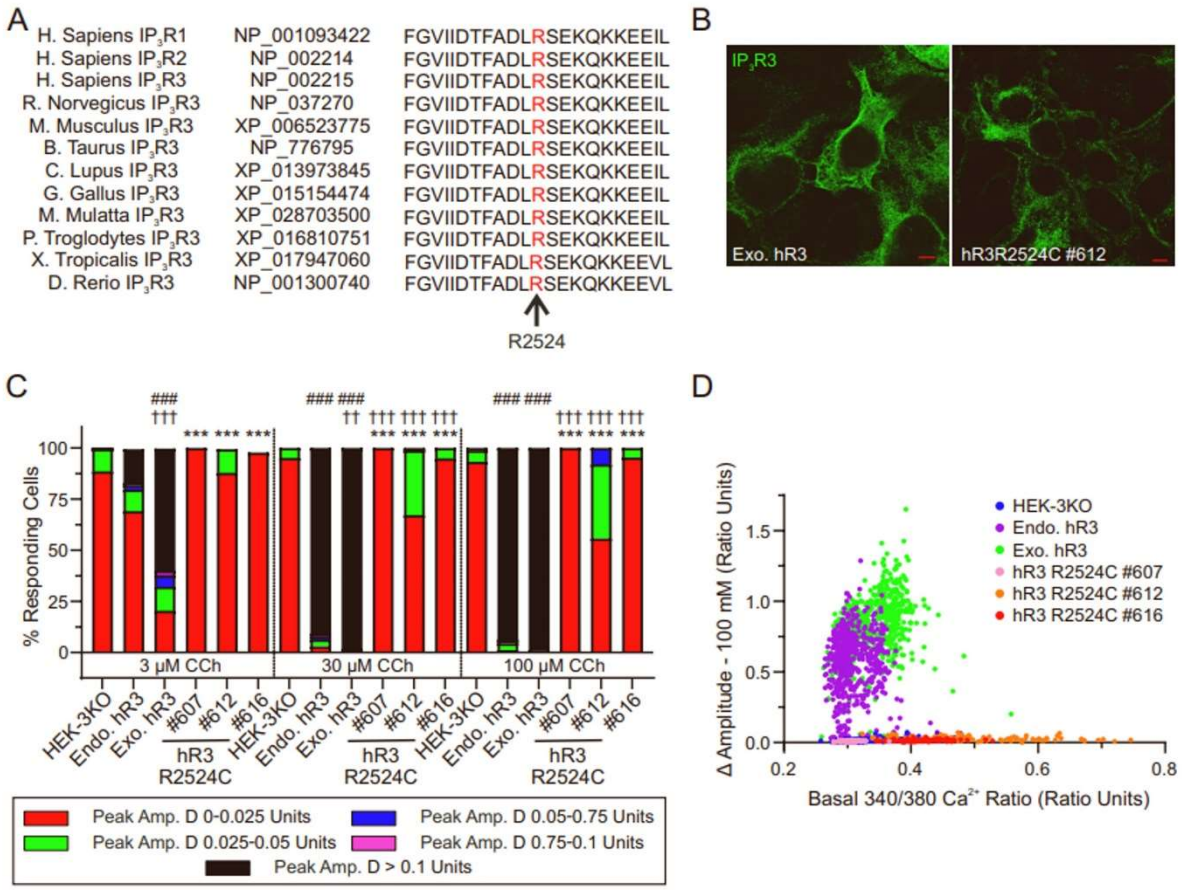

Supplementary Figure 5.6: hR3 R2524C is a conserved, properly localized mutant that does not exhibit Ca^{2+} channel function. Related to Fig. 5.6. **(A)** Multiple sequence alignment of Arg2524 (red) in human IP_3R1, human IP_3R2, human IP_3R3, and multiple species of the IP_3R3 isoform. **(B)** Localization of IP_3R3 in Exo. hR3 and hR3 R2524C #612 using immunocytochemistry. **(C)** Stacked bar graph summarizing the changes in 340/380 ratio from Fig. 5.6F with the percentage of those that are considered to be responding to the CCh stimulus shown in black. **(D)** Scatter plot summarizing the correlation between an elevated basal 340/380 Ca^{2+} ratio (Fig. 5.6E) and the change In 340/380 ratio following treatment with 30 μM CPA (Fig. 5.6F: maximum 100 μM CCh-induced amplitude – average of 20 340/380 ratio points prior to CCh addition) in HEK-3KO (blue), Endo. hR3 (purple), Exo. hR3 (green), and hR3 R2524C (pink, orange, red) cell lines in experiments similar to those in Fig. 5.6D. All data are mean ± SEM of at least three (n=3) independent experiments. Control HEK-3KO (blue), Endo. hR3 (purple), and Exo. hR3 (green) data in C, D repeated from Supplementary Fig. 5.1, 4 above. ### $p<0.001$ when compared to HEK-3KO; ttt $p<0.001$, tt $p<0.01$ when compared to Endo. hR3; *** $p<0.001$ when compared to Exo. hR3; one-way ANOVA with Tukey's test performed in (C).

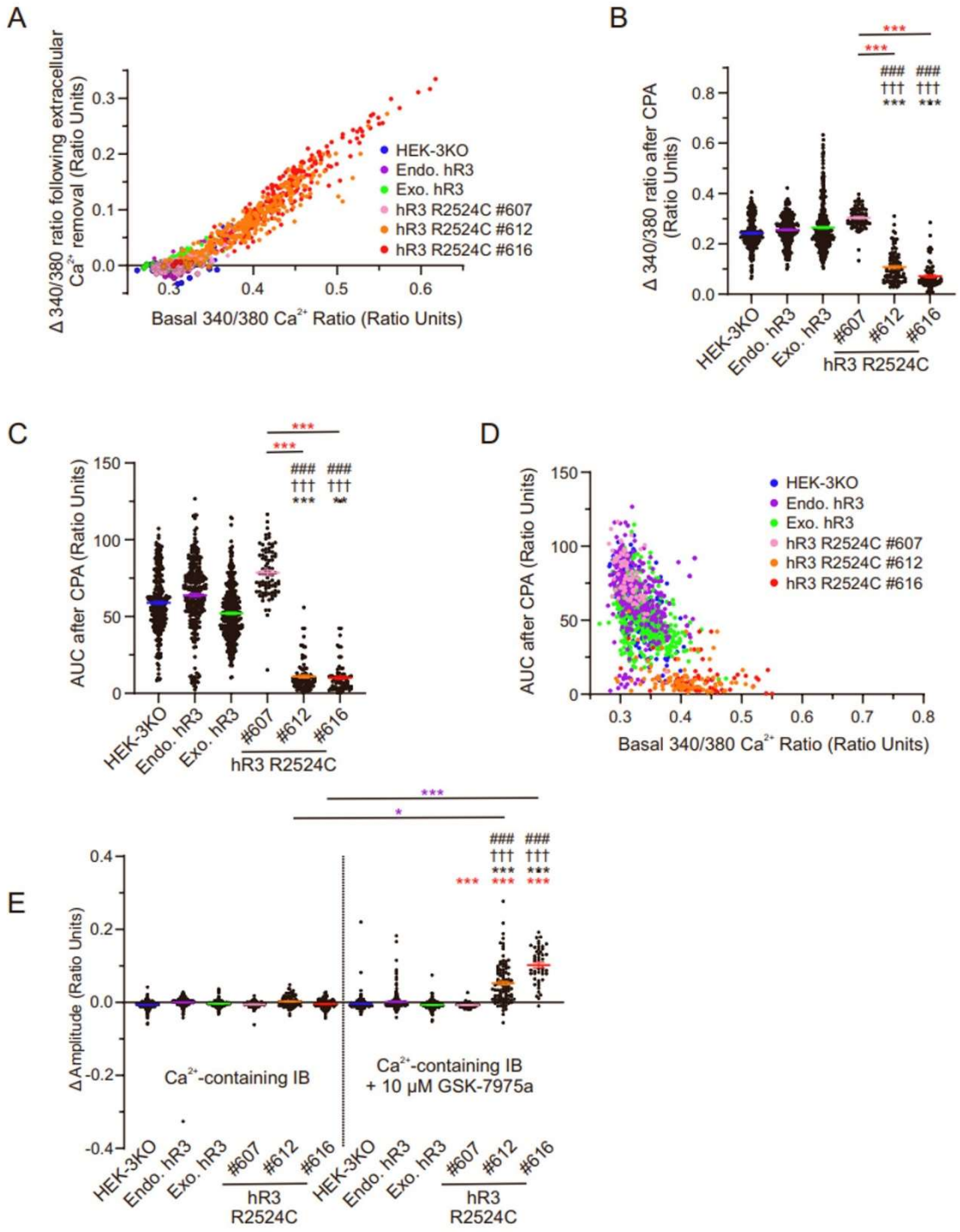

Supplementary Figure 5.7: hR3 R2524C cell lines exhibit depleted ER [Ca^{2+}] and SOCE in the absence of agonist stimulation. Related to Fig. 5.7. **(A)** Scatter plot summarizing the correlation between an elevated basal 340/380 Ca^{2+} ratio (Fig. 5.6E) and the change in 340/380 ratio following removal of extracellular Ca^{2+} (Fig. 5.5B) in HEK-3KO (blue), Endo. hR3 (purple), Exo. hR3 (green), and hR3 R2524C (pink, orange, red) cell lines in experiments similar to those in Fig. 5.7A. **(B)** Scatter plot summarizing the change in the change in 340/380 ratio following treatment with 30 μM CPA (maximum CPA-induced amplitude – basal 340/380 ratio following removal of extracellular Ca^{2+}) in experiments similar to those in Fig. 5.7A. **(C)** Scatter plot summarizing the AUC following treatment with 30 μM CPA in experiments similar to those in Fig. 5.7A. **(D)** Scatter plot summarizing the correlation between an elevated basal 340/380 Ca^{2+} ratio (Fig. 5.6E) and AUC following treatment with 30 μM CPA in experiments similar to those in Fig. 5.7A. **(E)** Scatter plot summarizing the changes in 340/380 ratio in the absence of any external stimulation and following the addition of GSK-7975a as shown in Fig. 5.7C, D. The change in 340/380 ratio was calculated by subtracting the average of 20 340/380 ratio points following 200 seconds of Ca^{2+}

IB in the absence of external stimulation or GSK-7975a addition from the average of the same 20 340/380 ratio points (prior to GSK-7975a addition). All data are mean ± SEM of at least three (n=3) independent experiments. Control HEK-3KO (blue), Endo. hR3 (purple), and Exo. hR3 (green) data in A, B, C, and D repeated from Supplementary Fig. 5.2, 3, and 5 above. ### p<0.001 when compared to HEK-3KO; ttt p<0.001 when compared to Endo. hR3; *** p<0.001, ** p<0.01 when compared to Exo. hR3; ***(red) p<0.001 when compared to other stably expressed hR3 R2524C cell lines; ***(purple) p<0.001, *(purple) p<0.05 when compared to the same hR3 R2524C cell line under different conditions; one-way ANOVA with Tukey's test performed in (B, C).

5.7.2 Supplementary Videos

The videos referred to in this chapter can be accessed either by scanning the QR code below or by following this link: https://doi.org/10.1016/j.isci.2022.105523.

6 General Discussion

6.1 Novel disease entities caused by variants in *ITPR3*

Variants in two of the three different isoforms of the Inositol 1,4,5-trisphosphate receptor (IP_3R), a ligand-gated Ca^{2+} channel mainly located in the ER membrane, had been causally linked to human hereditary disorders prior to the work presented in this thesis[220,364]. Despite the relevance of IP_3R-mediated Ca^{2+} flux in both excitable as well as non-excitable cells, the functional disruption of one of the subtypes results in surprisingly narrow disease phenotypes. Due to the predominant expression of IP_3R1 in Purkinje cells of the cerebellum, dominant and recessive variants in *ITPR1* most frequently cause ataxia with variable disease severity[185,223], a phenotype that is also observed in *Itpr1*$^{-/-}$ mice, although these mice often die *in utero* or shortly after birth[320]. In contrast, a homozygous missense variant in *ITPR2* was found to cause anhidrosis in a kindred with 5 affected individuals and this phenotype was replicated in mice lacking IP_3R2[186]. While variants in *ITPR3* were identified in recurrent head and neck squamous cell carcinoma, the primary tumours did not harbour these variants[193]. The occurrence of *ITPR3* variants has indeed been reported in several types of cancer[195,372,373], most likely owing to the involvement of IP_3R-mediated Ca^{2+} signalling in the regulation of metabolism and apoptosis[374,375]. However, most of the studies reporting these variants are association studies and lack the investigation of the effects on protein function and downstream signalling.

My work presented in this thesis adds *ITPR3*, the gene encoding the IP_3R subtype 3, to the genes causally linked to hereditary disorders by disrupting Ca^{2+} homeostasis and signalling when mutated. The results presented show that compound heterozygous variants in *ITPR3* can cause immune dysregulation with varying severity that is likely attributable to the location of the variants within the gene and protein. One of these patients was also diagnosed with CMT during adolescence and we describe two additional autosomal dominant kindreds with a total of five patients suffering from CMT. Following the identification of the variants, functional characterization of the mutated receptors showed that not only ligand-dependent gating was altered, but that they exhibited aberrant Ca^{2+} flux properties in resting conditions as well.

As mice completely lacking IP_3R3 did not show an overt phenotype in several studies[187,249,376], although they were reported to show excessive hair shedding in one study[377], it was proposed that absent IP_3R3 signalling could be compensated for by IP_3R1 and IP_3R2. However, it is important to distinguish between complete absence of a protein or the presence of a mutated version, which has also been described as niche-filling allele, where the mutated protein can still perform some of its functions and is not substituted[378], especially in light of the possibility of IP_3Rs to form heterotetramers. For example, Klar *et al.* showed residual sweat production in mice lacking IP_3R2 due to compensation by IP_3R1 and IP_3R3, while patients with a homozygous missense mutation in *ITPR2* were completely unable to produce sweat[186]. Due to the cooperative binding of both IP_3 and Ca^{2+} to the four channel subunits[253] and their possibly independent regulation by interaction partners and post-translational modifications,

the presence of one or more defective subunits could exert a dominant negative effect. It is however challenging to determine the exact stoichiometry of receptor subtypes under physiological conditions, but the use of concatenated receptors allows to define the composition of the tetramers *in vitro*[365]. Investigations using this system could shed light on the effect of dysfunctional IP_3R3 subunits on the wild-type and other IP_3R subtypes and provide insights into the tolerance of the number of malfunctioning subunits in one channel. We hypothesize that there will be differences in sensitivity due to the severity of the variant, as we for example show that the variants identified in the regulatory subunit were functional hypomorphs (R1850Q, F1628L, V615M) or showed increased signalling capacity (T1424M), while the variant located in the channel domain (R2524C) fully abrogated gating of homotetrameric channels.

In the following paragraphs the findings of the presented work will be discussed in relation to the phenotype they caused, namely immunodeficiency as an IEI and CMT, before comparing the observations on a functional background and finally providing an outlook on outstanding questions and the impact of the research.

6.1.1 Recessive *ITPR3* variants in Inborn Errors of Immunity

Ca^{2+} signalling is a central and non-redundant pathway in the activation of a number of immune cells. The severe phenotype in patients with STIM1 or ORAI1 deficiency, so-called CRAC channelopathies, often requiring HSCT early in life highlights the importance of Ca^{2+} signalling in order to successfully fight infections. Patients with autosomal dominant STIM1 or ORAI1 CRAC channelopathies show absent or severely impaired SOCE in T cells and therefore fail to increase $[Ca^{2+}]_{cyt}$ to levels necessary for downstream signalling. SOCE in these cells is mediated by the release of Ca^{2+} from the ER lumen through IP_3Rs, that is initiated by TCR engagement. However, although IP_3Rs operate in the same signalling pathway, they had not been implicated in hereditary immune disorders prior to the presented work. Recently, compound heterozygous variants in *CRACR2A*, a regulator of the pore-forming CRAC channel domain, have been described in one case of late-onset combined immunodeficiency, extending the clinical phenotype of CRAC channelopathies. Although IP_3Rs act upstream of the proteins involved in CRAC channelopathies, the clinical phenotypes we observed in IP_3R3 deficiency differ in several aspects. While more than half of the patients with STIM1-/ORAI1-deficiency presented with anhidrosis and most of them with hypotonia from birth, both of these features were not observed in either of the patients we described (**Table 6.1**). However, the two patients with IP_3R3 deficiency we reported in **chapter 3** show a great variability in severity of the immunodeficiency. P1 more closely resembles STIM1-/ORAI1-deficient patients in that this patient for example also showed defective enamel formation and hair abnormalities, and required HSCT, although at a later age than typically seen in the severe CRAC channelopathies. In contrast, P2 has milder disease and shares the late diagnosis of CVID-like disease with the adult patient with CRACR2A deficiency[164]. A major difference between P2 and

the CRACR2A-deficient patient is however that the former exhibited signs of immune dysregulation, while this was not observed in the latter.

Table 6.1: Overlap and differences in clinical phenotypes of Ca^{2+} signalling defects in IEI. AR = autosomal recessive; CID = combined immunodeficiency; AIHA = autoimmune haemolytic anaemia; ITP = immune thrombocytopenia; CMT = Charcot-Marie-Tooth.

CHARACTERISTIC	STIM1 DEFICIENCY	ORAI1 DEFICIENCY	IP_3R3 DEFICIENCY	CRACR2A DEFICIENCY
# PATIENTS	13	13	2	1
INHERITANCE	AR	AR	AR	AR
IMMUNODEFICIENCY	10/13	13/13	2/2	Late-onset CID
IMMUNE DYSREGULATION	AIHA, ITP (8/13)	5/5	AIHA, ITP (1/2)	No
ANHYDROSIS	6/10	7/9	No	No
ENAMEL DEFECT	9/13	6/9	½	No
SKIN INVOLVEMENT	Eczema/psoriasis (7/13)	Eczema/diaper rash (2)	Molluscum contagiosum /diaper rash (1/2)	No
HYPOTONIA	9/13	12/13	No	No
NEUROLOGICAL INVOLVEMENT	No	No	CMT (1/2)	No

Interestingly, while total T and B cell numbers are usually in the normal range in patients with CRAC channelopathies, P1 had severe reductions in T and B cell numbers, but normal NK cells. While the former observation suggests that SOCE is dispensable for B- and T-cell development, the preceding step of IP_3-mediated Ca^{2+} release from the ER mediated by IP_3Rs might not be. Although Ca^{2+}-mediated activation of calcineurin and subsequent translocation of NFAT to the nucleus were shown to be necessary for positive thymic T cell selection in mice[379], the precise frequency and amplitude of Ca^{2+} signals required are not yet fully understood. It could be possible that repeated Ca^{2+} puffs and waves without triggering full-blown and maintained SOCE are sufficient to allow positive thymic selection in the case of CRAC channelopathies. In contrast, when these more locally occurring IP_3R-mediated signals are severely impaired, as in P1, T-cell development may be impaired as well. P2 in our study showed normal numbers of T cells, suggesting that residual functionality of the hypomorphic variants allows sufficient Ca^{2+} signalling for positive T cell selection. Despite normal T cell numbers, we did observe an inverted CD4/CD8 ratio in P2 that could be a result of reduced Ca^{2+} signalling, as reduced calcineurin activity[380] and shortened stimulation periods[381], both possible consequences of impaired IP_3R-mediated signalling, were found to favour development of CD8 over CD4 single positive thymocytes. In line with the finding in a number of patients with STIM1 or ORAI1 deficiency[163,258], while total T-cell numbers were normal, P2 had reduced numbers of Tregs. This is consistent with the finding that strong CRAC-mediated SOCE is required for thymic Treg development[152] as well as the

differentiation into effector Tregs[382]. Together with the likely defective negative selection due to absent or reduced SOCE, this would provide a possible explanation for the observed autoimmune manifestations in these patients.

While the impact of variants in STIM1 and ORAI1 have been extensively studied especially in T cells, B-cell defects have been considered mostly secondary[165]. Our results however suggest that while the impairment is milder, there seems to be a B-cell intrinsic defect in IP_3R3 deficiency as well. With increasing numbers of patients and variants reported for IP_3R3 deficiency, further studies also investigating the effect in innate immune cells are needed to unravel whether defects in other cells could contribute to the observed clinical phenotype. IP_3-mediated Ca^{2+} signalling and SOCE are for example also crucial for appropriate degranulation of granulocytes and mast cells[383,384] and killing of target cells through the release of lytic granules was shown to be impaired in NK cells of STIM1-/ORAI1-deficient patients[385]. Moreover, studies in the differentiated neutrophil-like cell line HL-60 suggested a role for SOCE in the production of reactive oxygen species (ROS) that aid in the killing of phagocytosed pathogens[386], although direct investigation of SOCE in neutrophils of STIM1 and ORAI1 deficient patients did not show any impairment[387].

From a clinical point of view, the presented work should increase awareness about different types of Ca^{2+}-mediated defects in IEI, apart from the more well-known CRAC channelopathies. It is important to point out that for example a normal *in vitro* T-cell proliferation assay following antigenic stimulation, that is routinely performed in a clinical setting, can be observed. This was noted in both reported IP_3R3-deficient patients and seems to contradict a TCR pathway defect, however, as our data showed, the degree of impairment seen *in vitro* is highly dependent on signal strength and clinical testing may exceed physiological signal strengths, thereby obscuring the underlying deficiency. The same phenomenon was described for a number of patients with STIM1 and ORAI1 deficiency[388,389]. Additionally, as T-cell development may be unaffected by variants in *ITPR3*, as seen only in P2, and as highlighted in a report by Mendez-Echevarria *et al.* on a patient with ORAI1 deficiency[390], these patients could be missed in TREC assays, that are included in newborn screenings of a few developed countries. The description of increasing numbers of IP_3R3-deficient patients may however reveal a range of disease severity based on the impact of the variants that could cover milder disease with intact T-cell development and normal TREC screening, as observed in P2, up to severe disease with impaired T-cell development and abnormal TREC screening that may require HSCT. At the time of patient recruitment TREC screening was not yet implemented and therefore not performed for P1, so this hypothesis will need to be confirmed in additional patients.

6.1.2 Dominant *ITPR3* variants in Charcot-Marie-Tooth disease

Variants in *ITPR3* have previously been suggested as candidates causing the most classical form of inherited peripheral neuropathies, namely hereditary motor and sensory neuropathy, also known as

CMT[188,189], although no functional studies were performed to verify this finding. Our work confirms functional impairments of a homotetrameric receptor for one of these reported heterozygous variants described in a patient diagnosed with demyelinating CMT (T1424M, **chapter 5**). We also tested two additional heterozygous variants we identified in a three-generation Finnish family and in an isolated case with demyelinating CMT (patients described in **chapter 4**). Homotetrameric IP_3R3 channels with these variants showed abnormal signalling as well, providing evidence for their pathogenicity.

All individuals we described with an isolated neuropathy phenotype were diagnosed with demyelinating neuropathy, suggesting that Schwann cells are more dependent on IP_3R3 signalling than neurons. Progressive worsening of axonal neuropathy over time in the affected Finnish family was considered to be secondary, due to dysfunctional axon myelination. However, the patient we describe with a combined immunodeficiency and neuropathy (**chapter 3**) was diagnosed with axonal CMT and, although exhibiting a compound heterozygous genotype, shares one LOF variant with the single neuropathy patient. As clear separations between axonal and demyelinating neuropathies can be difficult due to the close interaction between neurons and Schwann cells, further patients and in-depth investigations will be needed to resolve whether the primary driver of neuropathy in IP_3R3 deficiency is due to disruptions in neurons, Schwann cells, or both. It will be necessary to investigate the precise pathways disrupted by different variants and characterising IP_3R3-mediated Ca^{2+} flux under homeostatic and activating conditions for example in (genetically manipulated) neurons derived from human induced pluripotent stem cells, as they could be more relevant to the observed phenotype and would express a more relevant Ca^{2+} signalling toolkit than other cell types. Considering that IP_3-mediated Ca^{2+} signalling also regulates mitochondrial function and dysfunctional mitochondria have been implicated in axonal as well as demyelinating CMT[370,391,392], investigating how these pathways are implicated by the variants in *ITPR3* may shed further light on the disease pathomechanism.

Lastly, while all *ITPR3* variants identified in CMT patients result in a very similar clinical presentation with the exception of notably earlier disease onset for the R2524C variant, their impact on protein function differs among all of them. When expressed on a triple knockout background, homotetrameric channels all showed leakiness under steady-state conditions, although no significant difference in ER Ca^{2+} storage has been observed in fibroblasts of the Finnish patients with the V615M variant (**chapter 4**). This observation could be explained by a non-dominant impact of the variant in heterotetramers on leakiness of the channel. Additionally, elevated basal [Ca^{2+}] was predominantly observed in cells with extreme overexpression of the mutant IP_3R3 and comparable to basal [Ca^{2+}] levels in cells endogenously expressing WT IP_3R3 when expressed at similar levels. These results would indicate a continued burden on the cell to maintain basal Ca^{2+} homeostasis that could be counteracted at physiological protein expression levels but not when excessive numbers of leaky channels are present. In contrast to the uniform effect of all variants on channel leakiness, upon IP_3 stimulation V615M exhibited reduced, T1424M increased, and R2524C absent Ca^{2+} flux. The absent flux due to the R2524C is in line with

more severe/early-onset CMT diagnosed in the patients harbouring this variant. Unfortunately, the scarcity of clinical information about the patient with the previously published variant (T1424M) makes it difficult to formulate a hypothesis regarding the impact of the adverse effect on IP_3R3 signalling capacity on the clinical presentation. However, as was also observed for variants in *ITPR1* in SCA29, both LOF as well as GOF can result in the same clinical presentation[185,340].

6.1.3 Understanding the different disease phenotypes caused by *ITPR3* variants

The presented work highlights the wide spectrum of disease presentations due to *ITPR3* variants, ranging from isolated immunodeficiency to isolated CMT. We do however also describe one patient that presents features of both disease entities. It remains to be investigated why the variants result in such diverse phenotypes, although variants in *ITPR1* and *ITPR2* cause rather distinct disorders, namely cerebellar ataxia and anhidrosis. Sézary syndrome is the only exception as variants in both, *ITPR1* and *ITPR2*, were found to result in this phenotype, although in both cases variants were somatic and therefore not drivers of hereditary disease[193]. While the different phenotypes comparing the subtypes can partly be explained by their differential expression patterns in distinct cell types[90,252], our two patient studies ask for an additional explanation as variants occurred in the same receptor subtype. As discussed, IP_3Rs act as signalling hubs and are positively as well as negatively regulated by a large number of proteins[393]. Some of these interactions are indeed subtype-specific[394] and the lower sequence homology in the regulatory domain supports the diversity in regulation of the various subtypes. We therefore hypothesise that the variants we describe within the regulatory domain result in the disruption of distinct regulatory pathways that are important and non-redundant either in immune cells or the nervous system, but not in both. However, considering that the heterozygous parents of the immunodeficient P2 in **chapter 3** were clinically healthy, the disruption of the respective isolated regulatory mechanisms can seemingly be tolerated and may actually show some level of redundancy, while the additive disruption of two pathways causes a clinical phenotype in the compound heterozygous patient. This would be in line with observations in the single patient described with compound heterozygous variants in *CRACR2A* and reportedly healthy heterozygous parents[164]. In order to identify possibly disrupted protein interactions, the overexpression of mutated IP_3R3 receptors on a triple knockout background without endogenous IP_3R expression could be used in combination with co-immunoprecipitation or BioID with subsequent proteomic assessment to identify interaction partners. The latter approach allows to also identify proteins with transient interactions, as opposed to those interacting with the protein of interest at the time point of cell lysis[395]. Comparing the interaction partners to those identified when overexpressing the wild-type IP_3R3 could provide valuable insight into which regulatory pathways may be affected. It needs to be considered however that regulation remains cell type- and context-dependent, and choosing relevant cell types and conditions as relevant to the phenotype as possible will therefore be crucial.

We identified the R2524C variant, located in the highly conserved channel domain of the receptor, in one patient with severe immunodeficiency and axonal CMT and one patient with demyelinating CMT

only. Due to the severe impact of the mutation that was already suggested by studies identifying the residue as crucial for channel gating[254,255] and confirmed in our studies by proving the complete LOF in homotetramers *in vitro*, a dominant negative effect on wild-type channel subunits could be expected. Although we did not experimentally validate this hypothesis, a recent conference report from Wysocki *et al.* (2023 Clinical Immunology Society Annual Meeting, St. Louis, Missouri, USA) supports this proposition. They reported two children with immunodeficiency and a phenotype similar to that of P1 in our immunology manuscript (**chapter 3**), who both harbour a heterozygous R2524C variant and therefore the same *ITPR3* genotype as the CMT-only patient we report in **chapter 4**. The patients were 5 and 12 years old and no CMT phenotype was reported at the time. The group went on to generate a heterozygous knock-in mouse model of this specific variant and indeed reported a dominant negative effect with severe T- and B-cell immunodeficiency. While this work is not yet published and the development of CMT in these patients may need to be followed-up closely, it suggests a dominant detrimental effect on IP_3R function *in vivo* resulting in immunodeficiency, and is not conform with our initial hypothesis of the immune phenotype only arising in compound heterozygous genetic backgrounds. Currently, there is however no explanation for the absence of severe immunological symptoms in the heterozygous CMT-only patient, however, the complex genetic background in highly consanguineous populations such as Ashkenazi Jews could contribute to the observed discrepancy. Additionally, as primary cells were not available for analysis and no clinical immunological investigations have been performed, it cannot be ruled out that there is variable expressivity of this characteristic.

While the observed pleiotropy of *ITPR3* variants possibly due to the differential impact on regulatory mechanisms has been discussed before, the effect on protein interactions with downstream-signalling partners needs to be considered and investigated as well. Our investigations showed that the Ca^{2+}-dependent nuclear translocation of NFAT is defective in the patient with isolated immunodeficiency, selecting this prototypical pathway as a proof-of-concept. However, as introduced in **chapter 1**, Ca^{2+} is involved in the regulation of a number of additional pathways such as energy metabolism, autophagy, and apoptosis. We did not study the impact of the variants on these pathways but considering that their mediation is often also contact-dependent, they may contribute to the pleiotropy due to different cell-specific dependencies on these pathways. As an example, IP_3Rs are known to interact with Grp75, that bridges the contact to VDAC1 in the outer mitochondrial membrane, which in turn is associated with the MCU in the inner mitochondrial membrane[134]. Disrupted interaction between IP_3Rs and Grp75 could abolish this complex and thereby prevent increased metabolism during Ca^{2+}-mediated activation. On the other hand, the finding that homotetrameric channels with both CMT-specific variants (T1424M and V615M) as well as the R2524C variant resulted in leaky IP_3Rs, if interaction with Grp75 is not disrupted, the increased Ca^{2+} flux to mitochondria could render cells more prone to undergoing apoptosis due to accelerated Ca^{2+} overload. Small changes in Ca^{2+} homeostasis could be especially important in cellular

contexts that result in high ER stress or require autophagy to satisfy high energy consumption, such as in plasma cells[52,396]. Alternatively, disrupted IP_3R/Grp75/VDAC1/MCU interaction and thereby impaired draining of cytosolic Ca^{2+} into the mitochondrial "sink" could cause high local Ca^{2+} concentrations that in turn could inhibit continued IP_3R gating[397] and prevent sufficient emptying of ER stores to induce downstream signalling. While the results presented in this combined work investigated $[Ca^{2+}]_{cyt}$ and indirectly the filling of ER stores, additional studies for example using ER- or mitochondria-specific Ca^{2+} indicators alone or in combination with cytosolic indicators could provide a more detailed overview on the extent of disruption of homeostatic and induced Ca^{2+} signals within the cell[398].

6.2 Considerations for therapeutic intervention in IP_3R3 deficiency

While reaching a genetic diagnosis is often already an important step for the patients as well as their caretakers, the ultimate goal is to be able to provide targeted treatment to reduce disease burden and prevent complications. When it comes to Calcium signalling, the complex dependencies and cross-talk between proteins as well as its importance many cell types and pathways complicate drug development. Nonetheless, a number of molecules inhibiting Ca^{2+} channels directly or reducing activity of Ca^{2+}-dependent signalling have been developed and are used in clinical practice. For example, inhibitors of different subtypes of VOCCs are used to treat hypertension, pain, and seizures, but often exhibit side effects due to insufficient channel selectivity or the requirement of high-dose administration for the target cell type that could damage other tissues[399].

Especially in situations requiring immune suppression, for example after organ transplantation, Calcineurin inhibitors (CNIs) such as Cyclosporin A (CsA) or Tacrolimus, are often used with the aim of preventing NFAT translocation to the nucleus, thereby inhibiting lymphocyte activation. These drugs are very successfully used and despite the widespread expression profile of Calcineurin show preferential selectivity for lymphocyte-restricted effects. This may be due to varying degrees of sensitivity to drug doses in different cell types. However, patients treated with CNIs do exhibit a number of side effects with acute or chronic nephrotoxicity being the most common, also in patients receiving non-renal transplants. In addition to other side effects related to electrolyte homeostasis and cardiovascular function[400], neurotoxicity has been reported with lower frequencies[401,402]. While mild symptoms such as tremor or neuralgia are more common under Tacrolimus treatment but often do not require dose adjustment[403], severe complications like seizures and cerebellar ataxia are more rare but can still affect up to 5% of patients[404]. Occurrence of neurotoxicity can be linked to pre-disposing conditions or drugs taken simultaneously, although discontinuation of CsA or isolated use thereof have been shown to reverse or induce neurotoxicity, respectively[405,406]. Interestingly, while CNIs inhibit the same pathway affected in IP_3R3-deficient patients with immunodeficiency (**chapter 3**), we did not

observe any effect on renal function so far, although this may require close monitoring especially in P1 harbouring the LOF R2524C variant. Moreover, the neurotoxicity observed in combination with CNIs typically affects the CNS, which seems to be unaffected in P1 as well as the CMT patients we describe in **chapter 4**. One possible explanation could be the limited dependency of the peripheral nervous system on Calcineurin-mediated signalling with other Ca^{2+}-mediated pathways driving peripheral neuropathy. The residual activity of IP_3Rs and thereby Calcineurin signalling would be sufficient to prevent CNS pathology in these patients, whereas this activity may be reduced below the tolerable threshold under CNI treatment.

Several attempts have been made to develop small molecules that could be used to directly modulate IP_3R activity, but have so far only been successful for experimental approaches in simplified models[407]. This is due to the complexity of IP_3R regulation in particular and Ca^{2+} signalling in general pointed out several times throughout this thesis. In order to develop useful drugs appropriate for clinical application, many more in-depth studies need to be performed to allow the design of subtype-specific modulators and investigate the sensitivity of different cell types to these molecules. Considering the tight regulation of Ca^{2+} signalling, it may be required to develop drugs that act in a state-dependent way and only exert their activating or inhibiting function when the pathway is triggered, although this is extremely challenging to achieve. Additionally, considering our description of patients with variants in the same gene but completely different phenotypes based on the affected cell type, a "one-fits-all" drug in IP_3R3 deficiency seems to be challenging to achieve. Although all patients described may benefit from selective IP_3R3 agonists, targeted delivery to the respective cell type would have to be ensured to prevent adverse events. Nonetheless, as the previously reported T1424M CMT variant showed increased Ca^{2+} signalling at low agonist levels, disease burden caused by GOF variants could probably be partially alleviated with the use of CNIs, at least when they affect the immune system. As despite the advances presented in this thesis little is known however on the effect of IP_3R3 deficiency on other immune cell subsets, further investigation is needed to be able to safely administer known drugs in these patients.

6.3 Conclusion and future perspectives

The work presented in this thesis describes a novel gene, *ITPR3*, as a cause of hereditary disorders that should be considered for diagnosis in a clinical setting. It highlights the importance of in-depth genetic investigations if no known genetic disease causes can be identified following initial assessment. Although the combined number of four unrelated kindreds – two patients of two kindreds presenting with immunodeficiency with or without neuropathy and five individuals of two kindreds presenting with neuropathy – is still low, their study provided first insights into the pathology of IP_3R3 deficiency. Some of the important questions that will need to be addressed in future studies are (i) the cause of the seeming cell-type specificity of some of the identified variants causing either immune dysregulation or

neuropathy, (ii) the possibility for incomplete penetrance or variable expressivity of a single variant causing variable phenotypes, and (iii) the impact of the variants in heteromultimeric channel configurations. Insights gained from these studies may also advance the development of subtype-specific and targeted modulators of IP_3R activity. The identification and study of new patients and variants in *ITPR3* will be crucial for recognizing and explaining possible genotype-phenotype correlations and the work presented here paves the way for improved diagnosis and genetic counselling of these patients.

7 References

1 Abbott S, Fairbanks DJ. Experiments on Plant Hybrids by Gregor Mendel. *Genetics* 2016; **204**: 407–422.

2 Chan K-W, Wong C-Y, Leung D, Yang X, Fok SFS, Mak PHS *et al.* Targeted Gene Sanger Sequencing Should Remain the First-Tier Genetic Test for Children Suspected to Have the Five Common X-Linked Inborn Errors of Immunity. *Front Immunol* 2022; **13**. doi:10.3389/fimmu.2022.883446.

3 Karimi E, Mahmoudian F, Reyes SOL, Bargir UA, Madkaikar M, Artac H *et al.* Approach to genetic diagnosis of inborn errors of immunity through next-generation sequencing. *Mol Immunol* 2021; **137**: 57–66.

4 Mazzarotto F, Olivotto I, Walsh R. Advantages and Perils of Clinical Whole-Exome and Whole-Genome Sequencing in Cardiomyopathy. *Cardiovasc Drugs Ther* 2020; **34**: 241–253.

5 Meyts I, Bosch B, Bolze A, Boisson B, Itan Y, Belkadi A *et al.* Exome and genome sequencing for inborn errors of immunity. *J Allergy Clin Immunol* 2016; **138**: 957–969.

6 Bamshad MJ, Ng SB, Bigham AW, Tabor HK, Emond MJ, Nickerson DA *et al.* Exome sequencing as a tool for Mendelian disease gene discovery. *Nat Rev Genet* 2011; **12**: 745–755.

7 Bucciol G, Van Nieuwenhove E, Moens L, Itan Y, Meyts I. Whole exome sequencing in inborn errors of immunity: use the power but mind the limits. *Curr Opin Allergy Clin Immunol* 2017; **17**: 421–430.

8 Sefid Dashti MJ, Gamieldien J. A practical guide to filtering and prioritizing genetic variants. *Biotechniques* 2017; **62**: 18–30.

9 Karczewski KJ, Francioli LC, Tiao G, Cummings BB, Alföldi J, Wang Q *et al.* The mutational constraint spectrum quantified from variation in 141,456 humans. *Nature* 2020; **581**: 434–443.

10 Cingolani P, Platts A, Wang LL, Coon M, Nguyen T, Wang L *et al.* A program for annotating and predicting the effects of single nucleotide polymorphisms, SnpEff: SNPs in the genome of Drosophila melanogaster strain w1118; iso-2; iso-3. *Fly (Austin)* 2012; **6**: 80–92.

11 Adzhubei I, Jordan DM, Sunyaev SR. Predicting functional effect of human missense mutations using PolyPhen-2. *Curr Protoc Hum Genet* 2013; **Chapter 7**: Unit7.20.

12 Kircher M, Witten DM, Jain P, O'Roak BJ, Cooper GM, Shendure J. A general framework for estimating the relative pathogenicity of human genetic variants. *Nat Genet* 2014; **46**: 310–5.

13 Bousfiha AA, Jeddane L, Ailal F, Benhsaien I, Mahlaoui N, Casanova J-L *et al.* Primary immunodeficiency diseases worldwide: more common than generally thought. *J Clin Immunol* 2013; **33**: 1–7.

14 Tangye SG, Al-Herz W, Bousfiha A, Cunningham-Rundles C, Franco JL, Holland SM *et al.* Human Inborn Errors of Immunity: 2022 Update on the Classification from the International Union of Immunological Societies Expert Committee. *J Clin Immunol* 2022; **42**: 1473–1507.

15 Asano T, Khourieh J, Zhang P, Rapaport F, Spaan AN, Li J *et al.* Human STAT3 variants underlie autosomal dominant hyper-IgE syndrome by negative dominance. *J Exp Med* 2021; **218**. doi:10.1084/jem.20202592.

16 Leiding JW, Vogel TP, Santarlas VGJ, Mhaskar R, Smith MR, Carisey A *et al.* Monogenic early-onset lymphoproliferation and autoimmunity: Natural history of STAT3 gain-of-function syndrome. *J Allergy Clin Immunol* 2023; **151**: 1081–1095.

17 Wong HH, Seet SH, Maier M, Gurel A, Traspas RM, Lee C *et al.* Loss of C2orf69 defines a fatal autoinflammatory syndrome in humans and zebrafish that evokes a glycogen-storage-associated mitochondriopathy. *Am J Hum Genet* 2021; **108**: 1301–1317.

18 Lausberg E, Gießelmann S, Dewulf JP, Wiame E, Holz A, Salvarinova R *et al.* C2orf69 mutations disrupt mitochondrial function and cause a multisystem human disorder with recurring autoinflammation. *J Clin Invest* 2021; **131**. doi:10.1172/JCI143078.

19 Bordignon C, Notarangelo LD, Nobili N, Ferrari G, Casorati G, Panina P *et al.* Gene Therapy in Peripheral Blood Lymphocytes and Bone Marrow for ADA − Immunodeficient Patients. *Science (80-)* 1995; **270**: 470–475.

20 Blaese RM, Culver KW, Miller AD, Carter CS, Fleisher T, Clerici M *et al.* T Lymphocyte-Directed Gene Therapy for ADA − SCID: Initial Trial Results After 4 Years. *Science (80-)* 1995; **270**: 475–480.

21 Cavazzana-Calvo M, Hacein-Bey S, Basile G de Saint, Gross F, Yvon E, Nusbaum P *et al.* Gene Therapy of Human Severe Combined Immunodeficiency (SCID)-X1 Disease. *Science (80-)* 2000; **288**: 669–672.

22 Aiuti A, Slavin S, Aker M, Ficara F, Deola S, Mortellaro A *et al.* Correction of ADA-SCID by Stem Cell Gene Therapy Combined with Nonmyeloablative Conditioning. *Science (80-)* 2002; **296**: 2410–2413.

23 Cowan MJ, Yu J, Facchino J, Fraser-Browne C, Sanford U, Kawahara M *et al.* Lentiviral Gene Therapy for Artemis-Deficient SCID. *N Engl J Med* 2022; **387**: 2344–2355.

24 Hacein-Bey Abina S, Gaspar HB, Blondeau J, Caccavelli L, Charrier S, Buckland K *et al.* Outcomes Following Gene Therapy in Patients With Severe Wiskott-Aldrich Syndrome. *JAMA* 2015; **313**: 1550.

25 Kohn DB, Booth C, Kang EM, Pai S-Y, Shaw KL, Santilli G *et al.* Lentiviral gene therapy for X-linked chronic granulomatous disease. *Nat Med* 2020; **26**: 200–206.

26 Arlabosse T, Booth C, Candotti F. Gene Therapy for Inborn Errors of Immunity. *J Allergy Clin Immunol Pract* 2023; **11**: 1592–1601.

27 Kong FK, Chen CL, Six A, Hockett RD, Cooper MD. T cell receptor gene deletion circles identify recent thymic emigrants in the peripheral T cell pool. *Proc Natl Acad Sci U S A* 1999; **96**: 1536–40.

28 Serana F, Chiarini M, Zanotti C, Sottini A, Bertoli D, Bosio A *et al.* Use of V(D)J recombination excision circles to identify T- and B-cell defects and to monitor the treatment in primary and acquired immunodeficiencies. *J Transl Med* 2013; **11**: 119.

29 Elsink K, van Montfrans JM, van Gijn ME, Blom M, van Hagen PM, Kuijpers TW *et al.* Cost and impact of early diagnosis in primary immunodeficiency disease: A literature review. *Clin Immunol* 2020; **213**: 108359.

30 Farnaes L, Hildreth A, Sweeney NM, Clark MM, Chowdhury S, Nahas S *et al.* Rapid whole-genome sequencing decreases infant morbidity and cost of hospitalization. *npj Genomic Med* 2018; **3**: 10.

31 Lankester AC, Albert MH, Booth C, Gennery AR, Güngör T, Hönig M *et al.* EBMT/ESID inborn errors working party guidelines for hematopoietic stem cell transplantation for inborn errors of immunity. *Bone Marrow Transplant* 2021; **56**: 2052–2062.

32 King JR, Grill K, Hammarström L. Genomic-Based Newborn Screening for Inborn Errors of Immunity: Practical and Ethical Considerations. *Int J Neonatal Screen* 2023; **9**: 22.

33 Limbäck-Stokin K, Korzus E, Nagaoka-Yasuda R, Mayford M. Nuclear Calcium/Calmodulin Regulates Memory Consolidation. *J Neurosci* 2004; **24**: 10858–10867.

34 Berridge MJ, Lipp P, Bootman MD. The versatility and universality of calcium signalling. *Nat Rev Mol Cell Biol* 2000; **1**: 11–21.

35 IINO M. Spatiotemporal dynamics of Ca2+ signaling and its physiological roles. *Proc Japan Acad Ser B* 2010; **86**: 244–256.

36 Berridge MJ, Bootman MD, Roderick HL. Calcium signalling: dynamics, homeostasis and remodelling. *Nat Rev Mol Cell Biol* 2003; **4**: 517–29.

37 Bootman MD, Bultynck G. Fundamentals of Cellular Calcium Signaling: A Primer. *Cold Spring Harb Perspect Biol* 2020; **12**. doi:10.1101/cshperspect.a038802.

38 Lytton J. Na+/Ca2+ exchangers: three mammalian gene families control Ca2+ transport. *Biochem J* 2007; **406**: 365–82.

39 Secondo A, Petrozziello T, Tedeschi V, Boscia F, Pannaccione A, Molinaro P *et al.* Nuclear localization of NCX: Role in Ca2+ handling and pathophysiological implications. *Cell Calcium* 2020; **86**: 102143.

40 Palty R, Silverman WF, Hershfinkel M, Caporale T, Sensi SL, Parnis J *et al.* NCLX is an essential component of mitochondrial Na+/Ca2+ exchange. *Proc Natl Acad Sci U S A* 2010; **107**: 436–41.

41 Boyman L, Williams GSB, Khananshvili D, Sekler I, Lederer WJ. NCLX: the mitochondrial sodium calcium exchanger. *J Mol Cell Cardiol* 2013; **59**: 205–13.

42 Schultz JM, Yang Y, Caride AJ, Filoteo AG, Penheiter AR, Lagziel A *et al.* Modification of human hearing loss by plasma-membrane calcium pump PMCA2. *N Engl J Med* 2005; **352**: 1557–64.

43 Zanni G, Calì T, Kalscheuer VM, Ottolini D, Barresi S, Lebrun N *et al.* Mutation of plasma membrane Ca2+ ATPase isoform 3 in a family with X-linked congenital cerebellar ataxia impairs Ca2+ homeostasis. *Proc Natl Acad Sci U S A* 2012; **109**: 14514–9.

44 Krebs J. Structure, Function and Regulation of the Plasma Membrane Calcium Pump in Health and Disease. *Int J Mol Sci* 2022; **23**. doi:10.3390/ijms23031027.

45 Olesen C, Sørensen TL-M, Nielsen RC, Møller JV, Nissen P. Dephosphorylation of the Calcium Pump Coupled to Counterion Occlusion. *Science (80-)* 2004; **306**: 2251–2255.

46 Olesen C, Picard M, Winther A-ML, Gyrup C, Morth JP, Oxvig C *et al.* The structural basis of calcium transport by the calcium pump. *Nature* 2007; **450**: 1036–42.

47 Lemos FO, Bultynck G, Parys JB. A comprehensive overview of the complex world of the endo- and sarcoplasmic reticulum Ca2+-leak channels. *Biochim Biophys Acta - Mol Cell Res* 2021; **1868**: 119020.

48 Das HK, Tchedre K, Mueller B. Repression of transcription of presenilin-1 inhibits γ-secretase independent ER Ca^{2+} leak that is impaired by FAD mutations. *J Neurochem* 2012; **122**: 487–500.

49 Thebault S, Lemonnier L, Bidaux G, Flourakis M, Bavencoffe A, Gordienko D *et al.* Novel Role of Cold/Menthol-sensitive Transient Receptor Potential Melastatine Family Member 8 (TRPM8) in the Activation of Store-operated Channels in LNCaP Human Prostate Cancer Epithelial Cells. *J Biol Chem* 2005; **280**: 39423–39435.

50 Van Coppenolle F, Vanden Abeele F, Slomianny C, Flourakis M, Hesketh J, Dewailly E *et al.* Ribosome-translocon complex mediates calcium leakage from endoplasmic reticulum stores. *J Cell Sci* 2004; **117**: 4135–4142.

51 Tu H, Nelson O, Bezprozvanny A, Wang Z, Lee S-F, Hao Y-H *et al.* Presenilins form ER Ca2+ leak channels, a function disrupted by familial Alzheimer's disease-linked mutations. *Cell* 2006; **126**: 981–93.

52 Van Nieuwenhove E, Barber JS, Neumann J, Smeets E, Willemsen M, Pasciuto E *et al.* Defective

Sec61α1 underlies a novel cause of autosomal dominant severe congenital neutropenia. *J Allergy Clin Immunol* 2020; **146**: 1180–1193.

53 Eltit JM, Yang T, Li H, Molinski TF, Pessah IN, Allen PD *et al.* RyR1-mediated Ca2+ leak and Ca2+ entry determine resting intracellular Ca2+ in skeletal myotubes. *J Biol Chem* 2010; **285**: 13781–7.

54 Schwaller B. Cytosolic Ca2+ Buffers. *Cold Spring Harb Perspect Biol* 2010; **2**: a004051–a004051.

55 Prins D, Michalak M. Organellar calcium buffers. *Cold Spring Harb Perspect Biol* 2011; **3**. doi:10.1101/cshperspect.a004069.

56 Pauls TL, Cox JA, Berchtold MW. The Ca2+-binding proteins parvalbumin and oncomodulin and their genes: new structural and functional findings. *Biochim Biophys Acta - Gene Struct Expr* 1996; **1306**: 39–54.

57 Henzl MT, Tanner JJ. Solution structure of Ca2+-free rat α-parvalbumin. *Protein Sci* 2008; **17**: 431–438.

58 Ingersoll RJ, Wasserman RH. Vitamin D3-induced calcium-binding protein. Binding characteristics, conformational effects, and other properties. *J Biol Chem* 1971; **246**: 2808–14.

59 Hong E-J, Jeung E-B. Biological Significance of Calbindin-D9k within Duodenal Epithelium. *Int J Mol Sci* 2013; **14**: 23330–23340.

60 Lièvremont JP, Rizzuto R, Hendershot L, Meldolesi J. BiP, a major chaperone protein of the endoplasmic reticulum lumen, plays a direct and important role in the storage of the rapidly exchanging pool of Ca2+. *J Biol Chem* 1997; **272**: 30873–9.

61 Macer DR, Koch GL. Identification of a set of calcium-binding proteins in reticuloplasm, the luminal content of the endoplasmic reticulum. *J Cell Sci* 1988; **91 (Pt 1)**: 61–70.

62 Dudek J, Benedix J, Cappel S, Greiner M, Jalal C, Müller L *et al.* Functions and pathologies of BiP and its interaction partners. *Cell Mol Life Sci* 2009; **66**: 1556–69.

63 Suzuki CK, Bonifacino JS, Lin AY, Davis MM, Klausner RD. Regulating the retention of T-cell receptor alpha chain variants within the endoplasmic reticulum: Ca(2+)-dependent association with BiP. *J Cell Biol* 1991; **114**: 189–205.

64 Biswas C, Ostrovsky O, Makarewich CA, Wanderling S, Gidalevitz T, Argon Y. The peptide-binding activity of GRP94 is regulated by calcium. *Biochem J* 2007; **405**: 233–41.

65 Pankratov Y, Lalo U, Krishtal OA, Verkhratsky A. P2X receptors and synaptic plasticity. *Neuroscience* 2009; **158**: 137–148.

66 Schenk U, Westendorf AM, Radaelli E, Casati A, Ferro M, Fumagalli M *et al.* Purinergic Control of T Cell Activation by ATP Released Through Pannexin-1 Hemichannels. *Sci Signal* 2008; **1**. doi:10.1126/scisignal.1160583.

67 Yip L, Woehrle T, Corriden R, Hirsh M, Chen Y, Inoue Y *et al.* Autocrine regulation of T-cell activation by ATP release and P2X 7 receptors. *FASEB J* 2009; **23**: 1685–1693.

68 Eisner DA, Caldwell JL, Kistamás K, Trafford AW. Calcium and Excitation-Contraction Coupling in the Heart. *Circ Res* 2017; **121**: 181–195.

69 Cabral MD, Paulet P-E, Robert V, Gomes B, Renoud M-L, Savignac M *et al.* Knocking down Cav1 calcium channels implicated in Th2 cell activation prevents experimental asthma. *Am J Respir Crit Care Med* 2010; **181**: 1310–7.

70 Rosa N, Triffaux E, Robert V, Mars M, Klein M, Bouchaud G *et al.* The β and α2δ auxiliary

subunits of voltage-gated calcium channel 1 (Cav1) are required for TH2 lymphocyte function and acute allergic airway inflammation. *J Allergy Clin Immunol* 2018; **142**: 892-903.e8.

71 Erdogmus S, Concepcion AR, Yamashita M, Sidhu I, Tao AY, Li W *et al.* Cavβ1 regulates T cell expansion and apoptosis independently of voltage-gated Ca2+ channel function. *Nat Commun* 2022; **13**: 2033.

72 SMEDT H De, MISSIAEN L, PARYS JB, HENNING RH, SIENAERT I, VANLINGEN S *et al.* Isoform diversity of the inositol trisphosphate receptor in cell types of mouse origin. *Biochem J* 1997; **322**: 575–583.

73 Newton CL, Mignery GA, Südhof TC. Co-expression in vertebrate tissues and cell lines of multiple inositol 1,4,5-trisphosphate (InsP3) receptors with distinct affinities for InsP3. *J Biol Chem* 1994; **269**: 28613–28619.

74 Takeshima H, Nishimura S, Matsumoto T, Ishida H, Kangawa K, Minamino N *et al.* Primary structure and expression from complementary DNA of skeletal muscle ryanodine receptor. *Nature* 1989; **339**: 439–445.

75 Nakai J, Imagawa T, Hakamata Y, Shigekawa M, Takeshima H, Numa S. Primary structure and functional expression from cDN A of the cardiac ryanodine receptor/calcium release channel. *FEBS Lett* 1990; **271**: 169–177.

76 Hakamata Y, Nakai J, Takeshima H, Imoto K. Primary structure and distribution of a novel ryanodine receptor/calcium release channel from rabbit brain. *FEBS Lett* 1992; **312**: 229–235.

77 Evellin S, Nolte J, Tysack K, vom Dorp F, Thiel M, Weernink PAO *et al.* Stimulation of Phospholipase C-ε by the M3Muscarinic Acetylcholine Receptor Mediated by Cyclic AMP and the GTPase Rap2B. *J Biol Chem* 2002; **277**: 16805–16813.

78 Newbern J, Birchmeier C. Nrg1/ErbB signaling networks in Schwann cell development and myelination. *Semin Cell Dev Biol* 2010; **21**: 922–8.

79 Birchmeier C, Nave K. Neuregulin-1, a key axonal signal that drives Schwann cell growth and differentiation. *Glia* 2008; **56**: 1491–1497.

80 Bootman M, Niggli E, Berridge M, Lipp P. Imaging the hierarchical Ca2+ signalling system in HeLa cells. *J Physiol* 1997; **499**: 307–314.

81 Parker I, Smith IF. Recording single-channel activity of inositol trisphosphate receptors in intact cells with a microscope, not a patch clamp. *J Gen Physiol* 2010; **136**: 119–127.

82 Yao Y, Choi J, Parker I. Quantal puffs of intracellular Ca2+ evoked by inositol trisphosphate in Xenopus oocytes. *J Physiol* 1995; **482 (Pt 3**: 533–53.

83 Stathopulos PB, Zheng L, Li G-Y, Plevin MJ, Ikura M. Structural and Mechanistic Insights into STIM1-Mediated Initiation of Store-Operated Calcium Entry. *Cell* 2008; **135**: 110–122.

84 Wu MM, Buchanan J, Luik RM, Lewis RS. Ca2+ store depletion causes STIM1 to accumulate in ER regions closely associated with the plasma membrane. *J Cell Biol* 2006; **174**: 803–813.

85 Prole DL, Taylor CW. Inositol 1,4,5-trisphosphate receptors and their protein partners as signalling hubs. *J Physiol* 2016; **594**: 2849–66.

86 Uchida K, Miyauchi H, Furuichi T, Michikawa T, Mikoshiba K. Critical Regions for Activation Gating of the Inositol 1,4,5-Trisphosphate Receptor. *J Biol Chem* 2003; **278**: 16551–16560.

87 Fan G, Baker MR, Wang Z, Seryshev AB, Ludtke SJ, Baker ML *et al.* Cryo-EM reveals ligand induced allostery underlying InsP3R channel gating. *Cell Res* 2018; **28**: 1158–1170.

88 Fan G, Baker MR, Terry LE, Arige V, Chen M, Seryshev AB *et al.* Conformational motions and

ligand-binding underlying gating and regulation in IP3R channel. *Nat Commun* 2022; **13**: 6942.

89 Alzayady KJ, Wang L, Chandrasekhar R, Wagner LE, Van Petegem F, Yule DI. Defining the stoichiometry of inositol 1,4,5-trisphosphate binding required to initiate Ca 2+ release. *Sci Signal* 2016; **9**. doi:10.1126/scisignal.aad6281.

90 Miyakawa T, Maeda A, Yamazawa T, Hirose K, Kurosaki T, Iino M. Encoding of Ca2+ signals by differential expression of IP3 receptor subtypes. *EMBO J* 1999; **18**: 1303–8.

91 Vanlingen S, Sipma H, De Smet P, Callewaert G, Missiaen L, De Smedt H *et al.* Ca2+ and calmodulin differentially modulate myo-inositol 1,4, 5-trisphosphate (IP3)-binding to the recombinant ligand-binding domains of the various IP3 receptor isoforms. *Biochem J* 2000; **346 Pt 2**: 275–80.

92 Iino M. Biphasic Ca2+ dependence of inositol 1,4,5-trisphosphate-induced Ca release in smooth muscle cells of the guinea pig taenia caeci. *J Gen Physiol* 1990; **95**: 1103–22.

93 Marshall IC, Taylor CW. Two calcium-binding sites mediate the interconversion of liver inositol 1,4,5-trisphosphate receptors between three conformational states. *Biochem J* 1994; **301 (Pt 2**: 591–8.

94 Foskett JK, Daniel Mak D-O. Regulation of IP(3)R Channel Gating by Ca(2+) and Ca(2+) Binding Proteins. *Curr Top Membr* 2010; **66**: 235–72.

95 Arige V, Terry LE, Wagner LE, Malik S, Baker MR, Fan G *et al.* Functional determination of calcium-binding sites required for the activation of inositol 1,4,5-trisphosphate receptors. *Proc Natl Acad Sci* 2022; **119**. doi:10.1073/pnas.2209267119.

96 Bezprozvanny I, Ehrlich BE. ATP modulates the function of inositol 1,4,5-trisphosphate-gated channels at two sites. *Neuron* 1993; **10**: 1175–1184.

97 Tu H, Wang Z, Nosyreva E, De Smedt H, Bezprozvanny I. Functional Characterization of Mammalian Inositol 1,4,5-Trisphosphate Receptor Isoforms. *Biophys J* 2005; **88**: 1046–1055.

98 Ando H, Mizutani A, Matsu-ura T, Mikoshiba K. IRBIT, a novel inositol 1,4,5-trisphosphate (IP3) receptor-binding protein, is released from the IP3 receptor upon IP3 binding to the receptor. *J Biol Chem* 2003; **278**: 10602–12.

99 Ando H, Mizutani A, Kiefer H, Tsuzurugi D, Michikawa T, Mikoshiba K. IRBIT Suppresses IP3 Receptor Activity by Competing with IP3 for the Common Binding Site on the IP3 Receptor. *Mol Cell* 2006; **22**: 795–806.

100 Ferris CD, Cameron AM, Bredt DS, Huganir RL, Snyder SH. Inositol 1,4,5-trisphosphate receptor is phosphorylated by cyclic AMP-dependent protein kinase at serines 1755 and 1589. *Biochem Biophys Res Commun* 1991; **175**: 192–8.

101 Yamamoto H, Maeda N, Niinobe M, Miyamoto E, Mikoshiba K. Phosphorylation of P400 protein by cyclic AMP-dependent protein kinase and Ca2+/calmodulin-dependent protein kinase II. *J Neurochem* 1989; **53**: 917–23.

102 Ferris CD, Huganir RL, Bredt DS, Cameron AM, Snyder SH. Inositol trisphosphate receptor: phosphorylation by protein kinase C and calcium calmodulin-dependent protein kinases in reconstituted lipid vesicles. *Proc Natl Acad Sci U S A* 1991; **88**: 2232–5.

103 Bare DJ, Kettlun CS, Liang M, Bers DM, Mignery GA. Cardiac type 2 inositol 1,4,5-trisphosphate receptor: interaction and modulation by calcium/calmodulin-dependent protein kinase II. *J Biol Chem* 2005; **280**: 15912–20.

104 Soghoian D, Jayaraman V, Silane M, Berenstein A, Jayaraman T. Inositol 1,4,5-trisphosphate receptor phosphorylation in breast cancer. *Tumour Biol* 2005; **26**: 207–12.

105 Bai G-R, Yang L-H, Huang X-Y, Sun F-Z. Inositol 1,4,5-trisphosphate receptor type 1 phosphorylation and regulation by extracellular signal-regulated kinase. *Biochem Biophys Res Commun* 2006; **348**: 1319–27.

106 Tang T-S, Tu H, Wang Z, Bezprozvanny I. Modulation of type 1 inositol (1,4,5)-trisphosphate receptor function by protein kinase a and protein phosphatase 1alpha. *J Neurosci* 2003; **23**: 403–15.

107 Nakade S, Rhee SK, Hamanaka H, Mikoshiba K. Cyclic AMP-dependent phosphorylation of an immunoaffinity-purified homotetrameric inositol 1,4,5-trisphosphate receptor (type I) increases Ca2+ flux in reconstituted lipid vesicles. *J Biol Chem* 1994; **269**: 6735–42.

108 Straub S V, Giovannucci DR, Bruce JIE, Yule DI. A role for phosphorylation of inositol 1,4,5-trisphosphate receptors in defining calcium signals induced by Peptide agonists in pancreatic acinar cells. *J Biol Chem* 2002; **277**: 31949–56.

109 LeBeau AP, Yule DI, Groblewski GE, Sneyd J. Agonist-dependent phosphorylation of the inositol 1,4,5-trisphosphate receptor: A possible mechanism for agonist-specific calcium oscillations in pancreatic acinar cells. *J Gen Physiol* 1999; **113**: 851–72.

110 Giovannucci DR, Groblewski GE, Sneyd J, Yule DI. Targeted phosphorylation of inositol 1,4,5-trisphosphate receptors selectively inhibits localized Ca2+ release and shapes oscillatory Ca2+ signals. *J Biol Chem* 2000; **275**: 33704–11.

111 Wojcikiewicz RJ, Luo SG. Phosphorylation of inositol 1,4,5-trisphosphate receptors by cAMP-dependent protein kinase. Type I, II, and III receptors are differentially susceptible to phosphorylation and are phosphorylated in intact cells. *J Biol Chem* 1998; **273**: 5670–7.

112 Ivanova H, Vervliet T, Monaco G, Terry LE, Rosa N, Baker MR *et al.* Bcl-2-Protein Family as Modulators of IP3 Receptors and Other Organellar Ca2+ Channels. *Cold Spring Harb Perspect Biol* 2020; **12**. doi:10.1101/cshperspect.a035089.

113 Distelhorst CW, Bootman MD. Creating a New Cancer Therapeutic Agent by Targeting the Interaction between Bcl-2 and IP3 Receptors. *Cold Spring Harb Perspect Biol* 2019; **11**. doi:10.1101/cshperspect.a035196.

114 Li C, Wang X, Vais H, Thompson CB, Foskett JK, White C. Apoptosis regulation by Bcl-x(L) modulation of mammalian inositol 1,4,5-trisphosphate receptor channel isoform gating. *Proc Natl Acad Sci U S A* 2007; **104**: 12565–70.

115 White C, Li C, Yang J, Petrenko NB, Madesh M, Thompson CB *et al.* The endoplasmic reticulum gateway to apoptosis by Bcl-X(L) modulation of the InsP3R. *Nat Cell Biol* 2005; **7**: 1021–8.

116 Rosa N, Ivanova H, Wagner LE, Kale J, La Rovere R, Welkenhuyzen K *et al.* Bcl-xL acts as an inhibitor of IP3R channels, thereby antagonizing Ca2+-driven apoptosis. *Cell Death Differ* 2022; **29**: 788–805.

117 Babu YS, Sack JS, Greenhough TJ, Bugg CE, Means AR, Cook WJ. Three-dimensional structure of calmodulin. *Nature* 1985; **315**: 37–40.

118 Meador WE, Means AR, Quiocho FA. Modulation of calmodulin plasticity in molecular recognition on the basis of x-ray structures. *Science* 1993; **262**: 1718–21.

119 Crivici A, Ikura M. Molecular and structural basis of target recognition by calmodulin. *Annu Rev Biophys Biomol Struct* 1995; **24**: 85–116.

120 Ikura M, Clore GM, Gronenborn AM, Zhu G, Klee CB, Bax A. Solution structure of a calmodulin-target peptide complex by multidimensional NMR. *Science* 1992; **256**: 632–8.

121 Bennett MK, Erondu NE, Kennedy MB. Purification and characterization of a calmodulin-dependent protein kinase that is highly concentrated in brain. *J Biol Chem* 1983; **258**: 12735–44.

122 Ye Q, Wang H, Zheng J, Wei Q, Jia Z. The complex structure of calmodulin bound to a calcineurin peptide. *Proteins* 2008; **73**: 19–27.

123 Juranic N, Atanasova E, Filoteo AG, Macura S, Prendergast FG, Penniston JT *et al.* Calmodulin wraps around its binding domain in the plasma membrane Ca2+ pump anchored by a novel 18-1 motif. *J Biol Chem* 2010; **285**: 4015–4024.

124 Braun AP, Schulman H. The Multifunctional Calcium/Calmodulin-Dependent Protein Kinase: From Form to Function. *Annu Rev Physiol* 1995; **57**: 417–445.

125 Alev C, Urschel S, Sonntag S, Zoidl G, Fort AG, Höher T *et al.* The neuronal connexin36 interacts with and is phosphorylated by CaMKII in a way similar to CaMKII interaction with glutamate receptors. *Proc Natl Acad Sci* 2008; **105**: 20964–20969.

126 Barria A, Muller D, Derkach V, Griffith LC, Soderling TR. Regulatory phosphorylation of AMPA-type glutamate receptors by CaM-KII during long-term potentiation. *Science* 1997; **276**: 2042–5.

127 Omkumar R V, Kiely MJ, Rosenstein AJ, Min KT, Kennedy MB. Identification of a phosphorylation site for calcium/calmodulindependent protein kinase II in the NR2B subunit of the N-methyl-D-aspartate receptor. *J Biol Chem* 1996; **271**: 31670–8.

128 Nair JS, DaFonseca CJ, Tjernberg A, Sun W, Darnell JE, Chait BT *et al.* Requirement of Ca2+ and CaMKII for Stat1 Ser-727 phosphorylation in response to IFN-gamma. *Proc Natl Acad Sci U S A* 2002; **99**: 5971–6.

129 Jain J, McCafffrey PG, Miner Z, Kerppola TK, Lambert JN, Verdine GL *et al.* The T-cell transcription factor NFATp is a substrate for calcineurin and interacts with Fos and Jun. *Nature* 1993; **365**: 352–355.

130 Kiani A, Viola JP, Lichtman AH, Rao A. Down-regulation of IL-4 gene transcription and control of Th2 cell differentiation by a mechanism involving NFAT1. *Immunity* 1997; **7**: 849–60.

131 Rengarajan J, Tang B, Glimcher LH. NFATc2 and NFATc3 regulate TH2 differentiation and modulate TCR-responsiveness of naïve TH cells. *Nat Immunol* 2002; **3**: 48–54.

132 Liu J, Farmer JD, Lane WS, Friedman J, Weissman I, Schreiber SL. Calcineurin is a common target of cyclophilin-cyclosporin A and FKBP-FK506 complexes. *Cell* 1991; **66**: 807–815.

133 Lee J-U, Kim L-K, Choi J-M. Revisiting the Concept of Targeting NFAT to Control T Cell Immunity and Autoimmune Diseases. *Front Immunol* 2018; **9**: 2747.

134 Szabadkai G, Bianchi K, Várnai P, De Stefani D, Wieckowski MR, Cavagna D *et al.* Chaperone-mediated coupling of endoplasmic reticulum and mitochondrial Ca2+ channels. *J Cell Biol* 2006; **175**: 901–11.

135 Rizzuto R, Marchi S, Bonora M, Aguiari P, Bononi A, De Stefani D *et al.* Ca(2+) transfer from the ER to mitochondria: when, how and why. *Biochim Biophys Acta* 2009; **1787**: 1342–51.

136 Denton RM. Regulation of mitochondrial dehydrogenases by calcium ions. *Biochim Biophys Acta* 2009; **1787**: 1309–16.

137 Bootman MD, Chehab T, Bultynck G, Parys JB, Rietdorf K. The regulation of autophagy by calcium signals: Do we have a consensus? *Cell Calcium* 2018; **70**: 32–46.

138 Harr MW, McColl KS, Zhong F, Molitoris JK, Distelhorst CW. Glucocorticoids downregulate Fyn and inhibit IP 3 -mediated calcium signaling to promote autophagy in T lymphocytes. *Autophagy* 2010; **6**: 912–921.

139 Singh A, Chagtoo M, Tiwari S, George N, Chakravarti B, Khan S *et al.* Inhibition of Inositol 1, 4, 5-Trisphosphate Receptor Induce Breast Cancer Cell Death Through Deregulated Autophagy

and Cellular Bioenergetics. *J Cell Biochem* 2017; **118**: 2333–2346.

140 Decuypere J-P, Welkenhuyzen K, Luyten T, Ponsaerts R, Dewaele M, Molgó J *et al.* Ins(1,4,5) P 3 receptor-mediated Ca 2+ signaling and autophagy induction are interrelated. *Autophagy* 2011; **7**: 1472–1489.

141 Luyten T, Welkenhuyzen K, Roest G, Kania E, Wang L, Bittremieux M *et al.* Resveratrol-induced autophagy is dependent on IP3Rs and on cytosolic Ca2+. *Biochim Biophys Acta - Mol Cell Res* 2017; **1864**: 947–956.

142 Yang J, Vais H, Gu W, Foskett JK. Biphasic regulation of InsP3 receptor gating by dual Ca2+ release channel BH3-like domains mediates Bcl-xL control of cell viability. *Proc Natl Acad Sci U S A* 2016; **113**: E1953-62.

143 Baumgartner HK, Gerasimenko J V, Thorne C, Ferdek P, Pozzan T, Tepikin A V *et al.* Calcium elevation in mitochondria is the main Ca2+ requirement for mitochondrial permeability transition pore (mPTP) opening. *J Biol Chem* 2009; **284**: 20796–803.

144 Parks RJ, Murphy E, Liu JC. Mitochondrial Permeability Transition Pore and Calcium Handling. *Methods Mol Biol* 2018; **1782**: 187–196.

145 Bonora M, Patergnani S, Ramaccini D, Morciano G, Pedriali G, Kahsay AE *et al.* Physiopathology of the Permeability Transition Pore: Molecular Mechanisms in Human Pathology. *Biomolecules* 2020; **10**. doi:10.3390/biom10070998.

146 Ouyang K, Leandro Gomez-Amaro R, Stachura DL, Tang H, Peng X, Fang X *et al.* Loss of IP3R-dependent Ca2+ signalling in thymocytes leads to aberrant development and acute lymphoblastic leukemia. *Nat Commun* 2014; **5**: 4814.

147 Aifantis I, Gounari F, Scorrano L, Borowski C, von Boehmer H. Constitutive pre-TCR signaling promotes differentiation through Ca2+ mobilization and activation of NF-κB and NFAT. *Nat Immunol* 2001; **2**: 403–409.

148 Melichar HJ, Ross JO, Herzmark P, Hogquist KA, Robey EA. Distinct Temporal Patterns of T Cell Receptor Signaling During Positive Versus Negative Selection in Situ. *Sci Signal* 2013; **6**. doi:10.1126/scisignal.2004400.

149 McCarl C-A, Khalil S, Ma J, Oh-hora M, Yamashita M, Roether J *et al.* Store-Operated Ca2+ Entry through ORAI1 Is Critical for T Cell-Mediated Autoimmunity and Allograft Rejection. *J Immunol* 2010; **185**: 5845–5858.

150 Beyersdorf N, Braun A, Vögtle T, Varga-Szabo D, Galdos RR, Kissler S *et al.* STIM1-Independent T Cell Development and Effector Function In Vivo. *J Immunol* 2009; **182**: 3390–3397.

151 Canté-Barrett K, Gallo EM, Winslow MM, Crabtree GR. Thymocyte Negative Selection Is Mediated by Protein Kinase C- and Ca2+-Dependent Transcriptional Induction of Bim. *J Immunol* 2006; **176**: 2299–2306.

152 Oh-hora M, Komatsu N, Pishyareh M, Feske S, Hori S, Taniguchi M *et al.* Agonist-Selected T Cell Development Requires Strong T Cell Receptor Signaling and Store-Operated Calcium Entry. *Immunity* 2013; **38**: 881–895.

153 Bennett CL, Christie J, Ramsdell F, Brunkow ME, Ferguson PJ, Whitesell L *et al.* The immune dysregulation, polyendocrinopathy, enteropathy, X-linked syndrome (IPEX) is caused by mutations of FOXP3. *Nat Genet* 2001; **27**: 20–21.

154 Schrank S, Barrington N, Stutzmann GE. Calcium-Handling Defects and Neurodegenerative Disease. *Cold Spring Harb Perspect Biol* 2020; **12**. doi:10.1101/cshperspect.a035212.

155 Mangolini A, de Stephanis L, Aguiari G. Role of calcium in polycystic kidney disease: From

signaling to pathology. *World J Nephrol* 2016; **5**: 76–83.

156 Zhang L, Zhang Y, Jiang Y, Dou X, Li S, Chai H *et al.* Upregulated SOCC and IP3R calcium channels and subsequent elevated cytoplasmic calcium signaling promote nonalcoholic fatty liver disease by inhibiting autophagy. *Mol Cell Biochem* 2021; **476**: 3163–3175.

157 Hund TJ, Ziman AP, Lederer WJ, Mohler PJ. The cardiac IP3 receptor: uncovering the role of 'the other' calcium-release channel. *J Mol Cell Cardiol* 2008; **45**: 159–61.

158 Partiseti M, Le Deist F, Hivroz C, Fischer A, Korn H, Choquet D. The calcium current activated by T cell receptor and store depletion in human lymphocytes is absent in a primary immunodeficiency. *J Biol Chem* 1994; **269**: 32327–35.

159 Zweifach A, Lewis RS. Rapid inactivation of depletion-activated calcium current (ICRAC) due to local calcium feedback. *J Gen Physiol* 1995; **105**: 209–26.

160 Premack BA, McDonald T V, Gardner P. Activation of Ca2+ current in Jurkat T cells following the depletion of Ca2+ stores by microsomal Ca(2+)-ATPase inhibitors. *J Immunol* 1994; **152**: 5226–40.

161 Vig M, Peinelt C, Beck A, Koomoa DL, Rabah D, Koblan-Huberson M *et al.* CRACM1 Is a Plasma Membrane Protein Essential for Store-Operated Ca 2+ Entry. *Science (80-)* 2006; **312**: 1220–1223.

162 Feske S, Gwack Y, Prakriya M, Srikanth S, Puppel S-H, Tanasa B *et al.* A mutation in Orai1 causes immune deficiency by abrogating CRAC channel function. *Nature* 2006; **441**: 179–185.

163 Picard C, McCarl C-A, Papolos A, Khalil S, Lüthy K, Hivroz C *et al.* STIM1 mutation associated with a syndrome of immunodeficiency and autoimmunity. *N Engl J Med* 2009; **360**: 1971–80.

164 Wu B, Rice L, Shrimpton J, Lawless D, Walker K, Carter C *et al.* Biallelic mutations in calcium release activated channel regulator 2A (CRACR2A) cause a primary immunodeficiency disorder. *Elife* 2021; **10**. doi:10.7554/eLife.72559.

165 Feske S, Picard C, Fischer A. Immunodeficiency due to mutations in ORAI1 and STIM1. *Clin Immunol* 2010; **135**: 169–82.

166 Lacruz RS, Feske S. Diseases caused by mutations in ORAI1 and STIM1. *Ann N Y Acad Sci* 2015; **1356**: 45–79.

167 Misceo D, Holmgren A, Louch WE, Holme PA, Mizobuchi M, Morales RJ *et al.* A Dominant STIM1 Mutation Causes Stormorken Syndrome. *Hum Mutat* 2014; **35**: 556–564.

168 Borsani O, Piga D, Costa S, Govoni A, Magri F, Artoni A *et al.* Stormorken Syndrome Caused by a p.R304W STIM1 Mutation: The First Italian Patient and a Review of the Literature. *Front Neurol* 2018; **9**. doi:10.3389/fneur.2018.00859.

169 Nesin V, Wiley G, Kousi M, Ong E-C, Lehmann T, Nicholl DJ *et al.* Activating mutations in STIM1 and ORAI1 cause overlapping syndromes of tubular myopathy and congenital miosis. *Proc Natl Acad Sci* 2014; **111**: 4197–4202.

170 Reilly MM, Murphy SM, Laurá M. Charcot-Marie-Tooth disease. *J Peripher Nerv Syst* 2011; **16**: 1–14.

171 SHY ME, LUPSKI JR, CHANCE PF, KLEIN CJ, DYCK PJ. Hereditary Motor and Sensory Neuropathies: An Overview of Clinical, Genetic, Electrophysiologic, and Pathologic Features. In: *Peripheral Neuropathy*. Elsevier, 2005, pp 1623–1658.

172 Barreto LCLS, Oliveira FS, Nunes PS, de França Costa IMP, Garcez CA, Goes GM *et al.* Epidemiologic Study of Charcot-Marie-Tooth Disease: A Systematic Review. *Neuroepidemiology* 2016; **46**: 157–165.

173 Szigeti K, Lupski JR. Charcot-Marie-Tooth disease. *Eur J Hum Genet* 2009; **17**: 703–10.

174 Timmerman V, Strickland A, Züchner S. Genetics of Charcot-Marie-Tooth (CMT) Disease within the Frame of the Human Genome Project Success. *Genes (Basel)* 2014; **5**: 13–32.

175 Juneja M, Burns J, Saporta MA, Timmerman V. Challenges in modelling the Charcot-Marie-Tooth neuropathies for therapy development. *J Neurol Neurosurg Psychiatry* 2019; **90**: 58–67.

176 Suter U, Scherer SS. Disease mechanisms in inherited neuropathies. *Nat Rev Neurosci* 2003; **4**: 714–726.

177 Evgrafov O V, Mersiyanova I, Irobi J, Van Den Bosch L, Dierick I, Leung CL *et al.* Mutant small heat-shock protein 27 causes axonal Charcot-Marie-Tooth disease and distal hereditary motor neuropathy. *Nat Genet* 2004; **36**: 602–6.

178 Antonellis A, Lee-Lin S-Q, Wasterlain A, Leo P, Quezado M, Goldfarb LG *et al.* Functional analyses of glycyl-tRNA synthetase mutations suggest a key role for tRNA-charging enzymes in peripheral axons. *J Neurosci* 2006; **26**: 10397–406.

179 Fernyhough P, Calcutt NA. Abnormal calcium homeostasis in peripheral neuropathies. *Cell Calcium* 2010; **47**: 130–9.

180 González-Sánchez P, Pla-Martín D, Martínez-Valero P, Rueda CB, Calpena E, Del Arco A *et al.* CMT-linked loss-of-function mutations in GDAP1 impair store-operated Ca2+ entry-stimulated respiration. *Sci Rep* 2017; **7**: 42993.

181 Cuesta A, Pedrola L, Sevilla T, García-Planells J, Chumillas MJ, Mayordomo F *et al.* The gene encoding ganglioside-induced differentiation-associated protein 1 is mutated in axonal Charcot-Marie-Tooth type 4A disease. *Nat Genet* 2002; **30**: 22–5.

182 González-Sánchez P, Satrústegui J, Palau F, Del Arco A. Calcium Deregulation and Mitochondrial Bioenergetics in GDAP1-Related CMT Disease. *Int J Mol Sci* 2019; **20**. doi:10.3390/ijms20020403.

183 Sun S-C, Ma D, Li M-Y, Zhang R-X, Huang C, Huang H-J *et al.* Mutations in C1orf194, encoding a calcium regulator, cause dominant Charcot-Marie-Tooth disease. *Brain* 2019; **142**: 2215–2229.

184 Furuichi T, Yoshikawa S, Miyawaki A, Wada K, Maeda N, Mikoshiba K. Primary structure and functional expression of the inositol 1,4,5-trisphosphate-binding protein P400. *Nature* 1989; **342**: 32–8.

185 Casey JP, Hirouchi T, Hisatsune C, Lynch B, Murphy R, Dunne AM *et al.* A novel gain-of-function mutation in the ITPR1 suppressor domain causes spinocerebellar ataxia with altered Ca2+ signal patterns. *J Neurol* 2017; **264**: 1444–1453.

186 Klar J, Hisatsune C, Baig SM, Tariq M, Johansson AC V, Rasool M *et al.* Abolished InsP3R2 function inhibits sweat secretion in both humans and mice. *J Clin Invest* 2014; **124**: 4773–80.

187 Inaba T, Hisatsune C, Sasaki Y, Ogawa Y, Ebisui E, Ogawa N *et al.* Mice Lacking Inositol 1,4,5-Trisphosphate Receptors Exhibit Dry Eye. *PLoS One* 2014; **9**: e99205.

188 Schabhüttl M, Wieland T, Senderek J, Baets J, Timmerman V, De Jonghe P *et al.* Whole-exome sequencing in patients with inherited neuropathies: outcome and challenges. *J Neurol* 2014; **261**: 970–982.

189 Laššuthová P, Šafka Brožková D, Krůtová M, Neupauerová J, Haberlová J, Mazanec R *et al.* Improving diagnosis of inherited peripheral neuropathies through gene panel analysis. *Orphanet J Rare Dis* 2016; **11**: 118.

190 Walker MD, Silverberg SJ. Primary hyperparathyroidism. *Nat Rev Endocrinol* 2018; **14**: 115–

125.

191 Cetani F, Pardi E, Aretini P, Saponaro F, Borsari S, Mazoni L *et al.* Whole exome sequencing in familial isolated primary hyperparathyroidism. *J Endocrinol Invest* 2020; **43**: 231–245.

192 Prasad A, Rabionet R, Espinet B, Zapata L, Puiggros A, Melero C *et al.* Identification of Gene Mutations and Fusion Genes in Patients with Sézary Syndrome. *J Invest Dermatol* 2016; **136**: 1490–1499.

193 Hedberg ML, Goh G, Chiosea SI, Bauman JE, Freilino ML, Zeng Y *et al.* Genetic landscape of metastatic and recurrent head and neck squamous cell carcinoma. *J Clin Invest* 2015; **126**: 169–180.

194 Rezuchova I, Hudecova S, Soltysova A, Matuskova M, Durinikova E, Chovancova B *et al.* Type 3 inositol 1,4,5-trisphosphate receptor has antiapoptotic and proliferative role in cancer cells. *Cell Death Dis* 2019; **10**: 186.

195 Shibao K, Fiedler MJ, Nagata J, Minagawa N, Hirata K, Nakayama Y *et al.* The type III inositol 1,4,5-trisphosphate receptor is associated with aggressiveness of colorectal carcinoma. *Cell Calcium* 2010; **48**: 315–23.

196 Ouyang K, Leandro Gomez-Amaro R, Stachura DL, Tang H, Peng X, Fang X *et al.* Loss of IP3R-dependent Ca2+ signalling in thymocytes leads to aberrant development and acute lymphoblastic leukemia. *Nat Commun* 2014; **5**: 4814.

197 Jayaraman T, Ondriasová E, Ondrias K, Harnick DJ, Marks AR. The inositol 1,4,5-trisphosphate receptor is essential for T-cell receptor signaling. *Proc Natl Acad Sci U S A* 1995; **92**: 6007–11.

198 Hirota J, Baba M, Matsumoto M, Furuichi T, Takatsu K, Mikoshiba K. T-cell-receptor signalling in inositol 1,4,5-trisphosphate receptor (IP3R) type-1-deficient mice: is IP3R type 1 essential for T-cell-receptor signalling? *Biochem J* 1998; **333 (Pt 3**: 615–9.

199 Sugawara H, Kurosaki M, Takata M, Kurosaki T. Genetic evidence for involvement of type 1, type 2 and type 3 inositol 1,4,5-trisphosphate receptors in signal transduction through the B-cell antigen receptor. *EMBO J* 1997; **16**: 3078–88.

200 Le Deist F, Hivroz C, Partiseti M, Thomas C, Buc H, Oleastro M *et al.* A primary T-cell immunodeficiency associated with defective transmembrane calcium influx. *Blood* 1995; **85**: 1053–1062.

201 Arige V, Yule DI. Spatial and temporal crosstalk between the cAMP and Ca2+ signaling systems. *Biochim Biophys Acta - Mol Cell Res* 2022; **1869**: 119293.

202 Scharenberg AM, Humphries LA, Rawlings DJ. Calcium signalling and cell-fate choice in B cells. *Nat Rev Immunol* 2007; **7**: 778–789.

203 Trebak M, Kinet J-P. Calcium signalling in T cells. *Nat Rev Immunol* 2019; **19**: 154–169.

204 Braiman A, Barda-Saad M, Sommers CL, Samelson LE. Recruitment and activation of PLCγ1 in T cells: a new insight into old domains. *EMBO J* 2006; **25**: 774–784.

205 Mikoshiba K. IP 3 receptor/Ca 2+ channel: from discovery to new signaling concepts. *J Neurochem* 2007; **102**: 1426–1446.

206 Liou J, Fivaz M, Inoue T, Meyer T. Live-cell imaging reveals sequential oligomerization and local plasma membrane targeting of stromal interaction molecule 1 after Ca 2+ store depletion. *Proc Natl Acad Sci* 2007; **104**: 9301–9306.

207 Zhang SL, Yu Y, Roos J, Kozak JA, Deerinck TJ, Ellisman MH *et al.* STIM1 is a Ca2+ sensor that activates CRAC channels and migrates from the Ca2+ store to the plasma membrane. *Nature* 2005; **437**: 902–905.

208 Lunz V, Romanin C, Frischauf I. STIM1 activation of Orai1. *Cell Calcium* 2019; **77**: 29–38.

209 Feske S. Calcium signalling in lymphocyte activation and disease. *Nat Rev Immunol* 2007; **7**: 690–702.

210 Dolmetsch RE, Lewis RS, Goodnow CC, Healy JI. Differential activation of transcription factors induced by Ca2+ response amplitude and duration. *Nature* 1997; **386**: 855–858.

211 Berridge MJ. The Inositol Trisphosphate/Calcium Signaling Pathway in Health and Disease. *Physiol Rev* 2016; **96**: 1261–1296.

212 Parys JB, Bultynck G. Calcium signaling in health, disease and therapy. *Biochim Biophys Acta - Mol Cell Res* 2018; **1865**: 1657–1659.

213 Pchitskaya E, Popugaeva E, Bezprozvanny I. Calcium signaling and molecular mechanisms underlying neurodegenerative diseases. *Cell Calcium* 2018; **70**: 87–94.

214 Silva-Rojas R, Laporte J, Böhm J. STIM1/ORAI1 Loss-of-Function and Gain-of-Function Mutations Inversely Impact on SOCE and Calcium Homeostasis and Cause Multi-Systemic Mirror Diseases. *Front Physiol* 2020; **11**. doi:10.3389/fphys.2020.604941.

215 Feske S, Draeger R, Peter H-H, Eichmann K, Rao A. The Duration of Nuclear Residence of NFAT Determines the Pattern of Cytokine Expression in Human SCID T Cells. *J Immunol* 2000; **165**: 297–305.

216 Milner JD, Fasth A, Etzioni A. Autoimmunity in Severe Combined Immunodeficiency (SCID): Lessons from Patients and Experimental Models. *J Clin Immunol* 2008; **28**: 29–33.

217 Fischer A, Provot J, Jais J-P, Alcais A, Mahlaoui N, Adoue D *et al.* Autoimmune and inflammatory manifestations occur frequently in patients with primary immunodeficiencies. *J Allergy Clin Immunol* 2017; **140**: 1388-1393.e8.

218 Liston A, Enders A, Siggs OM. Unravelling the association of partial T-cell immunodeficiency and immune dysregulation. *Nat Rev Immunol* 2008; **8**: 545–558.

219 Schmidt RE, Grimbacher B, Witte T. Autoimmunity and primary immunodeficiency: two sides of the same coin? *Nat Rev Rheumatol* 2018; **14**: 7–18.

220 Kerkhofs M, Seitaj B, Ivanova H, Monaco G, Bultynck G, Parys JB. Pathophysiological consequences of isoform-specific IP3 receptor mutations. *Biochim Biophys Acta - Mol Cell Res* 2018; **1865**: 1707–1717.

221 Terry LE, Alzayady KJ, Furati E, Yule DI. Inositol 1,4,5-Trisphosphate Receptor Mutations Associated with Human Disease. *Messenger* 2018; **6**: 29–44.

222 Parolin Schnekenberg R, Perkins EM, Miller JW, Davies WIL, D'Adamo MC, Pessia M *et al.* De novo point mutations in patients diagnosed with ataxic cerebral palsy. *Brain* 2015; **138**: 1817–1832.

223 Tada M, Nishizawa M, Onodera O. Roles of inositol 1,4,5-trisphosphate receptors in spinocerebellar ataxias. *Neurochem Int* 2016; **94**: 1–8.

224 Rönkkö J, Molchanova S, Revah-Politi A, Pereira EM, Auranen M, Toppila J *et al.* Dominant mutations in ITPR3 cause Charcot-Marie-Tooth disease. *Ann Clin Transl Neurol* 2020; **7**: 1962–1972.

225 Tang H, Wang H, Lin Q, Fan F, Zhang F, Peng X *et al.* Loss of IP3 Receptor–Mediated Ca2+ Release in Mouse B Cells Results in Abnormal B Cell Development and Function. *J Immunol* 2017; **199**: 570–580.

226 Foskett JK, White C, Cheung K-H, Mak D-OD. Inositol Trisphosphate Receptor Ca 2+ Release

Channels. *Physiol Rev* 2007; **87**: 593–658.

227 Emsley P, Lohkamp B, Scott WG, Cowtan K. Features and development of Coot. *Acta Crystallogr Sect D Biol Crystallogr* 2010; **66**: 486–501.

228 Adams PD, Afonine P V., Bunkóczi G, Chen VB, Davis IW, Echols N *et al.* PHENIX : a comprehensive Python-based system for macromolecular structure solution. *Acta Crystallogr Sect D Biol Crystallogr* 2010; **66**: 213–221.

229 Pettersen EF, Goddard TD, Huang CC, Couch GS, Greenblatt DM, Meng EC *et al.* UCSF Chimera?A visualization system for exploratory research and analysis. *J Comput Chem* 2004; **25**: 1605–1612.

230 Parys JB, De Smedt H, Missiaen L, Bootman MD, Sienaert I, Casteels R. Rat basophiliv leukemia cells as model system for inositol 1,4,5-trisphosphate receptor IV, a receptor of the type II family: functional comparison and immunological detection. *Cell Calcium* 1995; **17**: 239–249.

231 Ma H-T, Venkatachalam K, Parys JB, Gill DL. Modification of Store-operated Channel Coupling and Inositol Trisphosphate Receptor Function by 2-Aminoethoxydiphenyl Borate in DT40 Lymphocytes. *J Biol Chem* 2002; **277**: 6915–6922.

232 BULTYNCK G, SZLUFCIK K, KASRI NN, ASSEFA Z, CALLEWAERT G, MISSIAEN L *et al.* Thimerosal stimulates Ca2+ flux through inositol 1,4,5-trisphosphate receptor type 1, but not type 3, via modulation of an isoform-specific Ca2+-dependent intramolecular interaction. *Biochem J* 2004; **381**: 87–96.

233 Schindelin J, Arganda-Carreras I, Frise E, Kaynig V, Longair M, Pietzsch T *et al.* Fiji: an open-source platform for biological-image analysis. *Nat Methods* 2012; **9**: 676–682.

234 Schneider CA, Rasband WS, Eliceiri KW. NIH Image to ImageJ: 25 years of image analysis. *Nat Methods* 2012; **9**: 671–675.

235 Vaser R, Adusumalli S, Leng SN, Sikic M, Ng PC. SIFT missense predictions for genomes. *Nat Protoc* 2016; **11**: 1–9.

236 Quang D, Chen Y, Xie X. DANN: a deep learning approach for annotating the pathogenicity of genetic variants. *Bioinformatics* 2015; **31**: 761–763.

237 Zhang P, Bigio B, Rapaport F, Zhang S-Y, Casanova J-L, Abel L *et al.* PopViz: a webserver for visualizing minor allele frequencies and damage prediction scores of human genetic variations. *Bioinformatics* 2018; **34**: 4307–4309.

238 Paknejad N, Hite RK. Structural basis for the regulation of inositol trisphosphate receptors by Ca2+ and IP3. *Nat Struct Mol Biol* 2018; **25**: 660–668.

239 Azumaya CM, Linton EA, Risener CJ, Nakagawa T, Karakas E. Cryo-EM structure of human type-3 inositol triphosphate receptor reveals the presence of a self-binding peptide that acts as an antagonist. *J Biol Chem* 2020; **295**: 1743–1753.

240 Soulsby MD, Wojcikiewicz RJH. The type III inositol 1,4,5-trisphosphate receptor is phosphorylated by cAMP-dependent protein kinase at three sites. *Biochem J* 2005; **392**: 493–497.

241 Hornbeck P V., Zhang B, Murray B, Kornhauser JM, Latham V, Skrzypek E. PhosphoSitePlus, 2014: mutations, PTMs and recalibrations. *Nucleic Acids Res* 2015; **43**: D512–D520.

242 Fan G, Baker MR, Wang Z, Seryshev AB, Ludtke SJ, Baker ML *et al.* Cryo-EM reveals ligand induced allostery underlying InsP3R channel gating. *Cell Res* 2018; **28**: 1158–1170.

243 Rao A, Luo C, Hogan PG. TRANSCRIPTION FACTORS OF THE NFAT FAMILY:Regulation and Function. *Annu Rev Immunol* 1997; **15**: 707–747.

244 Park Y-J, Yoo S-A, Kim M, Kim W-U. The Role of Calcium–Calcineurin–NFAT Signaling Pathway in Health and Autoimmune Diseases. *Front Immunol* 2020; **11**. doi:10.3389/fimmu.2020.00195.

245 Jasiulewicz A, Lisowska KA, Pietruczuk K, Frąckowiak J, Fulop T, Witkowski JM. Homeostatic 'bystander' proliferation of human peripheral blood B cells in response to polyclonal T-cell stimulation in vitro. *Int Immunol* 2015; **27**: 579–588.

246 Feske S. CRAC channelopathies. *Pflügers Arch - Eur J Physiol* 2010; **460**: 417–435.

247 Monkawa T, Miyawaki A, Sugiyama T, Yoneshima H, Yamamoto-Hino M, Furuichi T *et al.* Heterotetrameric Complex Formation of Inositol 1,4,5-Trisphosphate Receptor Subunits. *J Biol Chem* 1995; **270**: 14700–14704.

248 Chandrasekhar R, Alzayady KJ, Yule DI. Using concatenated subunits to investigate the functional consequences of heterotetrameric inositol 1,4,5-trisphosphate receptors. *Biochem Soc Trans* 2015; **43**: 364–370.

249 Futatsugi A, Nakamura T, Yamada MK, Ebisui E, Nakamura K, Uchida K *et al.* IP 3 Receptor Types 2 and 3 Mediate Exocrine Secretion Underlying Energy Metabolism. *Science (80-)* 2005; **309**: 2232–2234.

250 Uchida K, Aramaki M, Nakazawa M, Yamagishi C, Makino S, Fukuda K *et al.* Gene Knock-Outs of Inositol 1,4,5-Trisphosphate Receptors Types 1 and 2 Result in Perturbation of Cardiogenesis. *PLoS One* 2010; **5**: e12500.

251 Parys JB, Vervliet T. New Insights in the IP3 Receptor and Its Regulation. 2020, pp 243–270.

252 Taylor CW, Genazzani AA, Morris SA. Expression of inositol trisphosphate receptors. *Cell Calcium* 1999; **26**: 237–251.

253 Marchant JS, Taylor CW. Cooperative activation of IP3 receptors by sequential binding of IP3 and Ca2+ safeguards against spontaneous activity. *Curr Biol* 1997; **7**: 510–518.

254 des Georges A, Clarke OB, Zalk R, Yuan Q, Condon KJ, Grassucci RA *et al.* Structural Basis for Gating and Activation of RyR1. *Cell* 2016; **167**: 145-157.e17.

255 Schmitz EA, Takahashi H, Karakas E. Structural basis for activation and gating of IP3 receptors. *Nat Commun* 2022; **13**: 1408.

256 Bhanumathy C, da Fonseca PCA, Morris EP, Joseph SK. Identification of Functionally Critical Residues in the Channel Domain of Inositol Trisphosphate Receptors. *J Biol Chem* 2012; **287**: 43674–43684.

257 Feske S, Müller JM, Graf D, Kroczek RA, Dräger R, Niemeyer C *et al.* Severe combined immunodeficiency due to defective binding of the nuclear factor of activated T cells in T lymphocytes of two male siblings. *Eur J Immunol* 1996; **26**: 2119–2126.

258 Lian J, Cuk M, Kahlfuss S, Kozhaya L, Vaeth M, Rieux-Laucat F *et al.* ORAI1 mutations abolishing store-operated Ca2+ entry cause anhidrotic ectodermal dysplasia with immunodeficiency. *J Allergy Clin Immunol* 2018; **142**: 1297-1310.e11.

259 Schaballie H, Rodriguez R, Martin E, Moens L, Frans G, Lenoir C *et al.* A novel hypomorphic mutation in STIM1 results in a late-onset immunodeficiency. *J Allergy Clin Immunol* 2015; **136**: 816-819.e4.

260 Parry DA, Holmes TD, Gamper N, El-Sayed W, Hettiarachchi NT, Ahmed M *et al.* A homozygous STIM1 mutation impairs store-operated calcium entry and natural killer cell effector function without clinical immunodeficiency. *J Allergy Clin Immunol* 2016; **137**: 955-957.e8.

261 Fuchs S, Rensing-Ehl A, Speckmann C, Bengsch B, Schmitt-Graeff A, Bondzio I *et al.* Antiviral and Regulatory T Cell Immunity in a Patient with Stromal Interaction Molecule 1 Deficiency. *J Immunol* 2012; **188**: 1523–1533.

262 Rice L, Stockdale C, Berry I, O'Riordan S, Pysden K, Anwar R *et al.* A Report of Novel STIM1 Deficiency and 6-Year Follow-Up of Two Previous Cases Associated with Mild Immunological Phenotype. *J Clin Immunol* 2019; **39**: 249–256.

263 Hajnóczky G, Csordás G, Madesh M, Pacher P. Control of apoptosis by IP3and ryanodine receptor driven calcium signals. *Cell Calcium* 2000; **28**: 349–363.

264 Decuypere J-P, Monaco G, Bultynck G, Missiaen L, De Smedt H, Parys JB. The IP3 receptor–mitochondria connection in apoptosis and autophagy. *Biochim Biophys Acta - Mol Cell Res* 2011; **1813**: 1003–1013.

265 Laurá M, Pipis M, Rossor AM, Reilly MM. Charcot-Marie-Tooth disease and related disorders: an evolving landscape. *Curr Opin Neurol* 2019; **32**: 641–650.

266 Pareyson D, Saveri P, Pisciotta C. New developments in Charcot-Marie-Tooth neuropathy and related diseases. *Curr Opin Neurol* 2017; **30**: 471–480.

267 Ivanova H, Vervliet T, Missiaen L, Parys JB, De Smedt H, Bultynck G. Inositol 1,4,5-trisphosphate receptor-isoform diversity in cell death and survival. *Biochim Biophys Acta* 2014; **1843**: 2164–83.

268 Wojcikiewicz RJ. Type I, II, and III inositol 1,4,5-trisphosphate receptors are unequally susceptible to down-regulation and are expressed in markedly different proportions in different cell types. *J Biol Chem* 1995; **270**: 11678–83.

269 Gerber S, Alzayady KJ, Burglen L, Brémond-Gignac D, Marchesin V, Roche O *et al.* Recessive and Dominant De Novo ITPR1 Mutations Cause Gillespie Syndrome. *Am J Hum Genet* 2016; **98**: 971–980.

270 Huang L, Chardon JW, Carter MT, Friend KL, Dudding TE, Schwartzentruber J *et al.* Missense mutations in ITPR1 cause autosomal dominant congenital nonprogressive spinocerebellar ataxia. *Orphanet J Rare Dis* 2012; **7**: 67.

271 McEntagart M, Williamson KA, Rainger JK, Wheeler A, Seawright A, De Baere E *et al.* A Restricted Repertoire of De Novo Mutations in ITPR1 Cause Gillespie Syndrome with Evidence for Dominant-Negative Effect. *Am J Hum Genet* 2016; **98**: 981–992.

272 van de Leemput J, Chandran J, Knight MA, Holtzclaw LA, Scholz S, Cookson MR *et al.* Deletion at ITPR1 underlies ataxia in mice and spinocerebellar ataxia 15 in humans. *PLoS Genet* 2007; **3**: e108.

273 Wagner M, Osborn DPS, Gehweiler I, Nagel M, Ulmer U, Bakhtiari S *et al.* Bi-allelic variants in RNF170 are associated with hereditary spastic paraplegia. *Nat Commun* 2019; **10**: 4790.

274 Wright FA, Bonzerato CG, Sliter DA, Wojcikiewicz RJH. The erlin2 T65I mutation inhibits erlin1/2 complex-mediated inositol 1,4,5-trisphosphate receptor ubiquitination and phosphatidylinositol 3-phosphate binding. *J Biol Chem* 2018; **293**: 15706–15714.

275 Rosa N, Sneyers F, Parys JB, Bultynck G. Type 3 IP3 receptors: The chameleon in cancer. *Int Rev Cell Mol Biol* 2020; **351**: 101–148.

276 Sneyers F, Rosa N, Bultynck G. Type 3 IP3 receptors driving oncogenesis. *Cell Calcium* 2020; **86**: 102141.

277 Ylikallio E, Konovalova S, Dhungana Y, Hilander T, Junna N, Partanen J V *et al.* Truncated HSPB1 causes axonal neuropathy and impairs tolerance to unfolded protein stress. *BBA Clin* 2015; **3**: 233–42.

278 Crépel V, Aronov D, Jorquera I, Represa A, Ben-Ari Y, Cossart R. A parturition-associated nonsynaptic coherent activity pattern in the developing hippocampus. *Neuron* 2007; **54**: 105–20.

279 Bonifazi P, Goldin M, Picardo MA, Jorquera I, Cattani A, Bianconi G *et al.* GABAergic hub neurons orchestrate synchrony in developing hippocampal networks. *Science* 2009; **326**: 1419–24.

280 Zhu X, Petrovski S, Xie P, Ruzzo EK, Lu Y-F, McSweeney KM *et al.* Whole-exome sequencing in undiagnosed genetic diseases: interpreting 119 trios. *Genet Med* 2015; **17**: 774–81.

281 Fan G, Baker ML, Wang Z, Baker MR, Sinyagovskiy PA, Chiu W *et al.* Gating machinery of InsP3R channels revealed by electron cryomicroscopy. *Nature* 2015; **527**: 336–41.

282 Toews JC, Schram V, Weerth SH, Mignery GA, Russell JT. Signaling proteins in the axoglial apparatus of sciatic nerve nodes of Ranvier. *Glia* 2007; **55**: 202–13.

283 Fecto F, Shi Y, Huda R, Martina M, Siddique T, Deng H-X. Mutant TRPV4-mediated toxicity is linked to increased constitutive function in axonal neuropathies. *J Biol Chem* 2011; **286**: 17281–91.

284 Zhang CL, Ho PL, Kintner DB, Sun D, Chiu SY. Activity-dependent regulation of mitochondrial motility by calcium and Na/K-ATPase at nodes of Ranvier of myelinated nerves. *J Neurosci* 2010; **30**: 3555–66.

285 Gentil BJ, Cooper L. Molecular basis of axonal dysfunction and traffic impairments in CMT. *Brain Res Bull* 2012; **88**: 444–53.

286 Auer-Grumbach M, Olschewski A, Papić L, Kremer H, McEntagart ME, Uhrig S *et al.* Alterations in the ankyrin domain of TRPV4 cause congenital distal SMA, scapuloperoneal SMA and HMSN2C. *Nat Genet* 2010; **42**: 160–4.

287 Woolums BM, McCray BA, Sung H, Tabuchi M, Sullivan JM, Ruppell KT *et al.* TRPV4 disrupts mitochondrial transport and causes axonal degeneration via a CaMKII-dependent elevation of intracellular Ca2. *Nat Commun* 2020; **11**: 2679.

288 Deng H-X, Klein CJ, Yan J, Shi Y, Wu Y, Fecto F *et al.* Scapuloperoneal spinal muscular atrophy and CMT2C are allelic disorders caused by alterations in TRPV4. *Nat Genet* 2010; **42**: 165–9.

289 Landouré G, Zdebik AA, Martinez TL, Burnett BG, Stanescu HC, Inada H *et al.* Mutations in TRPV4 cause Charcot-Marie-Tooth disease type 2C. *Nat Genet* 2010; **42**: 170–4.

290 Chow CY, Zhang Y, Dowling JJ, Jin N, Adamska M, Shiga K *et al.* Mutation of FIG4 causes neurodegeneration in the pale tremor mouse and patients with CMT4J. *Nature* 2007; **448**: 68–72.

291 Senderek J, Bergmann C, Weber S, Ketelsen U-P, Schorle H, Rudnik-Schöneborn S *et al.* Mutation of the SBF2 gene, encoding a novel member of the myotubularin family, in Charcot-Marie-Tooth neuropathy type 4B2/11p15. *Hum Mol Genet* 2003; **12**: 349–56.

292 Rossi A, Pizzo P, Filadi R. Calcium, mitochondria and cell metabolism: A functional triangle in bioenergetics. *Biochim Biophys acta Mol cell Res* 2019; **1866**: 1068–1078.

293 de Brito OM, Scorrano L. Mitofusin 2 tethers endoplasmic reticulum to mitochondria. *Nature* 2008; **456**: 605–10.

294 Perez-Siles G, Ly C, Grant A, Drew AP, Yiu EM, Ryan MM *et al.* Pathogenic mechanisms underlying X-linked Charcot-Marie-Tooth neuropathy (CMTX6) in patients with a pyruvate dehydrogenase kinase 3 mutation. *Neurobiol Dis* 2016; **94**: 237–44.

295 Larrea D, Pera M, Gonnelli A, Quintana-Cabrera R, Akman HO, Guardia-Laguarta C *et al.* MFN2 mutations in Charcot-Marie-Tooth disease alter mitochondria-associated ER membrane

function but do not impair bioenergetics. *Hum Mol Genet* 2019; **28**: 1782–1800.

296 Streb H, Irvine RF, Berridge MJ, Schulz I. Release of Ca2+ from a nonmitochondrial intracellular store in pancreatic acinar cells by inositol-1,4,5-trisphosphate. *Nature* 1983; **306**: 67–69.

297 Streb H, Bayerdörffer E, Haase W, Irvine RF, Schulz I. Effect of inositol-1,4,5-trisphosphate on isolated subcellular fractions of rat pancreas. *J Membr Biol* 1984; **81**: 241–253.

298 Berridge MJ. Inositol trisphosphate and calcium signalling. *Nature* 1993; **361**: 315–325.

299 Chin K, Cade C, Brostrom C, Galuska E, Brostrom M. Calcium-dependent regulation of protein synthesis at translational initiation in eukaryotic cells. *J Biol Chem* 1987; **262**: 16509–16514.

300 NICOTERA P, ORRENIUS S. Ca 2+ and Cell Death. *Ann N Y Acad Sci* 1992; **648**: 17–27.

301 Berridge MJ, Bootman MD, Lipp P. Calcium - a life and death signal. *Nature* 1998; **395**: 645–648.

302 Mattson MP, Chan SL. Calcium orchestrates apoptosis. *Nat Cell Biol* 2003; **5**: 1041–1043.

303 Harr MW, Distelhorst CW. Apoptosis and Autophagy: Decoding Calcium Signals that Mediate Life or Death. *Cold Spring Harb Perspect Biol* 2010; **2**: a005579–a005579.

304 Goonasekera SA, Molkentin JD. Unraveling the secrets of a double life: Contractile versus signaling Ca2+ in a cardiac myocyte. *J Mol Cell Cardiol* 2012; **52**: 317–322.

305 Mignery GA, Südhof TC, Takei K, De Camilli P. Putative receptor for inositol 1,4,5-trisphosphate similar to ryanodine receptor. *Nature* 1989; **342**: 192–195.

306 Patel S, Joseph SK, Thomas AP. Molecular properties of inositol 1,4,5-trisphosphate receptors. *Cell Calcium* 1999; **25**: 247–264.

307 Onoue H, Tanaka H, Tanaka K, Doira N, Ito Y. Heterooligomer of Type 1 and Type 2 Inositol 1, 4, 5-Trisphosphate Receptor Expressed in Rat Liver Membrane Fraction Exists as Tetrameric Complex. *Biochem Biophys Res Commun* 2000; **267**: 928–933.

308 Joseph SK, Bokkala S, Boehning D, Zeigler S. Factors Determining the Composition of Inositol Trisphosphate Receptor Hetero-oligomers Expressed in COS Cells. *J Biol Chem* 2000; **275**: 16084–16090.

309 Iwai M, Michikawa T, Bosanac I, Ikura M, Mikoshiba K. Molecular Basis of the Isoform-specific Ligand-binding Affinity of Inositol 1,4,5-Trisphosphate Receptors. *J Biol Chem* 2007; **282**: 12755–12764.

310 Yoshikawa F, Morita M, Monkawa T, Michikawa T, Furuichi T, Mikoshiba K. Mutational Analysis of the Ligand Binding Site of the Inositol 1,4,5-Trisphosphate Receptor. *J Biol Chem* 1996; **271**: 18277–18284.

311 Ramos-Franco J, Galvan D, Mignery GA, Fill M. Location of the Permeation Pathway in the Recombinant Type 1 Inositol 1,4,5-Trisphosphate Receptor. *J Gen Physiol* 1999; **114**: 243–250.

312 Boehning D, Mak D-OD, Foskett JK, Joseph SK. Molecular Determinants of Ion Permeation and Selectivity in Inositol 1,4,5-Trisphosphate Receptor Ca2+ Channels. *J Biol Chem* 2001; **276**: 13509–13512.

313 Schug ZT, da Fonseca PCA, Bhanumathy CD, Wagner L, Zhang X, Bailey B *et al.* Molecular Characterization of the Inositol 1,4,5-Trisphosphate Receptor Pore-forming Segment. *J Biol Chem* 2008; **283**: 2939–2948.

314 Yule DI, Betzenhauser MJ, Joseph SK. Linking structure to function: Recent lessons from inositol 1,4,5-trisphosphate receptor mutagenesis. *Cell Calcium* 2010; **47**: 469–479.

315 Baker MR, Fan G, Serysheva II. Structure of IP3R channel: high-resolution insights from cryo-EM. *Curr Opin Struct Biol* 2017; **46**: 38–47.

316 Hamada K, Miyatake H, Terauchi A, Mikoshiba K. IP 3 -mediated gating mechanism of the IP 3 receptor revealed by mutagenesis and X-ray crystallography. *Proc Natl Acad Sci* 2017; **114**: 4661–4666.

317 Joseph SK, Boehning D, Pierson S, Nicchitta C V. Membrane Insertion, Glycosylation, and Oligomerization of Inositol Trisphosphate Receptors in a Cell-free Translation System. *J Biol Chem* 1997; **272**: 1579–1588.

318 Joseph SK, Lin C, Pierson S, Thomas AP, Maranto AR. Heteroligomers of Type-I and Type-III Inositol Trisphosphate Receptors in WB Rat Liver Epithelial Cells. *J Biol Chem* 1995; **270**: 23310–23316.

319 Maranto AR. Primary structure, ligand binding, and localization of the human type 3 inositol 1,4,5-trisphosphate receptor expressed in intestinal epithelium. *J Biol Chem* 1994; **269**: 1222–1230.

320 Matsumoto M, Nakagawa T, Inoue T, Nagata E, Tanaka K, Takano H *et al.* Ataxia and epileptic seizures in mice lacking type 1 inositol 1,4,5-trisphosphate receptor. *Nature* 1996; **379**: 168–171.

321 Street VA, Bosma MM, Demas VP, Regan MR, Lin DD, Robinson LC *et al.* The Type 1 Inositol 1,4,5-Trisphosphate Receptor Gene Is Altered in the opisthotonos Mouse. *J Neurosci* 1997; **17**: 635–645.

322 Dudding TE, Friend K, Schofield PW, Lee S, Wilkinson IA, Richards RI. Autosomal dominant congenital non-progressive ataxia overlaps with the SCA15 locus. *Neurology* 2004; **63**: 2288–2292.

323 Hara K, Shiga A, Nozaki H, Mitsui J, Takahashi Y, Ishiguro H *et al.* Total deletion and a missense mutation of ITPR1 in Japanese SCA15 families. *Neurology* 2008; **71**: 547–551.

324 Ganesamoorthy D, Bruno DL, Schoumans J, Storey E, Delatycki MB, Zhu D *et al.* Development of a Multiplex Ligation-Dependent Probe Amplification Assay for Diagnosis and Estimation of the Frequency of Spinocerebellar Ataxia Type 15. *Clin Chem* 2009; **55**: 1415–1418.

325 Ohba C, Osaka H, Iai M, Yamashita S, Suzuki Y, Aida N *et al.* Diagnostic utility of whole exome sequencing in patients showing cerebellar and/or vermis atrophy in childhood. *Neurogenetics* 2013; **14**: 225–232.

326 Fogel BL, Lee H, Deignan JL, Strom SP, Kantarci S, Wang X *et al.* Exome Sequencing in the Clinical Diagnosis of Sporadic or Familial Cerebellar Ataxia. *JAMA Neurol* 2014; **71**: 1237.

327 Gonzaga-Jauregui C, Harel T, Gambin T, Kousi M, Griffin LB, Francescatto L *et al.* Exome Sequence Analysis Suggests that Genetic Burden Contributes to Phenotypic Variability and Complex Neuropathy. *Cell Rep* 2015; **12**: 1169–1183.

328 Sasaki M, Ohba C, Iai M, Hirabayashi S, Osaka H, Hiraide T *et al.* Sporadic infantile-onset spinocerebellar ataxia caused by missense mutations of the inositol 1,4,5-triphosphate receptor type 1 gene. *J Neurol* 2015; **262**: 1278–1284.

329 Valencia CA, Husami A, Holle J, Johnson JA, Qian Y, Mathur A *et al.* Clinical Impact and Cost-Effectiveness of Whole Exome Sequencing as a Diagnostic Tool: A Pediatric Center's Experience. *Front Pediatr* 2015; **3**. doi:10.3389/fped.2015.00067.

330 Shadrina MI, Shulskaya M V., Klyushnikov SA, Nikopensius T, Nelis M, Kivistik PA *et al.* ITPR1 gene p.Val1553Met mutation in Russian family with mild Spinocerebellar ataxia. *Cerebellum & Ataxias* 2016; **3**: 2.

331 Barresi S, Niceta M, Alfieri P, Brankovic V, Piccini G, Bruselles A *et al.* Mutations in the IRBIT

domain of ITPR1 are a frequent cause of autosomal dominant nonprogressive congenital ataxia. *Clin Genet* 2017; **91**: 86–91.

332 Das J, Lilleker J, Shereef H, Ealing J. Missense mutation in the ITPR1 gene presenting with ataxic cerebral palsy: Description of an affected family and literature review. *Neurol Neurochir Pol* 2017; **51**: 497–500.

333 Dentici ML, Barresi S, Nardella M, Bellacchio E, Alfieri P, Bruselles A *et al.* Identification of novel and hotspot mutations in the channel domain of ITPR1 in two patients with Gillespie syndrome. *Gene* 2017; **628**: 141–145.

334 Hsiao C-T, Liu Y-T, Liao Y-C, Hsu T-Y, Lee Y-C, Soong B-W. Mutational analysis of ITPR1 in a Taiwanese cohort with cerebellar ataxias. *PLoS One* 2017; **12**: e0187503.

335 Klar J, Ali Z, Farooq M, Khan K, Wikström J, Iqbal M *et al.* A missense variant in ITPR1 provides evidence for autosomal recessive SCA29 with asymptomatic cerebellar hypoplasia in carriers. *Eur J Hum Genet* 2017; **25**: 848–853.

336 van Dijk T, Barth P, Reneman L, Appelhof B, Baas F, Poll-The BT. A de novo missense mutation in the inositol 1,4,5-triphosphate receptor type 1 gene causing severe pontine and cerebellar hypoplasia: Expanding the phenotype of ITPR1 -related spinocerebellar ataxia's. *Am J Med Genet Part A* 2017; **173**: 207–212.

337 Zambonin JL, Bellomo A, Ben-Pazi H, Everman DB, Frazer LM, Geraghty MT *et al.* Spinocerebellar ataxia type 29 due to mutations in ITPR1: a case series and review of this emerging congenital ataxia. *Orphanet J Rare Dis* 2017; **12**: 121.

338 Carvalho DR, Medeiros JEG, Ribeiro DSM, Martins BJAF, Sobreira NLM. Additional features of Gillespie syndrome in two Brazilian siblings with a novel ITPR1 homozygous pathogenic variant. *Eur J Med Genet* 2018; **61**: 134–138.

339 De Silva D, Williamson KA, Dayasiri KC, Suraweera N, Quinters V, Abeysekara H *et al.* Gillespie syndrome in a South Asian child: a case report with confirmation of a heterozygous mutation of the ITPR1 gene and review of the clinical and molecular features. *BMC Pediatr* 2018; **18**: 308.

340 Synofzik M, Helbig KL, Harmuth F, Deconinck T, Tanpaiboon P, Sun B *et al.* De novo ITPR1 variants are a recurrent cause of early-onset ataxia, acting via loss of channel function. *Eur J Hum Genet* 2018; **26**: 1623–1634.

341 Wang L, Hao Y, Yu P, Cao Z, Zhang J, Zhang X *et al.* Identification of a Splicing Mutation in ITPR1 via WES in a Chinese Early-Onset Spinocerebellar Ataxia Family. *The Cerebellum* 2018; **17**: 294–299.

342 Elert-Dobkowska E, Stepniak I, Krysa W, Ziora-Jakutowicz K, Rakowicz M, Sobanska A *et al.* Next-generation sequencing study reveals the broader variant spectrum of hereditary spastic paraplegia and related phenotypes. *Neurogenetics* 2019; **20**: 27–38.

343 Gorski MM, Lecchi A, Femia EA, La Marca S, Cairo A, Pappalardo E *et al.* Complications of whole-exome sequencing for causal gene discovery in primary platelet secretion defects. *Haematologica* 2019; **104**: 2084–2090.

344 Stendel C, Wagner M, Rudolph G, Klopstock T. Gillespie's Syndrome with Minor Cerebellar Involvement and No Intellectual Disability Associated with a Novel ITPR1 Mutation: Report of a Case and Literature Review. *Neuropediatrics* 2019; **50**: 382–386.

345 Neumann J, Van Nieuwenhove E, Terry LE, Staels F, Knebel TR, Welkenhuyzen K *et al.* Disrupted Ca2+ homeostasis and immunodeficiency in patients with functional IP3 receptor subtype 3 defects. *Cell Mol Immunol* 2022; **20**: 11–25.

346 Ando H, Hirose M, Mikoshiba K. Aberrant IP 3 receptor activities revealed by comprehensive analysis of pathological mutations causing spinocerebellar ataxia 29. *Proc Natl Acad Sci* 2018; **115**: 12259–12264.

347 Sun B, Ni M, Tian S, Guo W, Cai S, Sondergaard MT *et al.* A gain-of-function mutation in the ITPR1 gating domain causes male infertility in mice. *J Cell Physiol* 2022; **237**: 3305–3316.

348 Yamazaki H, Nozaki H, Onodera O, Michikawa T, Nishizawa M, Mikoshiba K. Functional characterization of the P1059L mutation in the inositol 1,4,5-trisphosphate receptor type 1 identified in a Japanese SCA15 family. *Biochem Biophys Res Commun* 2011; **410**: 754–758.

349 Alzayady KJ, Chandrasekhar R, Yule DI. Fragmented Inositol 1,4,5-Trisphosphate Receptors Retain Tetrameric Architecture and Form Functional Ca2+ Release Channels. *J Biol Chem* 2013; **288**: 11122–11134.

350 Arige V, Emrich SM, Yoast RE, Trebak M, Yule DI. A protocol for detecting elemental calcium signals (Ca2+ puffs) in mammalian cells using total internal reflection fluorescence microscopy. *STAR Protoc* 2021; **2**: 100618.

351 Emrich SM, Yoast RE, Xin P, Arige V, Wagner LE, Hempel N *et al.* Omnitemporal choreographies of all five STIM/Orai and IP3Rs underlie the complexity of mammalian Ca2+ signaling. *Cell Rep* 2021; **34**: 108760.

352 Ellefsen KL, Settle B, Parker I, Smith IF. An algorithm for automated detection, localization and measurement of local calcium signals from camera-based imaging. *Cell Calcium* 2014; **56**: 147–156.

353 Nagappa M, Sharma S, Taly AB. *Charcot-Marie-Tooth Disease*. 2023http://www.ncbi.nlm.nih.gov/pubmed/25430934.

354 Yoshikawa F, Iwasaki H, Michikawa T, Furuichi T, Mikoshiba K. Cooperative Formation of the Ligand-binding Site of the Inositol 1,4,5-Trisphosphate Receptor by Two Separable Domains. *J Biol Chem* 1999; **274**: 328–334.

355 Lock JT, Alzayady KJ, Yule DI, Parker I. All three IP 3 receptor isoforms generate Ca 2+ puffs that display similar characteristics. *Sci Signal* 2018; **11**. doi:10.1126/scisignal.aau0344.

356 Hogan PG, Rao A. Store-operated calcium entry: Mechanisms and modulation. *Biochem Biophys Res Commun* 2015; **460**: 40–49.

357 Zhang X, Xin P, Yoast RE, Emrich SM, Johnson MT, Pathak T *et al.* Distinct pharmacological profiles of ORAI1, ORAI2, and ORAI3 channels. *Cell Calcium* 2020; **91**: 102281.

358 Thillaiappan NB, Smith HA, Atakpa-Adaji P, Taylor CW. KRAP tethers IP3 receptors to actin and licenses them to evoke cytosolic Ca2+ signals. *Nat Commun* 2021; **12**: 4514.

359 Baker MR, Fan G, Seryshev AB, Agosto MA, Baker ML, Serysheva II. Cryo-EM structure of type 1 IP3R channel in a lipid bilayer. *Commun Biol* 2021; **4**: 625.

360 Bánsághi S, Golenár T, Madesh M, Csordás G, RamachandraRao S, Sharma K *et al.* Isoform- and Species-specific Control of Inositol 1,4,5-Trisphosphate (IP3) Receptors by Reactive Oxygen Species. *J Biol Chem* 2014; **289**: 8170–8181.

361 Joseph SK, Young MP, Alzayady K, Yule DI, Ali M, Booth DM *et al.* Redox regulation of type-I inositol trisphosphate receptors in intact mammalian cells. *J Biol Chem* 2018; **293**: 17464–17476.

362 Xiao H, Jedrychowski MP, Schweppe DK, Huttlin EL, Yu Q, Heppner DE *et al.* A Quantitative Tissue-Specific Landscape of Protein Redox Regulation during Aging. *Cell* 2020; **180**: 968-983.e24.

363 Chandrasekhar R, Alzayady KJ, Wagner LE, Yule DI. Unique Regulatory Properties of Heterotetrameric Inositol 1,4,5-Trisphosphate Receptors Revealed by Studying Concatenated Receptor Constructs. *J Biol Chem* 2016; **291**: 4846–4860.

364 Terry LE, Alzayady KJ, Wahl AM, Malik S, Yule DI. Disease-associated mutations in inositol 1,4,5-trisphosphate receptor subunits impair channel function. *J Biol Chem* 2020; **295**: 18160–18178.

365 Alzayady KJ, Wagner LE, Chandrasekhar R, Monteagudo A, Godiska R, Tall GG *et al.* Functional Inositol 1,4,5-Trisphosphate Receptors Assembled from Concatenated Homo- and Heteromeric Subunits. *J Biol Chem* 2013; **288**: 29772–29784.

366 Nicke A, Rettinger J, Schmalzing G. Monomeric and Dimeric Byproducts are the Principal Functional Elements of Higher Order P2X 1 Concatamers. *Mol Pharmacol* 2003; **63**: 243–252.

367 Furuichi T, Simon-Chazottes D, Fujino I, Yamada N, Hasegawa M, Miyawaki A *et al.* Widespread expression of inositol 1,4,5-trisphosphate receptor type 1 gene (Insp3r1) in the mouse central nervous system. *Receptors Channels* 1993; **1**: 11–24.

368 Hanemann CO. Hereditary demyelinating neuropathies: from gene to disease. *Neurogenetics* 2001; **3**: 53–57.

369 Jerath NU, Shy ME. Hereditary motor and sensory neuropathies: Understanding molecular pathogenesis could lead to future treatment strategies. *Biochim Biophys Acta - Mol Basis Dis* 2015; **1852**: 667–678.

370 Niemann A, Berger P, Suter U. Pathomechanisms of mutant proteins in Charcot-Marie-Tooth disease. *NeuroMolecular Med* 2006; **8**: 217–241.

371 Martínez-Gómez A, Dent MAR. Expression of IP3 receptor isoforms at the nodes of Ranvier in rat sciatic nerve. *Neuroreport* 2007; **18**: 447–450.

372 Mound A, Vautrin-Glabik A, Foulon A, Botia B, Hague F, Parys JB *et al.* Downregulation of type 3 inositol (1,4,5)-trisphosphate receptor decreases breast cancer cell migration through an oscillatory Ca2+ signal. *Oncotarget* 2017; **8**: 72324–72341.

373 Sakakura C, Hagiwara A, Fukuda K, Shimomura K, Takagi T, Kin S *et al.* Possible involvement of inositol 1,4,5-trisphosphate receptor type 3 (IP3R3) in the peritoneal dissemination of gastric cancers. *Anticancer Res* 2003; **23**: 3691–7.

374 Boutin B, Tajeddine N, Monaco G, Molgo J, Vertommen D, Rider M *et al.* Endoplasmic reticulum Ca2+ content decrease by PKA-dependent hyperphosphorylation of type 1 IP3 receptor contributes to prostate cancer cell resistance to androgen deprivation. *Cell Calcium* 2015; **57**: 312–320.

375 Ando H, Kawaai K, Bonneau B, Mikoshiba K. Remodeling of Ca2+ signaling in cancer: Regulation of inositol 1,4,5-trisphosphate receptors through oncogenes and tumor suppressors. *Adv Biol Regul* 2018; **68**: 64–76.

376 Fukuda N, Shirasu M, Sato K, Ebisui E, Touhara K, Mikoshiba K. Decreased olfactory mucus secretion and nasal abnormality in mice lacking type 2 and type 3 IP3 receptors. *Eur J Neurosci* 2008; **27**: 2665–2675.

377 Sato-Miyaoka M, Hisatsune C, Ebisui E, Ogawa N, Takahashi-Iwanaga H, Mikoshiba K. Regulation of hair shedding by the type 3 IP3 receptor. *J Invest Dermatol* 2012; **132**: 2137–47.

378 Papathanasiou P, Perkins AC, Cobb BS, Ferrini R, Sridharan R, Hoyne GF *et al.* Widespread Failure of Hematolymphoid Differentiation Caused by a Recessive Niche-Filling Allele of the Ikaros Transcription Factor. *Immunity* 2003; **19**: 131–144.

379 Neilson JR, Winslow MM, Hur EM, Crabtree GR. Calcineurin B1 Is Essential for Positive but

Not Negative Selection during Thymocyte Development. *Immunity* 2004; **20**: 255–266.

380 Adachi S, Iwata M. Duration of calcineurin and Erk signals regulates CD4/CD8 lineage commitment of thymocytes. *Cell Immunol* 2002; **215**: 45–53.

381 Yasutomo K, Doyle C, Miele L, Germain RN. The duration of antigen receptor signalling determines CD4+ versus CD8+ T-cell lineage fate. *Nature* 2000; **404**: 506–510.

382 Vaeth M, Wang Y-H, Eckstein M, Yang J, Silverman GJ, Lacruz RS *et al.* Tissue resident and follicular Treg cell differentiation is regulated by CRAC channels. *Nat Commun* 2019; **10**: 1183.

383 Hann J, Bueb J-L, Tolle F, Bréchard S. Calcium signaling and regulation of neutrophil functions: Still a long way to go. *J Leukoc Biol* 2020; **107**: 285–297.

384 Ma H-T, Beaven MA. Regulation of Ca2+ signaling with particular focus on mast cells. *Crit Rev Immunol* 2009; **29**: 155–86.

385 Maul-Pavicic A, Chiang SCC, Rensing-Ehl A, Jessen B, Fauriat C, Wood SM *et al.* ORAI1-mediated calcium influx is required for human cytotoxic lymphocyte degranulation and target cell lysis. *Proc Natl Acad Sci* 2011; **108**: 3324–3329.

386 Steinckwich N, Schenten V, Melchior C, Bréchard S, Tschirhart EJ. An Essential Role of STIM1, Orai1, and S100A8–A9 Proteins for Ca2+ Signaling and FcγR-Mediated Phagosomal Oxidative Activity. *J Immunol* 2011; **186**: 2182–2191.

387 Elling R, Keller B, Weidinger C, Häffner M, Deshmukh SD, Zee I *et al.* Preserved effector functions of human ORAI1- and STIM1-deficient neutrophils. *J Allergy Clin Immunol* 2016; **137**: 1587-1591.e7.

388 Chou J, Badran YR, Yee CSK, Bainter W, Ohsumi TK, Al-Hammadi S *et al.* A novel mutation in ORAI1 presenting with combined immunodeficiency and residual T-cell function. *J Allergy Clin Immunol* 2015; **136**: 479-482.e1.

389 McCarl C-A, Picard C, Khalil S, Kawasaki T, Röther J, Papolos A *et al.* ORAI1 deficiency and lack of store-operated Ca2+ entry cause immunodeficiency, myopathy, and ectodermal dysplasia. *J Allergy Clin Immunol* 2009; **124**: 1311-1318.e7.

390 Mendez-Echevarria A, Gonzalez-Granado LI, Allende LM, De Felipe B, Teresa DR, Calvo C *et al.* Fatal Pneumocystis jirovecii and Cytomegalovirus Infections in an Infant With Normal TRECs Count. *Pediatr Infect Dis J* 2019; **38**: 157–160.

391 Baloh RH. Mitochondrial dynamics and peripheral neuropathy. *Neuroscientist* 2008; **14**: 12–8.

392 Viader A, Sasaki Y, Kim S, Strickland A, Workman CS, Yang K *et al.* Aberrant Schwann cell lipid metabolism linked to mitochondrial deficits leads to axon degeneration and neuropathy. *Neuron* 2013; **77**: 886–98.

393 Prole DL, Taylor CW. Structure and Function of IP 3 Receptors. *Cold Spring Harb Perspect Biol* 2019; **11**: a035063.

394 Vanderheyden V, Devogelaere B, Missiaen L, De Smedt H, Bultynck G, Parys JB. Regulation of inositol 1,4,5-trisphosphate-induced Ca2+ release by reversible phosphorylation and dephosphorylation. *Biochim Biophys Acta - Mol Cell Res* 2009; **1793**: 959–970.

395 Sears RM, May DG, Roux KJ. BioID as a Tool for Protein-Proximity Labeling in Living Cells. 2019, pp 299–313.

396 Pengo N, Scolari M, Oliva L, Milan E, Mainoldi F, Raimondi A *et al.* Plasma cells require autophagy for sustainable immunoglobulin production. *Nat Immunol* 2013; **14**: 298–305.

397 Bezprozvanny Ilya, Watras J, Ehrlich BE. Bell-shaped calcium-response curves of lns(l,4,5)P3-

and calcium-gated channels from endoplasmic reticulum of cerebellum. *Nature* 1991; **351**: 751–754.

398 Suzuki J, Kanemaru K, Ishii K, Ohkura M, Okubo Y, Iino M. Imaging intraorganellar Ca2+ at subcellular resolution using CEPIA. *Nat Commun* 2014; **5**: 4153.

399 Lanzetti S, Di Biase V. Small Molecules as Modulators of Voltage-Gated Calcium Channels in Neurological Disorders: State of the Art and Perspectives. *Molecules* 2022; **27**: 1312.

400 Ojo AO, Held PJ, Port FK, Wolfe RA, Leichtman AB, Young EW *et al.* Chronic Renal Failure after Transplantation of a Nonrenal Organ. *N Engl J Med* 2003; **349**: 931–940.

401 Wu G, Weng FL, Balaraman V. Tacrolimus-induced encephalopathy and polyneuropathy in a renal transplant recipient. *Case Reports* 2013; **2013**: bcr2013201099–bcr2013201099.

402 Miller LW. Cyclosporine-Associated Neurotoxicity. *Circulation* 1996; **94**: 1209–1211.

403 Pirsch JD, Miller J, Deierhoi MH, Vincenti F, Filo RS. A comparison of tacrolimus (FK506) and cyclosporine for immunosuppression after cadaveric renal transplantation. FK506 Kidney Transplant Study Group. *Transplantation* 1997; **63**: 977–83.

404 Bechstein WO. Neurotoxicity of calcineurin inhibitors: impact and clinical management. *Transpl Int* 2000; **13**: 313–326.

405 de Groen PC, Aksamit AJ, Rakela J, Forbes GS, Krom RAF. Central Nervous System Toxicity after Liver Transplantation. *N Engl J Med* 1987; **317**: 861–866.

406 Palestine AG, Nussenblatt RB, Chan C-C. Side effects of systemic cyclosporine in patients not undergoing transplantation. *Am J Med* 1984; **77**: 652–656.

407 Gambardella J, Morelli MB, Wang X, Castellanos V, Mone P, Santulli G. The discovery and development of IP3 receptor modulators: an update. *Expert Opin Drug Discov* 2021; **16**: 709–718.

8 Scientific Summary

Hereditary mendelian disorders are a group of disorders caused by dominantly or recessively inherited variants in a single gene. Although specific disorders can be very rare with only single families reported in the literature, their overall prevalence is estimated to be rather high and poses a serious burden on the health system. With the advent of NGS techniques, the number of identified genes responsible for mendelian disorders has been rising exponentially but there is still a large number of phenotypes – and therefore patients – without a genetic diagnosis. This can not only be a psychological burden to the patients not knowing what is causing their disease and if/how it might affect future children, but also for clinicians as they cannot administer targeted treatments and may need to rely on trial-and-error approaches. It is therefore important to genetically investigate cases with a strong suspicion for a monogenic disorder in the absence of previously described phenotype-associated variants. The work presented in this thesis illustrates that there are yet to be identified genes that can cause human disease and adds *ITPR3*, the gene encoding the ER Ca^{2+} channel inositol 1,4,5-trisphosphate (IP_3) receptor subtype 3 (IP_3R3), as genetic cause for different clinical phenotypes.

In **chapter 3** we describe two patients from unrelated kindreds with variable severity of immunodeficiency. While the first patient suffered from early-onset severe combined immunodeficiency, requiring hematopoietic stem cell transplantation, with syndromic features such as dental enamel formation defects, thin hair and later Charcot-Marie-Tooth (CMT) disease, the second patient showed a milder phenotype with later onset and a diagnosis of combined variable immunodeficiency with autoimmune manifestations such as immune thrombocytopenia and autoimmune haemolytic anaemia. Within the *ITPR3* gene, we identified a shared damaging variant inherited from both fathers, an additional *de novo* variant in the first patient, and another private variant inherited from the mother in the second patient. While all heterozygous individuals were clinically healthy, primary cells from the patients showed abnormal IP_3-mediated Ca^{2+} flux and Ca^{2+} homeostasis and T cells from the second patient showed impaired downstream signalling resulting in reduced activation and proliferation upon T cell receptor engagement. In an in vitro model investigating the isolated signalling capacity of each variant we established that two variants behave as functional hypomorphs with residual signalling, while the *de novo* variant in the severe patient resulted in complete loss-of-function.

Our work presented in **chapter 4** describes two kindreds with an isolated presentation of CMT and confirms the suggested pathogenicity of variants in *ITPR3* derived from population-based screening studies as a cause for inherited peripheral neuropathy. A novel variant in *ITPR3* segregated with the phenotype in a three-generation family and primary fibroblasts of the patients indeed revealed abnormal Ca^{2+} homeostasis and IP_3-mediated Ca^{2+} signalling. Additionally, a single patient from an Ashkenazi Jewish family harboured the loss-of-function variant described in chapter 3 in heterozygous state.

To gain a better understanding of the functional impact of *ITPR3* variants associated with CMT, in **chapter 5** we performed in-depth investigations on the channel properties under resting and activating conditions. We focused on the two variants described in chapter 4 and additionally investigated one of the variants previously suggested as candidate variant causing CMT and identified through linkage analysis. While all three variants induced similar properties at resting conditions, resulting in increased Ca^{2+} leak from the ER lumen into the cytosol, their signalling upon IP_3-mediated activation was either impaired, absent, or increased. Nonetheless, they all resulted clinically in a CMT phenotype, suggesting that different pathomechanisms may underlie disease development.

Together, the presented studies underscore the importance of IP_3R3-mediated Ca^{2+} signalling in a number of different cell types and adds them to the list of candidate genes that should be considered in patients with immunodeficiency, peripheral neuropathy, or both.

Personal contribution, scientific acknowledgements and conflict of interest

Personal contribution

I wrote the introduction and discussion of this thesis and created the figures and tables used therein. For my personal contribution to each chapter please refer to the respective sections. Schematic figures in the introduction were created with biorender.com.

Chapter 3 – scientific acknowledgements

Author contributions

IM and RS selected the patients and were responsible for immunophenotypic characterization and obtaining ethics approval. EVN and FS identified the genetic target. SHB and AL conceptualized the study. **JN**, EVN, and LET performed the formal analysis. **JN**, EVN, LET, FS, TK, KW, KA, MRB, MG, MW, JB, IIS, and SS were responsible for the investigation. IS, LDW, FV, IM, DIY, GB, and RS provided resources. **JN**, EVN, LET, FS, SHB, and AL wrote the original draft. **JN**, LET, MRB, IIS, IM, DIY, GB, RS, SHB, and AL reviewed and edited the manuscript. **JN** and LET were responsible for the graphics. SHB and AL supervised the study. IIS, DIY, GB, RS, SHB, and AL acquired funding.

Acknowledgements

This work was supported by the VIB Grand Challenges Program, the KU Leuven C1 program, the European Union's Horizon 2020 research and innovation program under grant agreement No 779295 (to AL), the Biotechnology and Biological Sciences Research Council (BBSRC) through Institute Strategic Program Grant funding BBS/E/B/000C0427 and BBS/E/B/000C0428 and the KU Leuven BOFZAP start-up grant (to SH-B). Work in the Bultynck team was supported by grants from the Research Council of the KU Leuven (C14/19/99 and AKUL/19/34) and Research Foundation – Flanders (G.0818.21N; G.0945.22N). DIY is supported by the National Institutes of Health (NIH) R01-DE0014756 grant. MRB and IIS are supported by the NIH R01GM072804 grant (to IIS), the Welch Foundation Research Grant AU-2014-20190331 (to IIS), and the American Heart Association grant 18CDA34110086 (to MRB). IIS, DIY, and GB are in the FWO Scientific Research Network CaSign (W0.019.17N). IM and RS are FWO senior clinical investigator fellows. IM and RS are members of the European Reference Network for Rare Immunodeficiency, Autoinflammatory and Autoimmune Diseases (project ID No. 739543). JN, EVN, and FS are FWO fellows. The authors acknowledge the important contributions of Tomas Luyten, Pier-Andrée Penttila, Reena Chinnaraj and the KU Leuven FACS Core, and Stefanie Sente and Giorgia Bucciol for clinical trial support.

Conflict of interest

IM holds the CSL Chair in Primary Immunodeficiencies, paid to KU Leuven. The other authors of this work have no competing interests to disclose.

Chapter 4 – scientific acknowledgements

Author contributions

JR, SM, MA, **JN,** GB, SHB, AdL, CR, HT, and EY contributed to the conception and design of the study. JR, SM, MA, JT, **JN**, AP, and EY performed the experiments. JR, ARP, EMP, JK, AnL, **JN**, GB, and MBH contributed to the acquisition and analysis of data. JR and EY wrote the manuscript with input from all authors.

Acknowledgements

The authors thank the patients for participating in the study. Riitta Lehtinen and Jana Pennonen are acknowledged for technical assistance. FIMM Technology Centre's Sequencing Laboratory (FIMM SeqLab) is acknowledged for exome sequencing. This study was supported by grants from Academy of Finland Clinical Researcher Funding, University of Helsinki 3 year grant, Emil Aaltonen foundation, Neurocenter Finland and HUS Helsinki University hospital to EY; Academy of Finland (312438), Sigrid Juselius Foundation and University of Helsinki to HT; Academy of Finland (AK1308265) and the French National Agency for Research, ANR, Eranet Neuron III program (Acrobat) to CR; European Union's Horizon 2020 research and innovation programme under grant agreement No 779295, KU Leuven (C14/19/099 and AKUL/19/034). This publication was supported by the National Center for Advancing Translational Sciences, National Institutes of Health, through Grant Number UL1TR001873. The content is solely the responsibility of the authors and does not necessarily represent the official views of the NIH.

Conflict of interest

The authors of this work have no competing interests to disclose.

Chapter 5 – scientific acknowledgments

Author contributions

LET, VA, **JN**, AMW, TRK, JWC, and SM were involved in conducting the investigation. LET and VA were involved in the analysis and visualization of the data. LET and DIY were involved in the conceptualization of the research and writing the original draft. GB, SHB, and AL were involved in project administration providing resources and editing the final draft. DIY and GB acquired the funding for the study.

Acknowledgements

The Authors wish to thank members of the Yule lab for helpful comments throughout the course of these studies. The authors wish to thank Dr. Ian Parker (UC Irvine) and Dr. Jeffrey Lock (UC Irvine) for assistance and advice with FLIKA. We thank Dr. Irina Serysheva and Dr. Mariah Baker (University of Texas, Health Science Center at Houston) for helpful insights into the structural consequences of these missense mutations. Funding: This work was supported by the National Institutes of Health Grant NIH/DE0014756 to DIY and F31 NIH/DE030670 to AMW. Research G.B was supported by Foundation Flanders (G094522N) the Research Council of the KU Leuven (AKUL/19/34). GB and DIY are part of the FWO Scientific Research Network CaSign (W0.019.17N; W001422N).

Conflict of interest

The authors of this work have no competing interests to disclose.

Curriculum Vitae

Julika Neumann

Mechelsestraat 161/404 • 3000 Leuven
Phone: +49 15237009883
E-mail: julika.neumann@kuleuven.be

Work Experience

Since 03/2019	**PhD candidate, University of Leuven/VIB** *Group of Dr. Stéphanie Humblet-Baron* *Supported by FWO Fundamental Research grant*
05/2018 – 02/2019	**Master thesis, University Clinic of Freiburg** *Group of PD Dr. Marta Rizzi*
12/2017 – 03/2018	**Internship, Walter and Eliza Hall Institute, Melbourne** *Group of Prof. Dr. Philip Hodgkin / Dr. Vanessa Bryant* *Supported by DAAD international internship grant*
01/2017 – 10/2017	**iGEM (international genetically engineered machines) advisor** *Support of a student's team competing in an international research competition in the field of synthetic biology*
09/2016 – 03/2017	**Student assistant, Center for Chronic Immunodeficiency, Freiburg** *Group of Prof. Dr. Bodo Grimbacher*
03/2016 – 08/2016	**Bachelor thesis, Center for Chronic Immunodeficiency, Freiburg** *Group of Prof. Dr. Bodo Grimbacher*
01/2015 – 10/2015	**iGEM (international genetically engineered machines)** *Team member in an international research competition for students in thefield of synthetic biology*
05/2014 – 02/2015	**Student assistant, Molecular Embryology, University of Freiburg** *Institute of Anatomy and Cell Biology, group of Prof. Dr. Tanja Vogel*

Education

Since 03/2019	**University of Leuven/VIB Center for Brain and Disease Research** *PhD student Doctoral School of Biomedical Sciences* *Thesis Title: IP_3R3 variants as a novel form of hereditary disorders*
10/2016 – 02/2019	**University of Freiburg** *Master of Science Molecular Medicine* *Thesis Title: Modulation of B-cell activation via DAXX-dependent Fas signalling*

Languages

German, native speaker	*English, fluent*	*Dutch, fluent*
Spanish, good	*French, basic*	

Trainings and workshops

2023	**Introduction to a Career in Clinical Research**, *ECCRT, Leuven, Belgium*
2023	**ESID Summer School for Primary Immunodeficiencies**, *ESID, Athens, Greece*
2022	**GMP-GLP-GCP course**, *ECCRT, Leuven, Belgium*
2022	**Introduction to Git and GitHub**, *VIB, Leuven, Belgium*
2021	**R introduction**, *VIB, Leuven, Belgium*
2020	**Python introduction**, *VIB, Leuven, Belgium*
2020	**Basic statistics theory**, *VIB, Leuven, Belgium*
2020	**How to prepare effective presentation slides**, *Principiae, Leuven, Belgium*
2019	**Scientific writing and publishing**, *VIB/Cofactor, Leuven, Belgium*

Active conference participations

2021	**Translational Immunology Conference (Ghent)**, *Poster Presentation: "Disrupted Ca^{2+} homeostasis and immunodeficiency in patients with functional Inositol 1,4,5- trisphosphate receptor subtype 3 defects"*
2020	**19th Biennial Meeting of the European Society of Immunodeficiency (online)**, *Oral Presentation (late-breaking research): "A new genetic basis for PID: novel compound heterozygous mutations in Inositol 1,4,5-trisphosphate receptor subtype 3"*

Other engagements

2022-present	**Editor and writer "The Optimist"** (PhD Journal for and from PhD students)
2022/23	**Supervision Master Student** (Leana De Vuyst)
2022/23	**Supervision Master Student** (Vaasudevan Sridhar)
2020/21	**Supervision Master Student** (Margaux David)

List of publications

Gerbaux M, Roos E, Willemsen M, Staels F, **Neumann J**, *Bücken L, Haughton J, Yshii L, Dooley J, Schlenner S, Humblet-Baron S, Liston A. CTLA4-Ig Effectively Controls Clinical Deterioration and Immune Condition in a Murine Model of Foxp3 Deficiency. J Clin Immunol. 2023 Aug;43(6):1393-1402. doi: 10.1007/s10875-023-01462-2. Epub 2023 May 8. PMID: 37156988; PMCID: PMC10354160.*

Willemsen M, Barber JS, Nieuwenhove EV, Staels F, Gerbaux M, **Neumann J**, *Prezzemolo T, Pasciuto E, Lagou V, Boeckx N, Filtjens J, De Visscher A, Matthys P, Schrijvers R, Tousseyn T, O'Driscoll M, Bucciol G, Schlenner S, Meyts I, Humblet-*

Baron S, Liston A. Homozygous DBF4 mutation as a cause of severe congenital neutropenia. J Allergy Clin Immunol. 2023 Jul;152(1):266-277. doi: 10.1016/j.jaci.2023.02.016. Epub 2023 Feb 24. PMID: 36841265.

Roca CP, Burton OT, **Neumann J***, Tareen S, Whyte CE, Gergelits V, Veiga RV, Humblet-Baron S, Liston A. A cross entropy test allows quantitative statistical comparison of t-SNE and UMAP representations. Cell Rep Methods. 2023 Jan 13;3(1):100390. doi: 10.1016/j.crmeth.2022.100390. PMID: 36814837; PMCID: PMC9939422.*

Neumann J*, Van Nieuwenhove E, Terry LE, Staels F, Knebel TR, Welkenhuyzen K, Ahmadzadeh K, Baker MR, Gerbaux M, Willemsen M, Barber JS, Serysheva II, De Waele L,Vermeulen F, Schlenner S, Meyts I, Yule DI, Bultynck G, Schrijvers R, Humblet-Baron S, Liston A. Disrupted Ca^{2+} homeostasis and immunodeficiency in patients with functional IP3 receptor subtype 3 defects. Cell Mol Immunol, 2022. doi: 10.1038/s41423-022-00928-4.*

Terry LE, Arige V, **Neumann J***, Wahl AM, Knebel TR, Chaffer JW, Malik S, Liston A, Humblet-Baron S, Bultynck G, Yule DI. Missense mutations in inositol 1,4,5-trisphosphate receptor type 3 result in leaky Ca^{2+} channels and activation of store-operated Ca^{2+} entry. iScience, 2022. doi: 10.1016/j.isci.2022.105523.*

Willemsen M, Staels F, Gerbaux M, **Neumann J***, Schrijvers R, Meyts I, Humblet-Baron S, Liston A. DNA replication-associated inborn errors of immunity. J Allergy Clin Immunol, 2022. doi: 10.1016/j.jaci.2022.11.003.*

Staels F, De Keukeleere K, Kinnunen M, Keskitalo S, Lorenzetti F, Vanmeert M, PrezzemoloT, Pasciuto E, Lescrinier E, Bossuyt X, Gerbaux M, Willemsen M, **Neumann J***, Van Loo S, Corveleyn A, Willekens K, Stalmans I, Meyts I, Liston A, Humblet-Baron S, Seppänen M, Varjosalo M, Schrijvers R. Common variable immunodeficiency in two kindreds with heterogeneous phenotypes caused by novel heterozygous NFKB1 mutations. Front Immunol, 2022. doi: 10.3389/fimmu.2022.973543.*

Staels F, Lorenzetti F, De Keukeleere K, Willemsen M, Gerbaux M, **Neumann J***, Tousseyn T, Pasciuto E, De Munter P, Bossuyt X, Gijsbers R, Liston A, Humblet-Baron S, Schrijvers R.A Novel Homozygous Stop Mutation in IL23R Causes Mendelian Susceptibility to Mycobacterial Disease. J Clin Immuno,. 2022. doi: 10.1007/s10875-022-01320-7.*

Canti L, Humblet-Baron S*, Desombere I*,* **Neumann J***, *Pannus P, Heyndrickx L, Henry A,Servais S, Willems E, Ehx G, Goriely S, Seidel L, Michiels J, Willems B, Liston A, Ariën KK, Beguin Y, Goossens ME, Marchant A, Baron F. Predictors of neutralizing antibody responseto BNT162b2 vaccination in allogeneic hematopoietic stem cell transplant recipients. J Hematol Oncol, 2021. doi: 10.1186/s13045-021-01190-3.*

Neumann J*, Prezzemolo T, Vanderbeke L, Roca CP, Gerbaux M, Janssens S, Willemsen M, Burton O, Van Mol P, Van Herck Y; CONTAGIOUS co-authors, Wauters J, Wauters E, Liston A, Humblet-Baron S. Increased IL-10-producing regulatory T cells are characteristic ofsevere cases of COVID-19. Clin Transl Immunology, 2020. doi: 10.1002/cti2.1204.*

Van Nieuwenhove E, Barber JS, **Neumann J***, Smeets E, Willemsen M, Pasciuto E, Prezzemolo T, Lagou V, Seldeslachts L, Malengier-Devlies B, Metzemaekers M, Haßdenteufel S, Kerstens A, van der Kant R, Rousseau F, Schymkowitz J, Di Marino D, Lang S, Zimmermann R, Schlenner S, Munck S, Proost P, Matthys P, Devalck C, Boeckx N, Claessens F, Wouters C, Humblet-Baron S, Meyts I, Liston A. Defective Sec61α1 underlies anovel cause of autosomal dominant severe congenital neutropenia. J Allergy Clin Immunol, 2020. doi: 10.1016/j.jaci.2020.03.034.*

Rönkkö J, Molchanova S, Revah-Politi A, Pereira EM, Auranen M, Toppila J, Kvist J, LudwigA, **Neumann J***, Bultynck G, Humblet-Baron S, Liston A, Paetau A, Rivera C, Harms MB, Tyynismaa H, Ylikallio E. Dominant mutations in ITPR3 cause Charcot-Marie-Tooth disease.Ann Clin Transl Neurol, 2020. doi: 10.1002/acn3.51190.*

Bender J, Bognar S, Camagna M, Donauer JAM, Eble JW, Emig R, Fischer S, Jesser R, Keilholz L, Kokotek DMU, **Neumann J***, Nicklaus S, Oude Weernink RRQPT, Stühn LG, Wössner N, Krämer SD, Schwenk P, Gensch N, Roth G, Ulbrich MH. Multiplexed antibody detection from blood sera by immobilization of in vitro expressed antigens and label-free readout via imaging reflectometric interferometry (iRIf). Biosens Bioelectron. 2018 Sep 15;115:97-103. doi: 10.1016/j.bios.2018.05.022.*

Gámez-Díaz L, **Neumann J***, Jäger F, Proietti M, Felber F, Soulas-Sprauel P, Perruzza L, Grassi F, Kögl T, Aichele P, Kilimann M, Grimbacher B, Jung S. Immunological phenotype of the murine Lrba knockout. Immunol Cell Biol. 2017 Oct;95(9):789-802. doi: 10.1038/icb.2017.5*